THE UNIVERSITY *of* EDINBURGH

Numerical Modelling of Full Scale Tidal Turbines Using the Actuator Disc Approach

Anas Abdul Rahman

THE UNIVERSITY *of* EDINBURGH

Doctor of Philosophy

2017

To my dearest wife,

Noradina Nordin

& my loving parents,

Mama and Abah

Lay Summary

Of late, numerical simulation has become an indispensable tool in the marine renewable energy sector to study the impacts of tidal energy extraction on the surrounding environment. One of the methods used in modelling the presence of a tidal stream device in numerical model is to employ the actuator disc approach. This method characterises a turbine as a simple disc of similar dimensions to the rotor and is also utilised to approximate the forces exerted to the flow.

Nonetheless, as most actuator studies are limited to simulating a very small scale disc (e.g. rotor diameter of 0.1 meter), there is a notable research gap in understanding the actuator disc's capability for representing a full size tidal turbine (e.g. 16-20 meter rotor diameter) within a regional scale tidal model. Moreover, as simulation outputs are sensitive to the experience and knowledge of the users, it is also crucial that validation studies are conducted to help understand various numerical parameters involved in the computation.

In light of this, the objectives of this doctoral research are threefold: (a) to comprehend the advantages and disadvantages of conducting hydrodynamic tidal resources analysis using two distinct free-to-use software, namely Telemac3D and Delft3D, and select one suitable software tool for further simulations. In this case, Telemac3D was chosen; (b) to examine the influence of selected numerical parameters on the predicted wake characteristics due to the implementation of a full size actuator disc within a small idealised channel; (c) to gain insight into the validity and robustness of the actuator disc approach in a regional scale simulation using the experience acquired from the previous two objectives.

The area of interest in this work is the Inner Sound of the Pentland Firth, Orkney Waters, for which both Telemac3D and Delft3D were applied. The models were calibrated and validated with measured tidal levels and current speeds. Although both hydrodynamic models performed equally in predicting tidal parameters, further parametric analyses and device modelling were undertaken only with Telemac3D, due to its capability to perform robust parallel computing when unstructured mesh is implemented in the computational domain.

The sensitivity studies performed on the actuator disc within an idealised channel

illustrated flow behaviours that agreed with published literature. Consequently, this lends credence to the use of actuator disc approach as a means of representing tidal turbines within a regional scale simulation.

This study illustrated that the accuracy of a full scale actuator disc is highly influenced by the technique used in defining the disc's swept area within the model code. The results of the analyses are presented graphically, accompanied by a relevant statistical dataset to enable ease of reference by stakeholders.

Abstract

In recent years, the actuator disc approach which employs the Reynolds-Averaged Navier-Stokes (RANS) solvers has been extensively applied in wind and tidal energy field to estimate the wake of a horizontal axis turbine. This method is simpler to administer and requires moderate computational resources in modelling a tidal turbines rotor. Nonetheless, the use of actuator disc approximation in predicting the performance of tidal devices has been limited to studies involving an extremely small disc (e.g. rotor diameter of 0.1 meter). The drawback of a small scale actuator disc model is the overestimation of essential parameters such as the mesh density and the resolution of the vertical layers, making them impractical to be replicated in a regional scale model.

Hence, this study aims to explore the methodology on implementation of the Three-Dimensional (3D) actuator disc-RANS model in an ocean scale simulation. Additionally, this study also aspires to examine the sensitivity of the applied momentum source term and its validity in representing full-size tidal devices. Nonetheless, before the effectiveness of an actuator disc in a regional model can be tested, tidal flow models for the area of interest needed to be set up first. This was essential for two reasons: (a) to ensure accurate hydrodynamic flow conditions at the deployment site were replicated, (b) to give confidence in the outputs produced by the regional scale actuator disc simulations, since in-situ turbine measurement data from a real deployment site were difficult to source.

This research was undertaken in two stages; in the first stage, a numerical model which can simulate the tidal flow conditions of the deployment sites was constructed, and, in the second stage, the actuator disc method which is capable of modelling an array of real scale-sized tidal turbines rotors has been implemented.

In the first stage, tidal flow simulations of the Pentland Firth and Orkney Waters (PFOW) were conducted using two distinct open-source software – Telemac3D, which is a finite element based numerical model, and Delft3D, which is a finite difference based model. Detailed methodologies in developing a 3D tidal flow model for the PFOW using both numerical models were presented, where their functionality, as well as limitations were explored. In the calibration and validation processes, both models demonstrated excellent comparison against the measured data. However, Telemac3D

was selected for further modelling of the actuator disc considering the model's capability to perform parallel computing, together with its flexibility to combine both structured and unstructured mesh.

In the second stage, to examine the actuator disc's accuracy in modelling a full size tidal device, the momentum source term was initially applied in an idealised channel study, where the presence of a 20-meter diameter turbine was simulated for both single and array configurations. The following parameters were investigated: (i) size of the unstructured mesh utilised in the computational domain, (ii) variation in disc's thickness, (iii) resolution of the imposed structured grid to represent turbine's enclosure, (iv) variation in the vertical layers, and (v) influence of hydrostatic and non-hydrostatic formulations on the models' outputs. It is to be noted that the turbine's support structures have not been included in the modelling.

The predicted velocities and computed turbulence intensities from the models were compared against laboratory measurement data sourced from literature, where excellent agreement between the model outputs and the data from literature was observed. In essence, these studies highlighted the efficiency and robustness of the applied momentum source term in replicating the wake profiles and turbulence characteristics downstream of the disc, hence providing credence in implementing the actuator disc method for a regional scale application.

Subsequently, the validated actuator disc method was applied to the Inner Sound region of the Pentland Firth to simulate arrays of up to 32 tidal turbine rotors. The wake development, flow interactions with the rotor arrays, and flow recovery at the Inner Sound region have been successfully mapped. Also, this study highlighted the importance of employing optimal numerical margins, specifically for the structured grid and horizontal planes, as both parameters were relevant in defining the disc's swept area. As published materials on the implementation of actuator disc approach within a regional scale model is still scarce, it was aspired that this work could provide some evidence, guidance and examples of suggested best practice in effort to fill the research gap in modelling tidal turbine arrays using the actuator disc approach.

Acknowledgements

I am indebted to my principal supervisor, Dr. Vengatesan Venugopal, for the patient guidance, encouragement, and unrelenting support he has provided throughout my time as his student. His deep insights and unrivalled patience truly helped me at various stages of my research. Likewise, I would also like to express my sincere gratitude to my second supervisor, Prof. David Ingram for his valuable feedback during my first year PhD review.

Thanks are due to my office mates Atul Agarwal, Andy MacGillivray, Tay Zhi Yung, and Guangming Li, for everything that good office mates should be thanked for. Special mention also goes to Duncan Sutherland and Krisna for being there to listen when I needed an ear. Others I would like to thank personally for their help with this project are Reddy Nemalidinne and Jerome Thiebot for their innovative ideas and endless support during my darkest hours when I faced complications with my numerical models. In a similar vein thanks also to the wider community of the Institute for Energy Systems (IES) for always making me feel welcome. For doing what is often a thankless job I would like to thank the staff of the IT department within the School of Engineering.

In particular, I would like to thank the Ministry of Higher Education of Malaysia, and the Universiti Malaysia Perlis (UniMAP), not only for providing the funding which allowed me to undertake this research, but also for giving me the opportunity to attend conferences and meet so many interesting people.

I am forever thankful to my 'Geng Kedai Kopi' friends Emran, Adib and Sofwan for the endless discussions (and gossips) during lunch and coffee breaks - you should know that your encouragement worth more that I can express on paper.

Finally, my deep and sincere gratitude to my family for their continuous and unparalleled love, help and support. I am eternally grateful to my wonderful wife Dina Nordin, who has been my bedrock of support in completing this amazing, yet challenging journey. I am forever indebted to my parents - Abah and Mama for giving me the opportunities and experiences that have made me who I am, along with their endless thoughts and prayers. And not forgotten, my awesome siblings - Ayu, Asyraf and Anis for their continuous encouragement. This journey would not have been possible if not for my family, and I dedicate this milestone to them.

Declaration

I declare that this thesis was composed by myself, that the work contained herein is my own except where explicitly stated otherwise in the text, and that this work has not been submitted for any other degree or professional qualification except as specified.

Anas Rahman

Contents

List of Figures

List of Tables

Nomenclature

Δx	Structured grid spacing in x direction
Δx_t	Disc thickness
Δy	Structured grid spacing in y direction
Δz	Structured grid spacing in z direction
ε	Energy dissipation
∂t	Time step
θ	Ratio of turbine frontal area to the cross-sectional area of the surrounding flow passage (i.e. open area ratio)
A	Turbine swept area
a	Induction factor
C_p	Power coefficient
C_μ	Dimensionless constant of 0.009
C_T	Thrust coefficient
K	Resistance coefficient in computing turbine thrust force
k	Turbulent kinetic energy
ls	Turbulence length scale
lx	Structured grid property in x direction
ly	Structured grid property in y direction
lz	Structured grid property in z direction
n_p	n power law
P_w	Power produced by turbine
T_r	Turbine thrust
U_∞	Unperturbed flow velocity
U_{cut-in}	Cut in velocity
U_{def}	Velocity reduction experienced by the flow due to the presence of turbine
U_{rated}	Rated velocity
U_w	Velocity at any point downstream of the turbine
U_y	Velocity at a certain point (y) above the seabed
y^+	Wall function
δ	Boundary layer thickness
$\Delta 2m$	2 meter structured grid size

$\Delta 4m$	4 meter structured grid size
$\Delta\rho$	Variation of density around the reference density
Δt	Model time step
$\dot{m}$	mass flow rate
$\hat{z}$	Relative roughness
κ	von Karman's constant
λ	Average latitude
μ	Dynamic viscosity
ω	Earth's rotational velocity
$\overline{h}$	Mean water depth
$\overline{U}$	Depth-averaged velocity vector
$\overline{u}$	Mean stream-wise velocity in x direction
$\overline{x}_o$	Mean of observed (field) data
$\overrightarrow{\tau}_{d3d}$	Bed shear stress in Delft3D
$\overrightarrow{u_b}$	Magnitude of the horizontal velocity in the first layer just above the bed
$\overrightarrow{U}$	Velocity of current far enough from the wall
ρ	Water density
ρ_0	Reference density
σ	Sigma mesh transformation
τ_b	Bed shear-stress
$\tau_{b(3D)}$	Bed shear stress
ζ	Water level in Delft3D
B	Dimensionless blockage ratio
b,y	Channel width
C_{3d}	3D Chézy coefficient
d,y	Water depth in relation to a reference level
f	Coriolis force
F_x	Source term in the x direction (Telemac3D)
F_y	Source term in the y direction (Telemac3D)
F_z	Source term in the z direction (Telemac3D)
$F_{x,R}$	Reynolds stresses in the x direction (Delft3D)
$F_{y,R}$	Reynolds stresses in the y direction (Delft3D)
g	Acceleration of gravity (9.81 m/s)
H,h	Total water depth
K_s	Nikuradse roughness length
M_x	Source term in the x direction in Delft3D

M_y	Source term in the y direction in Delft3D
N	Sample size
n	Manning roughness coefficient
P	Mean pressure
P_{atm}	Atmospheric pressure
P_x	Pressure term from Boussinesq assumption in the x direction in Delft3D
P_y	Pressure term from Boussinesq assumption in the y direction in Delft3D
Q	Momentum source term (Telemac3D)
S_{d3d}	The term due to water discharge or withdrawal in Delft3D
S_i	Momentum source/sink term
T	Passive/active tracer (Telemac3D)
U	Velocity component in the x direction
u	Constant upstream velocity
u'	Instantaneous velocity fluctuation in x direction
U_c	Characteristic wave speed
U_i	Averaged velocity component
u_{rmse}	Standard deviation of velocity fluctuation
V	Velocity components in the y direction
v	Tracer diffusion coefficient
v_v	Eddy viscosity in vertical direction in Delft3D
W	Velocity components in the z direction
w	velocity components in the z direction
x_0	Observed (field) data
x_m	Model data
x_i	Spatial geometrical scale
z	Vertical space component
Z_s	Free surface elevation
D	Rotor diameter
l	Mesh edge length
Q	Volumetric flowrate

Abbreviations

2D Two-Dimensional.
3D Three-Dimensional.

ADCP Acoustic Doppler Current Profiler.
AHH Andritz Hydro Hammerfest.
ARL Atlantis Resources Limited.

BEM Blade element method.

CFD Computational Fluid Dynamics.
CFL Courant–Friedrichs–Lewy.

DNS Direct Numerical Simulation.

EDF Electricite de France.
EMEC European Marine Energy Centre.
EU European Union.

GEBCO 08 General Bathymetric Chart of the Oceans 2008.
GEODAS-NG GEOphysical DAta System - Next Generation.

HTM Horizontal Turbulence Model.

IHO International Hydrographic Organization.
IPCC Intergovernmental Panel on Climate Change.

LES Large Eddy Simulation.
LHNE National Hydraulic and Environment Laboratory.

MLWS Mean Low Water Springs.

NOAA National Oceanic and Atmospheric Administration.

PFOW Pentland Firth and Orkney Waters.

r Pearson's Correlation Coefficient.
RANS Reynolds-Averaged Navier-Stokes.

RMSE Root Mean Square Error.
ROMS Regional Ocean Modeling System.

SI Scatter Index.

TEC Tidal Energy Converters.
TI Turbulence Intensities.
TLP Tidal Lagoon Power.
TPXO7 TOPEX/Poseidon Global Inverse solution - version 7.
TPXO8 TOPEX/Poseidon Global Inverse solution - version 8.

UKMED UK Marine Energy Database.
UTM Universal Transverse Mercator.

VLX The University of Edinburgh's Linux Computers Cluster.
VTM Vertical Turbulence Model.

WGS 84 World Geodetic System 1984.

Chapter 1

Introduction

Over recent years, electricity generation from renewable technologies has been aggressively promoted by governments around the world partly due to the Intergovernmental Panel on Climate Change (IPCC)'s reports [1] on the unprecedented climate change observed over the decades to millennia. For perspective, with burgeoning global population, energy consumption worldwide in 2014 was recorded at 9500 million tonnes of oil equivalent (Mtoe) - more than double the 1973 figure at 4600 Mtoe [2].

While onshore wind has typically provided the largest growth in alternative energy over the last few decades, marine technologies (i.e. wave and tidal) are now quickly emerging as one of the viable options in meeting the world's energy demands. Nonetheless, the wave and tidal energy sector is still at an early stage of its development, presenting plenty of challenges to industries, researchers as well as regulators.

Specifically, Scotland is well placed to exploit its ocean energy potential to the fullest and deliver a sustainable, world-leading renewable energy industry. Studies have indicated that renewable resources from wind, wave and tidal on the Scottish Waters, especially near the Islands of the Western Isles, as well as Orkney and Shetland are considerable. Hence, it is no surprise that Scotland is expected to play a significant role in meeting the 2020 renewable targets set by both the UK and Scottish governments [3, 4]. Table 1.1 highlights the ambitious targets set by the Scottish government to reduce its dependency on conventional energy.

Interestingly, while the Scottish government is making enormous strides to reduce dependency from the North Sea's oil, and is well on its way to achieve longer term de-carbonisation objectives, UK still lags behind. Latest reports indicated that the UK is one of only three member states (besides Denmark and Poland) to become more dependent on imported energy in the last decade [8–10], while the European Union (EU) is making good progress towards the goal of using 20% of final energy consumption from renewable sources by 2020. To emphasize, the UK's figure is just

Table 1.1: Scotland's and UK's renewable targets.

Scottish targets

• 100% of electricity demand from renewables by 2020
• Achieved its target of 50% electricity demand equivalent from renewables by 2015 [5]
• Emission reduction target of 80% by 2050
• Interim target of 42% by 2020
• Under the newly presented Scottish Energy Strategy [6]
  ◦ 50% renewable energy target by 2030
  ◦ Reducing greenhouse gas emissions by 66% by 2032

UK targets
• 15% of total energy from renewables by 2020 • Currently at 8.2% [7] • 27% of total energy from renewables by 2030 • Emission reduction target 80% by 2050

8.2 per cent based on a 2017 report [7].

As of 2014, the share of renewables reached 16% of the gross final energy consumption of the EU. With the UK legally bound to provide for 15% of its energy needs—including 30% of its electricity, 12% of its heat, and 10% of its transport fuel—from renewable sources by 2020, this highlight the importance of Scotland to help push the figure forward to achieve the outlined targets. It has been disclosed that renewables are the single largest contributor to electricity generation in Scotland—higher than both nuclear generation (33%) and fossil fuel generation (28%), and made up approximately 26% of total UK renewable generation in 2015 [11].

The Pentland Firth and Orkney Waters (PFOW), which is located between the Orkney Islands and the northern tip of Scottish mainland, is known to has a significant proportion of UK's extractable tidal resource. This region is well known for the high speed of its tidal currents, and has consequently attracted significant attention as a possible site for the deployment of tidal energy converters. Two locations with the highest tidal stream velocities are at the Outer Sound, which is between the islands of Stroma and Swona, and also the Inner Sound, a channel between Stroma islands and the Scottish mainland.

Figure 1.1, published by Shields et al. [12], displays the mean spring velocity contour

of the PFOW regions, with current speed higher than 2.26 m/s was observed within the Outer Sound area. Additionally, the Inner Sound's mean spring velocity was recorded to be between 1.76-2.00 m/s. In particular, current speeds within these regions are highly influenced by local ocean topography, coastline, and also narrow constrictions (e.g. straits between two oceans), which consequently have an impact on the flows' direction [12, 13].

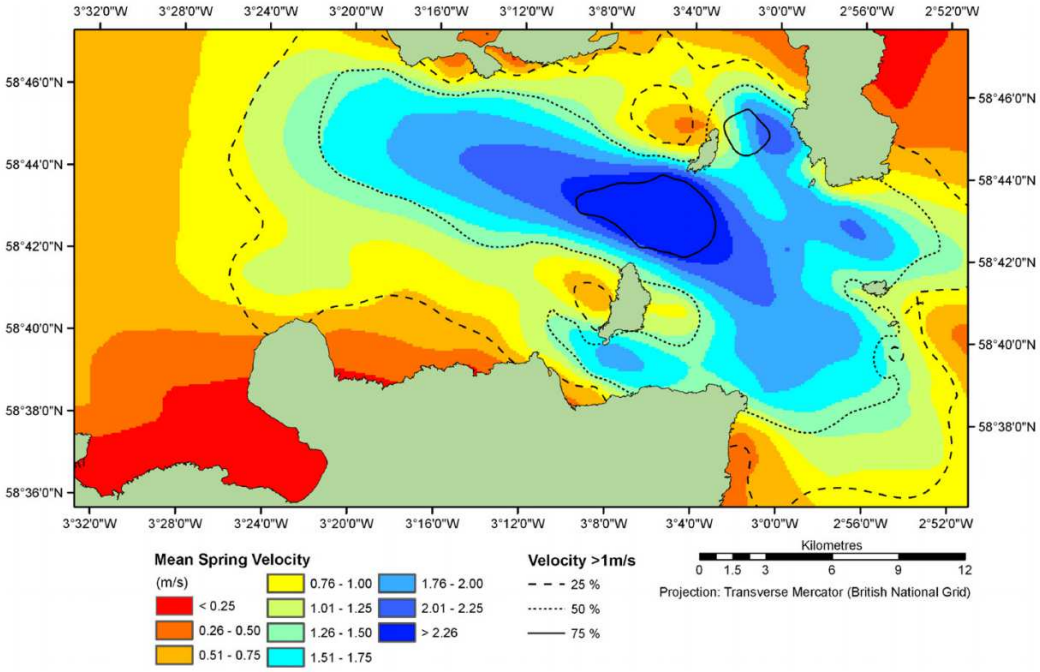

Figure 1.1: Tidal current regime of the Pentland Firth and Orkney Waters illustrating the mean spring velocity. Figure sourced from [12].

Commercial exploitation of tidal energy resource is currently under way in the Inner Sound by MeyGen Ltd, with plans to deploy a demonstration array of 1 MW rated tidal turbines. More importantly, this would signal the beginning of a staged development process, where the end target is to employ turbine arrays that could generate up to 398 MW of electricity in its foreseeable future [14]. Although the locations for arrays deployment are device specific, a number of generalised assumptions were introduced to provide a guideline when assessing potential sites. Such assumptions include [12, 15]:

- 22 m shipping clearance
- slope gradients of less than 0.5^{o}
- limited or no sediment deposition
- more than 1km away from nationally designated protected areas

- current speeds that exceed a typical device cut-in speed for more than 50% of the time

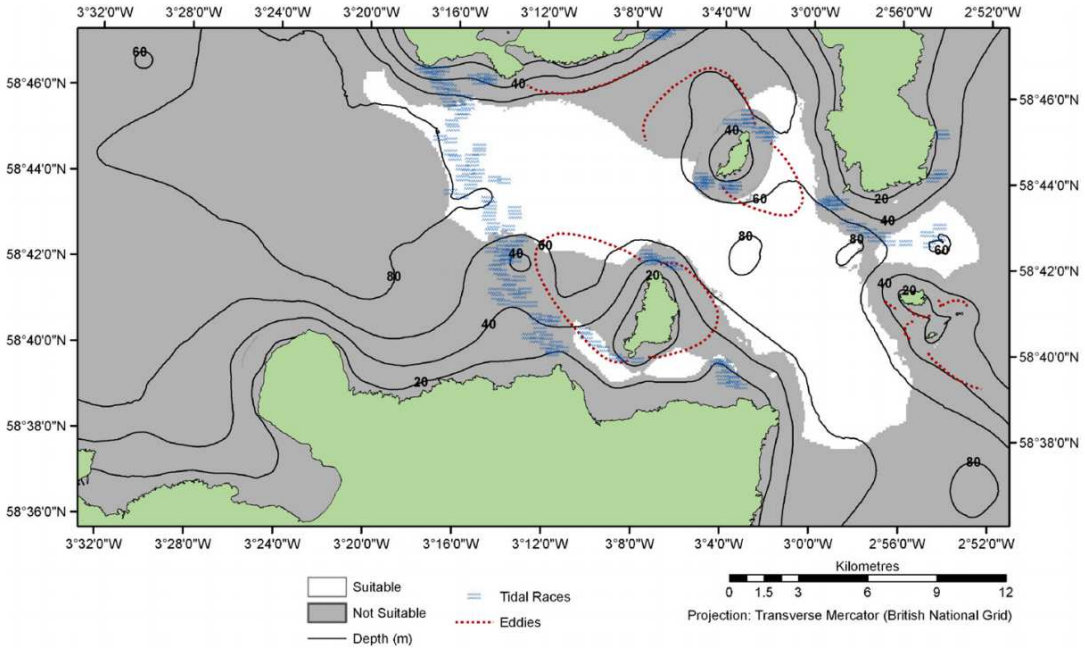

Figure 1.2: Potential development sites at the Pentland Firth and Orkney Waters based on specific sets of assumptions. Figure sourced from [12].

Figure 1.2 illustrates potential development sites at the PFOW based on the stated assumptions, which complements the mean spring velocity contour previously observed in Figure 1.1. Equally important, the influence of flow turbulence/eddies within the deployment areas should also be considered to avoid extreme loading on the turbines' blades and structures that may shorten their operational lives.

In recent years, numerical modelling has proven to be an indispensable tool in assessing possible impact of marine energy converters before their deployment. Several studies (e.g. [16–18]) have attempted to include tidal stream converters at various locations using a wide range of numerical models. Nonetheless, due to constraints on spatial mesh resolutions [19], it has proven to be a challenge for many researchers to accurately model individual turbines within the flow. Generally, there are four common approaches to represent a 3D tidal turbine in a numerical model; by using (a) actuator disc approach (b) Blade element method (BEM) method (c) actuator line approach (d) fully resolved model.

This research project seeks to address the challenges and constraints involved in simulating full size tidal devices within an ocean scale model by employing the 3D actuator

disc approach for the PFOW regions. The objectives of this study are elaborated in the subsequent sections.

1.1 Research objectives

This doctoral research attempts to provide detailed methodology in simulating a full size tidal stream devices via the actuator disc approach within a regional scale model. The chosen location for implementing the turbines was Inner Sound region of the Pentland Firth, which is the largest planned tidal stream project in the world [20].

Actuator disc approach is favoured due to its generality and simplicity. More importantly, this method can be used to represent any generic tidal turbine since the blades are not being characterised in the model, hence reducing the model's complexity. Nonetheless, the application of actuator disc for modelling tidal stream devices has been focused mainly on a very small domain, where the input of essential parameters are often exaggerated.

As the implementation of this approach on a full size tidal turbine is yet to be fully explored, this work made an attempt to model a full scale rotor using the actuator disc approximation within an ocean scale numerical flow model. This research aims to answer the following questions:

- What are the optimal numerical settings to be used in a regional scale simulation to ensure accurate hydrodynamic conditions at the deployment site are replicated?
- Are there any differences, if any, in the outputs' produced by two distinct modelling suites for similar input conditions?
- What are the critical numerical parameters involved in simulating full size actuator disc model?
- What are the best modelling practices to be adopted in the implementation of actuator disc momentum source term?

Additionally, this study also aims to examine the sensitivity of the applied momentum source term and its validity in representing full-size tidal devices. Nonetheless, before the effectiveness of an actuator disc in a regional model can be tested, tidal flow models for the area of interest needed to be set up first. In order to achieve the aims outlined above, this research project is divided into the following tasks:

- Explore and determine which open-source software is most suitable in conducting 3D tidal flow simulations at the area of interest. This is essential so that hydrodynamics condition observed at the sites can be properly reproduced.

- Perform detailed parametric analyses on the numerical models to assess the sensitivity of input parameters. Correspondingly, this will also ensure the models' robustness.
- Conduct inter-comparison study for the selected numerical models to comprehend the advantages and limitations of each software in setting up a regional scale flow model.
- Set up a small-idealised channel domain to try out the actuator disc momentum source term, and examine its accuracy by comparing the model's outputs against published literature. This includes assessment of uncertainty in model's outputs, sensitivity to model tuning parameters and development of a robust approach for model calibration.
- Adopt similar methodology as used in the idealised channel study to investigate the accuracy and sensitivity of the applied actuator disc momentum source term within an ocean scale simulation.

1.2 Contribution to knowledge

The need for this research project arises due to the scarcity of Computational Fluid Dynamics (CFD) studies concerning the implementation of actuator disc momentum sink term to model a full size tidal stream device.

The innovative part of this thesis is that this is the first study that concentrates on the development of methodology for modelling 3D tidal turbine arrays using full scale actuator disc approach at a real deployment site (i.e. the Inner Sound regions, Pentland Firth).

In recent years, several studies have utilised the actuator disc method in investigating various flow characteristics in the presence of tidal devices (e.g. [21–25]). However, these research works were primarily concentrated on validating a very small-scale actuator disc model, where a 0.1 meter diameter disc was commonly employed, against experimental results from the flume configuration. To some extent, this can be attributed to the lack of field data from any deployment sites that can be used for calibrating and validating a full scale turbine model.

For this very reason, the purpose of this project is to bridge the said research gap by providing detailed methodology in the application of a full size actuator disc approach to simulate the wake and flow effects in a regional scale domain. The most significant original contributions to knowledge of this work are summarised as follows:

- Detailed methodology in setting up 3D tidal flow models for the Pentland Firth regions using two distinct modelling suites were presented (i.e. by using Telemac3D and Delft3D), highlighting previously unspecified limitations and constraints between the two commonly used numerical models.
- The physical, numerical and general parameters employed in the simulations were thoroughly explored and discussed, since the input required for a 3D hydrodynamics model differs remarkably from one used in Two-Dimensional (2D) model.
- A methodology for implementing the actuator disc momentum source term to replicate the presence of full size tidal turbines in an idealised channel was presented and proven to be effective upon benchmarking against published experimental dataset.
- The use of structured grid at deployment's locations was pivotal to accurately define the turbine's features/swept area. Notably, the relationship between structured grid density and vertical resolution was demonstrated to have a significant impact on the predicted wake characteristics within the idealised channel.
- The use of non-slip boundary condition for the channel's bed, which was commonly utilised in small scale simulations, was not feasible to be implemented in a full size idealised channel domain since it required a very fine mesh near the bottom to satisfy the wall function.
- For the idealised channel set up, while flow retardation characteristics behind the simulated disc was successfully replicated, the model failed to resolve properly the bottom turbulence mixing in the near wake regions. Nonetheless, the model's outputs significantly improved when the non-hydrostatic solver was introduced.
- Employing similar methodology as used in the idealised channel study, an adapted momentum source term was applied into a regional scale domain, specifically at the Inner Sound of the Pentland Firth to imitate the presence of tidal stream devices in the area.
- Detailed parametric analyses for several key variables utilised in the regional scale simulation were presented. Outputs from this study were shown to be able to reproduce the wake characteristics as well as flow interactions as anticipated from the models, highlighting the robustness of the applied actuator disc momentum source term.

It is expected the knowledge gained in this work will serve as a guideline for simulating a 3D actuator disc model within an ocean scale domain. Chiefly, it highlights several good modelling practices that could be helpful for early stage researchers who are

interested in implementing this approach to model full size tidal stream devices.

1.3 Thesis outline

This thesis comprises of **8 Chapters** and **3 Appendices**. The current chapter introduces the context of this research work and outlines the scope and objectives of the study.

Chapter 2 gives a brief overview on the current status of marine renewable energy, particularly in the UK. Literature relating to innovations in tidal technologies are discussed, with update on tidal energy projects worldwide are shown. Furthermore, a wide range of physical and numerical modelling methodologies employed to study the technologies is also highlighted, hence setting the background of this doctoral work.

Chapter 3 and **4** provides an overview of the simulation of tidal current flow at potential tidal energy sites in the PFOW using two commonly used hydrodynamic software packages, namely Telemac3D and Delft3D. The governing equations as solved by the models are briefly introduced followed by an extended description of the models' set up and calibration exercises performed. Detailed parametric analyses conducted on various input parameters are also presented. In particular, this inter-comparison study highlights the advantages and limitations of both modelling suites, where numerical outputs are validated against the International Hydrographic Organization (IHO) tidal gauges and Acoustic Doppler and Current Profiler (ADCP) measurements data.

Chapter 5 and **6** outlines the methodology in implementing the actuator disc approach via RANS momentum source term for a 20-meter diameter turbine in an idealised channel. Validity of the applied actuator disc source term in predicting the wake decay and flow interactions for both single and multiple turbines configurations are thoroughly explored. Detailed parametric analyses to determine the optimum grid interval for the turbine's enclosure, as well as a mesh dependency study are carried out to ensure robustness of the models. More significantly, model outputs are compared with published data from literature to give credence to numerical simulations.

The work presented in **Chapter 7** translates the knowledge and experiences gained from the foregoing chapters into the simulation of a real size tidal turbine at a commercial deployment site within the Inner Sound region of the PFOW. Notably, the methodology and model set up in this chapter also follows the guidelines provided by European Marine Energy Centre (EMEC) [26] in an effort to provide realistic working and hydrodynamic conditions experienced by the devices in operation. The

robustness, as well as sensitivity of the applied momentum source term in representing a full size tidal turbine for a 3D ocean scale model is properly inspected. Criteria used in deciding the deployment locations of the turbines are also presented, along with detailed configurations for the actuator disc models. Particularly, some of the constraints faced in this research work are also discussed.

Chapter 8 summarises the main findings from each chapter that influences the body of work as a whole. These include limitations and constraints of the numerical models used, variations and inaccuracies observed in the output dataset against the measured data and literature, as well as examples of suggested best practice in an effort to bridge the research gap for ocean scale actuator disc simulations. Recommendations for future work which would further deepen and widen knowledge and improve confidence in current models are also detailed.

Chapter 2

Background

2.1 Marine energy

The UK Government has estimated that the combined wave & tidal stream energy has the potential to deliver around 20% of the UK's current electricity needs, which equates to an installed capacity of around 30 – 50GW [27]. More significantly, it has been widely accepted that the UK has 50% of Europe's tidal energy [28] and 35% of its wave energy [29].

Among the locations identified for harnessing marine energy are the Solent and Isle of Wight, Scottish Highlands and Islands and Wales, as well as Cornwall [30]. What is more, it has been noted that this sector can deliver industrial benefit to Britain ranging from engineering design and construction, through university-industry research collaboration, and also shipping ports. Additionally, tourism industry and professional services are also expected to be influenced by the growth of marine energy sector.

Scotland has some of the best tidal and wave power resources in the world, with The Crown Estate directly involved in ground-breaking projects such as the MeyGen tidal power development in the Pentland Firth. This £10 million investment is the first commercial scale tidal stream array in the world, and now part of the Crown Estate Scotland portfolio [31]. Detailed maps illustrating the potential sites for all known current and pipeline wave and tidal projects across the UK, which are compiled by the UK Marine Energy Database (UKMED) [32], are readily available in the EMEC's webpage [33].

2.1.1 Status of the industry

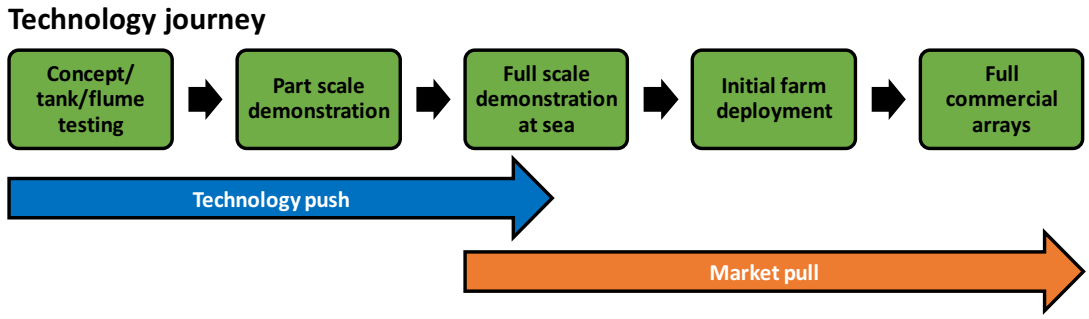

Figure 2.1: Stages involved in the development of marine energy conversion device. Figure adapted from [34].

Figure 2.1 highlights the steps involved in the development of devices to generate electricity from waves or tidal currents. It generally started with research and development stage, which is mostly driven by the technology push from the industries and academics. The demonstration and deployment steps, meanwhile, are primarily governed by the market pull. According to the 2011 report by Carbon Trust [34], leading developers are installing full-scale prototypes and working towards their first deployment of devices in an array. Nonetheless, in the last couple of years, great strides have been made by a number of players in the industry towards commercialisation of the marine technology, especially for tidal stream devices.

At present, tidal stream energy extraction technology can be said to be more mature than wave technologies [35], which is reflected by the number of tidal stream technology developers at full-scale demonstration stage. Notably, tidal devices are approaching a convergence of design, with the horizontal axis turbine concept accounts for close to 76% of the total tidal devices' development worldwide [36]. While a number of very different wave devices are currently under development or already on full scale demonstration at the sea, not much design convergence has taken place.

A comprehensive list of all tidal developers, along with their respective device type are available on the EMEC's webpage [37]. Overall, there are more than 90 companies worldwide who have invested in the development of tidal stream technology. Figure 2.2 displays the distribution of tidal energy developers according to countries and regions. As expected, the EU accounts for more than 61% of the tidal energy companies. Additionally, quite a large number of companies are also coming from countries such

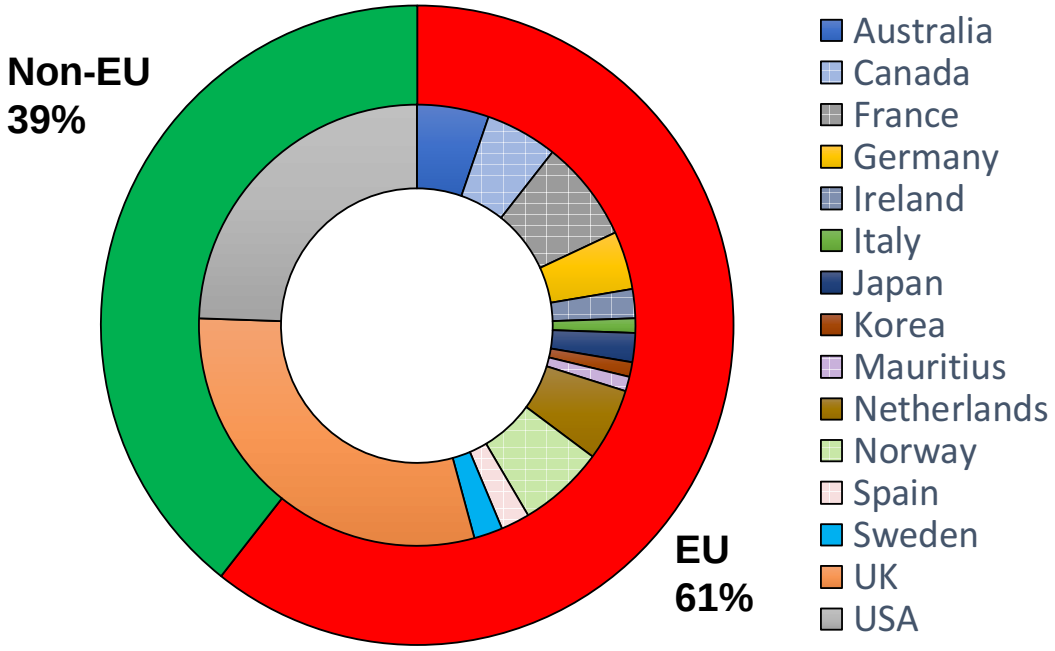

Figure 2.2: Distribution of tidal energy developers worldwide. Sourced from [37]. Note that the UK was counted as one of the EU's countries in this chart.

as the USA, Australia and Canada. On the other hand, there are only a handful of tidal developers in the Asian region due to its nascent stage of development on that part of the world.

Some of the world-leading innovations and important achievements from key tidal energy players are highlighted as follows:

- Based in Orkney, EMEC is the world's leading wave and tidal energy test and demonstration centre. This company is also spearheading efforts in developing international standards for marine energy, as well as building global network of test centres across the Americas, Asia, and Europe [38]
- Atlantis Resources Ltd [39] is the owner and developer of the world's first commercial scale tidal array at the PFOW in Scotland. The company is a global developer of renewable energy projects with more than 1,000 MW in various stages of development around the world.
- A subsidiary of DP Energy, Fair Head Tidal [40] is developing one of the world's first commercial-scale tidal energy generation projects on the North Antrim coast in Northern Ireland. It is estimated that their array system of tidal turbines is capable of generating a total of 100 MW power – enough to power 70,000 homes.
- A leading tidal engineering company, Nova Innovation Ltd [41] has successfully

delivered the world's first offshore tidal energy array in the Bluemull Sound and exporting power to the Shetland grid. Recently, it has been reported that Nova Innovation is working with renewable energy organization YnNi Llyn to explore the development of a tidal energy project off north Wales coast [42].

- Oceanflow Energy Ltd [43] is the developer of Evopod - a semi-submerged, floating, tethered energy capture device. Additionally, this company has also patented a semi-submerged platform design that can be configured for single, twin or multiple turbines, since this design could allow for the tidal stream energy to be captured even in areas of very harsh wave environments.
- QED Naval Ltd [44] specialises in developing concepts for the marine renewables industry, with its platforms designed to be capable of hosting any of the tidal turbines on the market today. Notably, the foundation structure can be installed and maintained in a single offshore operation, hence reducing the overall operational cost.
- Scotrenewables Tidal Power Ltd [45] is an Orkney based company, and developer of a 2 MW turbine known as SR2000. To date, this is the largest and one of the most powerful tidal turbines in the world, with each unit capable of delivering a reliable generation for almost 1,000 homes.
- Minesto [46] is a spin-off company from the Swedish aerospace manufacturer Saab. While the majority of tidal energy technologies are large horizontal axis structures, Minesto have developed and patented a kite-like device called Deep Green. As this moment, Deep Green is the only proven technology to operate cost-efficiently in low-velocity tidal and ocean currents.

As previously mentioned, UK is currently leading the world in the development of tidal arrays for both large and community scale. Deployment sites for some of these arrays throughout the Scottish and UK waters are illustrated in Figure 2.3. Furthermore, the development of marine technologies also bring together myriad of institutions, from universities to Government agencies, along with industrial and enterprise partnerships, which will be the vehicle for commercialising UK's world leading research, specifically in understanding of how multiple tidal energy devices interact in the water.

At the centre of these achievements is the EMEC, a world renowned test and research centre focusing on wave and tidal power development based in the Orkney Islands, UK. As of 2017, a total of 27 devices from 17 companies from 9 countries had been tested there [38], along with 100s R&D projects they have been involved in. Notably, half of the companies testing new technologies at the EMEC are UK-based, while the

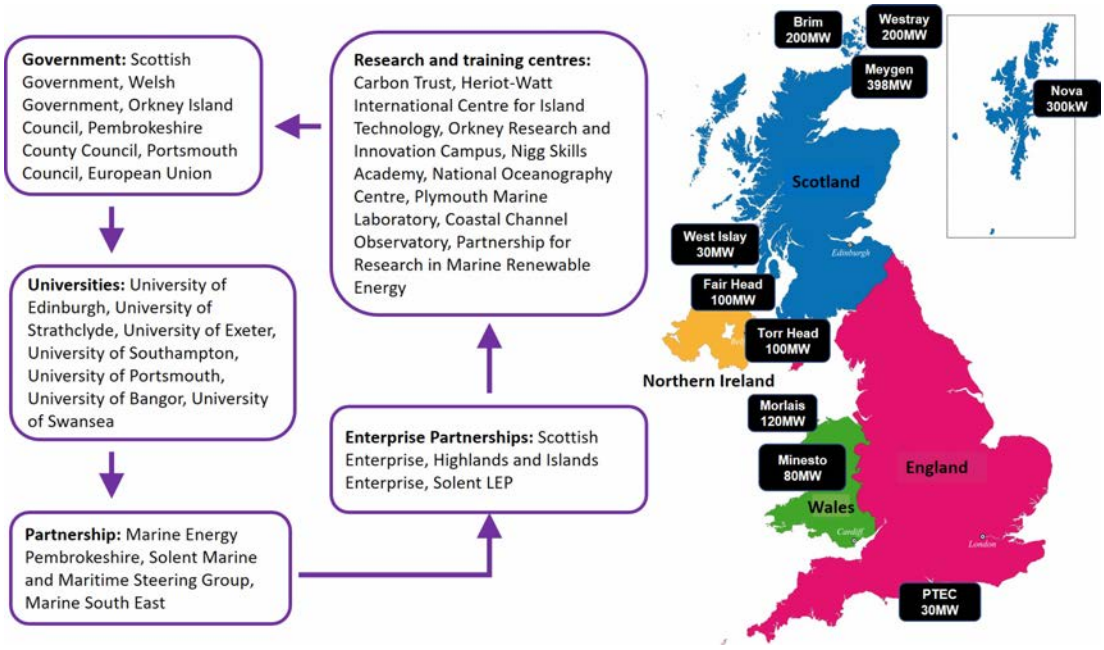

Figure 2.3: Planned development of tidal arrays for both large and community scale from across the UK, along with the networks of innovation and collaboration between relevant institutions and authorities. Adapted from [47].

rest are coming from abroad.

2.2 Harnessing energy from the tides

Tidal power uses the tides created by the gravitational effect of the sun and the moon on the earth causing cyclical movement of the seas, whereas wave power is created by the wind blowing over the sea. Due to its predictability, tidal power is seen as a more reliable source of renewable energy than some alternatives, such as wind or solar power, since tide movements can be calculated more reliably than weather. The UK is dominated by semi-diurnal regime, which consists of two high tides and two low tides each day.

Tidal energy is produced through the use of tidal energy generators. These large underwater turbines are placed in areas with high tidal movements, and are designed to capture the kinetic motion of the ebbing and surging of ocean tides in order to produce electricity. Tidal power has great potential for future power and electricity generation because of the massive size of the oceans.

Currently, there are two different ways for harnessing energy from the tides:

- exploiting the change in height of water as the tide flows and ebbs (**tidal range**).
- extracting energy directly from the flowing current (**tidal stream**).

2.2.1 Tidal range

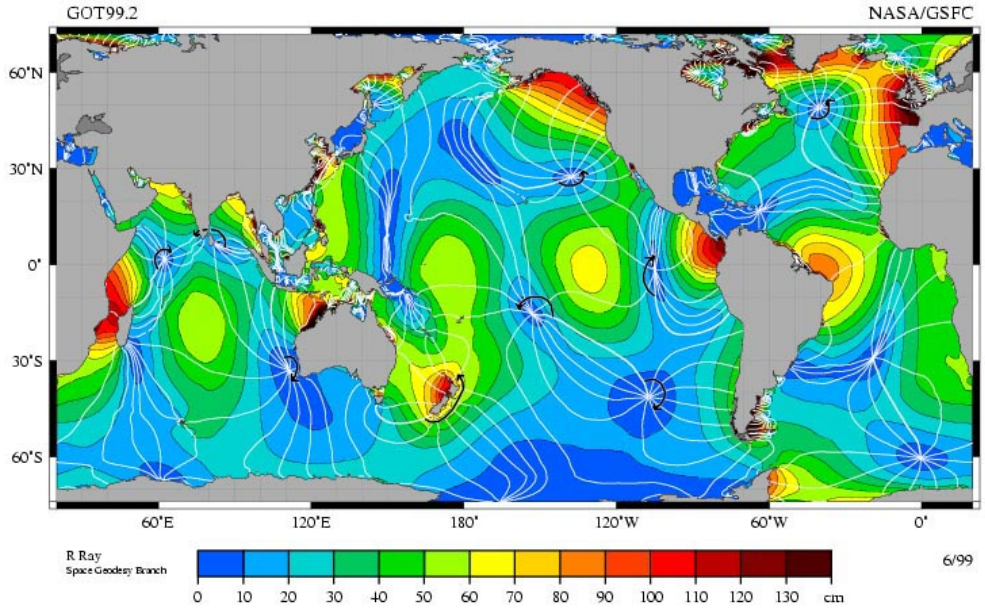

Figure 2.4: Tidal range resources worldwide, exemplified using world map of M2 tidal amplitude. Sourced from [48].

Tidal range technologies harvest the potential energy created by the difference in head between ebb tide and flood tide. Such resources exist in locations where due to geological and ecological conditions, large water masses flow into compounded areas or bays and estuaries. Figure 2.4 displays tidal range resources that is available worldwide.

The first tidal barrage was completed in the Rance River in north-western France (Brittany) in 1966, but due to plans for greater use of nuclear energy, the further pursuit of tidal energy was abandoned. Between 1966 and 2011, several small tidal plants were built in Canada, China [49], Iran [50, 51] and Russia, where tidal energy resource is abundant [52].

As of 2016, it has been estimated that over 500 MW of tidal range projects have been installed around the world to date [38]. Interestingly, there is not yet a commercial project in the UK, although a number of industry organisations have expressed their interests in building commercial tidal lagoon and tidal barrage schemes [53].

Early in 2016, the UK Government commissioned an independent review into the feasibility and practicality of tidal lagoon energy in the UK, led by Charles Hendry. This review was initiated following proposals for tidal lagoon projects, in particular a proposal by the company Tidal Lagoon Power (TLP) for a tidal lagoon project in Swansea Bay. The review was primarily intended to assess [54]:

(a) whether tidal lagoons could play a cost effective role as part of the UK energy mix
(b) potential scale of opportunity in the UK and internationally, including supply chain opportunities
(c) a range of possible structures for financing tidal lagoons
(d) different sizes of projects as the first of a kind
(e) whether a competitive framework could be put in place for the delivery of tidal lagoon projects.

The review's outcome was published in December 2016 [55], and it has been concluded that "*tidal lagoons can play a cost effective part of the UK's energy mix*". However, the report also cautioned that tidal lagoons projects are about *"very long-term, cheap indigenous power, the creation of an industry and the economic regeneration that it can bring in its wake"*, and most probably would not be the most cost effective solution in the shorter term.

Significantly, the Hendry's report made over 30 recommendations that will facilitate a tidal lagoon programme to take off in the UK. Subsequently, this review also highlighted the appeal of tidal lagoons as a source of constant, or as near as possible to constant power, which aligns with the Government's energy policy that is focused on ensuring secure, affordable, and low-carbon energy.

Elsewhere, the subject of tidal range technology, both existing and potential turbine designs have been widely discussed, and among others, published in [56–60]. Although tidal range projects are currently few and far between, the leading countries in terms of operational output are France and South Korea. Despite vast potential energy in tidal range around the world, many limiting factors, such as cost and accessibility impede the efforts to commercially harvest this energy. Table 2.1 outlines some of tidal range projects that are currently in operation, while Table 2.2 highlights various sites worldwide that have the potential to be developed effectively.

Table 2.1: Brief overview of existing tidal range projects worldwide. Adapted from [56].

Location	Built year	Capacity / Output	Turbine cycle
La Rance, France	1961–1967	24 turbines with 10MW power each/ 480 GWh per year	bi-directional cycle
Lake Sihwa, South Korea	1994	10 turbines with combined operating capacity of 254 MW	flood direction only
Annapolis, Canada	1984	single turbine with a peak output of 20MW	ebb tide only
Jiangxia, China Launched	1985	six turbines with installed capacity of 3.9MW	bi-directional cycle
Kislaya Guba, Russia	1968	the smallest power plant with a capacity of only 1.5MW	n/a

Table 2.2: Potential tidal range locations worldwide. Sourced from [61].

Country	Site	Mean tidal range (m)	Installed capacity (MW)	Approx. annual output (TWh)
Argentina	San Jose	5.9	6800	20
Australia	Secure Bay 1 Secure Bay 2	10.9 10.9		2.4 5.4
Canada	Cobequid Cumberland Shepody	12.4 10.9 10.0	5339 1400 1800	14 3.4 4.8
India	Gulf of Kutch Gulf of Cambay	5.3 6.8	900 7000	1.7 15
Korea	Garolim Cheonsu	4.7 4.5	480	0.53 1.2
Mexico	Rio Colorado Tiburon	6-7		5.4
UK	Severn Mersey Wyre Cnwy	7.0 6.5 6.0 5.2	8640 700 47 33	17 1.5 0.09 0.06
USA	Passamquoddy Knik Arm Turnagain Arm	5.5 7.5 5.5	2900 6500	7.4 16.6

2.2.2 Tidal stream

Tidal streams (or currents) are the ocean water mass response to tidal range, and are generated by horizontal movements of water. The fast sea currents are often magnified by topographical features, such as headlands, inlets and straits, or by the shape of the seabed when water is forced through narrow constrictions. Tidal current flows result from the rise and fall of the tide; although these flows can be slightly influenced by short-term weather fluctuations, their timing and magnitude are largely predictable and generally insensitive to impacts by climate change.

The tidal stream devices (also known as Tidal Energy Converters (TEC)), which utilise these currents, are broadly similar to submerged wind turbines and are used to exploit the kinetic energy in tidal currents. Due to the higher density of water, this means that the blades can be smaller and turn more slowly, but they still deliver a significant amount of power. To increase the flow and power output from the turbine, concentrators may be used around the blades to streamline and concentrate the flow towards the rotors. In general, there are six main types of TEC designs that have been predominantly researched, developed and deployed [62], as highlighted in Figure 2.5. Additionally, Table 2.3 provides a short overview of the companies involved in developing the TECs.

Nonetheless, placing turbines in tidal streams is a very complex task, due to the sheer size of the machines which would disrupt the tidal current they are trying to harness. Besides, the environmental impact due to the deployment of TEC could also be severe, depending on the size of the turbine and the location of the tidal stream. Conversely, the simplest scenario for determining the hydrodynamic forces acting on the TEC is to look at the effects of a uniform tidal current. Then again, in reality, the currents throughout the water column is commonly characterised by a high shear in the velocity profile, turbulence and surface waves and these all need to be taken into account in determining the loads on any particular device.

Work on the effects of highly shearing profiles and levels of turbulence have been considered by Zangiabadi et al. [70] and Mason-Jones et al. [71]. Particularly, key variables affecting the flow field around tidal turbines have been provided by Myers and Bahaj [69], as displayed in Figure 2.6. This figure provides a clear indication of the primary flow characteristics of the tidal current, where the scale of the variations in the bottom topography has a compelling effect on the shape of the flow profile across the water depth.

Additionally, while greater velocity shear is induced with increased seabed drags,

(a) Horizontal axis turbine [63].

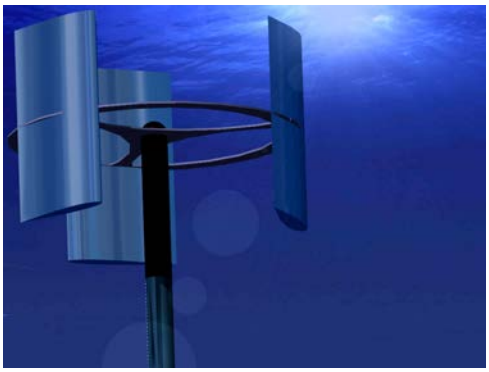

(b) Vertical axis turbine [64].

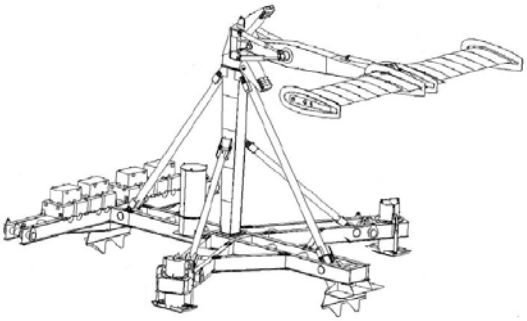

(c) Ocillating hydrofoil [65].

(d) Enclosed tips (venturi) [66].

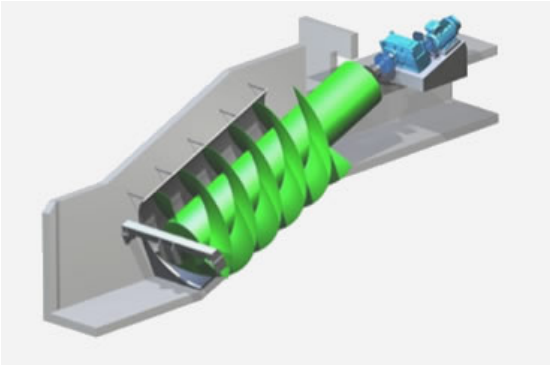

(e) Archimedis screw [67].

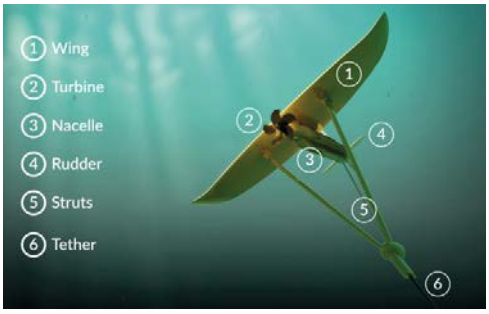

(f) Tidal kite [46]

Figure 2.5: Example of main tidal turbine designs that has been used/tested at research or deployment sites.

Table 2.3: Brief overview of existing tidal turbine developers with their respective technologies. Adapted from [62, 68].

Tidal energy device	Developer (Country base) / *Technology*
Horizontal axis turbine Similar mechanism to wind turbines	Hammerfest Strom (Norway) / *Tidal Stream Turbine* Marine Current Turbines (UK) / *Seagen & Seaflow* Ocean Flow Energy (UK) / *Evopod* Nautricity Ltd (UK) / *CoRMaT* Ocean Renewable Power Company (ORPC) (USA) / *OCGen & TidGen Power System*
Vertical axis turbine Similar to above but mounted vertically	New Energy Corp (Canada) / *EnCurrent Vertical Axis Hydro Turbine* Blue Energy (Canada) / *Davis Turbine* GCK Technology (USA) / *Gorlov Turbine*
Oscillating hydrofoil design Hydrofoil attached to an oscillating arm moved by tidal currents drives hydraulic fluid to generate electricity	Pulse Tidal (UK) / *Pulse Stream* The Engineering Business (UK) / *Stingray* EEL Energy (France) / *EEL Energy* Integrated Power Technology Corporation (USA) / *TURBOFOIL*
Venturi effect Tidal flow is concentrated in a funnel-like device to drive a turbine	Hydro Green Energy (USA) / *Hydrokinetic Turbine* Tidal Energy Pty Ltd (Australia) / *DHV Turbine* Lunar Energy (UK) / *Rotech Tidal Turbine (LTT)* OpenHydro (Ireland) / *Open Centre Turbine*
Archimedes screw With its helical corkscrew-shaped design, this device draws power from the tidal stream as the water moves up/through the spiral turning the turbines.	Flumill (Norway) / *Flumill Power Tower* Jupiter Hydro Inc (Canada) / *not available*
Tidal kite A tidal kite is tethered to the sea bed and carries a turbine below the wing. The kite 'flies' in the tidal stream, swooping in a figure-of-eight shape to increase the speed of the water flowing through the turbine	Minesto (Sweden) / *Deep Green* Seapower scrl (Italy) / *GEM* SeaCurrent (Netherlands) / *SeaCurrent TidalKite*

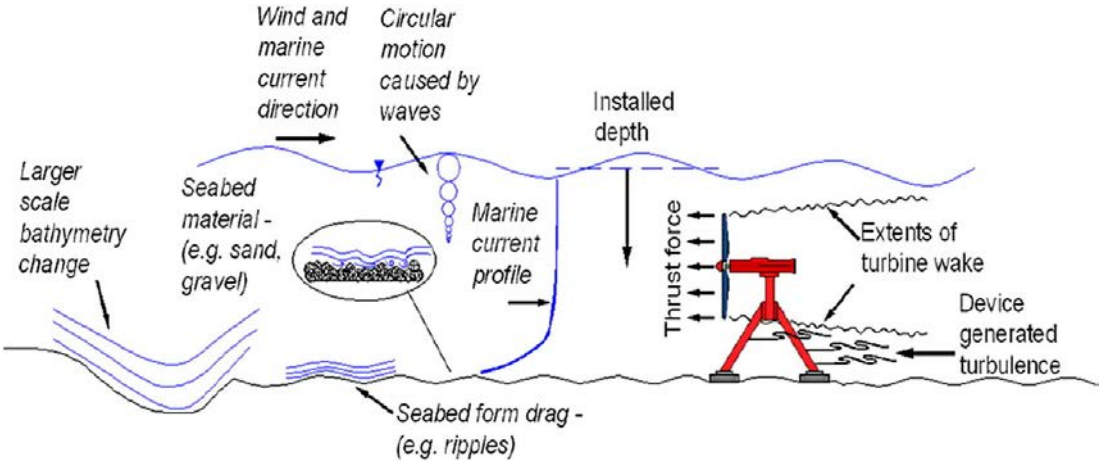

Figure 2.6: Variables affecting the flow field around tidal turbines. Sourced from [69].

sea surface gravity waves result in an oscillatory motion under the water surface. For instance, if particles are considered to be suspended through the water column, they would move in an orbital fashion with the magnitude of the oscillations slowly weakening the further they travel from the water surface. The motion will then finally halt at a depth of approximately half the wavelength of the wave [72].

In addition to the categories of devices identified in Figure 2.5, there is also a range of methods to fix the converter to the seabed. A short overview of the existing tidal turbine foundations are given in Table 2.4. For details regarding status of tidal energy development, device category, foundation type and energy capacity of the farms, please refer to this documentation [73].

However, it is worth noticing that despite various tidal turbine designs or projects reported in some state-of-the-art research papers, a large percentage of these projects were only at the design stage when the papers were published [75]. Some projects do not have further developments during the several years after the first announcement, such as the Anglesey Skerries tidal stream array project.

This project was given planning permission by the Welsh Government back in 2013, before it was shelved by developer Marine Current Turbines/Siemens. Although the company was bought by Atlantis in 2014, sparking hopes the scheme would now progress to development, the project was officially cancelled in 2016 when the parent company returned the "Agreement for Lease" for the seabed to the Crown Estate.

An overview of tidal energy developers whose technologies are at an advanced status of developments and are aiming to the deployment of single device or at development of pre-commercial or small commercial arrays has been comprehensively summarised by

Table 2.4: Brief overview of the existing design for tidal turbine foundations. Adapted from [62] and [74].

Foundation type	Water depth	Advantages	Drawbacks
Gravity foundations The structure is is physically attached to the seabed or is fixed by virtue of its massive weight.	20 - 80 meters	Easy installations	Concrete is too heavy, the footprint causes damages, erosion
Pile mounted Analogous structure used to mount most large wind turbines, whereby the device is attached to a pole penetrating the ocean floor. This may also allow the turbine to be raised above the water level for maintenance.	up to 30 meters	Simple design, easy fabrication, most common concept	Possible bending and fatigue cracks, seabed penetration installation is restricted in certain area due to environmental concerns
Floating structures (with three sub-divisions) ***Flexible mooring***: The device is tethered via a cable/chain to the seabed allowing considerable freedom of movement ***Rigid mooring***: The device is secured into position using a fixed mooring system, allowing minimal leeway. ***Floating structure***: This allows several turbines to be mounted to a single platform, which can move in relation to changes in sea level.	from 80 meters	feasible for deeper waters	prone to corrosion and wave loading if moored or anchored
Suction Bucket or Caisson Foundations Water is pumped out of 'bucket' to lower the pressure inside bucket skirt, which causes negative pressure. At the same time, weight of foundation causes the foundation to sink into sea floor	0-25 meters	Better bearing capacities, ease of decommis-sioning, little to no seabed preparation needed	Costly fabrication and difficult installation

Magagna and Uihlein [36]. Additionally, 4C Offshore, which is a consultancy company targeting the offshore energy markets, provides an up to date project status for any tidal farm development in the world on their webpage [76].

2.3 Tidal turbine representation

There are various levels of detail in which a TEC/tidal rotor can be idealised in a numerical model, ranging from a simple model to detailed modelling technique. Nonetheless, the objectives of hydrodynamic modelling at the turbine scale can be categorised as follows [77]:

(a) to validate the design and performance of a particular type of turbine
(b) to understand fundamental effects of local flow conditions, such as blockage, sheared flow, turbulence and waves
(c) to develop a simplified, lower-order model of turbines for larger scale (array/site scale) modelling

To address the concern stated in the first category, a turbine with detailed design is commonly used in high-fidelity computer simulation. Moreover, to predict the performance of a full size rotor quantitatively requires the model to be able to capture "dynamic stall", which is caused by massive separation of flow from the surface of turbine flow [78]. This can only be achieved by using Large Eddy Simulation (LES), since this model could resolve large eddies that are present in; (i) wake of turbine blades (ii) boundary layer attached to the blades. However, only recently have such LES model become feasible in terms of computational cost, albeit still only at relatively low Reynolds numbers [79, 80].

Next, in order to understand fundamental effects of local flow conditions such as blockage, sheared flow etc., both detailed and simplified turbine model can be used to examine the effects qualitatively. To emphasize, the importance of blockage on the flow passage has been thoroughly studied in [81–83]. More often than not, the effects observed for that particular turbine model are more or less universal and could be presumed to apply for many different types of actual turbines as well. As for the third category, which is to develop a simplified turbines model for arrays simulation, the main challenge is to replicate the wake mixing from the devices while at the same time maintaining the model's simplicity [77].

In general, there are three computational low-order models commonly used to represent tidal rotor:

(a) actuator disc approach

(b) blade-element method

(c) actuator line method

A review of these approaches has been extensively compiled in [77, 84, 85]. In particular, the selection of the most appropriate approach depends on the aim of each study. For instance, a BEM model is suitable for the design and optimization of turbine blades, while an actuator line model is suitable for investigating the time-dependent dynamics of turbine wakes and tip vortices [86]. Specifically, Olczak et al. [87] has prescribed detailed overview on the capabilities and typical applications of turbine wake modelling approaches, as shown in Figure 2.7.

Method	Predicted				Modelled					Applications
	Mean loads	Unsteady loads	Far-wake	Near wake	Wake rotation	Blade scale flow	Onset shear	Onset turbulence	Computational cost	
Linear momentum theory					Zonal idealisation				Low	Analytical
Blade element momentum theory (BEMT)	✓				No wake				Low	Fast numerical method for rotor design, inc. onset shear
RANS porous disc					N	N	Y	N	Med	Simple steady numerical model with far wake
RANS BEM	✓		✓		Y	N	Y	N	Med	Rotation, efficient, steady numerical model, up- stream shear
RANS actuator line	✓		✓	(a)	Y	N	Y	N	High	Unsteady, more efficient than blade resolved, up- stream shear
LES actuator line	✓	✓	✓	(a)	Y	N	Y	Y	v. high	Unsteady, wake length scales resolved
RANS blade resolved	✓	✓	✓	(a)	Y	Y	Y	N	v. high	Unsteady flow resolved
LES blade resolved	✓	✓	–	(a)	Y	Y	Y	Y	v. high	All flow scales resolved apart from sub grid

(a) - validation needed.

Figure 2.7: Summary of capabilities and typical applications of turbine wake modelling approaches. Sourced from [87].

2.3.1 Actuator disc approach

Actuator disc model, often embedded in either LES or RANS simulations, is the least accurate and most cost-efficient turbine model that can be used in CFD simulations. First proposed by Rankine and Froude in the late 19^{th} century, the basic idea of the theory is to represent the real turbine rotor with an equal area disk. Its main assumptions [89, 90], considering an ideal rotor as the one shown in Figure 2.8, are:

1. The disc is infinitely thin which means it is permeable for the fluid to pass through
2. Inviscid (thus not rotational), incompressible and isotropic flow

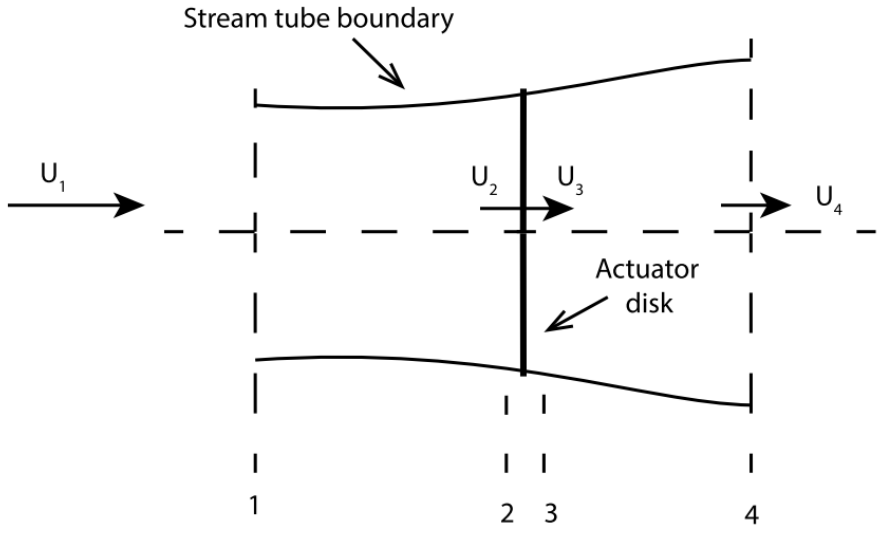

Figure 2.8: Illustration of an actuator disc diagram. Sourced from [88].

3. Thrust and velocity are uniformly distributed on the disc
4. Far up - and downstream pressure is the ambient pressure
5. Thrust loading and velocity are uniform over disc

The thrust (T_r) and the kinetic power extracted (P_w) are derived from the mass conservation law and the momentum balance, which gives:

$$T_r = \dot{m}(U_1 - U_4) \tag{2.1}$$

$$P_w = \frac{1}{2}\dot{m}(U_1^2 - U_4^2) \tag{2.2}$$

where $\dot{m}$ is the mass flow rate. With disc's area denoted as A, ρ is the fluid's density, $\dot{m} = (\rho AU)_1 = (\rho AU)_4$. Additionally, the axial induction factor, a, is defined as:

$$a = \frac{U_1 - U_2}{U_1} \tag{2.3}$$

Substituting Equation 2.3 into Equations 2.1 and 2.2, the expressions for thrust and power are as follows:

$$T_r = \frac{1}{2}\rho AU^2[4a(1-a)] \tag{2.4}$$

$$P_w = \frac{1}{2}\rho A U^3 [4a(1-a)^2] \tag{2.5}$$

Defining C_p as power non-dimensionalised by available power through disc area, and similarly defining C_T for thrust:

$$C_T = \frac{T_r}{\frac{1}{2}\rho U^2 A} = 4a(1-a) \tag{2.6}$$

$$C_p = \frac{T_r}{\frac{1}{2}\rho U^3 A} = 4a(1-a)^2 \tag{2.7}$$

This theory has been the foundation for initial approaches of modelling tidal stream devices by researchers in the early days. For example, an actuator disc in a flow of constant cross-section, bounded by parallel channel walls and a constant free surface profile was considered by Garrett and Cummins [91]. On the other hand, Whelan et al. [92] examined the flow field around an actuator disc in an open channel flow with non-uniform free surface. Nevertheless, the momentum actuator disc theory presented in those studies can only be applied to unbounded flows and ignores wake mixing. A more advanced method was derived by Houlsby et al. [93], whereby hydro-kinetic devices in free surface flows are no longer subject to the Betz limit. The summary of that approached are highlighted here.

One-dimensional channel containing an actuator disc with associated downstream mixing is displayed in Figure 2.9. The upstream conditions are assumed to be uniform with constant velocity u, and depth h, while the flow is inviscid. The channel, or centre-to-centre spacing between adjacent turbines, has a constant width b. At sections 1, 4 and 5 in Figure 2.9, it is assumed that the pressure is hydrostatic and the flow is uniform. At section 4, the velocity $u_{b4} = \beta_4 u$ denotes the bypass flow velocity, while $u_{t2} = \alpha_2 u$ and $u_{t4} = \alpha_4 u$ define the turbine flow velocity at sections 2 and 4 respectively. Additionally, T is the horizontal thrust force applied to the fluid from the turbine. $B = A/(hb)$ is a dimensionless blockage ratio, where A and hb are the actuator disc's occupied area and cross-section respectively.

Following Whelan et al. [92], applying continuity, energy and momentum conservation selectively between stations 1 and 4 leads to a quartic equation describing the bypass velocity:

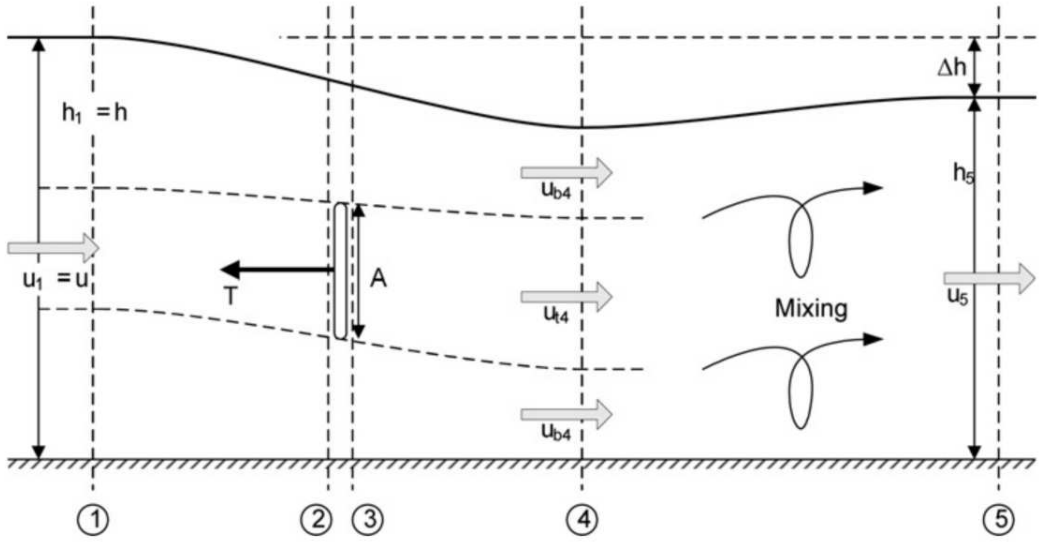

Figure 2.9: Illustration of the linear momentum actuator disc theory in an open channel flow. Sourced from [93].

$$\begin{aligned}&\frac{\mathrm{Fr}^2}{2}\beta_4^4 + 2\alpha_4\mathrm{Fr}^2\beta_4^3 - (2-2B+\mathrm{Fr}^2)\ \mathrm{x}\ \beta_4^2 \\ &-(4\alpha_4+2\alpha_4\mathrm{Fr}^2-4)\beta_4 + \left(\frac{\mathrm{Fr}^2}{2}+4\alpha_4-2B\alpha_4^2-2\right)=0\end{aligned} \tag{2.8}$$

where $\mathrm{Fr} = u/\sqrt{gh}$ is the upstream Froude number. Assuming that the upstream Froude number is known and the turbine is defined by a blockage ratio and the velocity coefficient α_4, Equation 2.8 can be solved for β_4. To solve for the remaining velocity coefficient α_2, both the Bernoulli and continuity equations are applied in the bypass flow:

$$\alpha_2 = \frac{\alpha_4(\beta_4-1)}{B(\beta_4-\alpha_4)}\left[1-\frac{\mathrm{Fr}^2}{2}(\beta_4+1)\right] \tag{2.9}$$

Alternatively, the blockage ratio and an induction factor a = 1 - α_2 can be used to define the turbine, in which case Equations 2.8 and 2.9 are solved concurrently for β_4 and α_4. Generally, any three independent parameters are sufficient to define the flow field provided that the bypass flow does not become critical (where the relevant physical root of Equation 2.8 becomes complex [93]). Next, the turbine's power and thrust can be determined in terms of a power coefficient C_p and a thrust coefficient C_T.

$$T = \frac{1}{2}\rho u^2 Bbh(\beta_4^2 - \alpha_4^2) = C_T \frac{1}{2}\rho u^2 Bbh \tag{2.10}$$

and

$$\begin{aligned} P = \alpha_2 uT &= \frac{1}{2}\rho u^3 Bbh\alpha_2(\beta_4^2 - \alpha_4^2) \\ &= C_p \frac{1}{2}\rho u^3 Bbh \end{aligned} \tag{2.11}$$

Since the flow is not uniform with depth at section 4, it is assumed that downstream mixing will occur. When momentum conservation is applied in the horizontal direction between sections 1 and 5, it leads to:

$$\frac{1}{2}\rho gb(h^2 - (h-\Delta h)^2) - T = \rho bhu\left(\frac{uh}{h-\Delta h} - u\right) \tag{2.12}$$

Substituting for the thrust coefficient from Equation 2.10 and rearranging then gives:

$$\begin{aligned} &\frac{1}{2}\left(\frac{\Delta h}{h}\right)^3 - \frac{3}{2}\left(\frac{\Delta h}{h}\right)^2 + \left(1 - \mathrm{Fr}^2 + \frac{C_T B \mathrm{Fr}^2}{2}\right) \\ &\text{x } \frac{\Delta h}{h} - \frac{C_T B \mathrm{Fr}^2}{2} = 0 \end{aligned} \tag{2.13}$$

This is a cubic expression that can be solved for the downstream depth change $\Delta h = h - h_5$. Significantly for zero Froude number, the relative depth change tends to the solutions $\Delta h/h \longrightarrow 0$, 1, and 2, with the former being the physically admissible solution. The power lost in the wake can then be determined in terms of Δh from:

$$\begin{aligned} P_W = &\frac{1}{2}\rho u^3 Bbh\alpha_2\alpha_4^2 + \frac{1}{2}\rho u^3 bh(1 - B\alpha_2) \\ &\text{x } \beta_4^2 - \frac{1}{2}\rho u^3 bh\left(\frac{h}{h-\Delta h}\right)^2 + hbu(h_4 - h_5)\rho g \end{aligned} \tag{2.14}$$

Combining Equation 2.14 with Equation 2.11, the following expression is obtained for the total power lost in the channel:

$$P + P_W = \rho gubh\Delta\left(1 - \mathrm{Fr}^2 \frac{1 - \Delta h/(2h)}{(1 - \Delta h/h)^2}\right) \tag{2.15}$$

Finally, a measure of efficiency, η defined as the ratio of power extracted by the tidal

energy converter to the total power removed from the tidal stream can then be written as:

$$\eta \simeq \alpha_2 \left(1 - \frac{1}{2}\frac{\Delta h}{h}\right) \tag{2.16}$$

Equation 2.16 is valid for small but finite Froude number and downstream depth change (so that $\mathrm{Fr}^2(1-\Delta h/h)^{-1} \ll 1$), which is often realistic for tidal flows. Additionally, Vennel [94] also discusses on how turbines in tidal farms can produce enough power to meet a stricter definition of what it means to exceed the Betz limit.

2.3.2 Blade element method

An increasingly popular method for representing tidal turbines is to employ a CFD-embedded Blade element method (BEM) model (e.g. [95, 96]). In the blade element theory, the blade is assumed to be divided into N segments as shown in Figure 2.10. Two key assumptions made are:

1. There are no aerodynamic interactions between the different blade elements
2. The forces on the blade elements are only determined by the lift and drag coefficients

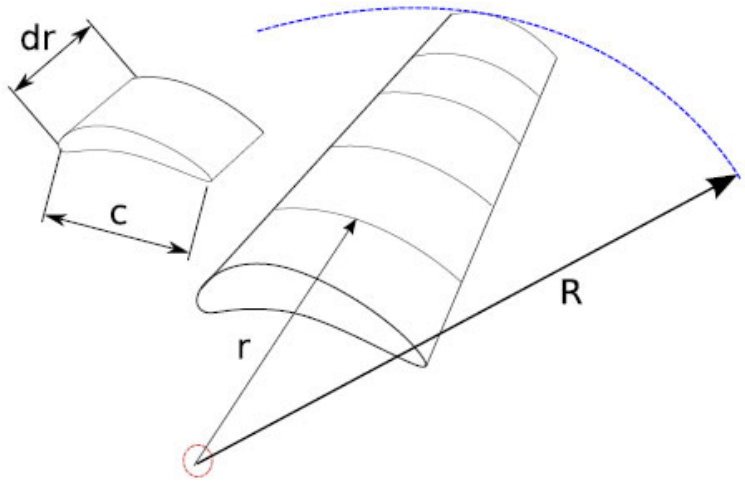

Figure 2.10: Schematic of blade elements. Sourced from [97].

BEM theory uses a one-dimensional momentum equation and predicts the performance of the turbine at a number of blade elements along the turbine radius. It is computationally efficient and can accurately predict the performance of a turbine across a range of

tip speed ratios, blade types, pitch angles, and inflow conditions [98]. Additionally, the prediction of turbine performance and wake mixing can be improved by incorporating the BEM approach into the actuator disc CFD to account for the effect of non-uniform loading (in both stream-wise and circumferential directions) [99, 100].

In BEM theory, the device is modelled by applying force data to the flow based on actual rotor characteristics. Using tabulated blade coefficient data, both linear momentum extraction as well as angular momentum effects can be reproduced. The discrete blade forces at a given radial location are evenly distributed over a rotor revolution, resulting in a set of concentric annuli acting essentially as separate actuator rings.

Due to the smearing of the blade forces across one revolution, discrete blade effects (such as tip vortices) are not captured in this approach [101]. Further, information gained from a BEM analysis consists of power, thrust and torque data for the tidal device. Computational times are very quick, of the order of fractions of seconds, and as such use of this type of analysis is commonplace at the preliminary design stage [102].

2.3.3 Actuator line method

Another recent model is the so-called actuator-line model, which is also based on the blade-element method. Furthermore, this model also relies on an actuator disc to extract momentum from the flow. Nonetheless, while the actuator disc method works by having a disc with uniformly distributed load, the rotor blades in actuator line approach are now characterised as a span wise sections with airfoil characteristics.

Detailed information about the actuator line method is provided by Mikkelsen [78] and Troldborg [103]. Additionally, numerical investigation using both actuator disc and actuator line method for wind turbine models has been conducted by Martinez and Leonardi [104], and also Keck [105]. Comparatively, Churchfield et al. [106] used a high-fidelity 3D model of turbines represented as rotating actuator lines to study wake propagation and power production in a small array.

To highlight, key differences between actuator disc and actuator line model are as follows:

- Actuator line model requires airfoil look-up tables (i.e. an airfoil file containing a list of lift and drag coefficients versus angle of attack)
- Unlike the actuator disc approach, actuator line method provides the information along the blade radius, hence allowing computation of the turbine's thrust and torque

- Actuator line method is also able to capture root and tip-vortices near the rotor as they are convected further downstream

2.4 Device chosen for analysis

In the current literature, the large majority of numerical investigations of wake interactions and characteristics have been conducted using either actuator disc or actuator line approaches [107]. Nonetheless, most of these studies have been limited for (a) idealised channel problems [13, 108] (b) modelling of single and multiple rows of turbines at actual sites, albeit using a 2D depth-averaged model (e.g. [109]).

Although it is widely acknowledged that higher resolution models such as fully-resolved blade can give a detailed or more accurate picture of wake interactions occurring within an array, they are usually limited to simplified cases. Indeed, the computational power needed to run such models limits their use to small spatial and temporal domains of simple bathymetries and geometries in which only basic forcing can be imposed [25].

Hence, the overachieving aim of this project is to answer the following two questions commonly associated with regional scale numerical modelling of tidal stream power generation [77]:

1. What is the best numerical modelling approach that should be used to develop a regional scale numerical model?
2. How can tidal energy extraction be represented in this model?

The first of these questions typically centres on a choice between a 2D shallow water model and a more computationally intensive 3D model, while the second problem of how to model tidal energy extraction in a regional scale model is usually approached by introducing a momentum sink. Since 2D tidal hydrodynamics modelling had been extensively researched in the past decades, it is only logical to move into 3D numerical model for examining the flow interactions. In addition, resolving all individual turbines to simulate directly the interaction between turbines is not only computationally more expensive, but also time consuming.

Considering the success in regional modelling so far (i.e. from literature) has been limited to 2D models, along with constraints on computational resources available to the author, the actuator disc approach was chosen to be used in this study as a means to simulate the presence of tidal stream devices in the numerical domain. To gain thorough understanding of the sensitivity and robustness of a full size 3D-actuator

disc model, the momentum source term was first implemented in an idealised channel. Subsequently, detailed analyses of various input parameters were conducted for the regional scale actuator disc model.

Chapter 3

Numerical Modelling of the Pentland Firth Region Using Telemac3D

This chapter gives an overview of the simulation of tidal current flow at potential tidal energy sites in the Pentland Firth in Scotland using Telemac3D[1]. The motivation behind this work is to investigate the influence of input parameters on the output parameters, as the majority of past research has mainly focused on using the 2D version of Telemac depth-averaged flow models for this region. An extended description of the model set up, along with the detailed parametric analysis on various input parameters is presented.

IHO tidal gauges and Acoustic Doppler and Current Profiler (ADCP) measurements were used in calibrating model output to ensure the robustness of the models. Further, extensive parametric studies on the impact of varying drag coefficients, roughness formulae and turbulence models has been conducted and reported. The results of the analyses are presented graphically, accompanied by relevant statistical dataset to facilitate data interpretation.

3.1 Introduction

Studies have estimated that 25% of Europe's tidal energy is located in the Scottish waters [110], where most of this resource is concentrated in the Pentland Firth (Figure 3.1). Tidal current speed up to 5 m/s has been observed surging through the firth [111], marking this area as one of the best sites for tidal stream power generation in the world. Due to the enormous potential for generating clean and predictable tidal stream energy, the PFOW has become the focal point in the marine renewable energy research.

1. Part of the contents from this chapter had been presented at two international conferences, and was also used in writing up a manuscript for journal publication. Please refer to Appendix B for details.

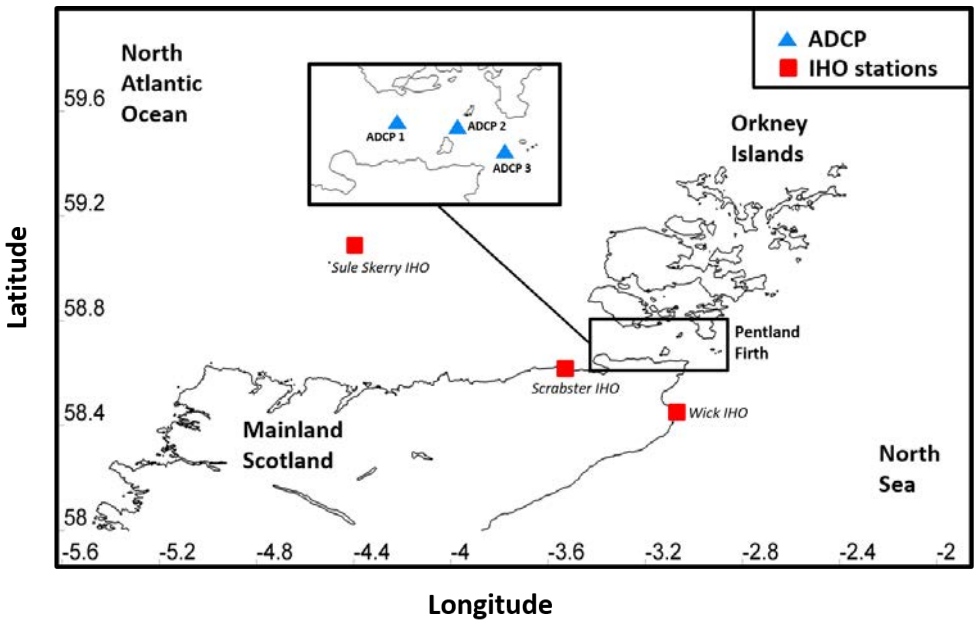

Figure 3.1: Map of the North of Scotland and Orkney Waters showing the location of study area (Pentland Firth), including the position of the ADCPs and IHO tidal stations.

Between 2008 and 2010, the Crown Estate has leased several sites in the PFOW for tidal energy deployments to industries such as ScottishPower, Renewables, SSE, MeyGen and Marine Current Turbine for commercial scale developments [112]. MeyGen is currently working on the world's first and largest tidal energy farm in the Inner Sound [113], while in Shetland, Nova Innovation Ltd is currently developing the world's first community scale array of five 100KW devices [114]. Furthermore, Orkney based Scotrenewables Tidal Power is well on track to build and test the world's largest floating tidal turbine, with 2MW output capacity [114].

The Pentland Firth is a 10 km wide strait that separates the Orkney archipelago and the Scottish mainland. The region is dominated by semi-diurnal tides, with primary M2 and secondary S2 tides propagating from the Atlantic Ocean on the west to the North Sea on the east. Davies et al. [115] have elaborated that the exceptional tidal current observed in the region can be attributed to the large differences in the tidal amplitude observed in the west and east of the channel. In addition, this area is also notable for being extremely turbulent and thus presents great challenges in obtaining field measurement data.

Direct measurement poses several limitations that are inherent in a hydrodynamic study. Wide spatial and long temporal data is very hard to collect since the measurement exercises are exceptionally expensive and time consuming. Therefore, accurate

and robust numerical modelling is essential in validating theoretical and analytical approaches for marine energy research. Furthermore, as PFOW is one of the most complex regions where strong tidal currents exist, the need to understand and characterise the depth-wise tidal flow behaviour becomes an important element in tidal resource prediction.

Although field measurements have been undertaken by developers, this does not cover the entire PFOW region, and the alternative is to employ a sophisticated numerical model for resource estimation. When a model is used for the resource prediction, the model has to be properly calibrated and validated before any longer term prediction can be performed. The objective of the calibration exercise is to select appropriate input parameters that would yield numerical output that is comparable to the measurement data. More importantly, model calibration for any 3D simulations is a laborious process as several additional input parameters need to be considered in comparison to 2D models, and one such exercise is presented here.

Several numerical models, both 2D depth-averaged and 3D models, have been utilised for hydrodynamics, morphodynamics and resource assessment studies in the Pentland Firth. Chatzirodou and Karunarathna [116] employed a 3D model to study the impacts of tidal energy extraction on sea bed morphology using the open source Delft3D software, where they found that locations favoured for tidal energy extraction (i.e. the Inner Sound channel) lie in proximity to highly sensitive sand and gravel deposits. Baston et al. [117] also utilised the Delft3D model to analyse the sensitivity of the algebraic and k-epsilon turbulence closure models, and concluded that although the models were able to satisfactorily reproduce the shape of the vertical current profile, further validation was required to provide a more 'statistically accurate' assessment on the vertical variation of current at the testing sites.

Venugopal and Nemalidinne [118] on the other hand used the commercial software, MIKE 21 and MIKE 3 to perform a 3D hydrodynamics simulation of combined wave and tidal flow in this area, where the coupled model yielded high correlation coefficients, and were able to provide a good match with ADCP measurements at different depths, despite using default values for most of the flow parameters. Easton et al. [119] also explored the flow dynamics at this location using the MIKE 21 2D hydrodynamics model. Using the quadratic friction law to calculate the energy dissipation, Easton et al. demonstrated that the mean rate of energy dissipation over two consecutive spring-neap tidal cycles in this region to be close to 5.24 GW, which agrees well with the 5.62 GW net energy flux calculated across the boundaries of the Pentland Firth.

Another 3D model, Stanford Unstructured Non-hydrostatic Terrain-following Adaptive Navier-Stokes Simulator (SUNTANS) was employed by Baston and Harris [120] in investigating the complex flow characteristic at the Pentland Firth, although the scope of this study was limited to the sensitivity analysis of the bottom friction coefficient. Furthermore, a discontinuous Galerkin, depth-averaged ADCIRC numerical model was applied by Adcock et al. [111] to explore the maximum extractable power for tidal stream resources, in which the actuator disc concept was used to model the effects of turbines on the flow.

Bowyer and Marchi [121] meanwhile constructed a depth-averaged model of the Princeton Ocean Model (POM) to inspect the influence of TEC and wind on the residual flows in the channel, and concluded that the installation of large scale TECs in arrays may influence the residual circulation and possibly increase tracer (i.e. sediments or particles) deposits within the channel. Finally, Telemac2D was used by Ortiz et al. [122] to present an approach in estimating the resources in the Pentland Firth, where their results demonstrated how an oversized tidal farm may produce less power due to reduced incoming current velocities. The study by Ortiz et al. further highlights the need to comprehend the overall effects of tidal arrays and the inherent momentum sinks, rather than just relying on the energy potential calculated from an undisturbed site evaluation.

From literature, it appears that the influence of 3D input parameters such as bottom frictions, turbulence, eddy, and boundary forcing on the numerical models are yet to be thoroughly explored, discussed, and understood, especially for Telemac3D. Moreover, most of the studies conducted in this region were completed using 2D depth averaged models, where the velocity across the water column cannot be accurately predicted. Although 3D models require more computational power to run, they are able to provide additional insights on the flow characteristic that is not possible with the 2D models, such as the turbulence component in the vertical direction, which is important to account for fluid mixing behind the turbines and dissipation of energy from the flow.

Hence, the purpose of this research is neither to examine the available resources in PFOW region nor to reproduce a resource map, as extensive studies on this subject have been conducted before, but to inspect how the values of selected model input parameters affect the results. Furthermore, since the accuracy of any numerical model is greatly dependent on open boundary conditions, input parameters and the numerical scheme, this study focuses on applying appropriate methodology in investigating the

critical parameters which are known to influence the output of 3D flow models.

The novelties of this study can then be summarised as follows; Firstly, the suitability of several input parameters for the Telemac3D model is explored, become to the author's knowledge, no detailed 3D studies are yet to be conducted in this region using this software. Secondly, the predicted output from two distinct numerical models – Telemac3D [123, 124] which is a finite element based numerical model, and Delft3D [125], which is a finite difference based model employing only the structured grid – are investigated and analysed. Overview of the numerical modelling conducted using Delft3D model will be presented in the subsequent chapter.

Emphasis on the technique in constructing a 3D hydrodynamics model for the PFOW using Telemac3D is presented and elaborated in the following section. Apart from conducting the parametric study, the aim of this chapter is to comprehend the limitations and shortcomings of the chosen numerical software. What is more, this research work (comprising of both Chapter 3 and Chapter 4) also presents the preliminary analysis of the efficiency for both Telemac3D and Delft3D models to produce accurate 3D flow characteristics, as the next progression of this study would involve inserting tidal turbines into the numerical models. It is hoped that this work could be used as a guideline for developing a 3D tidal model for this region by utilising the methodology presented.

3.2 Model description

Telemac3D is a finite element model that solves the Navier Stokes equations with a free surface, along with the advection-diffusion equations of salinity, temperature and other parameters. This model was developed by the National Hydraulic and Environment Laboratory (LHNE), a research and development unit under the Electricite de France (EDF) and has been made open source since July 2010. The numerical scheme is also comprised of the wind stress, heat exchange with the atmosphere, density and Coriolis effects. The 3D flow simulation (with hydrostatic assumption) is calculated by solving the following equations:

$$\frac{\partial U}{\partial x}+\frac{\partial V}{\partial y}+\frac{\partial W}{\partial z}=0 \tag{3.1}$$

$$\frac{\partial U}{\partial t}+U\frac{\partial U}{\partial x}+V\frac{\partial U}{\partial y}+W\frac{\partial U}{\partial z}=-g\frac{\partial Z_s}{\partial x}+v\Delta(U)+F_x \tag{3.2}$$

$$\frac{\partial V}{\partial t} + U\frac{\partial V}{\partial x} + V\frac{\partial V}{\partial y} + W\frac{\partial V}{\partial z} = -g\frac{\partial Z_s}{\partial x} + v\Delta(V) + F_y \tag{3.3}$$

where U, V and W are the three-dimensional components of the velocity, v is the tracer diffusion coefficient, F_x and F_y are the source terms of the process being modelled (e.g. sediment, wind, Coriolis force etc.), Z_s is the free surface elevation, and g is the acceleration due to gravity. The vertical velocity is then derived from the continuity equation, and the hydrostatic pressure is given as:

$$P = P_{atm} + \rho_0 g(Z_s - z) + \rho_0 g \int_z^{Z_s} \frac{\Delta\rho}{\rho_0} dz \tag{3.4}$$

where P_{atm} is the atmospheric pressure, ρ_o is the reference density, z is the vertical space component, and $\Delta\rho$ is the variation of density around the reference density. The second term on the right hand-side takes into account the buoyancy effects due to temperature and salinity. In addition, Telemac3D also solves the advection-diffusion equation in non-conservative form for a scalar quantity, T:

$$\frac{\partial T}{\partial t} + U\frac{\partial T}{\partial x} + V\frac{\partial T}{\partial y} + W\frac{\partial T}{\partial z} = v\Delta(T) + Q \tag{3.5}$$

In this equation, T is passive or active tracer (e.g. salinity and temperature), and Q is the tracer source or sink. Telemac3D offers the choice of using either the hydrostatic or non-hydrostatic pressure code. Hydrostatic pressure code simplifies the vertical velocity (W) assumption, ignoring the diffusion, advection and other terms. Thus, the pressure at a point is the sum of weight of the water column and the atmospheric pressure at the surface. Conversely, the non-hydrostatic option solves the vertical velocity equation with the additional gravity term, and is more computationally intensive. Elaboration on theoretical aspects of Telemac3D can be found in these articles [126–129].

Telemac3D uses the same unstructured mesh as the 2D model in the horizontal direction. Grids composing of triangular facets of diverse sizes and forms enable accurate representation of complex topography within the resolution of the elements. More importantly, the non-structured mesh offers unparalleled flexibility against the structured grid, in which the grid density can be effortlessly controlled to adapt to specific applications and geometries.

A more refined mesh geometry is usually applied in areas of special interest (e.g. complex coastlines, river channels and embankments), while the low resolution grid

is used in locations where details are not demanded. This is essential in maximising the computational efficiency. In addition, variable thickness can also be applied in the vertical direction of the whole computational domain, depending on the required grid resolution. Several options for vertical layer mesh transformation are available in Telemac3D. In this study, the terrain following sigma (σ) transformation is implemented.

3.3 Model set up

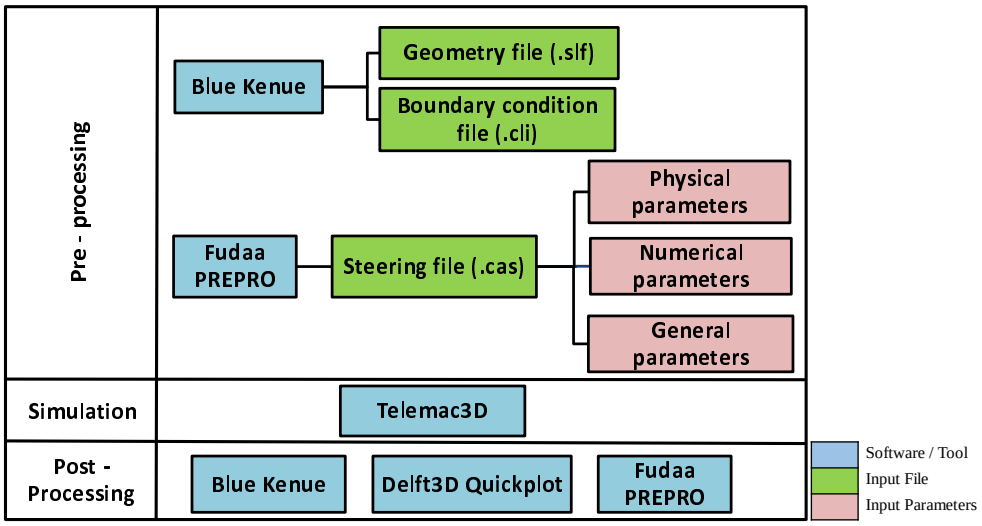

Figure 3.2: Process map for the development of a Telemac3D model.

Figure 3.2 illustrates the development procedure for generating a Telemac3D model. The pre-processing was performed using the Blue Kenue [130] and Fudaa PrePro (Fudaa) [131] software, which are both open source. Blue Kenue is an advanced pre and pro-processing tool developed by the National Research Council Canada for data preparation, analysis and visualisation for numerical modelling. Fudaa on the other hand is a tool for preparing a flow study (i.e. the steering file) developed by the Institute for Maritime and Inland Waterways (CETMEF) France.

Telemac3D requires three input files; the geometry file which contains the information of the model mesh, the boundary condition file which describes the boundary condition of the domain, and finally the steering file that describes the simulation configuration. The first two files can be generated by using Blue Kenue, while the latter is created using Fudaa.

The geometry file contains all the data about the geometry, including the number of points and elements in the grids, in addition to the bathymetric data for each point in the mesh. The boundary condition file on the other hand describes the domain's boundary, in which time varying values (e.g. velocity, water depth and flow rate) can be specified. The liquid or solid (default) boundaries of the model must also be defined during pre-processing. Conversely, the steering file contains a list of keywords that are crucial for executing the simulation.

It is imperative to highlight that the Telemac3D uses a library that is distinctive from Telemac2D in generating the steering file, which contains the selections of computational options (physical, numerical and general parameters). More importantly, the geometry and boundary conditions file generated from the Blue Kenue are requested upon the creation of a new steering file.

Consequently, once the simulation is completed, the results (in selafin format) can be viewed and extracted by using either the Blue Kenue, Fudaa Pre-Pro or Quickplot tool (from the Delft3D software). Selafin is the standard internal format used by the Telemac system and can be read by the previously mentioned post-processing tools. Blue Kenue reads the result file and can generate a vector map of the domain as well as temporal series. Additionally, it is also capable of extracting elements based on printed output variables. Nonetheless, from experience, model with longer simulation period (e.g. one month or more) would produce very large output file since it contains the model's information on both the horizontal and the vertical layer nodes. Invariably, this have caused Blue Kenue to crash when attempting to extract the variables.

In general, the use of the Delft3D Quickplot tool offers a slightly better experience for the post-processing, though it is not without a flaw. The tool's drawback is also apparent when procuring the variables from a large output file, more so when the file contains thousands of time steps, as the variables can only be acquired for a certain number of time step each time. Else, the maximum variable size allowed by the program could be exceeded causing the program to stop and crash. Hence, the post-processing of the models could be a time consuming process due to the limitation of the tools mentioned. Alternatively, users with programming knowledge can use the Python script to assess and acquire the variables stored in the selafin file.

The geometry used in the Telemac3D domain was acquired from the World Vector Shoreline database, available from the shoreline toolbox in the Delft Dashboard [125]. Alternatively, the GEOphysical DAta System - Next Generation (GEODAS-NG) coastline extractor from the National Oceanic and Atmospheric Administration (NOAA)

can be utilised in procuring the geometry for the domain. The geometry acquired using the GEODAS-NG tool uses Cartesian coordinate, and thus requires conversion to the Universal Transverse Mercator (UTM) coordinate system as Fudaa can only accept the latter coordinate system. In contrast, the shoreline extracted from the Delft Dashboard is readily available in the UTM system when the appropriate study zone is selected beforehand, along with the World Geodetic System 1984 (WGS 84) ellipsoid datum.

Upon importing the geometry into the Blue Kenue, it is imperative that the geometry lines are resampled before the mesh is generated. Figure 3.3a shows an example of the original geometry extracted from the Delft Dashboard, which clearly shows unbalanced spreading of the nodes along the line. Alternatively, Figure 3.3b demonstrates an evenly distributed points after the resampling procedure had been conducted. The purpose of resampling the lines is to allow smooth distribution of the geometry points, which is vital in producing a uniform and consistent mesh distribution for the domain. Resampling exercise is also intended in reducing the possibility of having too many points around the nodes. Apart from that, resampling also helps to produce nearly constant areas in the adjacent triangles.

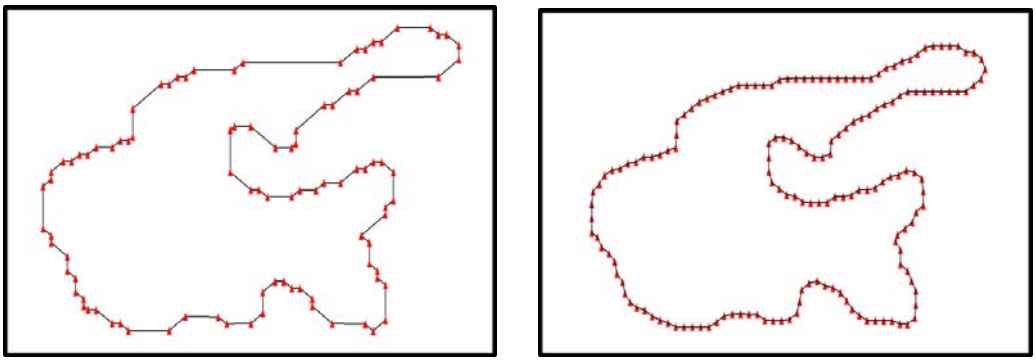

(a) Original geometry points upon importing into the Blue Kenue.

(b) Evenly distributed points after the resampling procedure.

Figure 3.3: Comparison of nodes distribution illustrating the impact of resampling procedure on a model's geometry.

In the process of resampling, it is possible that the profile of the coastline be altered, and attention must be paid in this regard to keep its shape as close to the original profile as possible. Telemac3D system requires that the maximum number of points or elements around a node in the mesh to be less than 10. Three resampling methods are offered in Blue Kenue; the **maximum distance** method ensures that the distance between points do not exceed the intended value; the **equal distance** option allow the lines to be redrawn with equal distance between each point; and finally the **segment**

count method will either increase or decrease the number of vertices on the lines based on the value specified by the user.

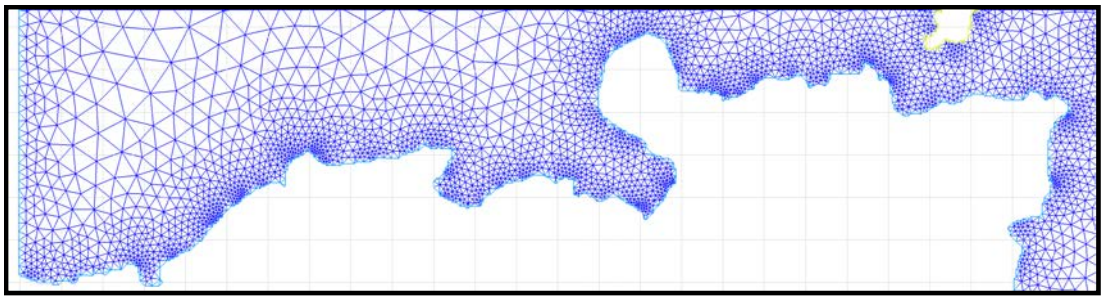

(a) Mesh created using the original geometry.

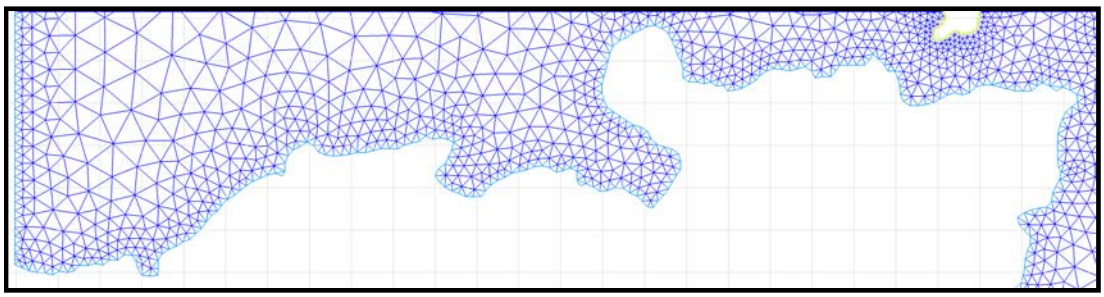

(b) Mesh generated upon resampling procedure.

Figure 3.4: Comparison of mesh growth illustrating the impact of resampling procedure on model's domain.

In this study, the lines are resampled so that the maximum distance between points is set at 200 m, as illustrated in Figure 3.3b. Figure 3.4a then demonstrates how the original geometry created an unbalanced spreading of the mesh in the domain. In contrast, uniform mesh distribution was observed using the altered line, as evident in Figure 3.4b. However, it is crucial that the resampling exercise is carefully administered. Proper care should be taken so that the newly created points on the corrected line maintain the shape of the original geometry. Figure 3.5 demonstrates how the newly created line using the equal distance value of 400 m was slightly smoothed by the resampling process, causing it to somewhat distorted from the original points and thus effecting the geometry's accuracy.

To create the domain's grid, the mesh density around the Pentland Firth channel was set to a minimum distance of 200 m, while the default edge length for the rest of the domain was assigned to 3000 m. The edge growth ratio, which is the parameter that defines the maximum ratio between the lengths of edges at a given node, was set to the

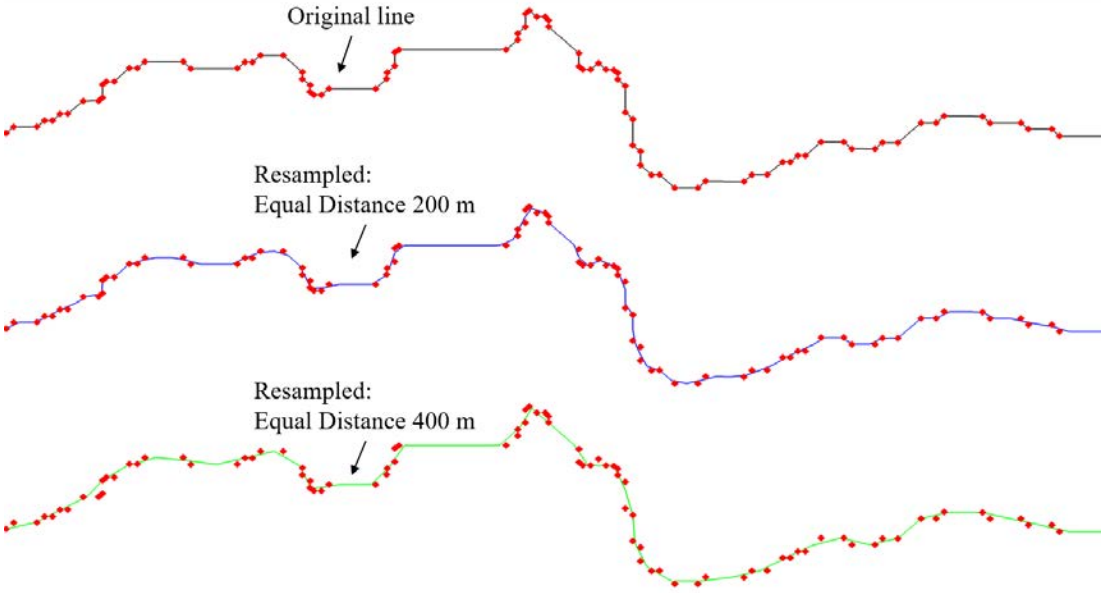

Figure 3.5: Illustration on how improper resampling approach may alter the object's contour. The nodes shown here are from the original geometry to highlight changes caused by the resampling process on the geometry's profiles.

default value of 1.2[2]. Furthermore, in an attempt to improve numerical accuracy and to establish a fixed node within the mesh, three hard points (50 m edge length) were used as the monitoring points at the ADCPs location.

Figure 3.6 shows the computational domain that was generated for use with the Telemac3D model. The domain contains 285,747 nodes (inclusive of nodes in the vertical layers) and 497,230 elements, with 10 equidistant sigma layers in the vertical direction, which was sufficient to represent the approximate depth where measurements were available. Additionally, the time step was set to 10 seconds, which was estimated using the known information (i.e. smallest mesh size, and the highest mean velocity in the study area) to meet the Courant–Friedrichs–Lewy (CFL) stability criterion.

For Telemac3D simulation, two sets of bathymetric data with distinctive resolution were inspected. The first was General Bathymetric Chart of the Oceans 2008 (GEBCO 08), a continuous terrain model for ocean and land bathymetry with a spatial resolution of 30 arc-seconds. This database can be extracted by using either the GEBCO Grid Display Software [132] or from the Bathymetry's toolbox in the Delft Dashboard, both of which are available for free. The second set of the bathymetric data utilised

2. A lower edge growth ratio value will provide a more refined mesh generation, hence substantially increasing the number of nodes within the computational domain.

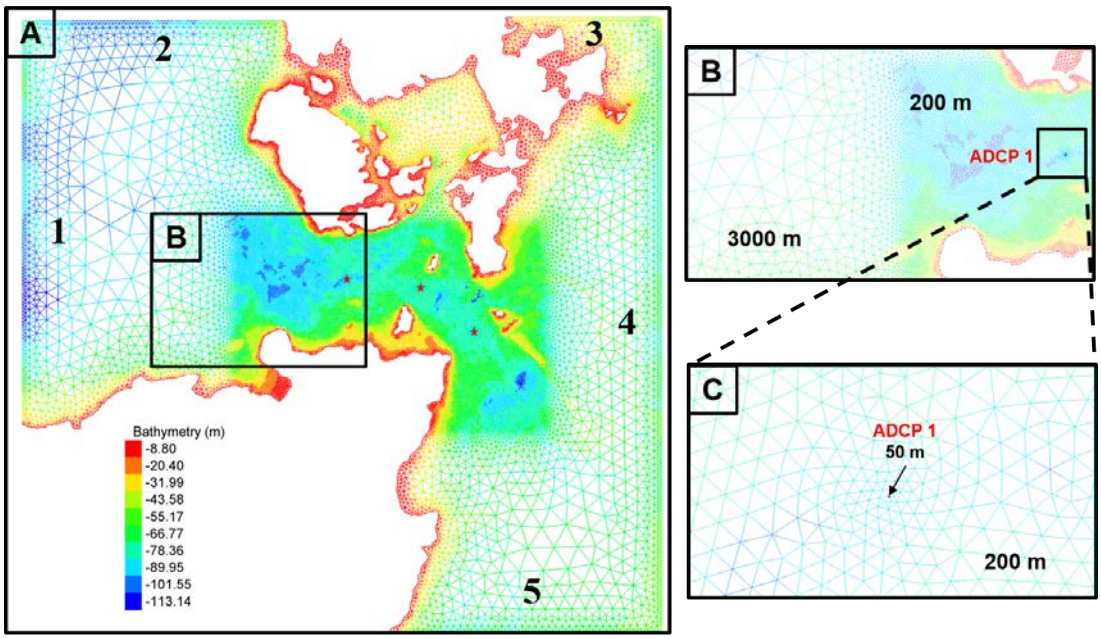

Figure 3.6: Computational domain used for the Telemac3D models. (A) Mesh with the interpolated bathymetry. Numeric 1 till 5 corresponds to the liquid boundaries in the domain. (B) View of the coarser mesh resolution outside of the Pentland Firth, and the 200 m mesh density in the study area. (C) Hard point with 50 m resolution at a monitoring station (ADCP location).

in this study was provided by the EPSRC-funded TeraWatt consortium [133], with a higher spatial resolution of 20 meters where the measurements were available. This bathymetric database were then combined and interpolated with the GEBCO 08 data to provide a comprehensive coverage of the PFOW region.

Open boundaries with prescribed depth (H) were applied to the liquid segment on the five sides of the domain (Figure 3.6), where the prescribed depth with free tracer (i.e. input from temperature and salinity are not considered) was used to supply the forcing required to drive the flow through the domain. The tidal harmonic database was derived from the Oregon State University (OSU) TOPEX/Poseidon Global Inverse solution - version 7 (TPXO7), with a spatial resolution of 0.25^{o} x 0.25^{o}. The database acquired is for the sea surface elevation, and consists of the following harmonic database; eight primary (M2, S2, N2, K2, K1, O1, P1, Q1), two long period (Mf, Mm) and 3 non-linear (M4, MS4, MN4) constituents.

While the majority of hydrodynamic modelling for the PFOW region extended their numerical domain to include the continental shelf (e.g. [111, 134, 135]), studies conducted by Rahman and Venugopal [136], as well as Gunn and Stock-Williams [137]

have shown that the use of a smaller domain is equally plausible, provided that the open boundaries were set to be far away from the area of interest. This is necessary in order to reduce their influence on the solution and to minimise numerical instability that might develop at the boundaries. As such, due to limited computing resources available to the author, the numerical domain employed in the present study did not cover the Scottish continental shelf.

In preparing the steering file, the time step used in the simulation should be carefully selected so that the CFL stability criterion is satisfied. The CFL condition is defined by:

$$CFL = U_c \frac{\Delta t}{[\Delta x, \Delta y]} \tag{3.6}$$

where U_c denotes the characteristic wave speed of the system (m/s), Δt is the time step in seconds, and $\Delta x, \Delta y$ is the minimal value of the grid spacing in either direction. CFL condition is an essential parameter of stability for both finite volume and finite difference methods, and it is directly influenced by the size of the meshing and the assigned model time step. For Telemac models, the CFL number is suggested to be less than two to achieve acceptable model validity [138, 139]. The accuracy of the numerical model may be affected in the presence of high CFL number, since the time taken for the fluid to travel across any given grid would be faster than the allocated time step.

For the initial boundary conditions, both the TPXO7 satellite altimetry and constant elevation options have been put to the test and demonstrated that the pair are suitable for this application. Brief overview of these two tested options are given in Appendix A (refer to Figure A.1 and Table A.1). The model simulation spin up time was set to three days before the intended comparison against the measured data to allow for the computation to achieve numerical stability, and the simulation period was set to 35 days. 'Tidal flat' keyword was also activated in this study to take into account the area that are periodically wet and dry during high and low tide respectively. The choice of the numerical and physical parameters used in the models will be presented and discussed in Section 3.5.

Meteorological input (e.g. wave and wind), along with density and temperature variation were not applied as their influence on the model output was expected to be lower than the astronomical forcing. Although a coupled model (with tidal and wave input) was needed to improve the model's accuracy, they are not considered in present study.

Furthermore, since the computational domain generated for Telemac3D models was not large enough for the Coriolis force to influence the computation, the (default) models were run without the Coriolis effect. In addition to that, the default hydrostatic code was applied for all models as no substantial differences were observed when using the more computationally demanding non-hydrostatic version. The U and V horizontal velocity components, along with the water elevation were set as the 3D output variables for the Telemac3D model.

3.4 Model calibration

In situ measurement data are critical for all numerical modelling in order to give credence to the model output. Acoustic Doppler Current Profiler (ADCP) data supplied by the TeraWatt project are used to validate the numerical models at three sites. Nonetheless, any errors or uncertainties that may present in the ADCP data are not known to the author, and it is assumed that the provided measurement data has undergone quality control procedure. ADCP data is very useful for 3D hydrodynamics modelling as it supplies data on flow velocities throughout the water column. The locations of these devices at the PFOW are given in Figure 3.1. The acquired data offered a measurement time step of every 10 minutes at 4 m intervals through the water column, with the deepest measurement approximately 5 m above the ocean floor. Details of the field data are given in Table 3.1.

Table 3.1: Details of the ADCP measurement data supplied by the TeraWatt project.

ADCP	Coordinate	Depth	Measurement data
Site 1	58º 43’ 34.00" N 3º 14’ 11.01" W	82 m	14/9/2001 - 16/10/2001
Site 2	58º 43’ 1.02" N 3º 5’ 9.02" W	80 m	19/9/2001 - 20/10/2001
Site 3	58º 40’ 13.02" N 2º 58’ 35.03" W	71 m	15/9/2001 - 14/10/2001

Water surface elevation measurement can be obtained via tidal gauges. Delft3D Dashboard software incorporates a worldwide tide stations database, together with the stations’ astronomical components within the software’s tide station toolbox. It is worth to note that the measurement data available from the tide stations include both astronomical and meteorological input, while the general models utilised in this study only consider the astronomical input.

The first step in validating the numerical model is to compare the predicted water surface elevation with the available IHO tidal gauges database in the computational domain. This procedure was performed to check the suitability of the chosen boundary conditions in simulating the hydrodynamics of the study. The comparison of the water surface elevation between the Telemac3D model and measured data was conducted at two tidal gauges; Scrabster IHO and Wick IHO. Figure 3.7 produced from the Telemac3D model shows an excellent comparison of the water elevation between the model output and the two tidal gauges. The comparisons shown here covered a full spring tidal cycle from 16/09/01-26/09/01, and demonstrated that the open boundary with the prescribed water level forcing is highly suitable for the hydrodynamics application in this computational domain.

3.5 Parametric study on Telemac3D model

Several sets of performance indices were utilised in comparing the measured data with the numerical models. Pearson's Correlation Coefficient (r), is a measure of the strength of the linear relationship between two data sets (Equations 3.7-3.8). An r value closer to 1.0 indicates a strong relationship between variables. The difference between predicted and observed values can be evaluated using Root Mean Square Error (RMSE), where a smaller value indicates good model performance (Equation 3.9). In addition to this, Scatter Index (SI), which is the root mean square difference between the model and the mean of the field data, was used in the analysis (Equation 3.10).

$$\mathrm{r} = \frac{\sum_{i=1}^{N}(x_{oi}-\bar{x}_o)(x_{mi}-\bar{x}_m)}{\sqrt{\sum_{i=1}^{N}(x_{oi}-\bar{x}_o)^2(x_{mi}-\bar{x}_m)^2}} \tag{3.7}$$

$$\bar{x}_o = \frac{1}{N}\sum_{i=1}^{N}(x_{oi}) \tag{3.8}$$

$$\mathrm{RMSE} = \sqrt{\frac{1}{N}\sum_{i=1}^{N}(x_{oi}-x_{mi})^2} \tag{3.9}$$

$$\mathrm{SI} = \frac{RMSE}{\bar{x}_o} \tag{3.10}$$

The general set up for the Telemac3D model used in this study was as follows: the law of bottom friction was set to the Chézy formulation; the coefficient for both horizontal

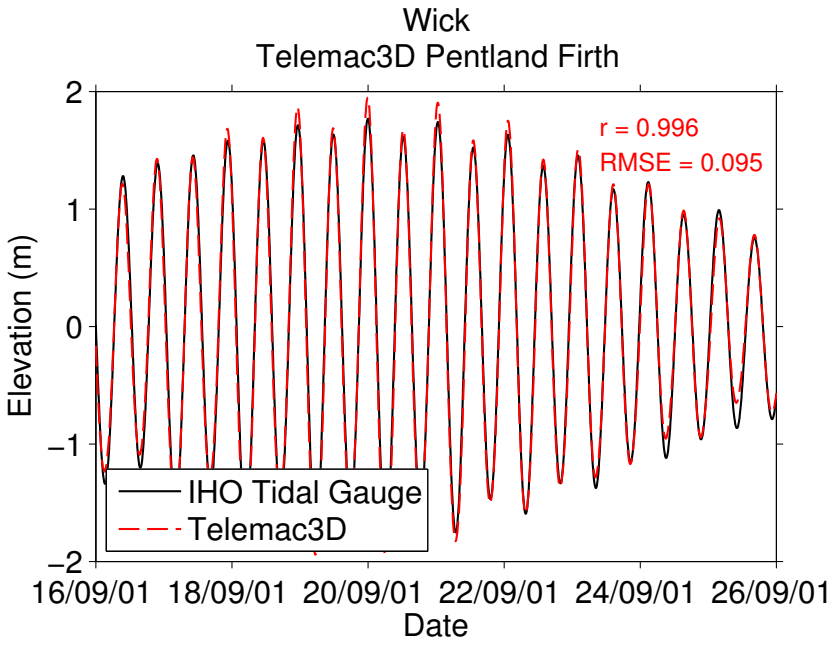

(a) Wick

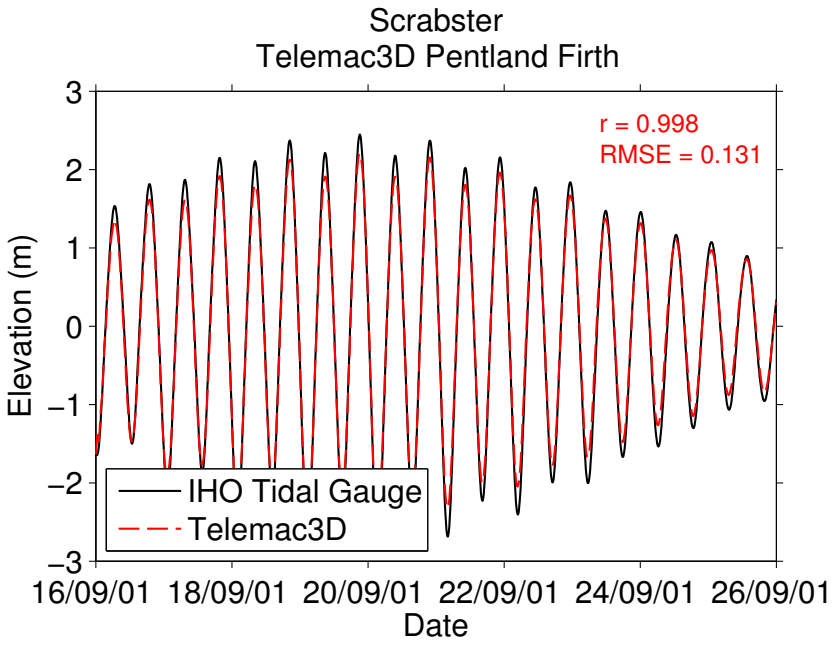

(b) Sule Skerry

Figure 3.7: Comparison of the water surface elevation between the predicted and the measured data for Telemac3D model.

and vertical diffusion of velocities were set to the default value of $1.0\text{x}10^{-6}$ m^2s^{-1}; the Coriolis force was not included in the model unless stated otherwise; the time step for the output file was set at 10 min interval; and the mixing length model using the Prandtl's theory and the constant viscosity (default option) were set as the vertical and horizontal turbulence models respectively. The results were then compared at three different depths; near the water surface (7 m), at the middle of the water column (39 m) and close to the ocean floor (65 m - 71 m).

3.5.1 Bottom roughness

Bottom friction has proven to be an important and sensitive parameter in tidal modelling, where it is often used to fine-tune models so that they give water levels and velocity vectors in agreement with relatively sparse spatial observations. Notably, researchers (e.g. [111, 134]) have found that no single value of the drag coefficient produces results in agreement with field data due to the fact that the bed shear will vary throughout the numerical domain because of spatially varying bottom features. However, a single value of the drag coefficient is often applied uniformly throughout the domain in a compromise between matching the tidal phase and matching the current magnitude at the PFOW.

In oceanographic modelling, the bed shear-stress, τ_b can be represented using a quadratic drag law as follows:

$$\tau_b = \rho Cd\overline{U}^2 \tag{3.11}$$

where ρ is the density of seawater and $\overline{U}$ is the depth-averaged velocity. Effects of bed roughness uncertainty on tidal stream power estimates have been examined by Kreitmar [140], where it was found that the power available for extraction can be increased by the introduction of uncertainty. Furthermore, Soulsby [141] has shown that there are eight different Cd models that can be derived from fitting experimental data to either a power law relationship (Equation 3.12), or a logarithmic law (Equation 3.13).

$$Cd = \alpha\hat{z}^{\beta} \tag{3.12}$$

$$Cd = \left[\frac{\kappa}{B + \ln(\hat{z})}\right]^2 \tag{3.13}$$

Where $\hat{z}$ is the relative roughness, β is equivalent to $4|\cos t'|^{3/2}$, κ is von Karman's constant and $B = (\delta/2h) - \log(\delta/2h)$, where δ and $\overline{h}$ are the boundary layer thickness and mean water depth respectively. Table 3.2 lists these two commonly used emperical formulae for estimating Cd, along with values of parameters α, β, B, and κ obtained from experimental and numerical data, where it can then be fitted to the eight Cd models mentioned by Soulsby.

Table 3.2: Bed roughness coefficient, Cd formulae from relative roughness $\hat{z}$ as summarised by Soulsby [141]. Adapted from [140].

Formula	Method/model	Parameters
Equation 3.12	Manning-Strickler	$\kappa = 0.0474$ $B = 1/3$
	Dawson-Jones	$\kappa = 0.0190$ $B = 0.208$
	Soulsby	$\kappa = 0.0415$ $B = 2/7$
Equation 3.13	Deep water Boundary-layer thickness, δ Colebrook-White $z_0 = (k_s/30) + (\nu/9u_*)$ Full-depth logarithmic Velocity profile	$\kappa = 0.4$ $B = (\delta/2h) - \log(\delta/2h)$ $\kappa = 0.45$ $B = 0.71$ $\kappa = 0.4$ $B = 1$

Several drag coefficients values have been suggested for the Pentland Firth model by previous studies and are summarised in Table 3.3. Nevertheless, the optimal roughness value for the study area using Telemac3D models was found to be 0.005 (as shown by Rahman and Venugopal [136, 142]), which is consistent with the one proposed by Easton et al. [119] who used the MIKE 21 model.

Figures 3.8 and 3.9 show the comparison of several roughness values as proposed in the literature against the measured ADCP data, for both the U and V-velocity components at the three sites. These figures display the results obtained during the spring tide from 16 - 21/09/2001 for Site 1 and Site 3, and 21 - 26/09/2001 for Site 2 since the available field data for this location starts from 19 September 2001. Figure 3.10 meanwhile displays the scatter plots and performance indices (obtained from the same data as presented in Figures 3.8 and 3.9) for the three bed friction coefficients inspected in this

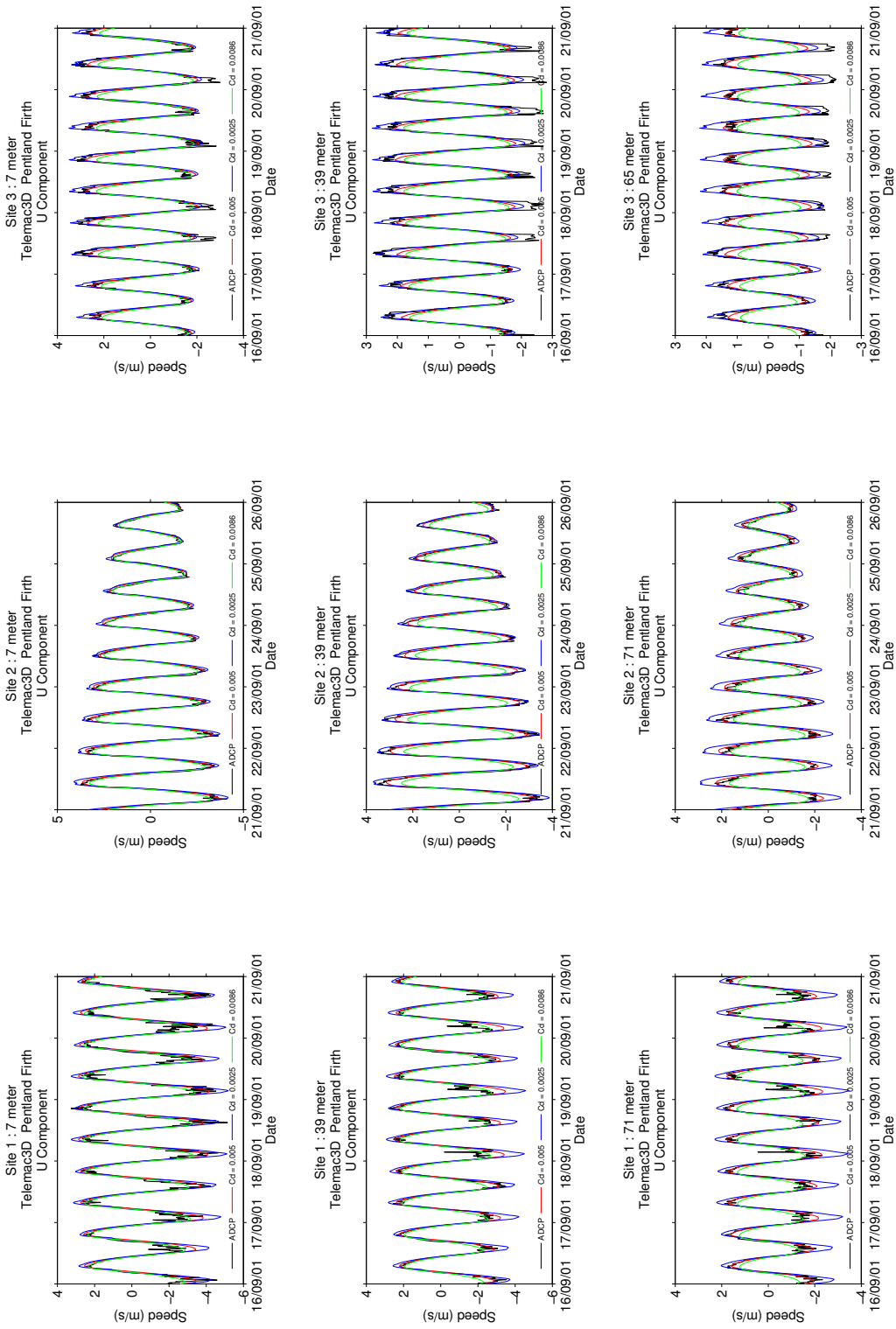

Figure 3.8: The influence of roughness values [Cd = 0.005 (—), 0.0025 (—), 0.0086 (—)] on the U-velocity component for Telemac3D models.

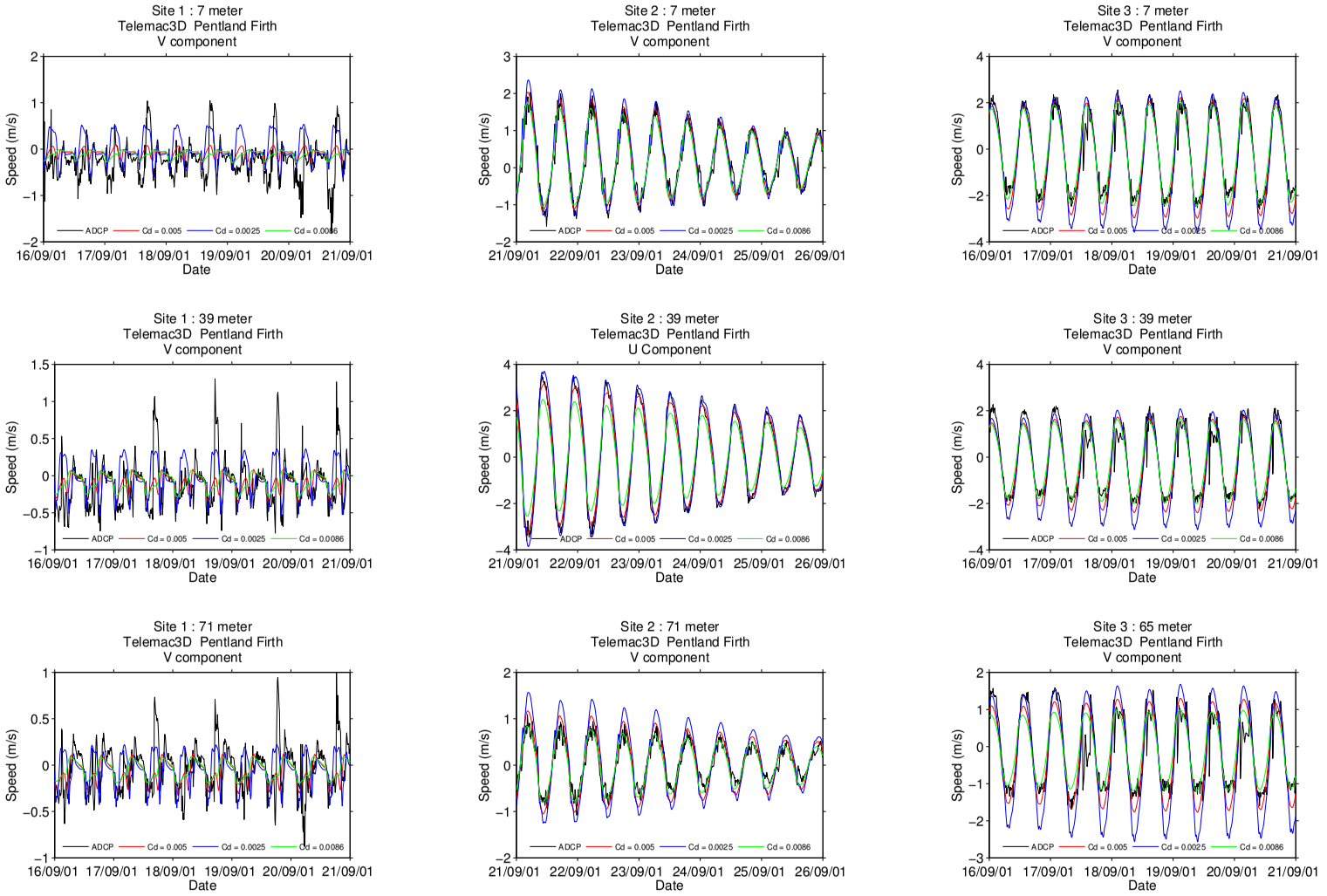

Figure 3.9: The influence of roughness values [Cd = 0.005 (—), 0.0025 (—), 0.0086 (—)] on the V-velocity component for Telemac3D models.

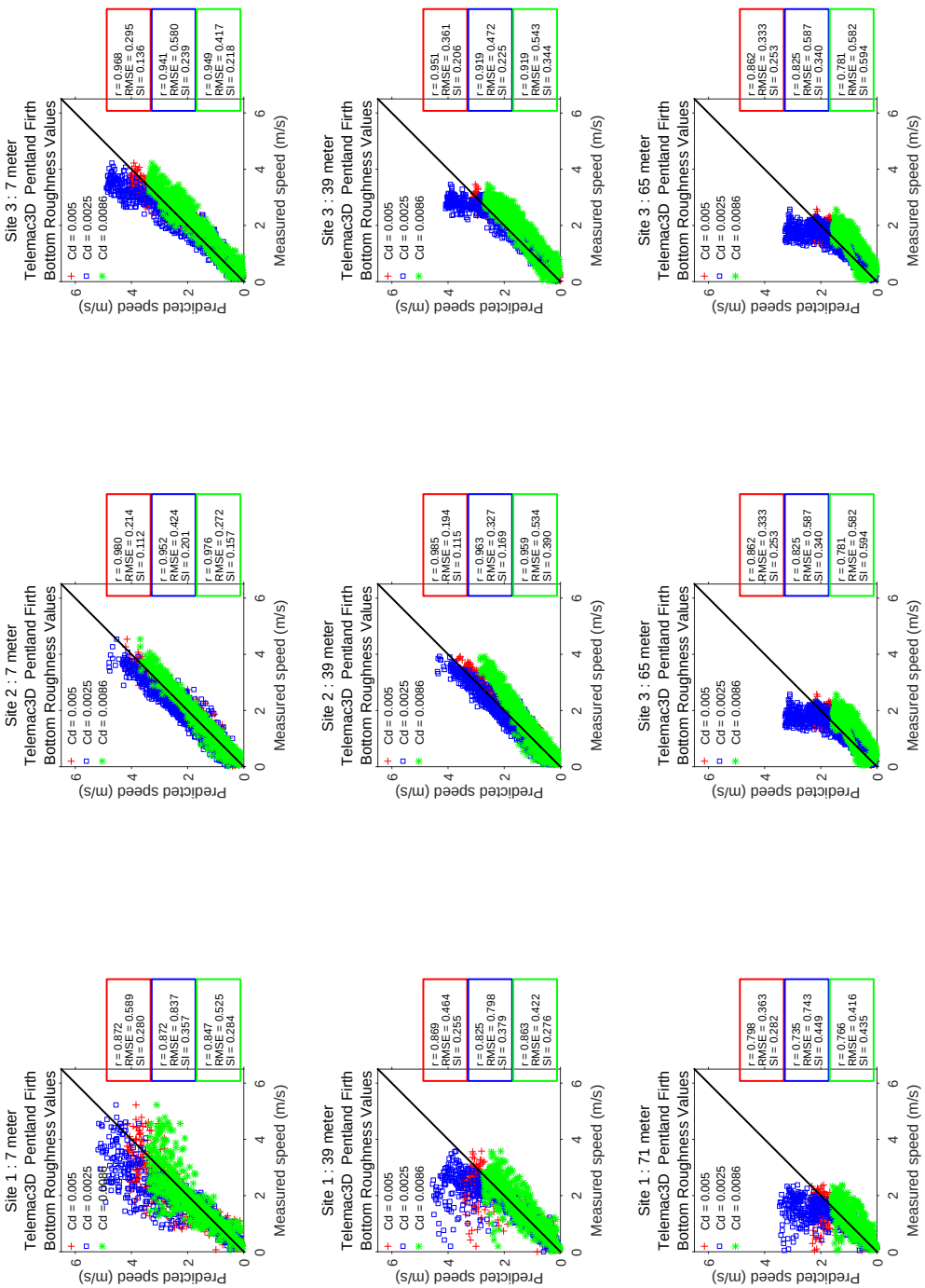

Figure 3.10: Scatter plots with performance indices for the three roughness values utilised in Telemac3D simulations.

Table 3.3: Proposed bottom friction coefficients for the PFOW region from various numerical studies.

Study by	Numerical model	Proposed Cd value
Salter (based on the paper by Campbell et al. [143])	n/a	0.0086
Baston et al. [117]	Delft3D	0.0025
Chatzirodou and Karunarathna [116]	Delft3D	Chézy 50
Rahman and Venugopal [136, 142]	Telemac3D	0.005
Easton et al. [119]	MIKE 21	0.005

study. It can be seen from the performance indices in Figures 3.10 that Cd = 0.005 consistently produced the highest r values, the lowest RMSE and SI outputs amongst the tested roughness values, indicating great correlation between the predicted and measured values.

Nonetheless, although the predicted velocity using Chézy 44 (corresponds to Cd = 0.005) yielded excellent comparison against the measurement data for the three monitoring points, random scatters were apparent for Site 1 as displayed in Figures 3.8 and Figures 3.9. Further inspection reveals that this was caused by the random fluctuation in the V-velocity component at this site. Also this could be due to the fact that the predominant flow is in U-component direction.

Complex turbulence and large eddy circulation, due to the uneven bed structure in this region, could have been attributed as possible causes of this phenomenon, in which the hydrostatic solver utilised in this study may not have been able to sufficiently resolve the turbulence fluctuations. These results are essentially similar to the one produced by Venugopal and Nemalidinne [118] who used the MIKE 3 model, where high and erratic V-velocity fluctuations were also demonstrated by the ADCP data at Site 1.

3.5.2 Bathymetric input

The accuracy of a tidal model can also be influenced by the quality of the bathymetry input [144]. Bathymetry data provides the depths and topography of the underwater terrain, and the term resolution is used to describe the level of its details. Obtaining detailed bathymetry and topographical information can be potentially very expensive, although a number of free databases are available. A comparative study between two different sets of bathymetric data was conducted to examine the impact they may have

on the numerical model. The results are illustrated by Figure A.2 in Appendix A.

The first bathymetry was from the GEBCO 08 with a spatial resolution of 30 arc-seconds, and the second was a high 20-m-resolution dataset supplied by the TeraWatt project. Interestingly, no noticeable differences (in terms of the predicted velocity) are observed between the two bathymetric data at the three monitoring stations. However, it is worth highlighting that detailed bathymetry is crucial when turbines are incorporated in the simulation as it may influence the hydrodynamics in the region where the devices are deployed.

3.5.3 Coriolis force

The Coriolis force, which is caused by the rotation of the earth, deflects tidal movement to the right in the northern hemisphere that causes a counter-clockwise rotation. In the southern hemisphere, this deflection is to the left. This effect, however, is very small in tidal basins and does not exist for motion along the equator. When the Coriolis terms are of the same magnitude as the gravitational terms, a geostrophical equilibrium is reached, and resulting in a Kelvin wave [145]. Kelvin wave cause the range of tide being greater on the right side of an estuary than on the left in the northern hemisphere. Notably, such characteristic is observed for the tidal wave in the North Sea. It also accounts for the tendency of the system to form an amphidromic point (refer to the dark blue areas where the lines come together in Figure 2.4). At this point, the vertical amplitude of the tide is (almost) zero.

In the model, the Coriolis force, f can be calculated through the following formula:

$$f = 2\omega \sin(\lambda) \tag{3.14}$$

where λ is the Earth's rotational velocity equal to $7.27\text{x}10^{-5}$ rad/s and λ is the average latitude of the model. The influence of the Coriolis on the Telemac3D model was investigated by applying the Coriolis coefficient of $1.24\text{x}10^{-5}$ to the model (using 58.7^{o} as the average latitude). Figure A.3 in Appendix A shows the scatter plots for the Telemac3D models (with and without the Coriolis effects) using the roughness value of 0.005 (i.e. Chézy 44). The performance indices for both models display very close similarity between one another, which is to be expected since the computational domain generated for the Telemac3D models are not large enough for the Coriolis force to have a notable influence on the computation.

3.5.4 Comparison of bottom roughness formulation

Two of the most commonly used formulation for the bottom roughness, Chézy and Manning were examined to inspect their influence on the numerical model. Bottom friction is associated to the drag coefficient and is a critical parameter in flow modelling as it has an effect on the predicted amplitude. The bed shear stress for the three dimensional model is given by the quadratic friction law:

$$\tau_{b(3D)} = C_d \rho |\overrightarrow{U_b}| \overrightarrow{U_b}| \tag{3.15}$$

where $\tau_{b(3D)}$, C_d, ρ, $|\overrightarrow{U_b}|$ are, respectively, the bed shear stress, drag coefficient, water density, and horizontal velocity component. The drag coefficient, along with the Manning and Chézy roughness can be parameterised as:

$$C_d = \frac{g}{(C_{roughness})^2} \tag{3.16}$$

$$C_{Manning} = \frac{\sqrt[6]{H}}{n} \tag{3.17}$$

$$C_{\text{Chézy}} = 18 log_{10} \frac{12H}{K_s} \tag{3.18}$$

where g, d, n and K_s refer to the gravitational acceleration, water depth, Manning roughness coefficient and Nikuradse roughness length. A constant Chézy and Manning roughness value of 44 $(m^{1/2}s^{-1})$ and 0.047 $(m^{-1/3}s)$, in which both corresponded to Cd = 0.005 were utilised in this comparison. From Figure A.4 in Appendix A, it can be deduced that both roughness formulae produced identical numerical output, and demonstrated that either bed friction law can be employed for the Telemad3D tidal flow model in this region.

3.5.5 Nikuradse roughness formula

The pioneering work on understanding the effect of roughness on pressure drop was done by Nikuradse [146] who carried out experiments on fluid flow in smooth and rough pipes. His study demonstrated that the characteristics of the friction factor were different for laminar and turbulent flow. In the laminar region, the roughness was shown to have very little influence, however in the turbulent region, roughness played a major role. In numerical modelling, Nikuradse roughness has been used in some of

the flow models (e.g. MIKE 3) and the influence of this parameter has also been tested with Telemac3D.

Three models with distinct roughness values were inspected using the Nikuradse formula, and presented in Figure 3.11. Friction coefficient of 0.001 (very smooth e.g. mud), 0.1, and 1.0 (very coarse and grainy e.g. sand) using the Nikuradse formula were simulated, which produced scatter plots that were rather poor. The models severely underestimated the current speed at Site 1 and Site 3, a RMSE value as high as 1.49 was observed at Site 1. Reasonable performance indices, however, were observed at Site 2 though the models again under predicted the current speed near the sea bed. Overall, the use of Nikuradse roughness formula for the bed friction resulted in substantial velocity reduction against the ADCP data.

These results seem to infer that the general numerical, physical or general parameters applied to the models are not compatible with the Nikuradse roughness option. In contrast with the Chézy and Manning bed friction, Nikuradse formula assumes a logarithmic profile near the bottom, and thus some refinement are needed for the vertical layers. Since this work employed the equidistant layer, it then seems plausible that the law of bottom friction using the Nikuradse formula is not compatible with the model. Models applying the equidistant layer are more suited for the Strickler-based formula, such as Manning and Chézy; therefore these two roughness formulae are more suited for this application as supported by the previously shown scatter plots in Figure A.4 in Appendix A.

3.5.6 Turbulence closure models

Telemac3D offers four options in defining the Horizontal Turbulence Model (HTM), namely constant viscosity, the k-epsilon ($k-\varepsilon$) model, Smagorinsky and also the k-omega ($k-\omega$) model. Two of the turbulence models, the constant viscosity and the Smagorinsky were applied to the Telemac3D models to assess their influence on the flow. The constant viscosity (default option in Telemac3D system) is the simplest turbulence model, and prescribes constant turbulent viscosities (both in the vertical and horizontal direction) throughout the domain. The Smagorinsky model on the other hand is recommended for simulations that involve highly non-linear flow [147–149].

In both cases, the coefficient for both horizontal and vertical diffusion of velocities were set to their default value of $1\text{x}10^{-6}$ m^2s^{-1}, while the vertical turbulence model was set using the default option of Prandtl's mixing length theory. Figure 3.12 displays the

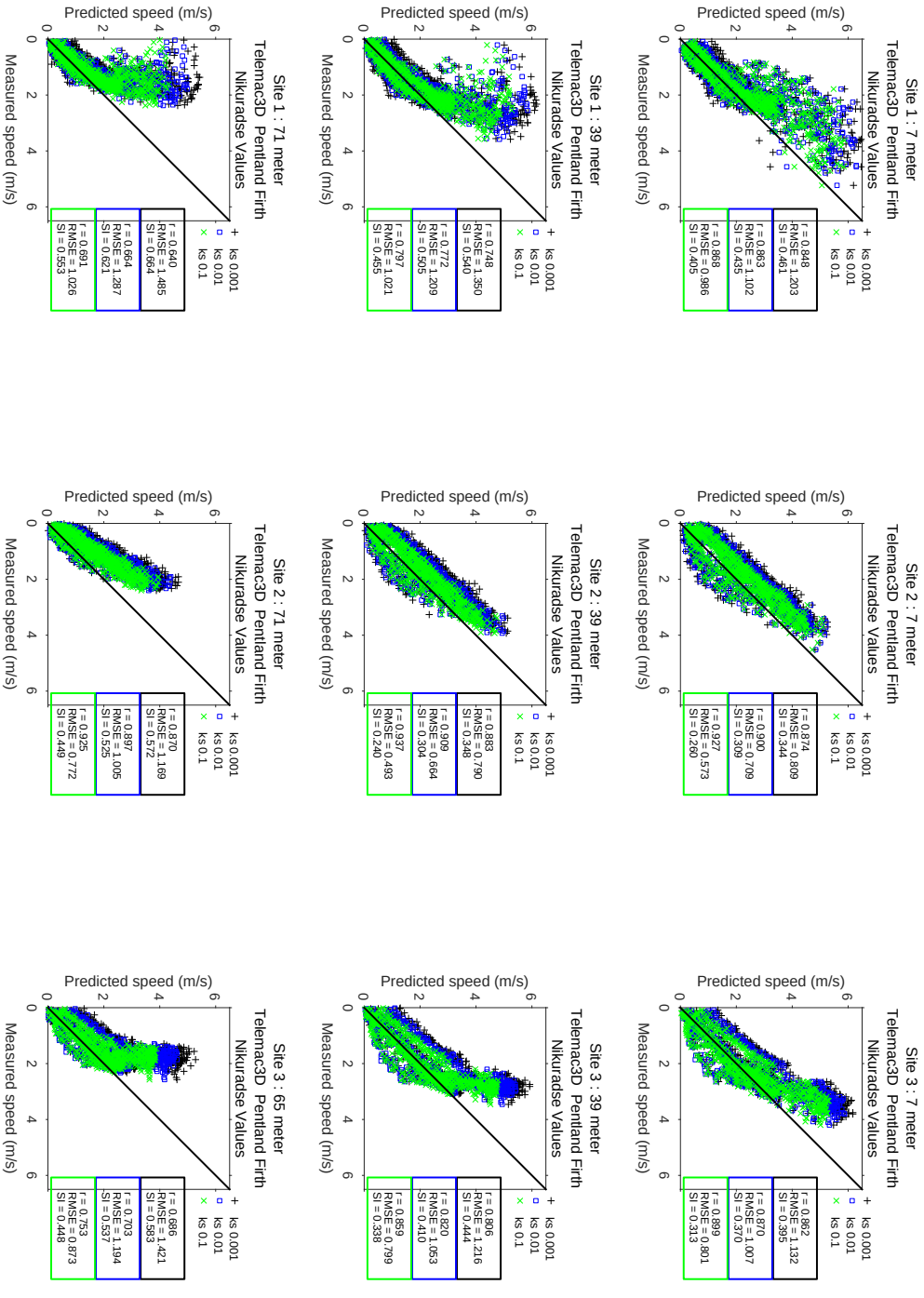

Figure 3.11: Comparison of several bottom roughness values using the Nikuradse formula on Telemac3D models.

scatter plots of the two horizontal turbulence models utilised in the simulation, where no apparent differences are displayed by the performance indices. This highlighted the nature of the flow at the PFOW, which is highly turbulent and non-linear since the use of Smagorinsky model matched the measured data well.

Next, the influence of the viscosity coefficients was investigated, where the selected coefficient values were expected to have some influence on the eddies and recirculation. These parameters are used to control the size and shape of the recirculation of eddies, where small size eddies can be dissipated using a small coefficient, while large sized recirculation can be reduced using a higher coefficient value [126]. Three values (ν = 1x10^{-6} m^{2}s^{-1} (default), ν = 0.01 m^{2}s^{-1}, ν = 1 m^{2}s^{-1}), for the coefficient for horizontal diffusion of velocities were selected, and applied for the model using the constant viscosity as illustrated by Figure 3.13.

Nonetheless, the performance indices in Figure 3.13 suggest that the models are unaffected by the value of the horizontal viscosity coefficients, which is somewhat unexpected. To corroborate this findings, several more coefficient values (ν = 1x10^{-8}, 1x10^{-4} an 1x10^{-3}) were also tested at Site 2 (refer to Figure A.5 in Appendix A). Nevertheless, like before, no noticeable differences were observed. This result seem to imply that the three coefficient values utilised in the models may have greatly dissipated the eddies to be smaller than a two mesh cell, and thus prompting the turbulence to have little to no influence on the computation [126].

3.5.7 Vertical turbulence model

There are four models to choose from upon selecting the mixing length as the Vertical Turbulence Model (VTM); the Prandtl model (default value) is suited for barotropic simulation such as tidal flows [150]; Nezu and Nakagawa; and also Quentin and Tsanis models, which offer a good representation of wind drift [151]. All four mixing length models were investigated in this study, and the results are shown in Figure 3.14 and Figure 3.15. Figure 3.14 shows the scatter plots and performance indices for the four mixing length models that were coupled together with constant viscosity as the horizontal turbulence model.

Figure 3.15 meanwhile displays the results using the Smagorinsky turbulence model in the horizontal direction. It is interesting to see that the four mixing length models compare well against each other, and the difference between the models are almost negligible. Furthermore, the use of either the constant viscosity or the Smagorinsky

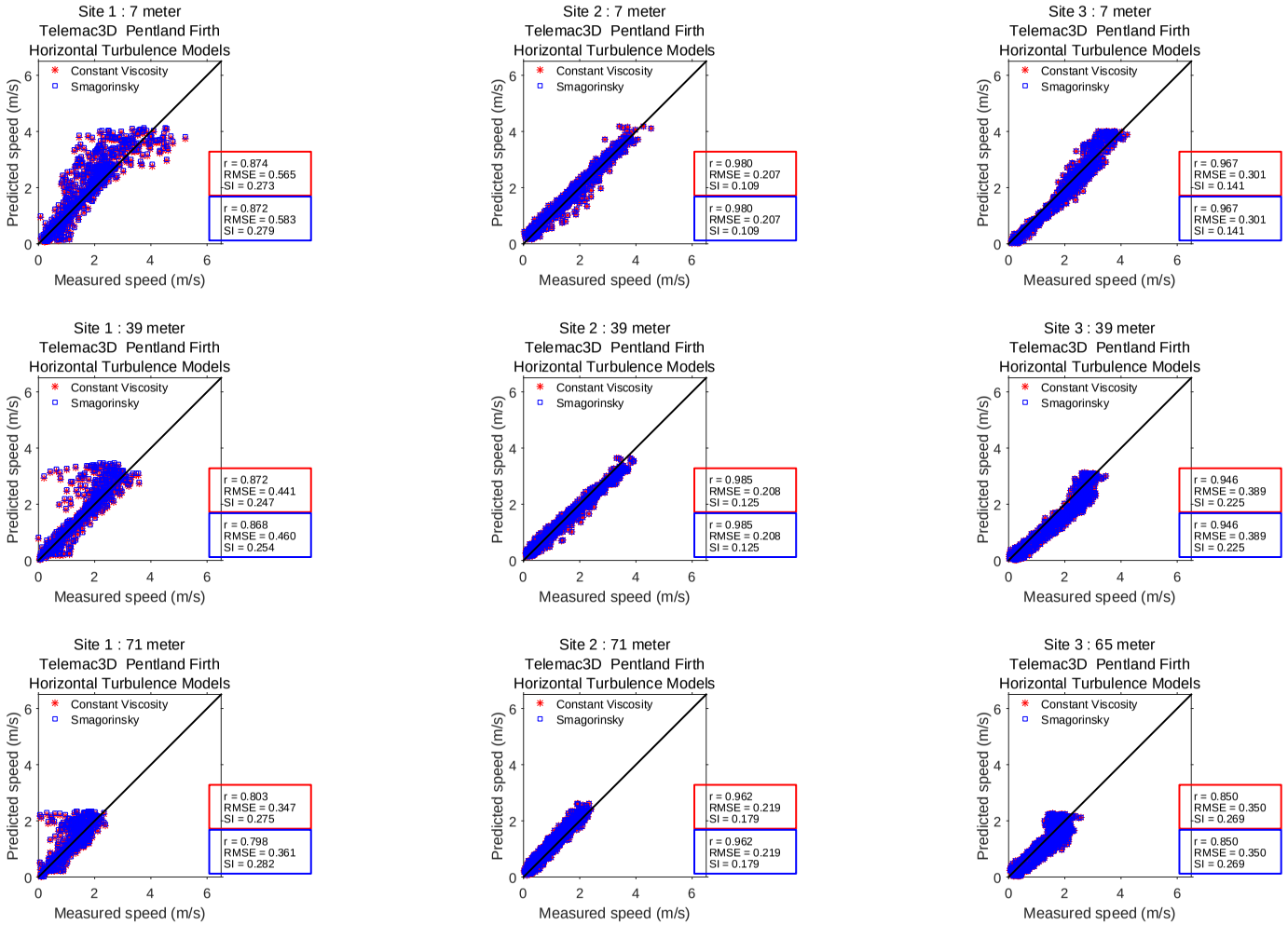

Figure 3.12: Comparison between constant viscosity and Smagorinsky (horizontal) turbulence models applied in Telemac3D models.

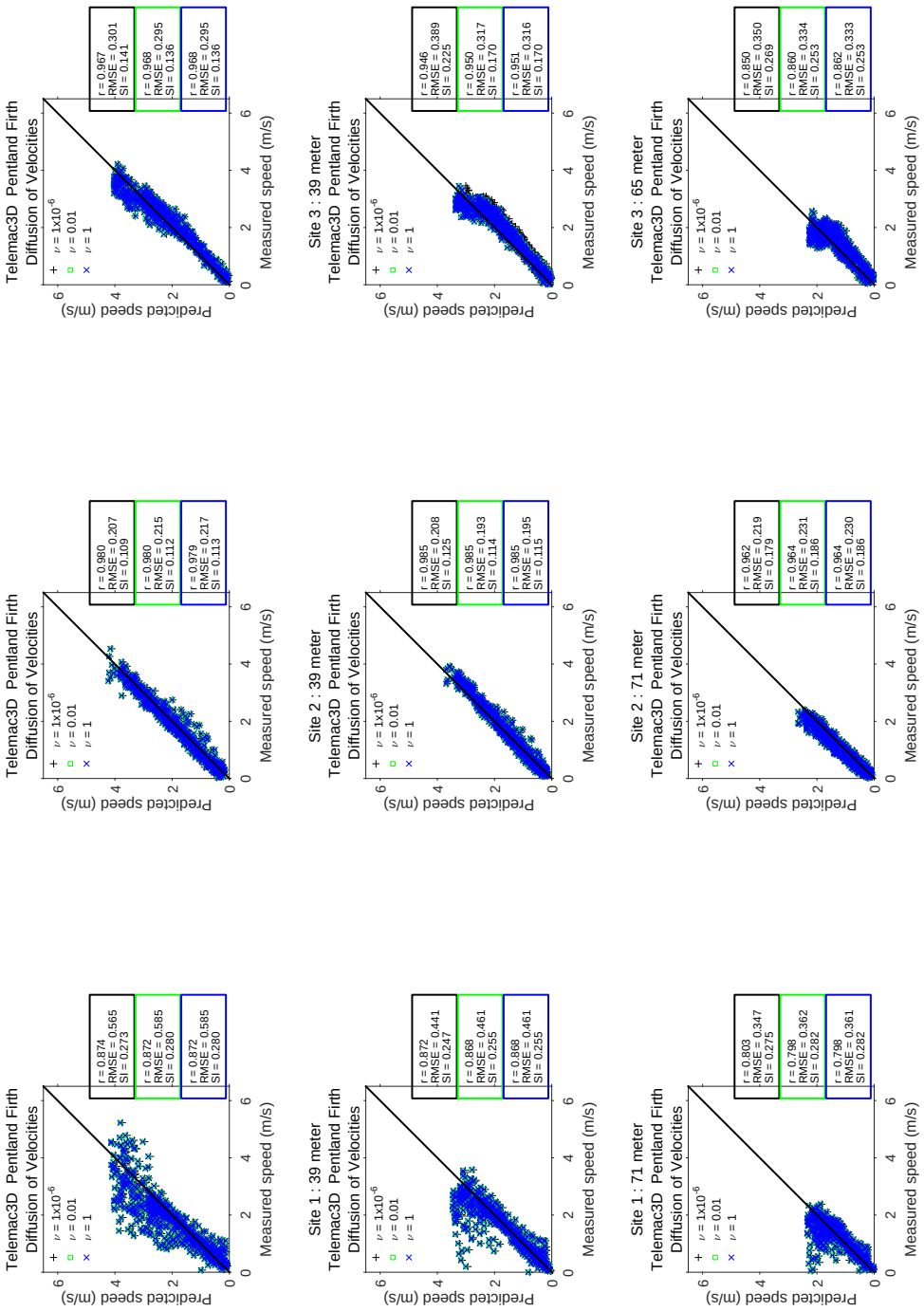

Figure 3.13: Comparison of several viscosity coefficients values applied to Telemac3D models.

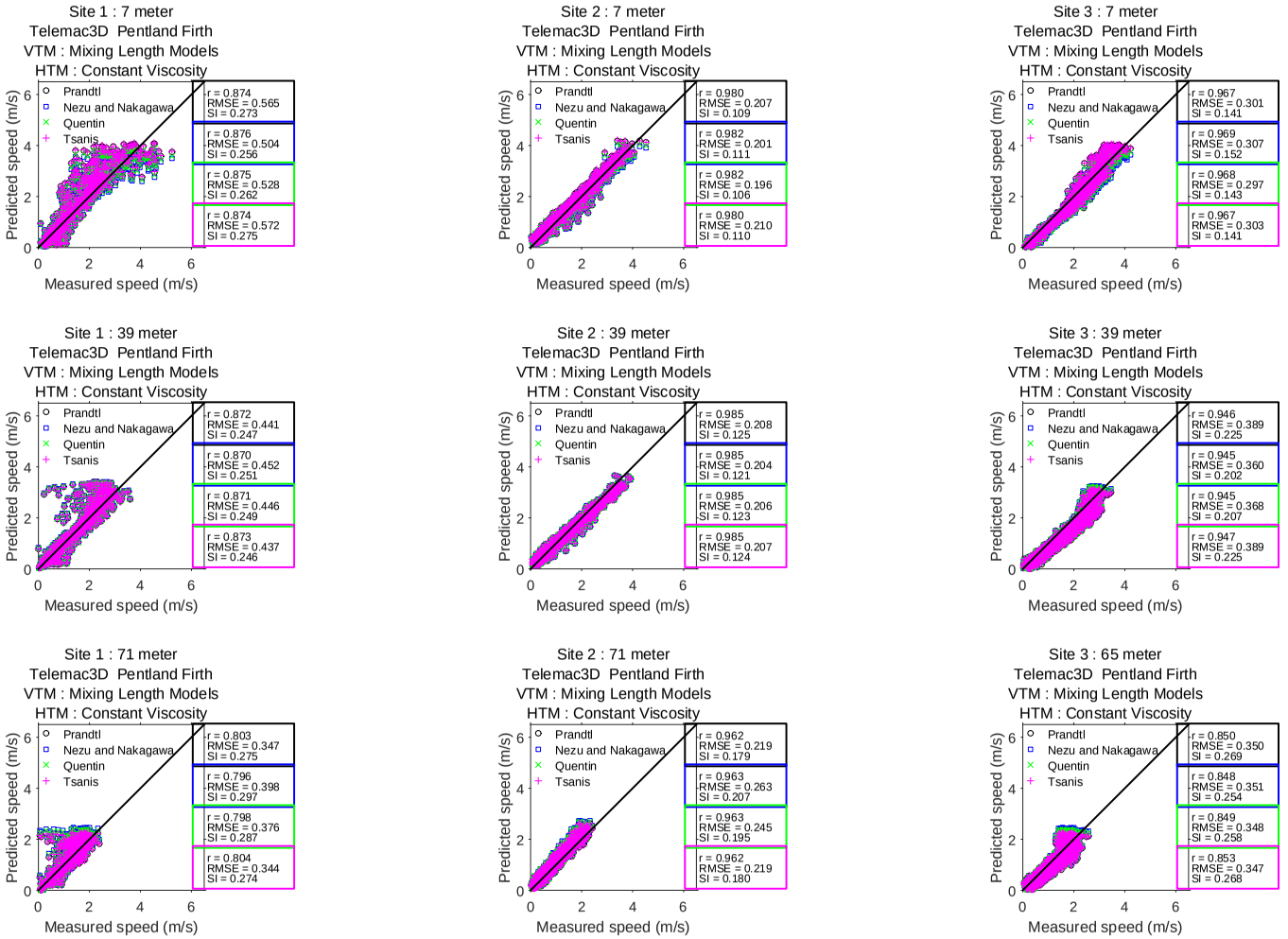

Figure 3.14: Analysis of the horizontal and vertical turbulence models using the constant viscosity and the mixing lengths options.

option as the horizontal turbulence model shows no noticeable influence on the output, which agrees well with previous finding in section 3.5.6.

3.6 Discussion

Since the majority of numerical models employed for hydrodynamics and resource assessment studies at the PFOW were conducted using 2D depth-averaged models, there is a gap that needs to be addressed to further understand the characteristic of 3D models, more so at an area with a highly turbulent flow like the Pentland Firth. Thus, in this chapter, appropriate methods in developing a 3D tidal flow model for the PFOW using Telemac3D numerical model were examined carefully. Great care was taken to ensure the robustness of the models, and the predicted values were validated against the observed data to give confidence to the model.

The physical, numerical and general parameters utilised in the numerical model were elaborated in detail, since the input required for a 3D model differs remarkably from the 2D model. The parametric study was conducted to examine the influence of key simulation parameters on the numerical output, and the performance indices were utilised in comparing the predicted and measured data.

Of the three tested bed friction values for Telemac3D models, Cd = 0.005 produced the best results and can be parameterised by using both Chézy and Manning formulation. The use of Nikuradse formulation as the bottom friction was not suitable in this study since it required highly refined vertical layers, especially near the sea bottom. These findings also demonstrated that the model output was unaffected when varying the values of the horizontal diffusion of velocities, indicating the presence of a highly turbulent flow in the area of interest. Additionally, four distinct mixing length models were investigated using Telemac3D, and the difference between the models were found to be negligible.

Furthermore, the influence of $k-\varepsilon$ and $k-\omega$ turbulence models on the model's output was not highlighted in current study since very rarely has an ocean-scale hydrodynamics model utilised these two turbulence options. Both models comprise a couple of equations solving the balance equations for k (turbulent energy) and ε (turbulent dissipation) / ω (specific rate of dissipation of kinetic energy), hence requiring a finer domain mesh than the tested constant viscosity and Smagorinsky models to ensure numerical stability. Consequently, Telemac3D models with basic turbulence schemes (i.e. using constant viscosity/Smagorinsky and the Prandtl mixing length model) were

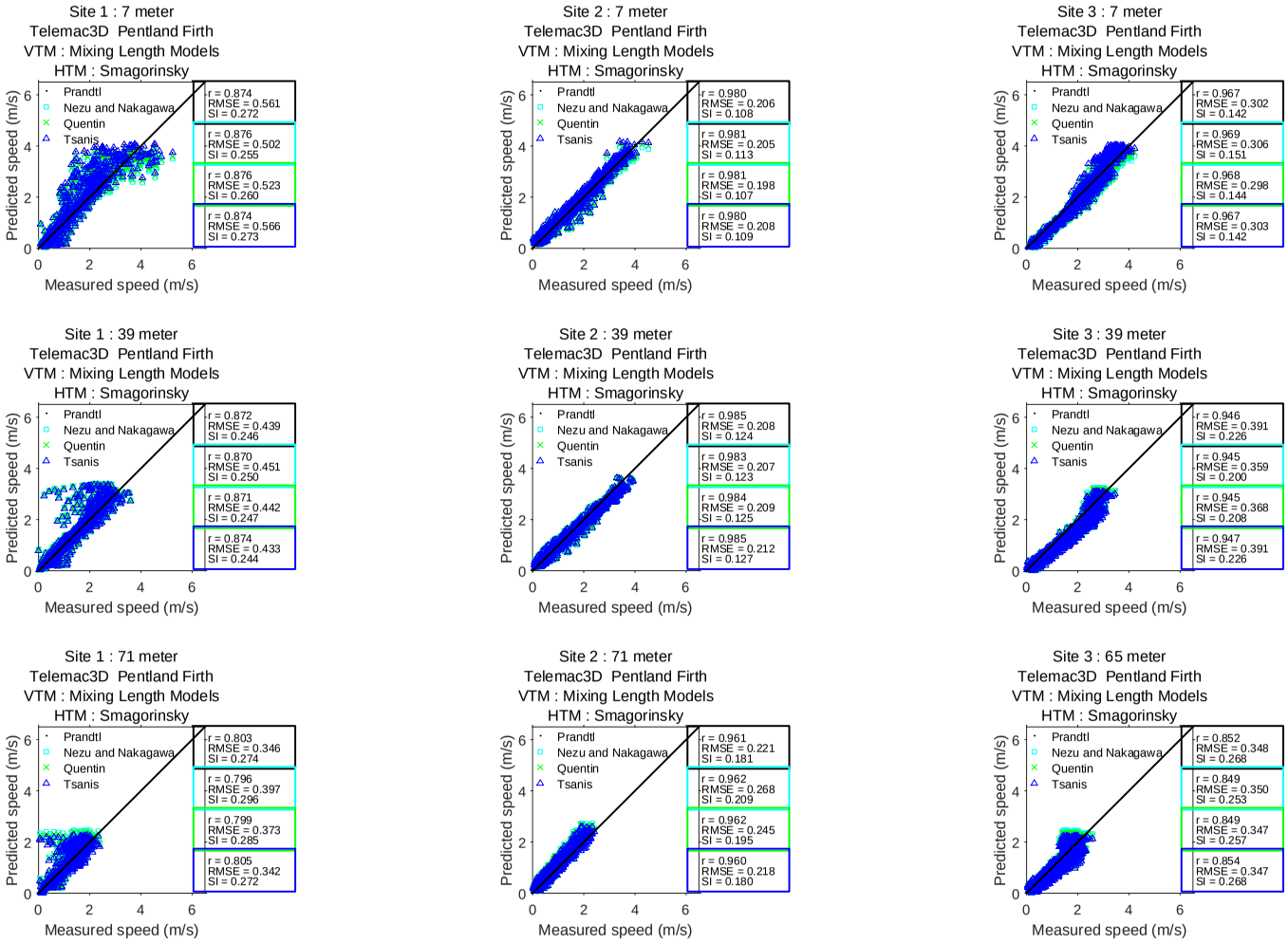

Figure 3.15: Analysis of the horizontal and vertical turbulence models using the Smagorinsky and the mixing lengths options.

therefore employed in preference to the $k-\varepsilon$ and $k-\omega$ turbulence schemes, which are both more complex and also computationally expensive.

Moreover, the choice of eddy viscosity parameter imposed on the model were perhaps quite low to have a meaningful impact on the simulation output. In retrospect, higher viscosity coefficients values should have been tested, which can be approximated using an equation proposed by Borthwick and Barber [152]:

$$\nu = 5.9\mathrm{H}|\overline{U}|\sqrt{Cd} \tag{3.19}$$

where H is the total water depth, $\overline{U}$ is the depth-averaged velocity vector, and Cd is the dimensionless bed drag coefficient. To highlight, Equation 3.19 was used by Bonar [153] to find suitable eddy viscosity coefficient for his depth-averaged DG-ADCIRC model. Subsequently, a sensitivity analysis was also performed by Bonar to ensure that his results were not sensitive to the chosen ν value.

The next chapter will introduce tidal flow modelling using another commonly used numerical tool - Delft3D software.

Chapter 4

Numerical Modelling of the Pentland Firth Region Using Delft3D

This chapter provides a brief overview of the hydrodynamics simulations conducted for the Pentland Firth region using another commonly used numerical model - Delft3D[1]. Moreover, the objective of this research offers a continuation from the work discussed in Chapter 3 - to investigate the influence of input parameters on a 3D hydrodynamics simulation, albeit using a different numerical model.

Extensive parametric study on critical numerical parameters has been conducted and discussed in the following sections. Furthermore, ADCP measurements supplied by the TeraWatt project were again used in calibrating model output to ensure the robustness of the models. The results of the analyses are presented graphically, accompanied by relevant statistical dataset to facilitate data interpretation.

At the end of this chapter, the predicted output from two distinct numerical models – Telemac3D which is a finite element based numerical model, and Delft3D, which is a finite difference based model employing only the structured grid – are compared and analysed. Equally important, the influence of the chosen parameters on both flow models are explored, to see which of the two software is more adaptable and able to produce accurate numerical output upon comparison with the measurement data. Finally, a few modelling constraints encountered in this research work are also discussed.

1. Part of the contents from this chapter had been presented at two international conferences, and was also used in writing up a manuscript for journal publication. Please refer to Appendix B for details.

4.1 Model description

Delft3D is a finite difference modelling suite developed by the Deltares, and consists of the flow, morphology, water quality and wave modules [25]. It applies the shallow water and Boussinesq assumptions to solve the Navier-Stokes equations, for both two and three dimensions. The numerical scheme then solves the continuity equation, momentum equations, the advection-diffusion transport equations, and turbulence model. The system of equations for the three-dimensional flow model are as follow:

$$\frac{\partial \zeta}{\partial t} + \frac{\partial[(\zeta + d)\overline{U}]}{\partial x} + \frac{\partial[(\zeta + d)\overline{V}]}{\partial y} = S_{d3d} \tag{4.1}$$

$$\frac{\partial U}{\partial t} + U\frac{\partial U}{\partial x} + V\frac{\partial U}{\partial y} + \frac{w}{h}\frac{\partial U}{\partial \sigma} - fV = -\frac{1}{\rho_0}P_x + F_{x,R} + M_x + \frac{1}{h^2}\frac{\partial}{\partial \sigma}(v_v\frac{\partial U}{\partial \sigma}) \tag{4.2}$$

$$\frac{\partial V}{\partial t} + U\frac{\partial V}{\partial x} + V\frac{\partial V}{\partial y} + \frac{w}{h}\frac{\partial V}{\partial \sigma} - fU = -\frac{1}{\rho_0}P_y + F_{y,R} + M_y + \frac{1}{h^2}\frac{\partial}{\partial \sigma}(v_v\frac{\partial V}{\partial \sigma}) \tag{4.3}$$

where S_{D3D} is the term due to water discharge or withdrawal, precipitation and evaporation per unit area, ζ is the water level, d is the water depth in relation to a reference level (and the term $(\zeta + d)$ refers to the total water depth,h), f is the Coriolis parameter, U and V are the horizontal velocity components, w is the vertical velocity component for sigma coordinate, $F_{x,R}$ and $F_{y,R}$ are the horizontal Reynolds stresses, v_v refers to the eddy viscosity in vertical direction, P_x and P_y are the horizontal pressure term from Boussinesq assumption, M_x and M_y are the source or sink terms, and ρ_0 is the reference density.

4.2 Model set up

A three-dimensional Delft3D flow model, with the Universal Transverse Mercator (UTM) coordinate system was constructed using the Delft Dashboard (DDB). It consists of structured computational grids that covered the whole Orkney Islands in the north of Scotland, as shown in Figure 4.1, from 1° 24' W - 4° 34' W and 58° 18' N - 59° 37' N. Delft3D offers the choice of both σ (sigma) and the Z-coordinate for generating the vertical layers in the 3D model. The σ layer is known for providing accurate representation of the bathymetry, and uses less computational resources because it is a terrain following model. On the contrary, the Z coordinate varies in space and generates a staircase layer boundary. Figure 4.2 illustrates how the σ and Z coordinate layers are represented in the numerical model.

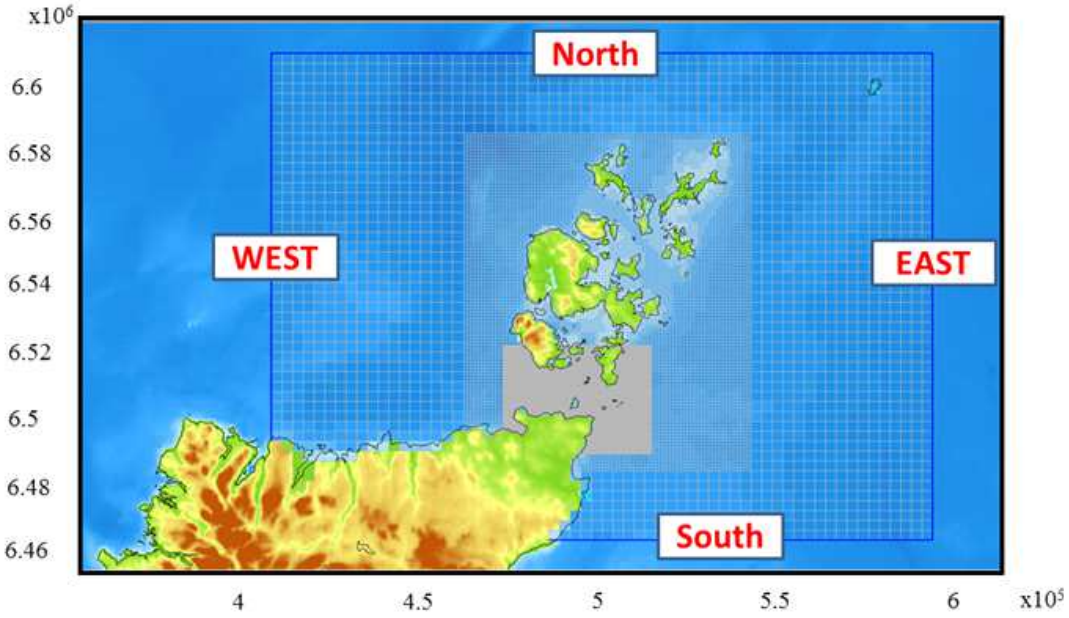

Figure 4.1: Computational domain and open boundary segments produced for the use in Delft3D model.

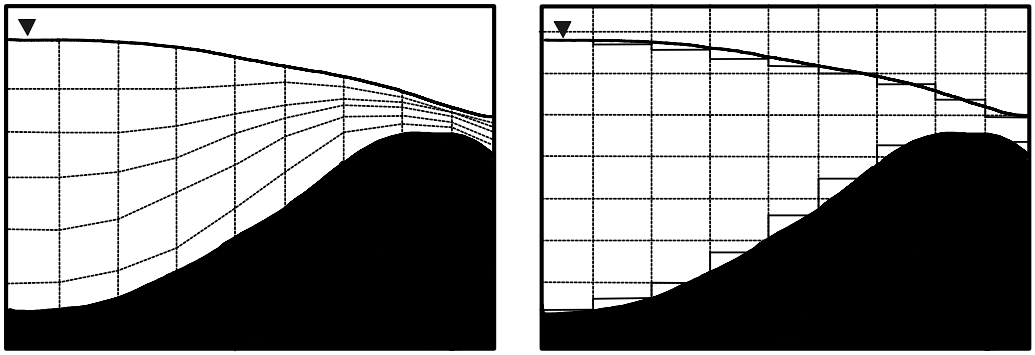

(a) Sigma layer **(b)** Z coordinate layer

Figure 4.2: Illustration of the σ and Z coordinate vertical layers in a numerical model.

The option of using either σ or Z layer grids is problem dependent. The terrain following σ layer was employed in this study since it is more suitable in modelling the physical processes near the bottom boundary layer [154]. Nonetheless, the distribution of the σ layer for the Delft3D model differs to Telemac3D. Vertical distribution of the Delft3D layers begin at the water surface, while for Telemac3D it starts from the ocean floor (refer to Figure A.6 in Appendix A). Next, as with the Telemac3D model, the TPXO7 database and GEBCO 08 were applied as the boundary conditions and bathymetry for the computational domain.

Domain decomposition, which allows for local grid refinement in both horizontal and vertical direction, was applied to increase the resolution at the area of interest and also to enhance the simulation accuracy. Using this method, domains can have independent vertical grid refinement, which is not possible when using nesting. Moreover, nesting technique is a one way coupling, in which there is no interaction between the domains. Nine domains were created for this work, with the largest grid resolution at 3000 m spacing for the outer domain that acts as the open boundary for the model. Although not apparent from Figure 4.1, two additional domains were assigned at each of the three monitoring points to allow for finer grid resolution at the measurement area.

The mesh resolution was then reduced to 1000 m grid for the domain that covered the Orkney Islands. The grid was further decreased to 200 m spacing specifically for the domain that covered the Pentland Firth. As for the monitoring stations, where the Acoustic Doppler Current Profiler (ADCP) is located, a more refined mesh resolution of 22 m was employed so that the flow propagation near the point of interests can be properly captured. It is also strongly recommended to employ a maximum horizontal refinement of 1 to 5 to allow gradual transition between resolutions and avert abrupt velocity change, which may cause instability in the model.

Furthermore, since Delft3D uses a structured grid, the monitoring points will be at the centre of the cell. This requires the use of multiple domains to ensure smooth grid transitions and fine mesh density are achieved at the monitoring locations so that the distance between monitoring and measurement points is not too great. Nevertheless, the use of multiple domain decomposition in Delft3D should be approached with caution. Aside from the suggested odd number grid refinement, users are also recommended not to place the domain boundary in a steep area to avoid potential errors caused by the large differences in depth at the adjacent cells.

Since the use of domain decomposition requires all the domain to be connected, it proves to be a hindrance especially with the presence of complex geometries and

countless islands in the computational domain. Hence, an appropriate mesh density needs to be meticulously selected so that it embraces the small islands that may exist in the domain, and more crucially the grid should also be able to characterize those geometries accurately. For the purpose of this study, 10 σ layers were applied specifically to the grid that covers the Pentland Firth, while the 3000 m and 1000 m grid spacing that covers the outer domain were set to one layer (i.e. a combination of 2D outer model with a 3D high resolution model). This approach was implemented to optimise the computational resources.

The Delft3D model was run with a time step of 0.1 min to satisfy the CFL condition, which should not exceed a value of ten [155]. Similar to the Telemac3D model, only astronomic forcing was included in this simulation, and default physical and numerical parameters were applied. Threshold depth was set to 0.2 m, above which the grid cell is set as wet during calculation, and k-epsilon was chosen to model the 3D turbulence. As with the Telemac3D, the simulation period was set to 35 days and the models were run without the Coriolis effect. The outputs extracted from the model were the water elevation and the U and V-horizontal velocity components.

4.3 Model calibration

As displayed in Figure 4.1, the Delft3D domain consists of four open boundaries: North, East, South, and West. The influence of the boundary forcing on Delft3D computational domain for this region has been investigated by Rahman and Venugopal [136, 142], and the use of water level forcing at all open boundaries has been proposed for the flow model at the Pentland Firth. In-situ measurement data is critical for all numerical modelling in order to give credence to the model output. Acoustic Doppler Current Profiler (ADCP) data supplied by the EPSRC Terawatt project [133] were once again used to validate the numerical models at three sites.

Nonetheless, any errors or uncertainties that may be present in the ADCP data are not known to the authors, and it is assumed that the provided measurement data has undergone quality control procedure. ADCP data is very useful for 3D hydrodynamics modelling as it supplies data on flow velocities throughout the water column. The locations of these devices at the Pentland Firth are already shown in Figure 3.1. The acquired data offered a measurement time step of every 10 min at 4 m intervals through the water column, with the deepest measurement approximately 5 m above the ocean floor. For details of the field data, please refer to Table 3.1 in Chapter 3.

Following similar procedure as discussed in previous chapter, the predicted water surface elevation is compared with the available tidal gauge database in the computational domain. This was done to check the suitability of the chosen boundary conditions in simulating the hydrodynamics of the study. The simulations were run for 35 day, and for clarity, the comparisons shown here covered a full spring tidal cycle, starting from 16 September 2001 till 26 September 2001.

Table 4.1: Two distincts boundary conditions applied to the Delft3D model.

Mix BC	Water Level BC
West : Current	West : Water Level
North : Water Level	North : Water Level
East : Water Level	East : Water Level
South : Water Level	South : Water Level

For Delft3D calibration, following the procedure set by Rahman and Venugopal [136, 142], two different models were created as part of the calibration process to inspect the influence of the boundary on the computational domain, as summarised in Table 4.1. The first model (denoted as Mix BC) employed a mixture of current and water level forcing for the boundaries, in which the current boundary condition was set for only the west segment. On the other hand, the second model (denoted as Water Level BC) on the other hand used water level for all four open boundaries.

The water elevations from the Delft3D models were compared with the tidal gauges at Wick IHO and Sule Skerry IHO and are represented in Figure 4.3. As evident from this figure, the predicted water surface elevation using the mix boundary (Mix BC) shows poor correlation against the tidal gauges at both locations, indicating that this boundary condition is ill-suited for this application and region. Two possible reasons may contribute to this observation. Firstly, it could be due to the inability of the current data from the tidal global model to be accurately resolved in the area of study due to the huge interval (i.e. 3000m) between the nodes along the open boundary. Although refining the grid density of the outer domain may improve the numerical output of the Mix BC model, it is not within the scope of the present study.

Secondly, currents may also be affected by waves and other oceanography processes. Since the present study did not consider the influence of waves, it might be plausible that the poor result shown by the Mix BC model was caused by the absence of wave

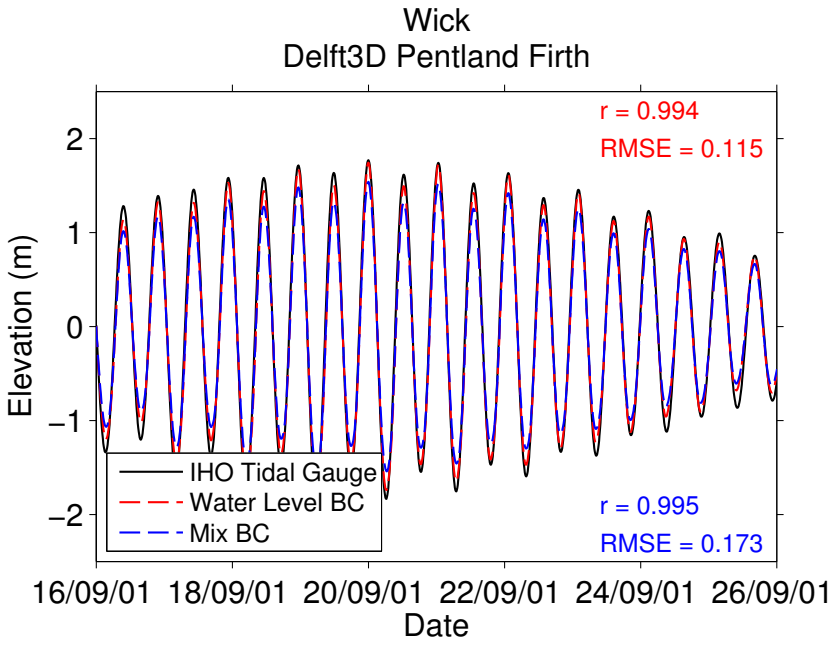

(a) Wick

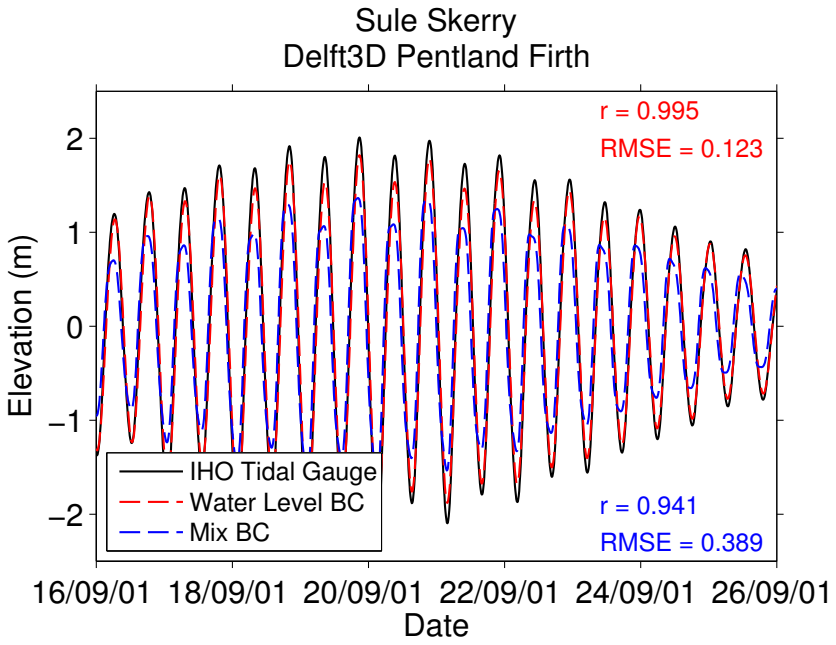

(b) Sule Skerry

Figure 4.3: Comparison of the water surface elevation between the predicted and the measured data for Delft3D models.

propagation at the open boundaries. On the other hand, the Water Level BC model displayed an excellent match with the measured data at the two sites since water elevation is highly predictable. The influence of the selected boundaries on the model's hydrodynamics will be discussed in Section 4.4.2.

4.4 Parametric Study on Delft3D model

For the Delft3D model set up, WGS 84 / UTM zone 30N was set as the coordinate system and GEBCO 08 bathymetry was employed. The roughness formula was set to the Chézy formulation unless stated otherwise, and default values were utilised for both the horizontal and vertical viscosity and diffusivity. Next, the history time step of 10 min was applied while the meteorological input was not considered.

The results were then compared at three different depths, the same as for the Telemac3D model, e.g. near the water surface (7 m), at the middle of the water column (39 m) and close to the ocean floor (65 m-71 m). The parametric study of the turbulence closure model was not performed since it had been studied by Baston et al. [117].

4.4.1 Bottom roughness

Table 4.2: Variable roughness coefficient applied to the Delft3D model.

Site	U velocity	*Cd*	V velocity	*Cd*
1	Chézy 50	0.0039	Chézy 20	0.0245
2	Chézy 60	0.0027	Chézy 55	0.0032
3	Chézy 60	0.0027	Chézy 50	0.0039

Under the physical parameters tab in the Delft3D Dashboard, several options for the roughness formula are available, which are the Manning, White-Colebrook, Chézy and Zo. Nonetheless, Chézy was selected as the default roughness formula and applied to the Delft3D models in this study. The formulation of the bottom friction in Delft3D is given in Equation 4.4 [155]:

$$\vec{\tau}_{d3d} = \frac{g\rho_0 \vec{u_b}|\vec{u_b}|}{C_{3D}^2} \tag{4.4}$$

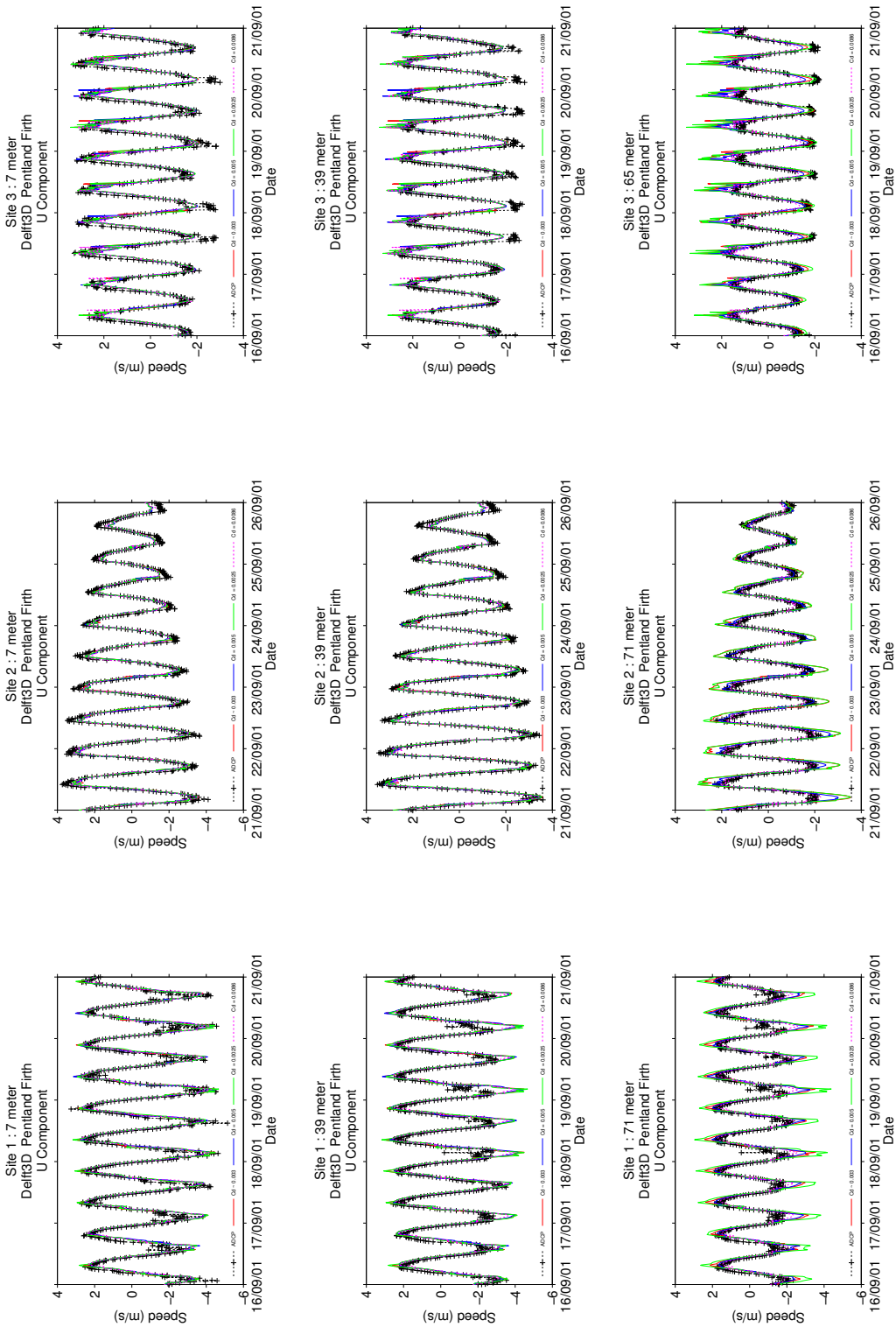

Figure 4.4: The influence of roughness values [Cd = 0.003 (—), 0.005 (—), 0.0025 (—), 0.0086 (—)] on the U-velocity component for Delft3D models.

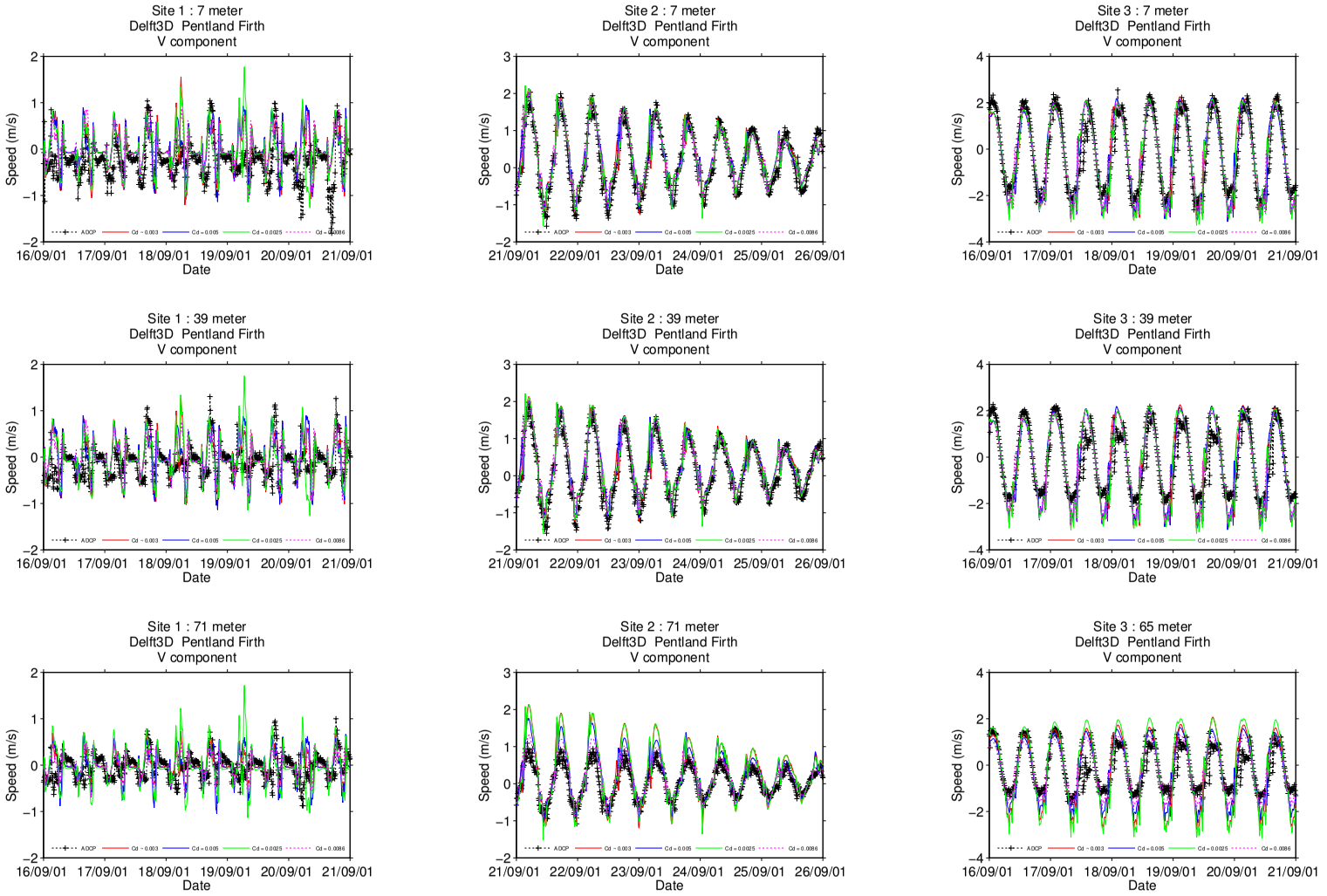

Figure 4.5: The influence of roughness values [Cd = 0.003 (—), 0.005 (—), 0.0025 (—), 0.0086 (—)] on the V-velocity component for Delft3D models.

where $\overrightarrow{\tau}_{d3d}$, $\overrightarrow{u_b}$, C_{3d}, and $\overrightarrow{U}$ are the bed shear stress, magnitude of the horizontal velocity in the first layer just above the bed, 3D Chézy coefficient and velocity of current far enough from the wall respectively. Apart from the bed friction values employed previously for the Telemac3D models, an additional roughness coefficient, shown here in Table 4.2, was tested to examine its influence on the output since Delft3D allows for variable roughness coefficient to be applied for the U and V-velocity components (i.e. different drag values can be applied in both x and y directions). Model with Water Level BC (from Table 4.1) was used in this set up.

Figures 4.4 and 4.5 illustrate the U and V-velocity components of the applied roughness values when compared against the measured data, while Table 4.3 presents the performance indices of the bed friction values (obtained from the same data) tested on the Delft3D model. At Site 1, high RMSE value and very low correlation coefficient can be seen from performance indices, though high V-velocity fluctuation was attributed to the poor results. Site 2 nonetheless showed a better comparison where high r values were observed at all depths. Overall, it can then be concluded that $Cd = 0.0086$ (Chézy 34) is the optimal bed friction value to be applied for the Delft3D flow model for this study area, based on the calculated performance indices.

However, it is compelling to see that this result appears to contradict the values proposed by both Baston et al. [117] and Chatzirodou and Karunarathna [116], where lower bed friction coefficients of $Cd = 0.0025$ and constant Chézy value of 50 were applied respectively in each of their studies using the same numerical software. These differences could be due to the size of the domain and also the mesh resolution that were utilised in their models. For instance, Baston et al. employed a shelf-scale domain that was significantly larger than the one used in this study, along with a finer grid density (2km x 2km) for the outer region.

4.4.2 Boundary forcing

Most flow models would apply either the Water Level or Current, or the combination of both as the boundary forcing. In addition to that, the reflection coefficient, alpha, should be chosen so that they are sufficiently large enough to damp the short waves introduced at the start of the simulation. An alpha value of 1000 was applied to reduce reflections at the open boundaries, and the wave from propagating back into the domain as a disturbance. The influence of boundary forcing on the domain was examined using two models (Mix BC and Water Level BC) with distinctive open boundaries as presented in Table 4.1. Additionally, scatter plots for the comparison between the

Table 4.3: Performance indices for the roughness values applied to the Delft3D models.

		SITE 1			SITE 2			SITE 3		
Depth	*Cd*	**r**	**RMSE**	**SI**	**r**	**RMSE**	**SI**	**r**	**RMSE**	**SI**
7m	0.0027-0.0032	0.793	0.696	0.348	0.921	0.438	0.260	0.879	0.518	0.254
	0.0050	0.790	0.687	0.347	0.933	0.426	0.257	0.888	0.520	0.264
	0.0025	0.779	0.722	0.361	0.925	0.429	0.254	0.871	0.537	0.264
	0.0086	0.781	0.687	0.347	0.935	0.416	0.249	0.900	0.525	0.274
39m	0.0027-0.0032	0.700	0.852	0.430	0.926	0.380	0.225	0.863	0.514	0.252
	0.0050	0.707	0.822	0.417	0.937	0.360	0.217	0.876	0.480	0.244
	0.0025	0.685	0.872	0.436	0.930	0.371	0.220	0.855	0.536	0.263
	0.0086	0.723	0.720	0.384	0.941	0.368	0.229	0.893	0.463	0.247
71m (65m)	0.0027-0.0032	0.615	0.766	0.485	0.911	0.669	0.416	0.750	0.745	0.407
	0.0050	0.638	0.653	0.442	0.922	0.368	0.281	0.788	0.494	0.316
	0.0025	0.587	1.071	0.572	0.917	0.684	0.420	0.770	0.882	0.441
	0.0086	0.638	0.496	0.394	0.934	0.216	0.199	0.807	0.410	0.322

two types of boundary forcing are shown in Figure 4.6.

The validation process demonstrated that Water Level BC model showed excellent agreement between the predicted and observed water surface, and thus considered as the suitable boundary forcing for this model. Nonetheless, the performance indices calculated in Table 4.4 have generated some interesting observations for the current speed using the two models (with Cd = 0.0086). At Site 1 and Site 3, Mix BC model showed slightly better agreement with r, RMSE and SI values compared to Water Level BC model for the three depths. Then for Site 2, the r values for both models are very close to one another, while the RMSE and SI for Water Level BC model are slightly better than Mix BC model.

The results seem to imply that there is not much difference between the two models when direct velocity comparisons are conducted. However, as noticed from the calibration procedure in Section 4.3, the Water Level boundary forcing showed the best fit against tidal gauges, and thus is best suited for hydrodynamics modelling in this region. All things considered, it is evident from this analysis that proper calibration and validation are essential in producing a flow model that is both robust and also accurate.

4.4.3 Coriolis force

The Coriolis effect in Delft3D model can easily be activated by inserting the latitude of the domain in the Dashboard, and the influence of the force on the model using the roughness value of 0.0086 is highlighted in Figure A.7 in Appendix A. Although some small differences in performance indices were spotted at Site 3, it can generally be concluded that the impact of the Coriolis force is too small on the domain used.

4.4.4 Comparison of bottom roughness formulation

As with the Telemac3D, two of the most commonly used formulations for the bottom roughness, Chézy and Manning were examined to inspect their influence on the numerical model. Constant Chézy and Manning roughness values of 34 ($m^{(1/2)}/s$) and 0.06 ($m^{-1/3}s$) respectively, of which both corresponded to Cd = 0.0086, were utilised for this comparison. The results for this comparison are presented in Figures 4.7 and 4.8 respectively. Interestingly, statistical analysis conducted on these two models shows contrasting output between the two numerical output, where the computed performance indices for the Manning formula were found to be considerably lower than the Chézy, as demonstrated in Table 4.5.

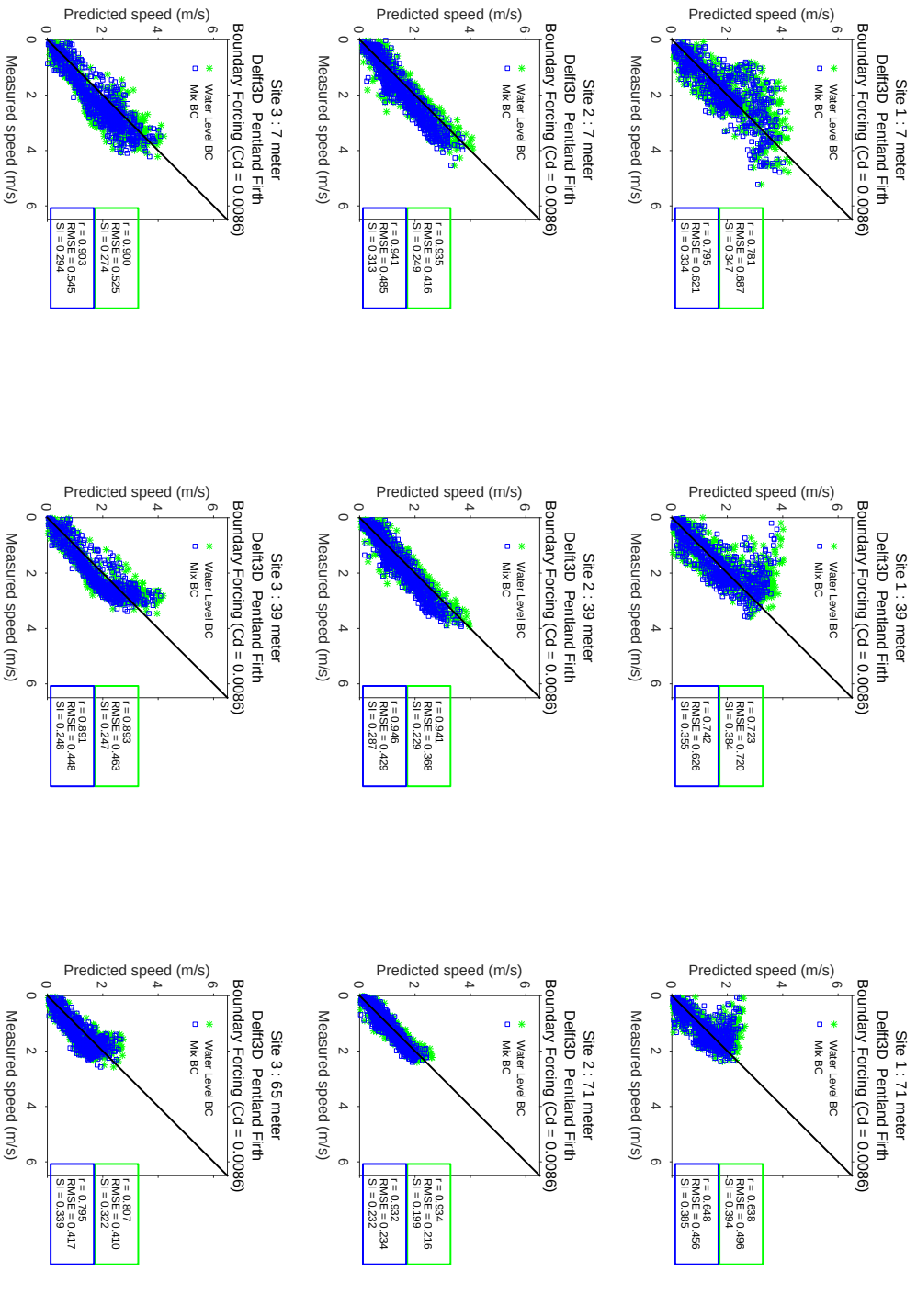

Figure 4.6: Comparison between two types of boundary conditions applied for Delft3D models using Cd = 0.0086.

Table 4.4: Performance indices for the boundary forcing analysis applied to the Delft3D models.

		SITE 1			SITE 2			SITE 3		
Depth	**Boundary forcing**	**r**	**RMSE**	**SI**	**r**	**RMSE**	**SI**	**r**	**RMSE**	**SI**
7m	**Water level**	0.781	0.687	0.347	0.935	0.416	0.249	0.900	0.525	0.274
	Water level and current	0.795	0.621	0.334	0.941	0.485	0.313	0.903	0.545	0.294
39m	**Water level**	0.723	0.720	0.384	0.941	0.368	0.229	0.893	0.463	0.247
	Water level and current	0.742	0.626	0.355	0.946	0.429	0.287	0.891	0.448	0.248
71m (65m)	**Water level**	0.638	0.496	0.394	0.934	0.216	0.199	0.807	0.410	0.322
	Water level and current	0.648	0.456	0.385	0.932	0.234	0.232	0.795	0.417	0.339

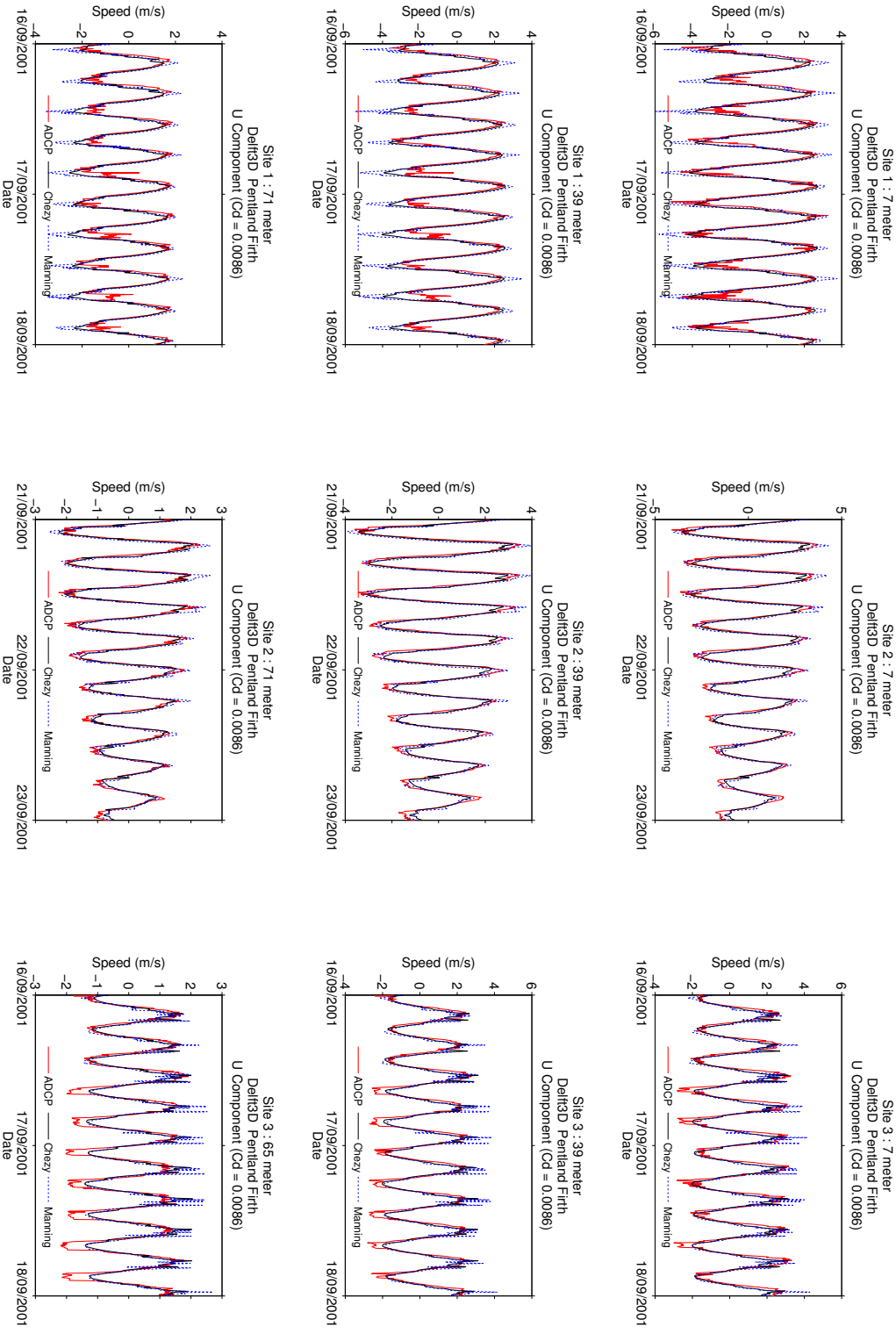

Figure 4.7: Comparison between Chézy and Manning bottom formulations (U-velocity component) for Delft3D models.

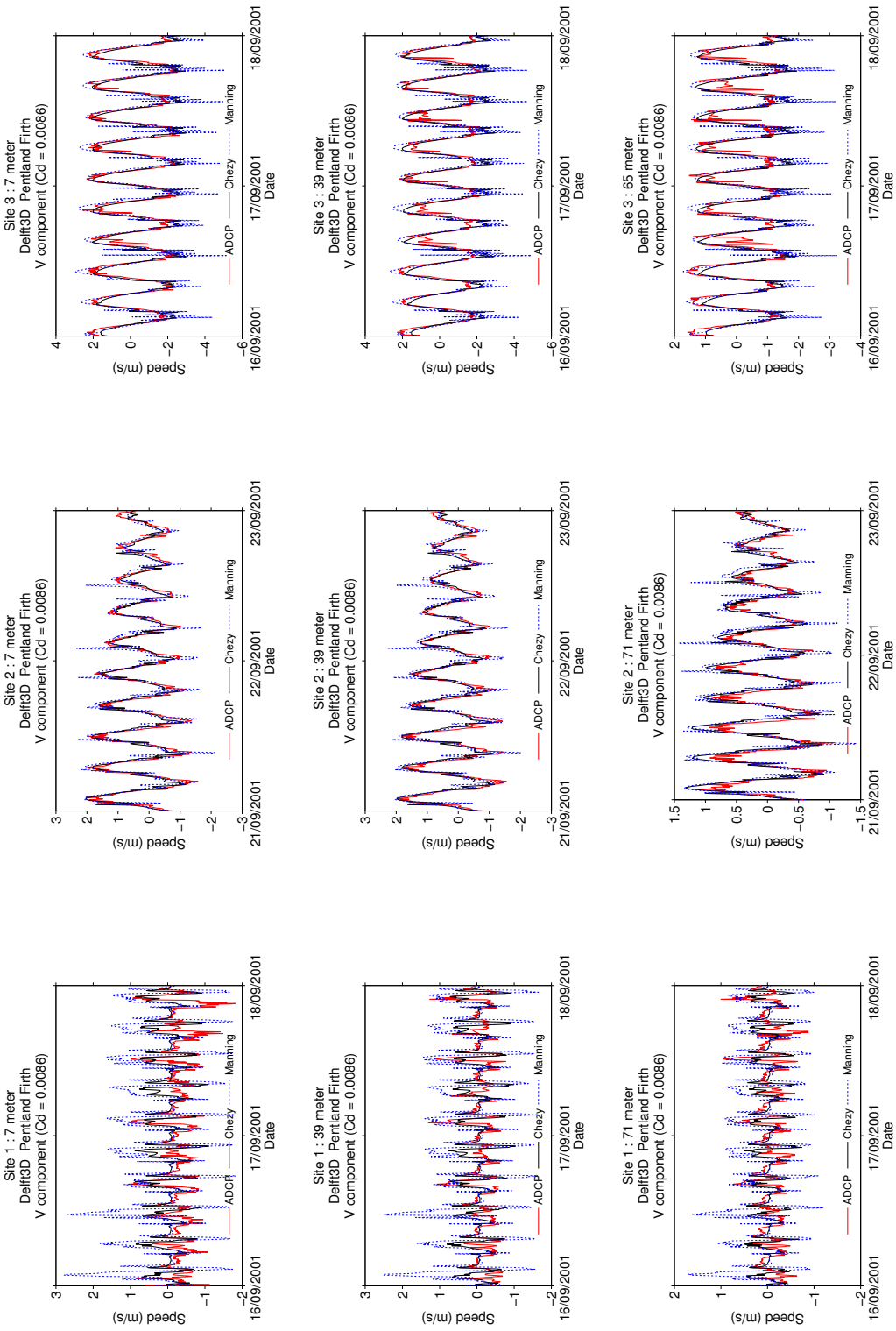

Figure 4.8: Comparison between Chézy and Manning bottom formulations (V-velocity component) for Delft3D models.

Table 4.5: Comparison between the Manning and Chézy bottom roughness formula for Delft3D models (Cd = 0.0086).

		SITE 1			SITE 2			SITE 3		
Depth	**Roughness formula**	**r**	**RMSE**	**SI**	**r**	**RMSE**	**SI**	**r**	**RMSE**	**SI**
7m	**Chézy**	0.781	0.687	0.347	0.935	0.416	0.249	0.900	0.525	0.274
	Manning	0.695	1.098	0.453	0.869	0.544	0.282	0.795	0.729	0.332
39m	**Chézy**	0.723	0.720	0.384	0.941	0.368	0.229	0.893	0.463	0.247
	Manning	0.576	1.130	0.505	0.881	0.492	0.271	0.793	0.701	0.336
71m (65m)	**Chézy**	0.638	0.496	0.394	0.934	0.216	0.199	0.807	0.410	0.322
	Manning	0.483	0.751	0.498	0.879	0.342	0.281	0.744	0.491	0.349

Table 4.6: Comparison between the Manning and Chézy bottom roughness formula for Delft3D models using variable roughness coefficient.

		SITE 1			SITE 2			SITE 3		
Depth	**Roughness formula**	**r**	**RMSE**	**SI**	**r**	**RMSE**	**SI**	**r**	**RMSE**	**SI**
7m	**Chézy**	0.793	0.696	0.348	0.921	0.438	0.260	0.879	0.518	0.254
	Manning	0.715	1.086	0.454	0.812	0.658	0.336	0.756	0.819	0.354
39m	**Chézy**	0.700	0.852	0.430	0.926	0.380	0.225	0.863	0.514	0.252
	Manning	0.598	1.291	0.548	0.815	0.669	0.341	0.737	0.892	0.386
71m (65m)	**Chézy**	0.615	0.766	0.485	0.911	0.669	0.416	0.750	0.745	0.407
	Manning	0.524	1.098	0.603	0.816	0.983	0.535	0.685	0.999	0.490

The Chézy model outperformed the Manning's at all sites and depths, where large scatter was apparent for the Manning output. The reason for this observation is not very clear to the author. In an effort to prove that the result is not due to the miscalculation or error in modelling, another set of performance indices for the model using the variable roughness values (as shown in Table 4.2) are presented in Table 4.6. Despite using a different bed coefficient, once again the same occurrence was noticed for the model utilising the Manning formula. It could be speculated that the Manning roughness formula is not suitable to be used in this location under the current setting. Extensive calibration is therefore highly recommended before the Manning roughness formula is applied to the Delft3D flow model for this region.

4.5 Discussions

Appropriate methods in developing a 3D tidal flow model for the PFOW using both Telemac3D and Delft3D numerical models (in Chapters 3 and 4 respectively), were thoroughly examined since they were not described in detail by previous studies. Great care was taken to ensure the robustness of the models, and the predicted values were validated against the observed data to give confidence to the model. Physical, numerical and general parameters utilised in the models were elaborated in detail, since the input required for a 3D model differs remarkably from the 2D model. The parametric study was conducted to examine the influence of key simulation parameters on the numerical output, and the performance indices were utilised in comparing the predicted and measured data.

As presented in the previous and current chapter, results from both Telemac3D and Delft3D models demonstrate that the physical and numerical parameters used for the simulations worked well. The use of unstructured mesh for the Telemac3D offers an excellent tool for users to accurately model the domain geometries. Delft3D on the other hand offers an easy to use interface to create and run a model. However, there are some inherent limitations with the current release of Delft3D Dashboard (e.g. choice of unstructured mesh). Currently the option of Flexible Mesh is yet to be made open source in Delft3D, and thus users are resigned to using a structured mesh for their model.

Structured mesh posed a problem in representing geometry with complex coastlines along with the presence of islands in the domain. Nonetheless, since the area of interest in this study is significantly deep, and the models are run without the waves input, the

shoreline may have little to no influence on the predicted model output. Besides, the option for physical, numerical and general parameters offered in the Dashboard are also not as extensive as the Telemac3D module. Nonetheless, data extraction for Delft3D model is fairly easy and fast, since the use of monitoring points eliminate the need to store data for all the points in the domain.

Of the three tested bed friction values for Telemac3D models, $Cd = 0.005$ produced the best results and can be parameterised by using both Chézy and Manning formulation. The use of Nikuradse formulation as the bottom friction was not suitable in this study since it required highly refined vertical layers, especially near the sea bottom. The findings also demonstrated that the model output was unaffected when varying the values of the horizontal diffusion of velocities, indicating the presence of a highly turbulent flow in the area of interest. Additionally, four distinct mixing length models were investigated on Telemac3D, and the difference between the models were found to be negligible.

Correspondingly, the use of Water Level BC as the boundary forcing in Delft3D produced the best agreement with the observed data. Of all the roughness values tested on Delft3D model, $Cd = 0.0086$ produced the best agreement with the measured data in this study. Moreover, the observed difference in the Cd values from the literature could be attributed to the choice of boundary conditions and the grid size, which may have an influence on the numerical model. Excellent correlation between the predicted and measured data was observed when Chézy formula was applied. Conversely, models utilising Manning formulation displayed a highly scattered plot, suggesting that it was not suitable to be adopted in this study.

Not surprisingly, since the drag coefficient definition (or mathematical meaning of the coefficient) employed in both models are non-identical, the best results for Telemac3D and Delft3D were obtained using two distinct Cd values. Moreover, other parameters that could contribute to the observed Cd variations include choice of spatial resolution and bathymetry data used by the numerical model, as well as how the domain mesh was constructed (e.g. unstructured mesh in Telemac3D and structured mesh in Delft3D). In essence, it can be inferred that each of the numerical models is unique and non-identical and that thorough calibration and validation is required to ensure the validity of the numerical output.

Nevertheless, the discrepancies between simulated and observed data may also have been contributed by the quality of the measurement data employed in this project. As previously mentioned, any errors or uncertainties that may present in the ADCP data

were not known, and the data were used as it were in calibrating the models. Only at the very end of this research project had it been highlighted to the author that the field data were actually clipped and incomplete. Some uncertainty in the reliability of the field results, due to reported "knock-down" of the mooring lines during the fastest flood and ebb currents, was briefly mentioned in [134, 156]. Consequently, this could potentially affect the accuracy and validity of the calibration exercises performed in Chapters 3 and 4, since the observed data provided by the TeraWatt consortium were actually synthesized between the observed and 'corrected' values.

In retrospect, there are several aspects of modelling practice that perhaps could have been done differently, either to improve the model's accuracy or speed up the computation run-time. These include (but not limited to):

- increasing the interval between nodes along the domain boundary to match the resolution of the TPXO's model used, consequently reducing the number of non-essential elements in the numerical domain.
- extending the domain to cover the northern Scottish continental shelf to examine the effect of open ocean to the dynamics inside the firth.
- broadening the sensitivity analysis to include the whole domain rather than the small area for which data are available. This is due to the fact that those three points (i.e. the ADCP locations) along the channel are unable to tell everything that is happening in the area (e.g. presence of eddies, bathymetry features etc).
- possible use of harmonic analysis to detect and evaluate errors associated with the observed tidal data. Additionally, this technique can also be used to determine tidal constituents representative of that exact location, which can then be applied for future prediction. However, it is worth to highlight that the quality of tidal constituents derived from this method is highly dependent on the length of the measurement record [157].

Moving forward, Telemac3D is chosen as the preferred modelling tools in the implementation of tidal turbines in this region. This commitment was made upon consideration of three critical factors from the modelling perspective, which are:

- ease of setting up a 3D numerical model, which include but are not limited to domain construction, choices of numerical parameters/settings available from the model, and access to the additional programming subroutines in order to implement changes to the basic hydrodynamics model.
- the amount of support available from the modelling community/users of the chosen software in regards to modifying the subroutines.

- ability to run the simulations using parallel computing, which is not possible using the current version of Delft3D [158].

Subsequent chapters will focus on the implementation of a full size actuator disc using Telemac3D, where the influence of selected numerical parameters on the predicted wake characteristics will be thoroughly investigated and discussed.

Chapter 5

Implementation of the Actuator Disc Approach in an Idealised Channel. Part I: Single Turbine Study

This chapter outlines the methodology in implementing the actuator disc approach via RANS momentum source term for a 20-m diameter turbine in an idealised channel[1]. To date, only few studies have examined the execution of the actuator disc approximation for a full size turbine. Small scale models have fewer constraints than large scale models because the range of time-scales and length-scales is smaller. In particular, applying a very dense mesh is possible at small scale but hardly feasible for large scale applications.

Thus, detailed parametric analyses to determine the optimum size of the structured grid cells that represent the turbine, as well as the ideal unstructured mesh size upstream and downstream of the turbine are conducted. It is to be noted that the turbine's support structures have not been included in the simulation due to the complexity in defining their respective parameters. The results of this study are illustrated using two plots - the models' predicted velocity and the corresponding turbulence level. More significantly, the model output parameters are also compared with published data from the literature to properly validate the applied actuator disc source term, as well as to give confidence to the numerical model.

1. Part of the contents from this chapter had been presented at two international conferences, and was also used in writing up a manuscript for journal publication. Please refer to Appendix B for details.

5.1 Introduction

Flow perturbation due to the deployment of tidal current devices has been extensively studied and discussed in the recent past as it is expected to have an influence on the power capture and may also alter the physical environment [116, 159, 160]. The analytical and computational studies are often validated with small scale experiments before using them for large scale implementations. In the current literature, most of the 3D numerical studies of wake characteristics have been executed using CFD models. In these models, the tidal device is represented either as a complete structure with blades, or as an actuator disc.

Often, the outputs from these numerical models were compared with results from experiments conducted in a flume, where porous discs are commonly employed to simulate the effects of a turbine on a fluid flow. Despite the assumption that the actuator disc approach may not accurately produce the vortices from the rotating blades, the concept seems to be able to accurately compute the wake decay as well as the turbulence intensity [21, 23].

Although the actuator disc approximation has been widely used in predicting the performance of tidal stream devices, its implementation so far has been restricted to studies involving an extremely small actuator disc, e.g. rotor diameter of 0.1 m. The drawback of a small scale turbine model includes overestimation of essential parameters such as the mesh density and also the resolution of the vertical layers, making them impractical to be replicated in a large scale model. As the application of the actuator disc approximation for a full size turbine is yet to be tested, this work made an attempt to model a full scale rotor by the actuator disc method within an ocean scale numerical flow model.

Contrary to fully meshed rotating turbines, the simplicity of the actuator disk concept permits it for ocean scale modelling [77]. This method does not demand detailed discretisation of the turbine structure as required for high fidelity simulations, and does not need the use of a computer cluster to run. Several recent studies have utilised the actuator disc method in investigating various flow characteristics in the presence of tidal devices. Sun et al. [21] used the commercial CFD software package FLUENT to simulate tidal energy extraction for both two and three dimensional models by applying a retarding force on the flow. This study found that free surface variations may have an influence on the wake and turbine performance. Daly et al. [22] examined the methods of defining the inflow velocity boundary condition using ANSYS CFX, and showed

that the $1/8^{th}$ power law profile was superior than others in replicating the wake region.

The same software was also used by Harrison et al. [23] in comparing the wake characteristics of the RANS model against the experimental data measured behind a disc with various porosities, where a detailed methodology on the implementation of the momentum sink was presented. With the aid of ANSYS CFX, the actuator disc approach was used by Lartiga and Crawford [24] in correcting the wall interference for their tunnel testing facilities. On the other hand, Roc et al. [25] proposed an adaption of the actuator disc method by applying appropriate turbulence correction terms to improve near wake performance for the Regional Ocean Modeling System (ROMS) model. A more recent study by Nguyen et al. [161] also demonstrated the need to adapt turbulence models when modelling a tidal turbine with an actuator disc to account for the near wake losses due to unsteady flow downstream of the disc.

With the exception of Roc et al. [25], all of these CFD studies were conducted in a small scale domain, where a 0.1 m diameter disc was commonly employed. As the implementation of the momentum sink for a full scale turbine has not been undertaken in the past, the purpose of this study is to demonstrate that the simulation of wake effects from a full scale actuator disc using a tidal flow model is possible. The experimental data published in [23] is used for validation and comparison purposes. In contrast with other studies where the model dimensions matched the size of the flume experiment, here the results of the scaled experiment is compared to the full scale model output.

Further, the model-experiment comparison is done by using dimensionless variables. This chapter presents detailed sensitivity analysis conducted on the disc/turbine/device enclosure and their influence on the wake profiles behind the turbine. The actuator disc is implemented using Telemac3D [124], where the effects of a 20 m diameter turbine is modelled and validated with data from literature. It is hoped that the knowledge from this study can be used in the implementation of tidal devices via the actuator disc approach for a realistic regional scale simulation.

5.2 Theory of the RANS actuator disc

Actuator disc model can be implemented using the RANS equations by inserting a momentum sink term in the region where the turbine is to be located. It then works by mimicking the effects of a turbine on the surrounding regions without the need to implement detailed features of a turbine. This method is adapted from the wind energy industry [107] where it has been widely used to model wind turbines. The

implementation of the RANS actuator disc approach on several distinct numerical models has been elaborated and discussed in [21, 23, 99], where the approximated forces exerted by the disc to the surrounding flow are applied as source terms in the RANS equations of momentum (5.1) and mass conservation (5.2).

$$\frac{\partial(\rho U_i)}{\partial t}+\frac{\partial(\rho U_i U_j)}{\partial x_j}=-\frac{\partial P}{\partial x_i}+\frac{\partial}{\partial x_j}\left[\mu\left(\frac{\partial U_i}{\partial x_j}+\frac{\partial U_j}{\partial x_i}\right)\right] + \frac{\partial}{\partial x_j}(-\rho\overline{u_i' u_j'})+\rho g_i+S_i \tag{5.1}$$

$$\frac{\partial U_i}{\partial x_i}=0 \tag{5.2}$$

where $U_i(i=u,v,w)$ is the fluid velocity component averaged over time t, P is the mean pressure, ρ is the fluid density, μ is the dynamic viscosity, u' is an instantaneous velocity fluctuation in time during the time step ∂t, $x_i(i=x,y,z)$ is the spatial geometrical scale, $-\rho\overline{u_i' u_j'}$ is the Reynolds stresses that must be solved using a turbulence model, g_i is the component of the gravitational acceleration, and S_i is an added source term for the i^{th} (where $i=x,y$ or z) momentum equations. In this study, the $k-\varepsilon$ turbulence model is utilised to close the RANS equations and solve for the Reynolds stresses.

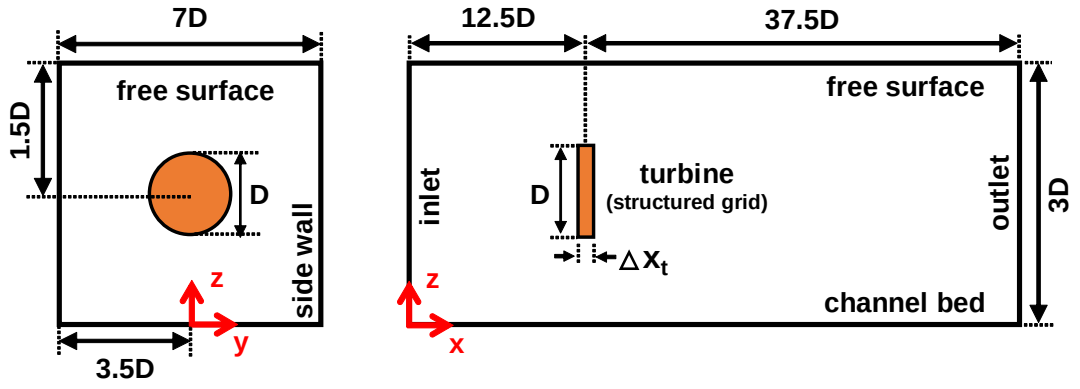

(a) Front view from inlet (*y-z* axis) **(b) Channel side view (*x-z* axis)**

Figure 5.1: Schematic diagram for the simple channel study illustrating the position of the actuator disc. Note that D corresponds to the diameter of the disc.

The momentum source term is imposed at the turbine location by discretising the RANS equation using a finite volume approach [23, 99]. The standard RANS momentum equation will apply to the overall flow domain, while the additional source term, S_i is added using equation (5.3) at the specified disc location, as shown in Figure 5.1:

$$S_i = \frac{1}{2}\rho \frac{\mathrm{K}}{\Delta x_t} U_i |U_i \tag{5.3}$$

where Δx_t is the thickness of the disc and K the resistance coefficient. Moreover, the actuator disc concept implies that the turbine is represented by applying a constant resistance to the incoming flow, which causes a thrust to act on the disc. In theory, this thrust should be close to the one acting on the turbine being simulated. The relationship between the resistance coefficient, K, thrust coefficient, C_T, open area ratio, θ, and induction factor, a has been discussed in [83, 162, 163] where;

$$C_T = \frac{\mathrm{K}}{(1+0.25\mathrm{K})^2} = 4a(1-a) \tag{5.4}$$

$$\theta^2 = \frac{1}{(1+\mathrm{K})} \tag{5.5}$$

The maximum value attainable for C_T, called the Betz limit, occurs at a = 1/3 and thus yields a value of $C_{t,max}$ = 0.89. From equation (5.4), the value of K for $C_{t,max}$ can then be calculated, which equals to 2.

5.2.1 Limitations of the actuator disc approach

Although the RANS actuator disc concept has been successfully employed as a means for imitating a tidal energy converter, the method is not without flaws. Some of the limiting aspects of this approach have been highlighted by [23, 77, 164],and summarised below:

- The overall turbine structure is not being represented and thus affecting the turbulence in the near wake region, known to be 2–5 rotor diameters downstream of the turbines.
- Kinematics of turbulence, such as vortices trailing from the edges of a blade cannot be replicated and thus they must be properly parameterised.
- Energy extraction due to mechanical motion of the turbine rotor cannot be reproduced; instead the energy removed from the disc will be converted into small scale turbulence eddies behind the disc. However, the influence of swirl on the far region is assumed to be minimal.
- This concept cannot be used to investigate the performance of a turbine (e.g. maximum power produced) since it does not include the blades.

Since most swirls and vortical components of a real tidal device would have dissipated beyond the near wake, the actuator disc should exhibit similar flow characteristics in the far wake region of the device, which reflects the principal assumption of the actuator disc approach. Furthermore, since RANS simulations only show the mean flow characteristic, this method is ill suited for applications that requires detail of the flow behind the disc as it cannot account for the physical phenomena caused by the rotating blades.

However, for studies that focus on a simplified model to explore the interaction between turbines in arrays, the actuator disc model is favoured since it can reproduce the wake mixing which generally occurs in the far wake region. Previous studies conducted by Whelan et al. [83] and Belloni and Willden [163] have verified that turbulence due to the blades has negligible influence on the flow far downstream.

5.3 Benchmarking and data validation

In order to validate the models produced in this study, a comparative study has been conducted against data from the physical scale set up published by Harrison et al. [23, 165]. Additional details of the experimental set up are presented by Myers and Bahaj [164]. The experimental work in [164] was focused on examining the wake structure and its recovery in the downstream region by using a scale mesh disc rotor. Furthermore, the flume set up was designed to respect both the Froude and Reynolds number, as well as to exhibit fully turbulent flow.

Similar experimental set up was also used by Harrison et al. [23] to validate their simulations using ANSYS CFX. Their numerical model utilised the RANS solver to analyse the characteristic of the wake of an actuator disc model, which was used as the principal reference in this study. Highlights of the experimental and numerical scale study from [23] are as follows:

- Flume dimensions were: 21 m long, 1.35 m wide and tank depth of 0.3 m.
- A perforated disc with diameter of 0.1m was used, where the porosity ranged from 0.48 to 0.35 (corresponding to coefficient of thrust, C_T = 0.61 to 0.97).
- The flow speed was approximately set to 0.3 m/s, with mean U velocity component of 0.25 m/s.
- The vertical velocity profile was developed to closely match the $1/7^{\text{th}}$ power law, with uniform velocity near the open surface.

- An Acoustic Doppler velocimeter was employed to measure downstream fluid velocities, starting from 3 to 20-disc diameters in the longitudinal direction, as well as up to 4-disc diameters along the lateral axis.

5.4 Methodology

5.4.1 Actuator disc representation in Telemac3D

Table 5.1: List of Telemac3D subroutines used in this study and their corresponding functions.

Telemac 3D subroutines	Function
CONDIM	To set the initial condition for the model's depth and velocity profile
VEL_PROF_Z	To specify the vertical velocity profile at the channel inlet
KEPCL3 and KEPINI	To be used with k-epsilon turbulence model
TRISOU	To implement the source terms for the momentum equations

Apart from hydrodynamic simulations of flows in three-dimensional space, Telemac3D software also allows the user to program specific functions that is beyond the code's standard structure. Every installation comes with a comprehensive library of programming subroutines for executing additional processes, which the user can modify to suit the objectives of any particular simulation. Table 5.1 summarises the adopted and modified subroutines used in this study. In Telemac3D, the momentum source term is implemented by modifying and activating the 'HYDROLIENNE' keyword in the TRISOU subroutine.

Since the actuator disc employs the same geometry as the swept area of the turbine and requires a reduction in momentum of the passing fluid, it is crucial that the calculation of the forces is appropriately appended into the discretised RANS equations. A sample of the programming code used in this study is available in Appendix C (page 230). The principal methodology for executing the approach in Telemac3D is summarised as follows:

(a) The turbine arrangement and the overall dimensions of the domain used in this study is highlighted in Figure 5.1, where the disc is located 250 m from the channel inlet. Additionally, its z and y axis centrelines are fixed at 30 m mid-depth and 70 m from the side wall.

(b) The use of structured grid at the turbine position is essential as it will allow for a better representation of the turbine shape, as well as maintaining the distance between nodes for refinement purposes. Figure 5.2 provides the graphical information on the dimensions and pertinent parameters concerning the implementation of the structured grid in the domain. The size of the structured grid, (i.e. lx = 26 m, ly = 40 m and lz = 60 m) are deliberately set to be larger than the turbine diameter (D = 20 m) and its width (Δx_t = 2 m) to allow for numerical tolerance upon the execution of the momentum sink in the TRISOU subroutine.

The grid element spacings within this structured grid are denoted by Δx, Δy and Δz in the x, y and z directions respectively. For the simulations, lx, ly and lz are kept constant, but the dimensions of Δx, Δy and Δz have been varied and their impact on the wake characteristics have been investigated and the results are presented in Section 5.5.

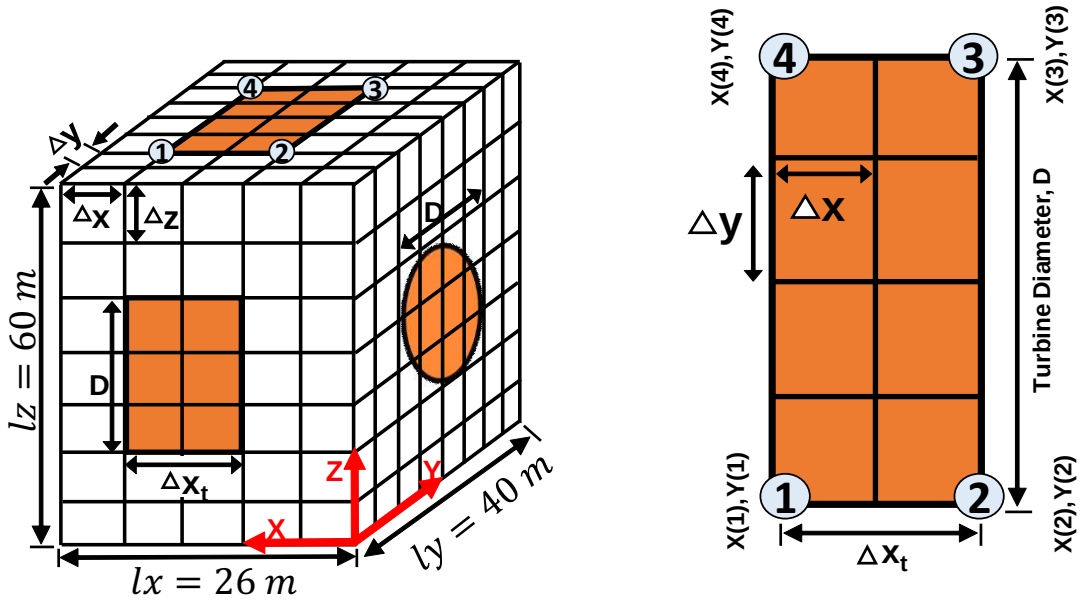

Figure 5.2: Graphical illustration of the structured grid properties (i.e. turbine enclosure) used in the implementation of the actuator disc. Note that these figures are not drawn to scale

(c) The location of the disc (i.e. the turbine) in the domain is specified by four

nodes in the horizontal plane (see Figure 5.2, denoted as 1, 2, 3 and 4, which will act as the enclosure for the turbine. Position of each nodes is represented by a pair of x and y coordinate. The distance between y(4) and y(1) refers to the turbine diameter, D, while the distance between x(1) and x(2) corresponds to the disc thickness, Δx_t.

(d) Although several mesh transformation options are available in the Telemac3D module, the σ coordinate system is chosen to represent the depth due to its simplicity, as shown in Figure 5.3a. In fact, the interval between the vertical planes, Δz as well as the mesh density in the y direction, Δy must be carefully selected since the intersections between the z and y axis nodes will determine the accuracy of the disc frame. Coarser resolution in both y and z directions will result in a limited number of nodes being available within the disc swept area, as shown in Figure 5.3b. Figure 5.3c meanwhile portrays unbalanced concentration of the nodes when one dimension uses a very fine grid resolution compared to the other. Section 5.5.4 will elaborate further on this subject matter.

(e) Once the optimal resolution for both Δz and Δy has been established, the momentum source term [see equation 5.3] is applied into the model through the existing nodes within the 10 m radius from the disc centre (refer to Figure 5.3b). For this purpose, equations 5.6 and 5.7 are employed to locate all the relevant nodes that formulate the disc's 20 m frame.

$$r = \sqrt{(\mathrm{Y}_i - \mathrm{Y}_c)^2 + (\mathrm{Z(I)}_i - \mathrm{Z}_c)^2} \tag{5.6}$$

$$\mathrm{Y}_c = \frac{y(4) - y(1)}{2} \tag{5.7}$$

Where r is the turbine radius, Y_i refers to the node in the y direction within the turbine enclosure, Y_c is the turbine centreline in the y direction (70 m), $\mathrm{Z(l)}_i$ is the vertical plane in the z direction where i = 24 σ layers, and Z_c is the depth where the turbine centre/hub is located (i.e. 30 m).

	Sigma Layer	Depth (meter)
$Z(I)_{24}$	24	0
$Z(I)_{23}$	23	2.61
$Z(I)_{22}$	22	5.22
$Z(I)_{21}$	21	7.83
$Z(I)_{20}$	20	10.44
$Z(I)_{19}$	19	13.05
$Z(I)_{18}$	18	15.66
$Z(I)_{17}$	17	18.27
$Z(I)_{16}$	16	20.88
$Z(I)_{15}$	15	23.49
$Z(I)_{14}$	14	26.1
$Z(I)_{13}$	13	28.71
$Z(I)_{12}$	12	31.32
$Z(I)_{11}$	11	33.93
$Z(I)_{10}$	10	36.54
$Z(I)_{9}$	9	39.15
$Z(I)_{8}$	8	41.76
$Z(I)_{7}$	7	44.37
$Z(I)_{6}$	6	46.98
$Z(I)_{5}$	5	49.59
$Z(I)_{4}$	4	52.2
$Z(I)_{3}$	3	54.81
$Z(I)_{2}$	2	57.42
$Z(I)_{1}$	1	60.00

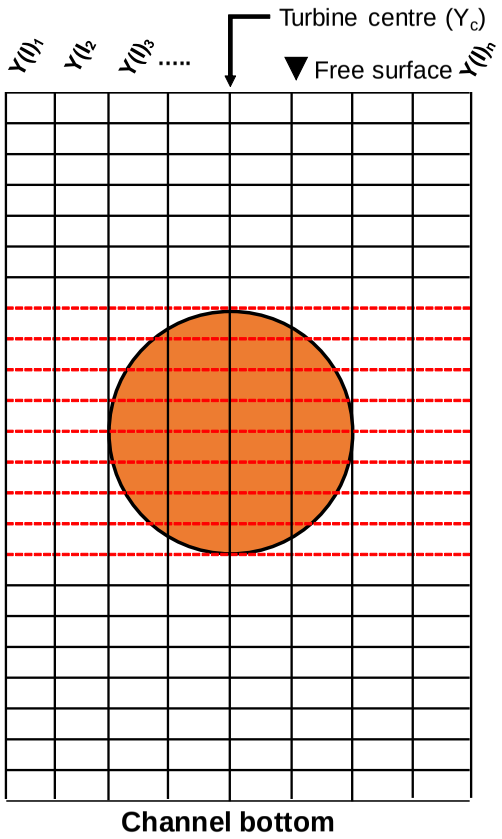

(a) Sigma layers and their corresponding depth

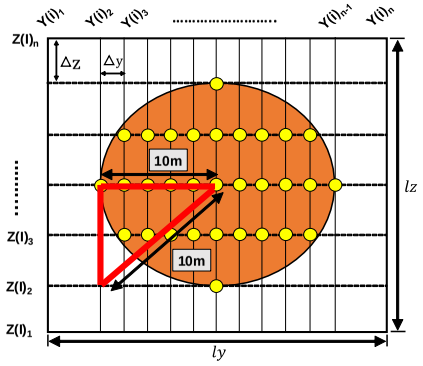

(b) Coarser vertical resolution (low density nodes)

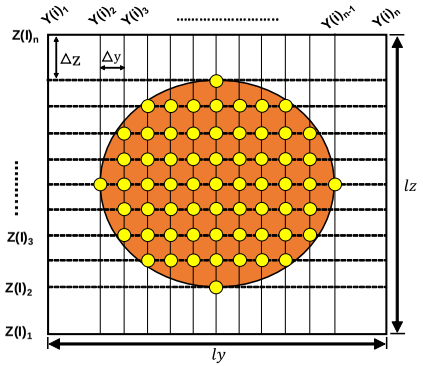

(c) Refined vertical resolution (higher density nodes)

Figure 5.3: Graphical information exhibiting the influence of vertical resolution (24 layers) on the model, where the respective planes that crossed the disc surface area are clearly shown. Detailed illustration on the comparison of the structured grid density nodes at the turbine swept area (y-z axes) are displayed via insets (b) and (c) respectively. $Y(I)_i$ refers to the nodes in the y orientation of the structured grid, while $Z(I)_i$ corresponds to the i^{th} vertical planes imposed on the model. Note that these figures are not drawn to scale.

5.4.2 Model set up for single disc

For a realistic modelling condition of a full size turbine, this study refers to a report by the EMEC [26] to get an idea for the generic characteristics of a tidal energy device. A 20-m diameter disc is used in this study since it is a reasonable size for a standard horizontal axis turbine in operation. Moreover, the deployment of tidal devices at any particular location is site and depth dependent, where depths between 40 m to 80 m are often quoted.

For this numerical study, the flow at the free surface and the channel depth is set to 3 m/s and 60 m respectively to resemble the general condition of the Pentland Firth area [166]. The disc z axis centreline is positioned at the mid depth (i.e. 30 m) to allow for a sufficient bottom clearance to minimize turbulence and shear loading from the bottom boundary layer. Also, the actuator disc is placed 250 m from the channel inlet to ensure that the flow is fully developed upon reaching the turbine area.

The resistance coefficient, K is one of the most important variables in simulating the actuator disc since it characterises the thrust exerted by the turbine on the flow. Changing the value of K will invariably influence the wake downstream of the disc. The relationship between C_T and K has been shown previously using equation (5.4). In this study, K is set to a constant value of 2, which corresponds to $C_T = 0.89$. This value was chosen since it replicates the measured resistance coefficient employed in [23]. Additionally, the disc thickness (Δx_t) was set to 4 m.

As mentioned previously, structured grid was imposed at the location of the turbine to give an accurate illustration of the disc's features. Conversely, unstructured mesh was used in the surrounding area with a maximum edge length of 10 m, while the edge growth ratio was set to 1.1 for a smoother mesh distribution. Figure 5.4 displays both the unstructured mesh used in the computational domain, and also the location of the structured grid where the turbine is housed.

The number of mesh elements varies significantly depending on the value of Δx, Δy and Δz chosen for different models, ranging from 70,000 to more than 900,000 cells. The model was run for 1500 seconds, at which point the results indicated that a steady state had been achieved (refer to Figure A.8 in Appendix A for details). The time step used for the simulation was 0.5 seconds, and met the CFL criterion. The simulations have been computed on an i7-3770 quad core computer with 16GB memory. Depending on test cases, it took between 3-5 hours for each simulations to be completed.

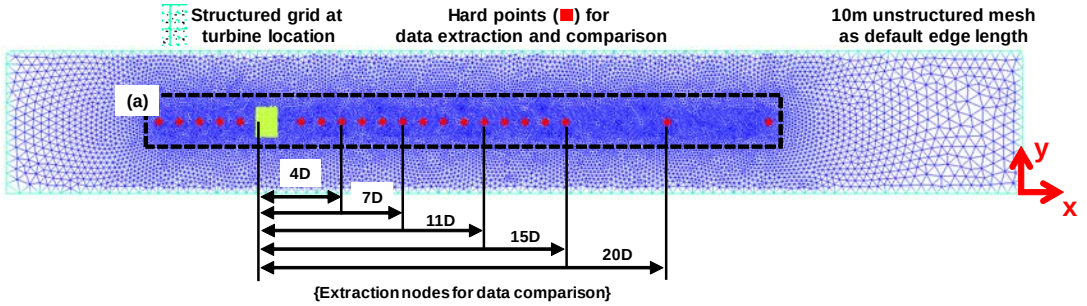

Figure 5.4: Geometry of the computational domain mesh used in the single actuator disc study. The extraction points for the model's outputs are denoted by the red nodes.

5.4.3 Boundary condition

A constant volume flowrate, Q of 21840 m^3/s was imposed at the channel inlet, where Q is equal to the surface area of the inlet (60 m x 140 m) multiplied by the mean flow velocity (2.6 m/s). Next, the downstream boundary was set to equal the channel water depth of 60 m to enable flow continuity. The Initial condition was set to 'PARTICULAR' (an option available in Telemac3D for defining the initial condition), where the initial depth of 60 m was specified in the CONDIM subroutine. Next, a commonly used method of defining inflow velocities is to use a power-law ($1/n^{th}$) profile. Although it is possible to use any value for n to approximate the flow conditions, a comparison of several values for n was considered to be beyond the scope of this study.

Thus the vertical velocity profile in the domain was imposed using one of the most commonly used power laws, $1/7^{th}$, so as to be similar to a full scale tidal site [167]. In addition, the Chézy formulation with a friction coefficient of 44 was applied to the bottom to reduce the flow velocity as well as to increase the shear near the bed. This value was chosen as it has been used previously in [142] to represent the bottom roughness in the PFOW region. Furthermore, a wide range of friction coefficient values have been examined by Rahman and Venugopal [168], and their influence on the model's output are found to be negligible. Also, both hydrostatic and non-hydrostatic codes were tested in this study, and their findings are discussed in Section 5.6.

The boundary condition on the bottom was set to a Neumann condition, which is a slip boundary condition. An attempt to implement a non-slip condition, where the bottom velocities can be set to 0 was not possible in this study since the model would require a very fine mesh near the bottom level to satisfy the wall function. Wall function, y^+ is a non-dimensional distance used to describe the ratio between the turbulent and laminar influences in a grid cell, as well as to indicate the mesh refinement for near

wall region in a flow model [169]. The rationale behind the wall function is to reduce computational time and also to increase both numerical stability and convergence speed when resolving the boundary layers.

However, because of the strong gradients of the flow and turbulence variables that exist in the viscous layer, highly refined grids are needed near the bottom [170]. Small scale models are known to be using a no slip wall at the bed (refer to [21–23]) since it is still computationally feasible to satisfy the y^+ requirement. Nonetheless, the flow details in the boundary layer were not of specific interest in this study. Further, the use of a very fine vertical resolution (e.g. 50 planes or more) for modelling a full size turbine is both impractical and not computationally feasible without the use of a computer cluster.

5.4.4 Turbulence input

Different values of stream-wise Turbulence Intensities (TI), have been reported in the literature for both in-situ measurements and flume experiments, which ranges from 3% to 25% [69, 164, 171–173]. TI is defined as the ratio of the turbulent fluctuations of the velocity fluctuation components to the mean stream-wise velocity of each sample, $\overline{u}$, and is one of the most common metrics utilised to quantify turbulence [174]. This parameter provides a quantification of the magnitude of the turbulent fluctuations and is considered to be a dominant driver of the fatigue loads on tidal turbine blades [175].

To properly validate the numerical simulations, the imposed turbulence intensity on the models should be as close to the one used by Harrison et al. [23] in their experimental work. Using an online tool [176] to extract the published data from [23], the measured turbulence intensities rate at the domain inlet can be approximated to vary from 5% - 15%. Nevertheless, with the largest intensity happened primarily near the flume's bed due to the bottom shear stress, the average intensity from the channel study can then be estimated to be just about 5%.

With the value of TI is now known, the $k-\varepsilon$ turbulence model can be adopted to define the turbulence at the channel inlet, where the turbulent kinetic energy, k and energy dissipation, ε are calculated using Equations 5.8 and 5.9:

$$k = \frac{3}{2}\mathrm{TI}^2 U^2 \tag{5.8}$$

$$\varepsilon = C_\mu^{3/4} \frac{k^{3/2}}{ls} \tag{5.9}$$

TI is the turbulence intensity rate of 5%, U refers to the velocity across the water column that follows the $1/7^{th}$ power law, C_μ is a dimensionless constant, equal to 0.09, and ls is the turbulence length scale. In the study, the value of ls was set to 20 m, which corresponded to one third of the channel depth as suggested by Rahman and Venugopal [168] and Blackmore et al. [177]. Table 5.2 summarises the inputs and values of the parameters adopted in the single actuator disc simulations.

Table 5.2: Default values of the numerical parameters employed in the simulation of a single actuator disc.

Numerical parameters	Input / Values
Law of bottom friction and Cd value	Chézy 44
Turbulence model	k-epsilon
Hydrostatic assumption	True
Initial condition	'PARTICULAR' where the initial elevation is equal to 60 m
Vertical resolutions	24 σ layers
Bottom boundary condition	Slip condition
Boundary forcing	Inlet: prescribed flowrate, Q = 21840 m^3/s Outlet: prescribed depth, H = 60 m
Resistance coefficient, K	2 (corresponding to C_T = 0.89)

5.5 Models' sensitivity and validation

5.5.1 Validation metric

An appropriate metric needs to be chosen for the model-data comparisons. As this study employs a full size turbine for the model, a dimensionless metric is needed for the validation against physical scale data. All parameters are made dimensionless by dividing them by a characteristic homogeneous quantity. A commonly used method employed to characterize the wake recovery is the rotor velocity deficit, U_{def} [see equation 5.10].

$$U_{def} = 1 - \frac{U_w}{U_\infty} \tag{5.10}$$

U_w refers to the wake velocity at any point downstream of the disc, while U_∞ is the unperturbed flow velocity. In this study, U_∞ corresponds to 3 m/s as defined by the maximum velocity of the incoming stream into the channel. Next, TI has been chosen as the benchmark quantity for turbulence behaviour [see equation 5.11].

$$\mathrm{TI} = \frac{\sqrt{\frac{2}{3}k}}{U} \tag{5.11}$$

where k is the turbulent kinetic energy from the flow. To examine the accuracy of the 3D models, focus will be placed on the modelled velocity reduction as well as the turbulence characteristics along the actuator disc centreline. The centreline is defined as the horizontal line that passes through the turbine centre along the x orientation of the flow direction.

For this study, the z and y disc centreline axes are located at 30 m mid-depth, and at 70 m mid-channel width respectively. Furthermore, to facilitate data extraction and for comparison purposes, hard points were applied into the geometry mesh during pre-processing stage to establish the positions of the fixed nodes within the domain. The implementation of hard points along the x centreline orientation for the desired longitudinal distances (in terms of turbine diameter, D) is illustrated in Figure 5.4.

5.5.2 Mesh dependency

Because of the approximations and averaging used in the RANS equations, the size as well as the number of cells in any given CFD domain can directly affect the results of a numerical model. A larger number of cells may result in a more accurate solution to a problem for a given set of boundary conditions and solver settings. However, increasing mesh density also requires greater processing time. In order to verify the robustness of the unstructured mesh used in the model, four meshes with varying resolutions were tested (i.e. the dimension of the edge length of the unstructured mesh); Case 1 = 1 m, Case 2 = 2 m, Case 3 = 5 m and Case 4 = 10 m. The refinement zone starts at 5D (where D is the rotor diameter) upstream of the disc and continues up to 25D downstream from the disc location. This region was selected since it covers the location of all hard points that will be used in extracting data for comparisons with published literature.

The mesh refinement zone as well as the fixed nodes that are used in validating the model are outlined in Figure 5.4. To properly compare against the published data, the

Table 5.3: Details on the mesh refinement used in the grid dependency study along with the extracted centreline velocity values at various downstream distances.

		Centreline velocity at various longitudinal position				
Mesh refinement	**Number of mesh elements**	**5D upstream**	**4D down-stream**	**7D down-stream**	**11D down-stream**	**20D down-stream**
Case1 = 1m	925,536	2.683	1.515	1.903	2.153	2.418
Case2 = 2m	316,584	2.680	1.735	2.092	2.315	2.554
Case3 = 5m	101,496	2.690	1.853	2.186	2.391	2.600
Case4 = 10m	72,936	2.694	1.846	2.247	2.464	2.659

Table 5.4: Details of the vertical resolutions examined in the single actuator disc study.

Sigma layers (σ)	**Distance between planes (in meter)**	**Number of mesh elements**
24	2.61	317,928
18	3.53	238,446
15	4.29	198,705
10	6.66	132,470

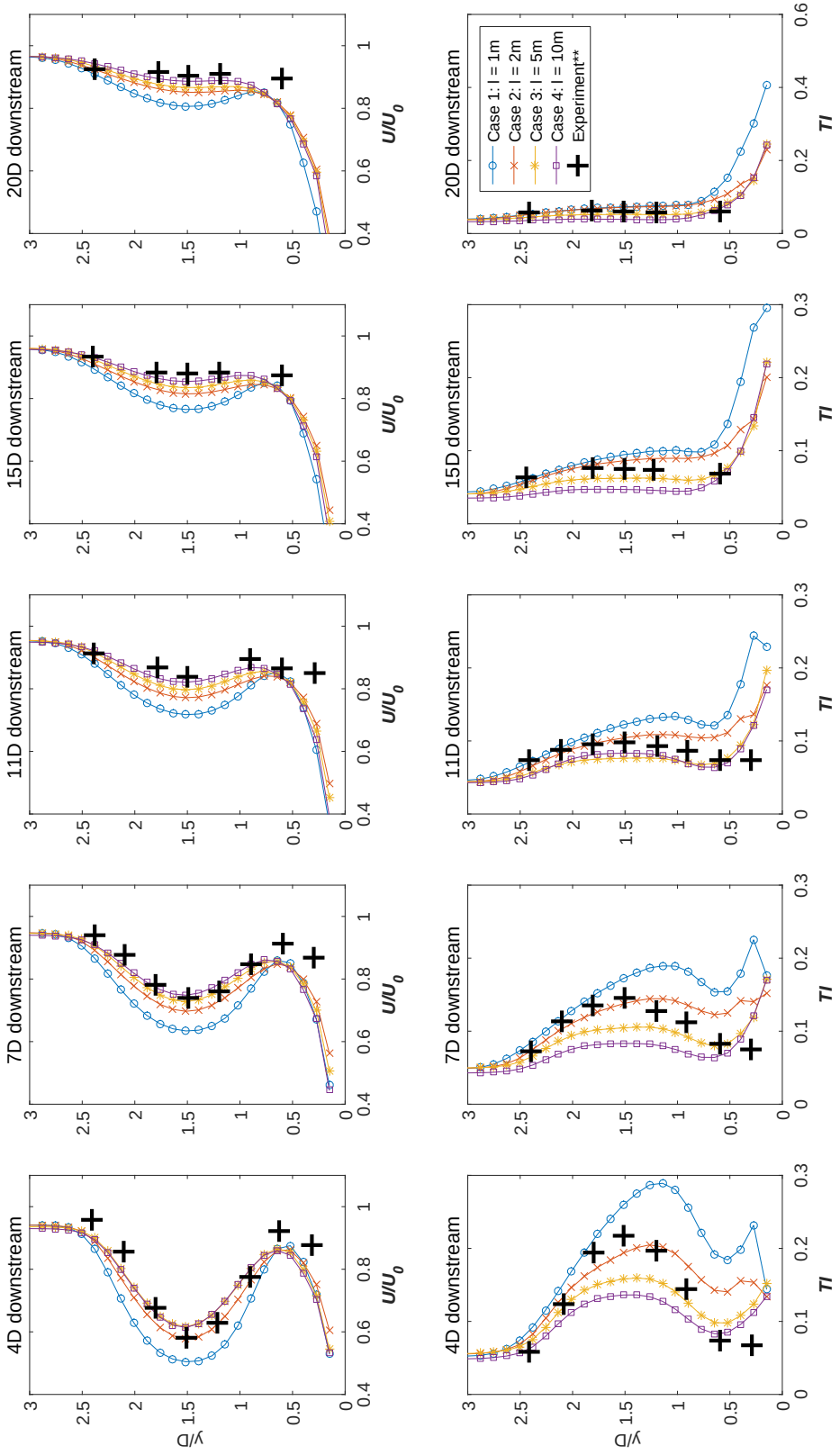

Figure 5.5: Mesh dependency study for the administered refinement zone at increasing distance downstream of the turbine. The mesh edge length, l within the refinement zone is varied according to the cases being explored. The experimental data used in the plots are from the work published by Harrison et al.[23].

model's outputs will be extracted from five locations within computational domains, specifically at the 4D, 7D, 11D, 15D and 20D downstream distances from the turbine centreline (refer to Figure 5.4 for details of the chosen nodes). Elsewhere, the default edge length of 10 m was applied. For this mesh dependency test, the structured grid at the turbine area was constructed using elements of size Δx,Δy = 2 m for all models, while the disc thickness, Δx_t was set to 4 m. Also, the model was run using only the hydrostatic assumption.

Table 5.3 highlights the models used in the grid dependency study, where four refinements values were tested. The most refined model (Case 1) consists of the highest number of elements at 925,536, while the model which has the lowest resolution (Case 4) is comprised of the least number of elements at about 70,000. The velocity data were then extracted at five distinct nodes (refer to Figure 5.4) and the outputs are listed in Table 5.3. In general, the results indicate that as the mesh density is becoming more refined, the corresponding velocity however is decreasing in value.

This finding is supported by Figure 5.5 which compares the models' velocity reduction (top plots) and TI (bottom graphs) against the laboratory measurement data from [23]. Overall, the results show that all models are able to replicate wake profiles similar to the one displayed by the experimental values for flows progressing through a disc. Interestingly, although a higher resolution domain was expected to give a better correlation against the experimental data, contradictory results were obtained.

Notably, the 1 m grid refinement seems to overestimate the velocity reduction by almost 10% in the near wake, before declining slowly in the far wake regions. Likewise, these scenarios are also reflected in the observation of TI, where the 1 m model appears to amplify the turbulence below the disc centreline in the 4D and 7D locations. This could be due to the fact that a higher resolution model contains a substantial number of points within the computational domains, which signifies that the cells are more sensitive to the flow characteristics in the surrounding region. Alternatively, it is also plausible that the Courant number for Case 1 model is rather large, causing it to be unstable. This implies that the flows are moving through two or more cells at each time step, affecting convergence negatively.

On the other hand, the 2 m mesh refinement (Case 2) agrees well with the measurement data, although a slightly higher velocity is observed in the far wake regions. Meanwhile, models with resolution of 5 m and 10 m are shown to be less accurate in the TI prediction in comparison with experimental data, where both models significantly underestimate the TI in the 4D and 7D regions. These results illustrate that the coarser

resolution models failed to properly represent the flow-rotor interactions, indicating that the models' output (i.e. velocity, and k for computing the TI) is susceptible to changes in mesh density.

Moreover, the use of a very fine mesh alongside the hydrostatic assumption may not necessarily provide superior numerical output as demonstrated by the 1 m mesh density test. While decreasing the simulation time step may help improve the outputs for Case 1, it may not be feasible or realistic for an ocean scale implementation. Consequently, as the simulation results for the 2 m mesh (Case 2) closely matched with the measurement, along with an acceptable simulation time step, it has been implemented as the optimal mesh generation for the following simulations.

5.5.3 Influence of disc thickness

Structured grid was employed to define the area of the actuator disc for two key reasons; First, to aid in identifying the nodes for momentum sink implementation. Second, to improve the accuracy of the approximated turbine forces by correctly asserting the physical shape of the disc. In this section, the influence of the turbine grid resolution (i.e. Δx and Δy) on the wake characteristics of a full scale actuator disc is explored.

For this test, a 2 m by 2 m (Δx and Δy) structured grid is embedded into the unstructured mesh domain where the turbine is located. The models are then run using three different turbine thickness values, Δx_t = 2 m, 4 m and 8 m. For clarification, when Δx_t is set to 4 m, the flow will have to pass through two Δx grid cells (each cell interval is 2 m as displayed in Figure 5.2 in the x direction where the momentum source terms will determine the forces exerted by the turbine). Figure 5.6 illustrates the comparison of the measurement data for the above three values of Δx_t.

Interestingly, the results show that thickness of the actuator disc has negligible influences on both the downstream wake, as well as the turbulence intensities. Although not shown here, a similar observation is also apparent when the density of the structured grid (i.e. Δx and Δy) is changed to other than 2 m resolution (e.g. 4 m refinement - which is presented in the subsequent section.). Therefore, it can be deduced that under current numerical setting, the downstream wakes and turbulences behind the turbine are independent of the actuator disc thickness for the tested domain.

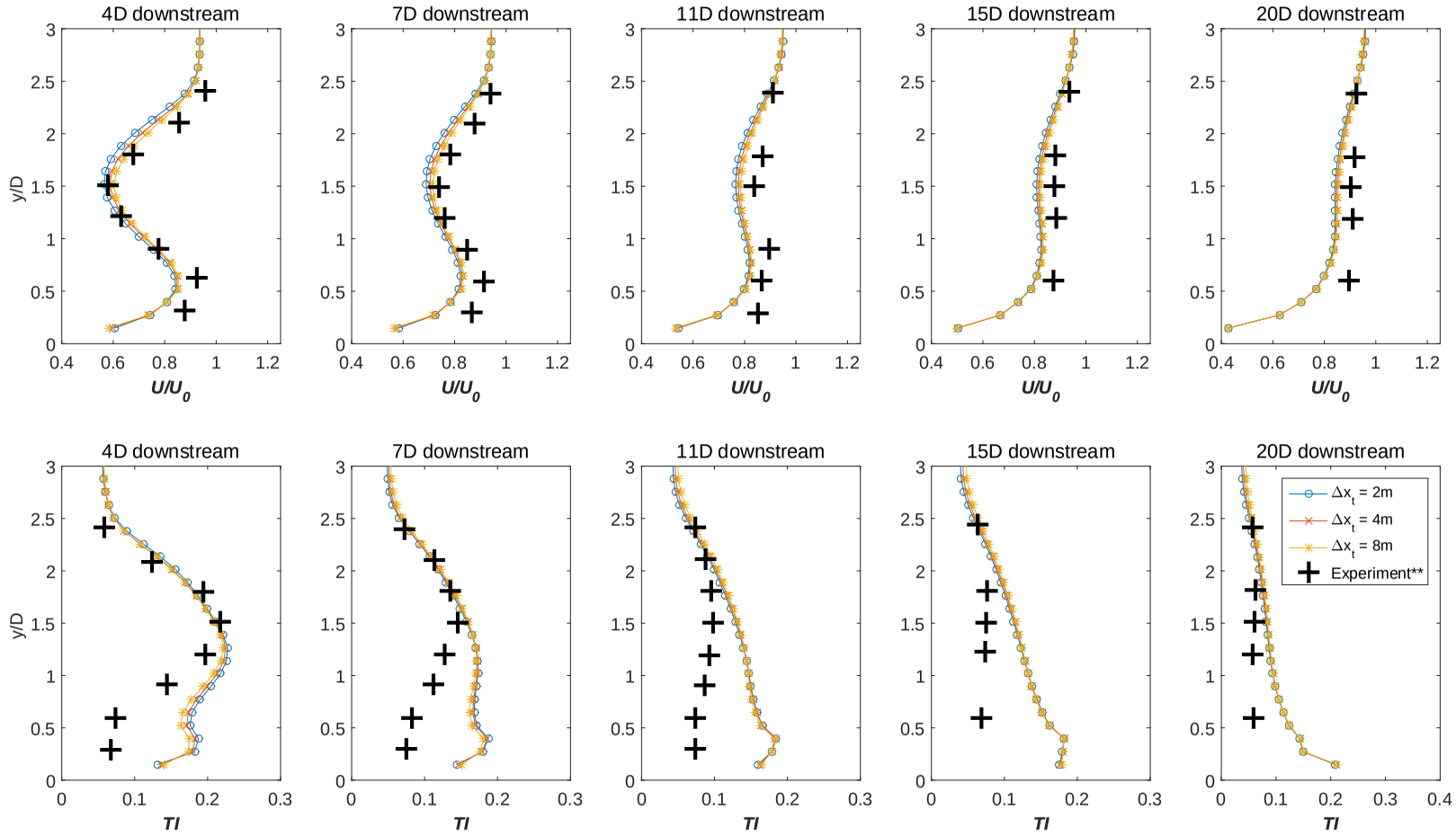

Figure 5.6: The influence of disc thickness, Δx_t on the wake formation at increasing distances downstream of the disc. The vertical resolution,Δz and the size of the structured grid (Δx,Δy) are maintained at 24 σ layers and 2 m respectively for all cases. The experimental data used in the plots are from the work published by Harrison et al.[23].

5.5.4 Resolution of structured grid

Interaction between the resistance loss coefficient (K / Δx_t) and resolution of the structured grids (Δx and Δy) at the actuator disc location is explored here. As previously mentioned, K is the constant resistance coefficient which corresponds to the experimental values of C_T. As the flow progresses through the turbine swept area, it expands and accelerates around the edge or 'width' of the disc. In the numerical model, the flow passing through the width or thickness of the turbine literally means that it is travelling across specific nodes in the x direction as defined by the enclosure of the disc. For a very fine mesh with constant Δx_t, the source term will be applied to a larger set of nodes when compared to a coarser grid.

To examine the relationship between the nodes and their impact on the wake characteristic, four structured grids with various densities are created and examined. The lowest resolution of Δx and Δy tested is 4 m, while the most refined is set to 0.5 m. Figure 5.7 highlights the disparity between the four models using a constant Δx_t of 4 m. Even though Δx_t was found to have no impact on the results as demonstrated in Section 5.5.3, the 4 m thickness was selected as this would be close to the projected thickness of a turbine in operation.

Model with the highest grid density (0.5 m) appears to overestimate the velocity reduction behind the disc by almost 20% in the near wake region, and continues to do so further downstream with a larger velocity deficit compared to other models. The same trend can also be observed for the model with 1 m grid, although the extent of velocity deficit is less pronounced as the flow started to reach homogeneity. In contrast, models utilising the 2 m and 4 m grids seem to be able to simulate the flow-rotor interaction appropriately and compare well with the experimental data.

Moreover, the 1 m grid produces greater velocity deficit in the near wake region, and this is reflected accordingly in the turbulence plots, where the intensities are less profound behind the disc due to wake mixing. A variation of TI up to 5% is seen for the case of 4D regions, then slowly recovers before matching other models at 15D downstream. However, a different trend is noticed for the 4 m grid model, as it shows some discrepancies for the TI in the near region, although it is not as dominant as the 0.5 m model.

The results presented in Figure 5.7 offer interesting insights for discussions. A less accurate output is expected from a coarser grid due to a limited (albeit uniformly scattered) number of nodes within the turbine enclosure as illustrated by Figure 5.3b.

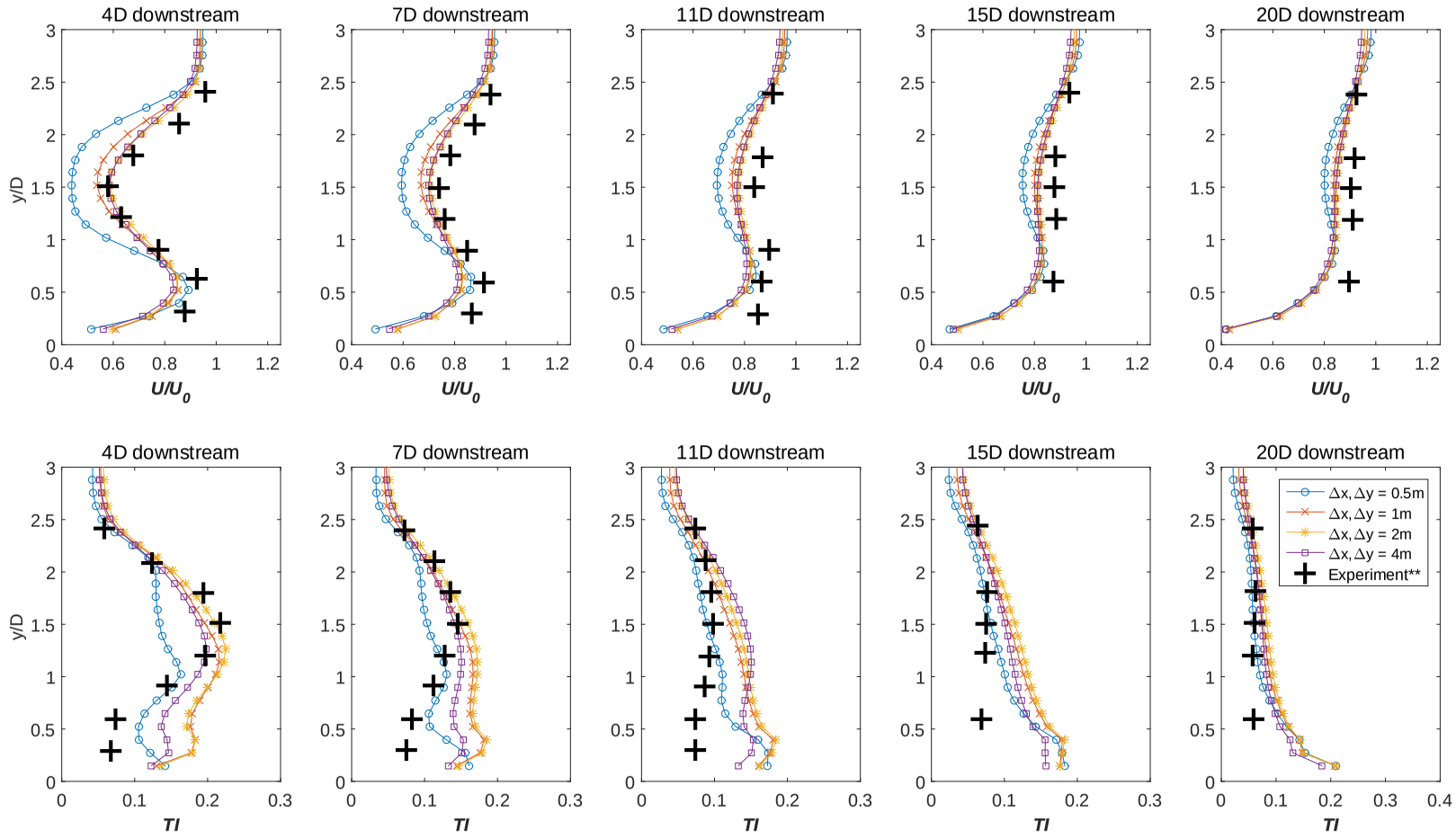

Figure 5.7: The influence of structured grid density, (Δx and Δy) on the wake formation at increasing distances downstream of the disc. The vertical resolution, Δz and the disc thickness, Δx_t are maintained at 24 σ layers and 4 m respectively for all cases. The experimental data used in the plots are from the work published by Harrison et al.[23].

Conversely, one would have thought that the simulation output could probably be improved by using a very fine mesh, although it appears that this is not always the case based on the results attained. As the density of Δx and Δy increases, the nodes that render the turbine swept area, as well as the turbine width, will also increase proportionally, as illustrated in Figure 5.3c. This figure clearly shows uneven distribution of the nodes at the face of the actuator disc for a higher density model, where they are concentrated prominently at the mid quarter of the disc.

Since increasing the mesh density only applies in the x and y direction, the top and bottom edges are devoid of nodes. As a result, the implementation of the momentum term would only be directed at the centre of the turbine, which consequently will cause inaccuracy in the approximation of the turbine force, as evidenced from the plots in Figure 5.7. To solve this, it is recommended that the vertical resolution should also be increased when employing a (very) fine mesh so that uniform node distribution can be achieved.

Nonetheless, increasing the vertical density while using a very fine grid will undoubtedly increase the computational overhead, especially when running a large scale simulation. Thus, finding an optimal ratio between the mesh density and vertical resolution is crucial so that the implementation of the actuator disc can correctly approximate the thrust exerted by a tidal turbine. Based upon the results presented in this case study, Δx = 2 m and Δy = 2 m have been chosen as the optimal structured grid density since they provide numerical accuracy and also computational balance needed for implementing the actuator disc.

5.5.5 Grid resolution in the y-direction

To recap, grid resolution in the y direction, Δy refers to the meshes that are perpendicular to the actuator disc surface swept area, as exhibited in Figure 5.2. It is anticipated that models with coarser Δy will perform poorly when compared with a more refined density, since the thrust force will only be computed at a larger nodes interval. In order to inspect this hypothesis, four Δy grids (2 m, 2.5 m, 5 m and 10 m) are tested, while Δx and Δx_t are both maintained at 2 m and 4 m cell interval respectively. This hypothesis is substantiated and illustrated by the velocity plots in Figure 5.8, where the 10 m grid somewhat underestimated the velocity deficit in the near wake region. Conversely, other Δy models show good comparison against the laboratory measurements.

Furthermore, because the coarser model (Δy = 10 m) contains a significantly smaller number of nodes, the model was unable to properly approximate the thrust on the

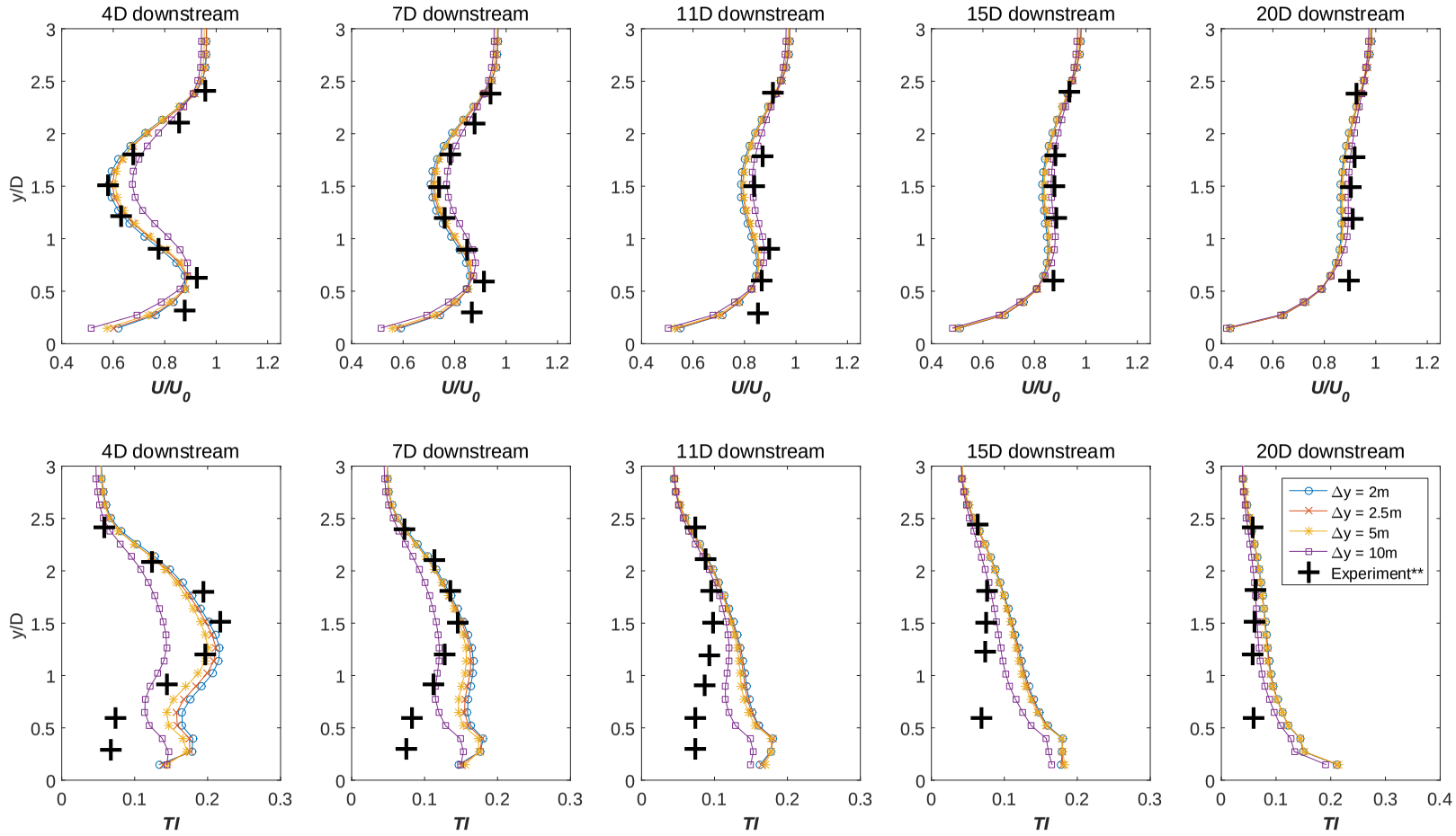

Figure 5.8: The influence of Δy resolution on the wake formation at increasing distances downstream of the disc. The value of Δy is varied, while Δx and Δz are maintained at 2 m and 24 σ layers respectively. The experimental data used in the plots are from the work published by Harrison et al.[23].

flow, resulting in distinctly lower turbulence intensities between 4D to 7D downstream regions. The other models, however, show a relatively similar characteristic for both U_{def} and TI. In essence, since the size of the disc adopted in this study is 20 m, Δy value of 10 m or more might not be suitable to accurately model the actuator disc since the number of nodes available is not sufficient for approximating both the forces as well as the size of the swept area. To conclude, based on the results observed, Δy = 2 m can be accepted as the optimal spacing in the y direction, and confirmed the remarks made previously in Section 5.5.4.

5.5.6 Sensitivity of the vertical resolution

To investigate the influence of vertical resolution, four σ layers are considered; 24 σ (default value), 18 σ, 15 σ and 10 σ. Table 5.4 provides the information of the models used in this study, where the largest (6.66 m) and smallest vertical interval (2.61 m) correspond to 10 σ and 24 σ layers respectively. Further, based on the findings in Sections 5.5.4 and 5.5.5, Δx and Δy were set to 2 m for all models. Additionally, Δx_t was set to 4 m. The simulated results are presented in Figure 5.9, where the model employing 10 σ layers has underestimated the TI as anticipated, since it has the least number of nodes to properly characterise the turbine swept area.

However, it is quite interesting to see the same model was able to reproduce the velocity wake that matched the measurement results. One possible reason for this observation could be due to the hydrostatic assumption used in the model. Nonetheless, the poor turbulence correlation observed for the 10 σ layers should be approached with caution. It shows that the region between 4D and 11D downstream of the disc is highly turbulence, and the flow fluctuations cannot be accurately reproduced using planes with large vertical intervals.

To get around this issue, instead of sigma layers, it is possible to utilise other types of mesh transformation for the distribution of vertical planes, such as by fixing planes at desired depths. With this option, the height of the vertical planes can be appropriately adapted to capture the influence of the disc on the flow. In brief, finding the optimal Δz values is crucial to achieve balance between computational efficiency and numerical accuracy - more so for simulations involving a very large domain. It is also important to realise, however, that both U_{def} and TI must be properly validated before coming to any conclusions, because the results in this section have clearly demonstrated how the computed TIs may not necessarily reflect the characteristics of the predicted velocity.

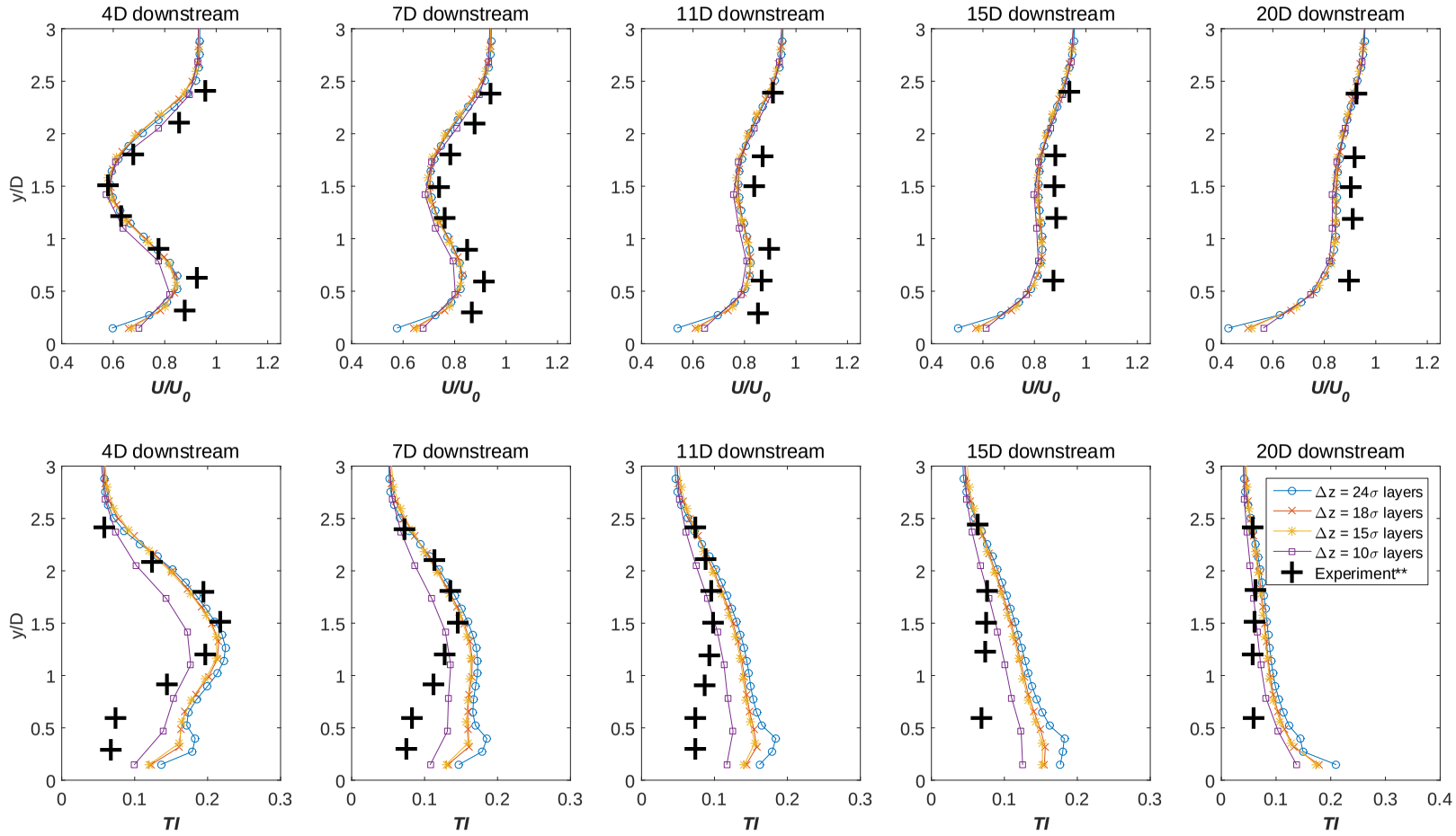

Figure 5.9: The influence of vertical resolution, Δz on the wake formation at increasing distances downstream of the disc. The value of Δz is varied, while the size of the structured grid (Δx,Δy) is maintained at 2 m. The experimental data used in the plots are from the work published by Harrison et al.[23].

5.6 Non-hydrostatic models for single turbine study

The influence of hydrostatic and non-hydrostatic assumptions on the numerical models have been investigated to ensure the robustness of the numerical models. The hydrostatic pressure equation assumes that the vertical accelerations are negligible, and is accurate when the ratio of the vertical to horizontal length scale is large. Conversely, the non-hydrostatic option employs the full incompressible Navier Stokes equations and is suitable for investigating small scale phenomena, albeit computationally more intensive. Similar with the 3D flow equations shown previously in Chapter 4 (Equations 3.1 - 3.3), the non-hydrostatic assumption adopted in this section is computed by the following additional equation:

$$\frac{\partial W}{\partial t} + U\frac{\partial W}{\partial x} + V\frac{\partial V}{\partial y} + W\frac{\partial W}{\partial z} = -g\frac{\partial Z_s}{\partial x} + v\Delta(W) + F_z \tag{5.12}$$

where W and F_z are the three-dimensional component of the velocity and sink term in the vertical direction respectively. Figure 5.10 demonstrates the principal difference between the two solvers using a resistance coefficient, K of 2 (corresponding to C_T = 0.86). The top plots reveal results of the predicted velocity reduction behind the disc at five distinct locations in terms of the turbine diameter, D. The plots at the bottom meanwhile depict the computed turbulence intensities from the models along the same downstream locations.

For the velocity plots, both hydrostatic and non-hydrostatic models demonstrate an almost indistinguishable output from one another for all the locations observed. Additionally, both models also show excellent agreement when compared against the experimental data, where flow characteristics behind the discs are accurately replicated. Despite that, slight differences can still be seen near the bottom half of the channel, where the hydrostatic model somewhat shows a closer agreement with the measurement points than the model using the non-hydrostatic approximations.

At the 4D and 7D regions, the distinction between the two models happens at about 0 < y/D < 1. Further downstream, however, discrepancies seem to develop slightly further upwards across the water column, with the point of divergence between the two models occurring in the region 0 < y/D < 1.5. In general, some variations between the two solvers are to be expected to some extent, since their mathematical formulations are inherently different. Another reason for this disagreement could also be attributed to the imposed parametric values (e.g. velocities and intensities) on the models, as they

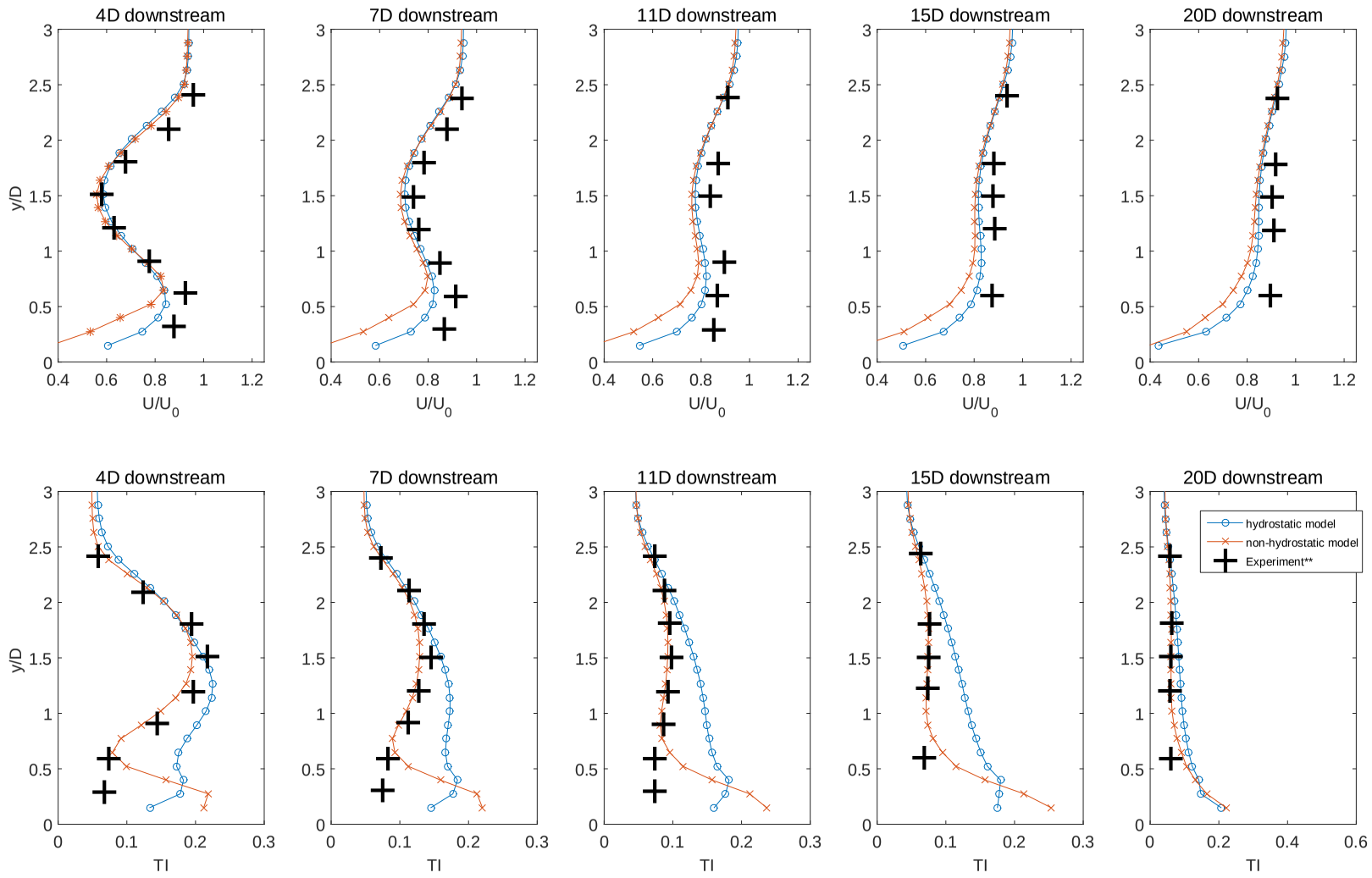

Figure 5.10: Comparison between hydrostatic and non-hydrostatic models examined in the single actuator disc study. The experimental data used in the plots are from the work published by Harrison et al.[23].

were just an approximation from the one used in the physical scale set up.

As for the computed turbulence intensity, TI, the non-hydrostatic model illustrates excellent agreement with the measured data, in which the turbulence mixing from the near till far wake regions are accurately resolved. On the contrary, the model utilising hydrostatic solver shows notable differences when compared with the experimental data, and can be clearly seen from the 4D to 15D plots in Figure 5.10. Reasonable TI agreement with the measured data is observed for the hydrostatic model at 4D downstream of the disc between $1.5 < y/D < 3$, before it gradually deviates from the data points as it gets nearer to the channel bed. A similar trend also occurs further downstream, where the variations in TIs between the two models are becoming more apparent.

At the 15D location, the hydrostatic model displays an intensity variation of up to 10% against both the experimental data and non-hydrostatic model. Moreover, at this location (15D), the computed TI from the hydrostatic solver only matched the experimental data near the water surface ($y/D > 2.5$), while the largest TI variation was observed very near to the bottom. Interestingly, far downstream at 20D, the two models illustrate an almost indistinguishable turbulence characteristic as the flow eventually recovers and reach homogeneity. The comparisons between these two models offer interesting insight on the choice of solvers to be used in the present study. The output by the non-hydrostatic model displays close agreement with the measurement data for both the predicted velocity and computed turbulence intensities, as evidence from Figure 5.10. This is to be expected since the non-hydrostatic assumptions accounts for the gravitational acceleration as well as the vertical velocity component, hence is more accurate.

Whereas the flow characteristics obtained using the hydrostatic pressure approximation only match the measured data for the predicted velocity reduction behind the disc, while the turbulence components greatly vary. This happens because the turbulence in the flow may not have been fully resolved because the non-slip criterion could not be implemented on the channel bed. The non-slip criterion requires the use of a highly refined mesh to resolve the size of the smallest eddy in the flow as it begins to transition from laminar to turbulence regime. And since the hydrostatic code ignores the advection and diffusion terms, the rotational properties of the fluid cannot be properly dissipated and thus influencing the turbulence characteristic in the wake regions.

Indeed, as the highest turbulence intensity zone is observed in the immediate vicinity behind the disc (4-7D) and then slowly dissipated further downstream, the hydrostatic

model can only reproduce the expected intensities in the far wake regions, as shown by the 20D downstream plot. Based upon the findings presented in this section, it can be concluded that the non-hydrostatic model performs substantially better that the hydrostatic mode in replicating the flow behaviour behind the disc. Due to this reason, the models presented onwards in this chapter were run using the the non-hydrostatic assumption.

5.6.1 Influence of bottom friction

As previously mentioned in Section 5.4.3, the model's bottom boundary is enforced using a slip condition. The application of the no-slip condition in modelling a full size turbine is just not reasonable since the model would require a highly refined vertical mesh (e.g. 50 planes or more), especially near the bottom to satisfy the wall function. In contrast, the use of slip condition requires the implementation of bottom friction for the domain bed. Bottom friction offers resistance to momentum of flow as well as increasing the shear near the bed. Moreover, the bottom or side-wall friction reflects the continuity of the constraint at the fluid-solid interface. Therefore, this parameter is crucial in any numerical simulation to represent hydrodynamic characteristics of current propagation.

The bed stress can be parameterised using the quadratic friction law as shown in Equation 5.13. Specifically, the drag coefficient is in this study is represented by the Chézy formulation, using the following equation:

$$C_d = \frac{g}{(\text{Chézy value, Ć})^2} \tag{5.13}$$

To examine the influence of the drag coefficient on the actuator disc model, a wide range of friction coefficient values have been examined: Chézy coefficient = 34, 44, 63, and 85 $m^{1/2}s^{-1}$ which correspond to C_d = 0.0086, 0.0051, 0.0025 and 0.0014. These C_d values were selected since they have been previously employed in the hydrodynamics modelling of the Pentland Firth region (refer to these articles [117],[119],[143],[142] and [178]).

Figure 5.11 displays the comparison plots between the four drag coefficients and their influence on the predicted velocity (top plots) and turbulence intensity (bottom plots) of the models. Interestingly, varying the values of the bottom friction has an almost indistinguishable impact for the velocity deficit around the near wake region, as shown by

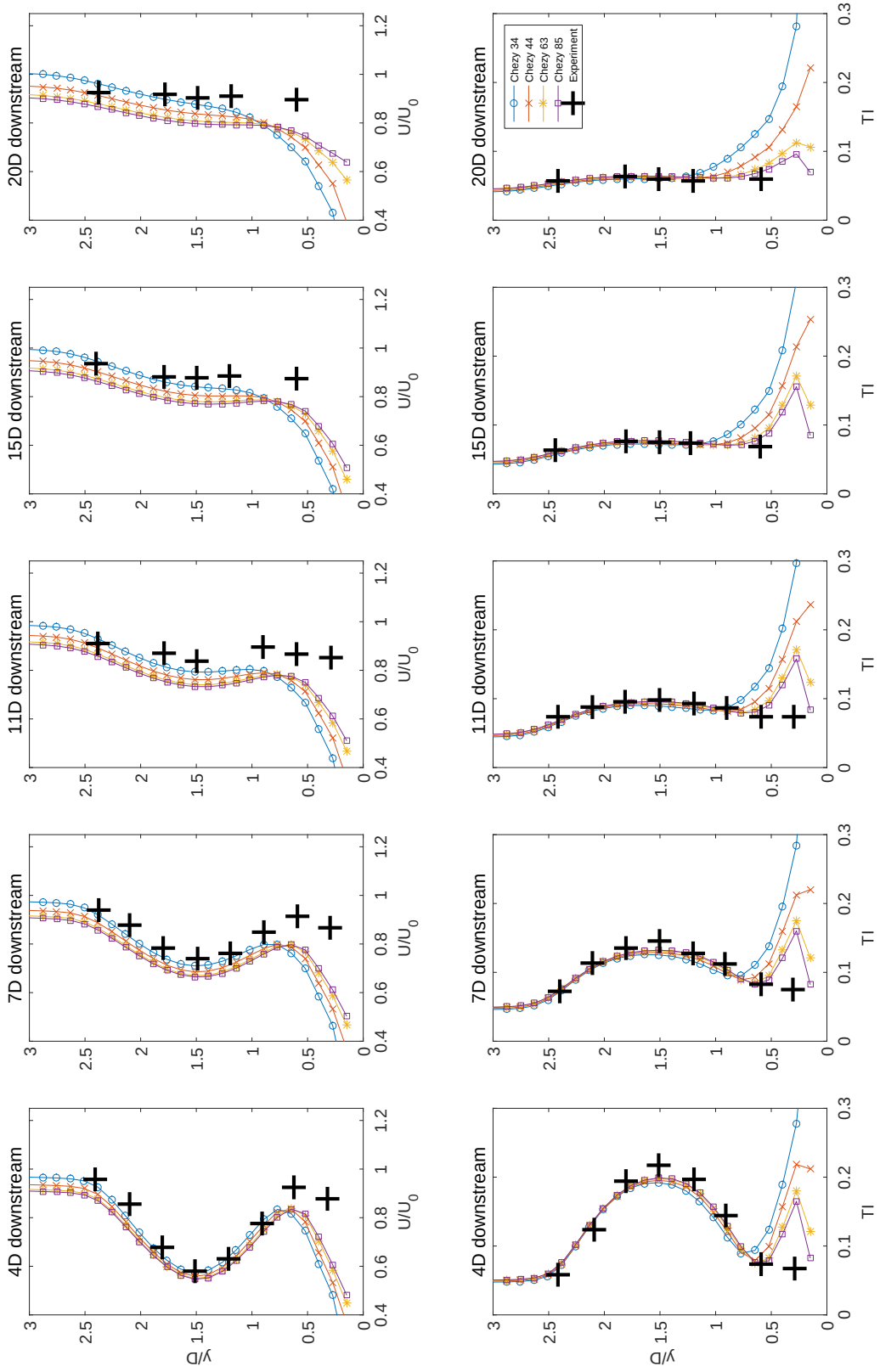

Figure 5.11: The influence of bed roughness on the wake formation of a non-hydrostatic model at increasing distances downstream of the disc. The experimental data used in the plots are from the work published by Harrison et al.[23].

the 4D and 7D plots. However, as the flow progresses further downstream, noticeable velocity differences can be observed between the four friction values. The largest bed friction values (i.e. Chézy 34) displays the most distinctive characteristics, influencing the water column up till y/D of 0.25, as well as retarding 60% of the flow speed at 20D downstream of the disc. In addition, the output from the model using the largest friction coefficient value also no longer conforms with the flow characteristic observed from the experimental data.

As evidenced from the 15D and 20D plots, the model (Chézy 34) slightly underestimated the predicted velocity near the surface (y/D > 2.5), whereas near the bottom (at y/D < 1), it showed substantial divergence from the measured data points. Model utilising Chézy 44 meanwhile shows a reasonable consistency on the flow behaviour at all the extraction points. On the other hand, models using the smallest drag coefficient (i.e. Chézy 63 and 85) illustrate an almost identical characteristic, where both models somewhat overestimate the flow retardation, as shown by the plots from 11D to 20D. This overestimation happens since small drag will exert less shear resistance on the flow, and thus cause the fluid to move at a much faster rate. Correspondingly, the predicted velocity using the two lowest friction values (i.e. Chézy 63 and 85) demonstrate substantial differences when compared with the experimental data.

In contrast, the computed TI for all four friction values precisely match the turbulence behaviour of the published data across the water column, albeit small disagreements near the bed are exhibited by the models, as illustrated by the bottom plots in Figure 5.11. Moreover, this dissimilarity is more pronounced at an increasing distance further downstream from the disc, where the largest divergence is shown by model using Ć 34. At 4D and 7D locations, the dissimilarity between the four tested drag coefficients is not that apparent since the flow in the immediate vicinity downstream of the disc is highly turbulent. This turbulent region observed in the near wake induced intense vortices, eddy and mixing, and thus reduced the impact of the imposed bed frictions. Nonetheless, as the wake begins to recover further downstream of the disc, the turbulence caused by the presence of the device would dissipate, while the influence of the mixing due to the bed frictions is expected to be more pronounced.

From Figure 5.11, it can be seen that the use of a large drag coefficient (C_d = 0.0086 / Chézy 34) value induce a huge amount turbulence that persists far downstream of the disc at 20D, where the effects of the mixing is shown to linger as high as y/D = 1.25 across the water column. Conversely, since models using Chézy 63 and 85 represent a smoother bottom surface, the TI variations from these two models are significantly

less notable when compared with the measured data. However, the two models utilising minimal drag coefficient (i.e. Chézy 63 and 85) are unable to correctly characterise the turbulence for the transitioning flow between the first and second vertical layer (from bottom). This observation is clearly presented in the TI plots in Figure 5.11, from 4D till 15D locations, where there is a sharp change in turbulence intensities values from a very smooth flow in the first layer, to intense mixing in subsequent layer.

Nonetheless, as the wake recovers to reach homogeneity at 20D region, the differences in TI values between the two layers reduces dramatically. Uniquely, model using Chézy 44 shows reasonable flow characteristic for both U_{def} and TI when compared with the experimental data and the other bed friction values. Due to this reason, the default friction coefficient values for subsequent simulations are imposed using Chézy 44. In essence, this exercise establishes that the model has successfully modelled and replicated what is expected upon the implementation of distinct bed friction coefficients; higher C_d increases the resistance to the flow momentum, and thus notably reducing the flow velocity. Consequently, high C_d value also imposes a larger shear stress on the flow, and thus inducing more turbulence and mixing into the model.

5.6.2 Influence of structured grid sizes for turbine's enclosure

The location (or the enclosure) of the disc is explicitly defined using the structured grid since it is crucial to properly assert the physical shape of the disc into the numerical model so that the turbine's thrust force can be reasonably approximated. Further, the use of structured grid at the turbine's position also facilitates in identifying the corresponding nodes in the horizontal and vertical direction for the implementation of the momentum source term. The interaction between the resistance loss coefficient (K / Δx_t) and the resolution of the structured grids, Δx and Δy at the actuator disc location is explored here. In this exercise, K (which corresponds to the experimental value of C_T) and Δx_t (disc thickness) are both set to 2 and 4 m respectively. Note that Δx_t is set to 4 m since the largest Δy examined here is 4 m.

As discussed in Section 5.5.4, for a high density mesh with constant Δx_t, the source term will be administered to a larger set of nodes (within the defined enclosure volume) when compared to a coarser grid. To explore the relationship between the nodes density and their influence on the wake characteristic, four structured grids with distinct density were once again employed. The most refined Δx and Δy was set to 0.5 m, while the coarsest grid inspected was 4 m. Figure 5.12 illustrates the results of these simulations, where excellent agreement against the experimental data is observed regardless of

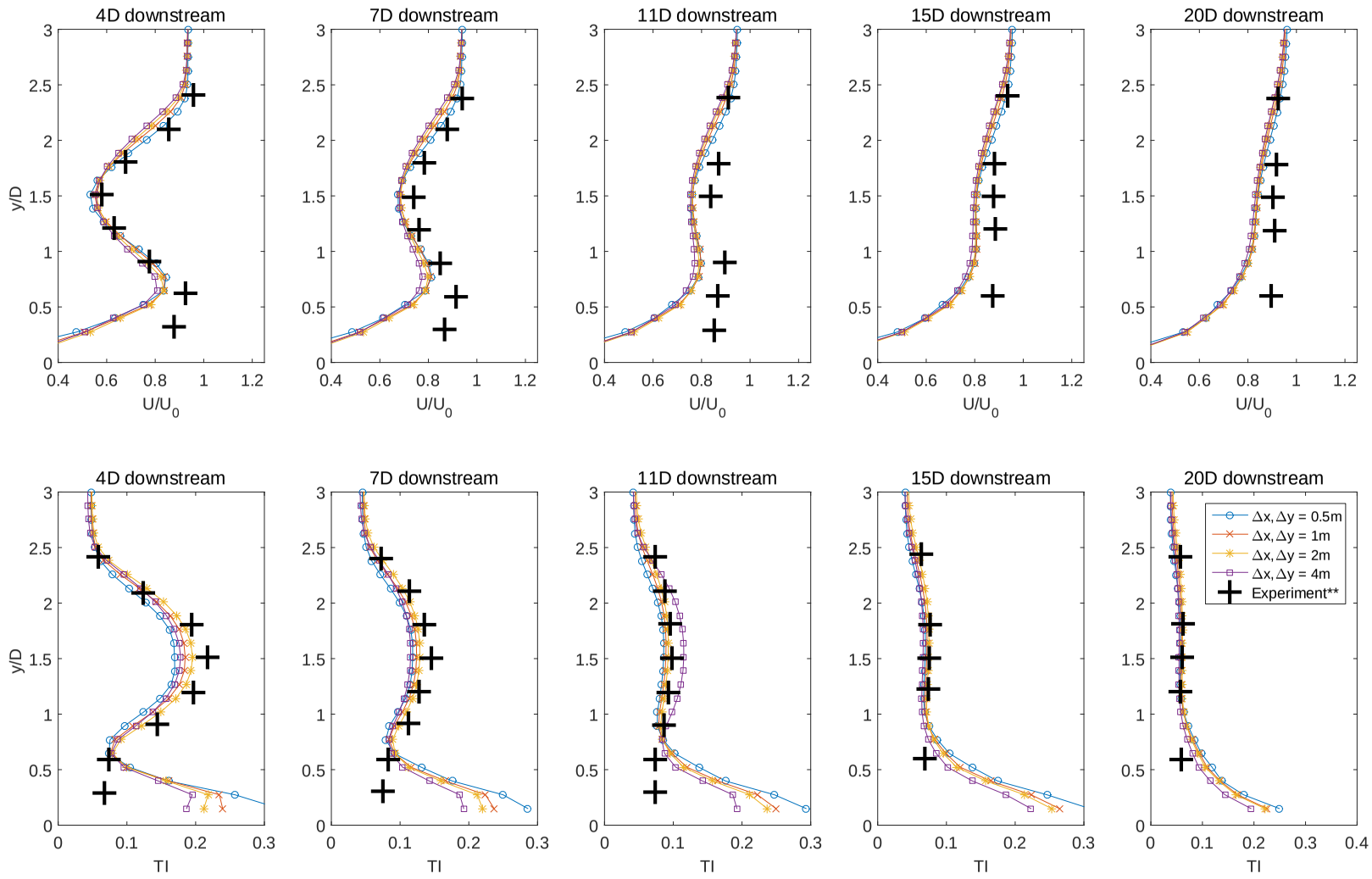

Figure 5.12: The influence of structured grid density on the wake formation of a non-hydrostatic model at increasing distances downstream of the disc. The experimental data used in the plots are from the work published by Harrison et al.[23].

the grids' resolution. All models exhibit indistinguishable velocity outputs from one another, starting from 4D extraction point until 20D position. A similar trend can also be seen in the TI plots, where the turbulence characteristics were accurately replicated by the models.

Nonetheless, slight variations between the grid sizes for the near wake turbulence are quite notable and require closer examination. From the 4D TI plot, it is clear that the 2 m grid size model produced the closest turbulence characteristic to the measurement data, while the others show slight TI underestimation around the disc's centreline. The same trend persists until the 7D extraction point, though the variation between the models was noticeably reduced. Then at 11D, the coarsest grid density (4 m) displayed substantial overestimation in the predicted turbulence, while the other three models conformed with the experimental data points. Finally, further downstream at 15D and 20D, all models exhibited an almost identical flow profile and compared well with the measured data.

The small differences observed in the TI plots in Figure 5.12 could be due to the inability of the coarser grid to sufficiently produce the thrust onto the flow to mimic the presence of an actuator disc. As the density of Δx and Δy decreases, the nodes that render the turbine swept area, as well as the turbine width will also reduce proportionally. As a result, the implementation of momentum term would only be directed at larger nodes interval within the turbine swept area, resulting in an inaccurate approximation of the turbine thrust. Conversely, the implementation of a highly refined mesh (0.5 m) is not without drawback. For instance, for a fixed number of vertical layers, higher resolution grid density will cause uneven distribution of nodes at the face of the actuator disc (refer to Figure 5.3c), because the increased density only applies in the x and y direction.

Because of this, the top and bottom edges are devoid of nodes since the nodes will be concentrated prominently at the mid quarter of the disc, and thus may cause inaccuracy in the approximation of the turbine force. Although this can be easily countered by decreasing that the vertical distance, Δz (i.e. increasing the number of vertical layers), the trade-off involves substantial increase in computational efforts, especially when running a large scale simulation. Thus, finding an optimal ratio for the mesh density and vertical resolution is crucial so that the implementation of the actuator disc can correctly approximate the thrust exerted by a turbine. Based upon the presented findings, Δx and Δy = 2 m has been chosen as the optimal structured grid density since it provides both numerical accuracy and computational balance needed for implementing

the actuator disc in this idealised channel study.

5.6.3 Influence of the imposed turbulence intensity

The effects of ambient turbulence intensity on the turbine wake have been shown to be significant in [179], where the shape of wake, length and strength largely depend on the upstream turbulence. Increasing the ambient turbulence intensity increases the mixing in the wake due to increased velocity fluctuations. Eventually, this results in higher momentum fluid entering the wake region, causing faster flow recovery to the free stream velocity [164]. To provide closure for the transport equations of the turbulent kinetic energy, k and turbulence dissipation, ε, it is necessary to provide the numerical domain with boundary and inlet values.

As previously elaborated in Section 5.4.4, the default inlet values for the turbulent kinetic energy can be calculated using Equation 5.8 by adopting the mean turbulence intensity similar to the one used in the experimental set up in [23, 165], which was approximated to be around 5%. Subsequently, the inlet values for turbulence dissipation can then be evaluated using Equation 5.9. To inspect the validity and accuracy of the imposed $k-\varepsilon$ values at the inlet of the numerical domain, three turbulence values are employed; TI = 5% (default), TI = 10%, and TI = 15%. From this exercise, it can then be explored whether the shape of the wake profile behind the actuator disc is appropriately reproduced in response to each of the imposed turbulence intensity values.

In essence, the actuator disc models used in this study were able to accurately replicate the wake characteristic based upon the free-stream turbulence input, as shown by the U_{def} plots in Figure 5.13. Imposing higher turbulence (i.e. 10% and 15%) into the model increases the velocity in the bypass region, which in turn increases the rate of far wake re-energisation. This translates into a faster recovery of the wake, as evidenced by the near wake plots of 4D and 7D. At 4D behind the disc, TI = 5% displays centreline velocity reduction of almost 40%, whereas velocity deficit for TI = 10% and 15% are just about 20% and 25% respectively. Overall, from the U_{def} plots presented in Figure 5.13, the fastest wake recovery is shown by model using the largest TI (i.e. 15%), followed by 10% and finally 5%. At 11D location, although models using TI = 10% and TI =15% already indicate that the wake has fully recovered, the velocity deficit remains around 20% where both models exhibit similar velocity profiles.

Conversely, using a much lower TI (default value of 5%) shows that the flow requires more than 20D behind the turbine to fully regain homogeneity. More importantly, the

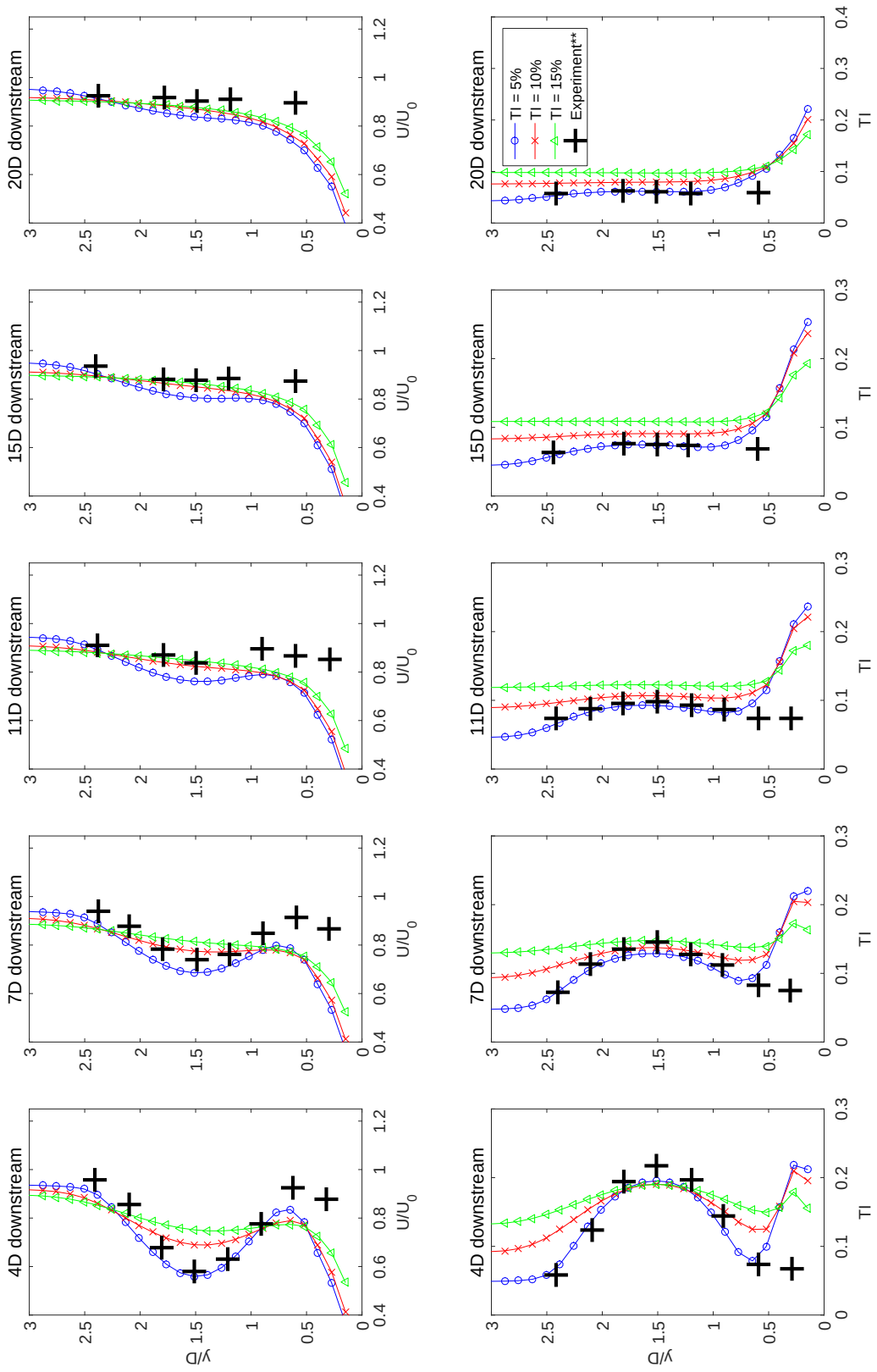

Figure 5.13: The influence of imposed turbulence intensity (TI) level on the wake formation of a non-hydrostatic model at increasing distances downstream of the disc. The experimental data used in the plots are from the work published by Harrison et al.[23].

turbulence intensity plots in Figure 5.13 are able to corroborate all these findings. The greatest turbulence region, with turbulence intensities of almost 20%, is observed at turbine centreline of the 4D plot. This is due to the intense mixing and vertical motions in the flow in the immediate vicinity behind the disc. Moreover, the influence of the flow mixing is still visible up until 11D region, before showing sign of recovering at 15D downstream of the disc. Moreover, the applied actuator disc source term has also successfully demonstrated its capability in replicating the turbulent profile from the 10% and 15% turbulence input.

Higher TI input causes strong velocity fluctuations as the flow passes through the actuator disc, causing greater turbulence at the edges of the disc, and is clearly depicted in all the plots. Interesting, although the three models illustrate notable dissimilarity in intensities at the bypass region, the turbulence characteristics at the turbine's centreline location are comparable to one another, as evidenced from the 4D and 7D plots. In brief, the findings from this study have highlighted the capability of the numerical model to accurately replicate the anticipated wake characteristics for various turbulence inputs, and verify the robustness of the actuator disc approach undertaken in this research work. Not only that, the use of TI = 5% as the default value for the mean turbulence intensities is justifiable because it has exhibited excellent agreement with experimental data for both U_{def} and TI.

5.6.4 Validity of the resistance coefficient

Among the parameters required in the implementation of the actuator disc, the resistance coefficient, K is probably the most pivotal numerical input of all. This parameter imitates the production of the thrust force from by the physical device due to the incoming flow, which is essential in reducing the flow momentum bypassing the simulated disc. For comparison purposes, the estimated value of K used in the numerical model must be proportionate to the thrust coefficient value used in the experimental set up. This is important to ensure that the momentum source terms can be properly administered into the finite element model, so that the forces experienced by the porous disc in the experiment can be accurately replicated.

To examine the robustness and sensitivity of the actuator disc to changes of resistance coefficient, the following thrust coefficient values are tested; C_T = 0.61, C_T = 0.86 (default), and C_T = 0.98. The corresponding K values for these C_Ts are then computed using equation (5.4), which are comparable to K = 0.93, K = 2 (default), and K = 3 respectively. Note that these three thrust coefficient values are selected since they were

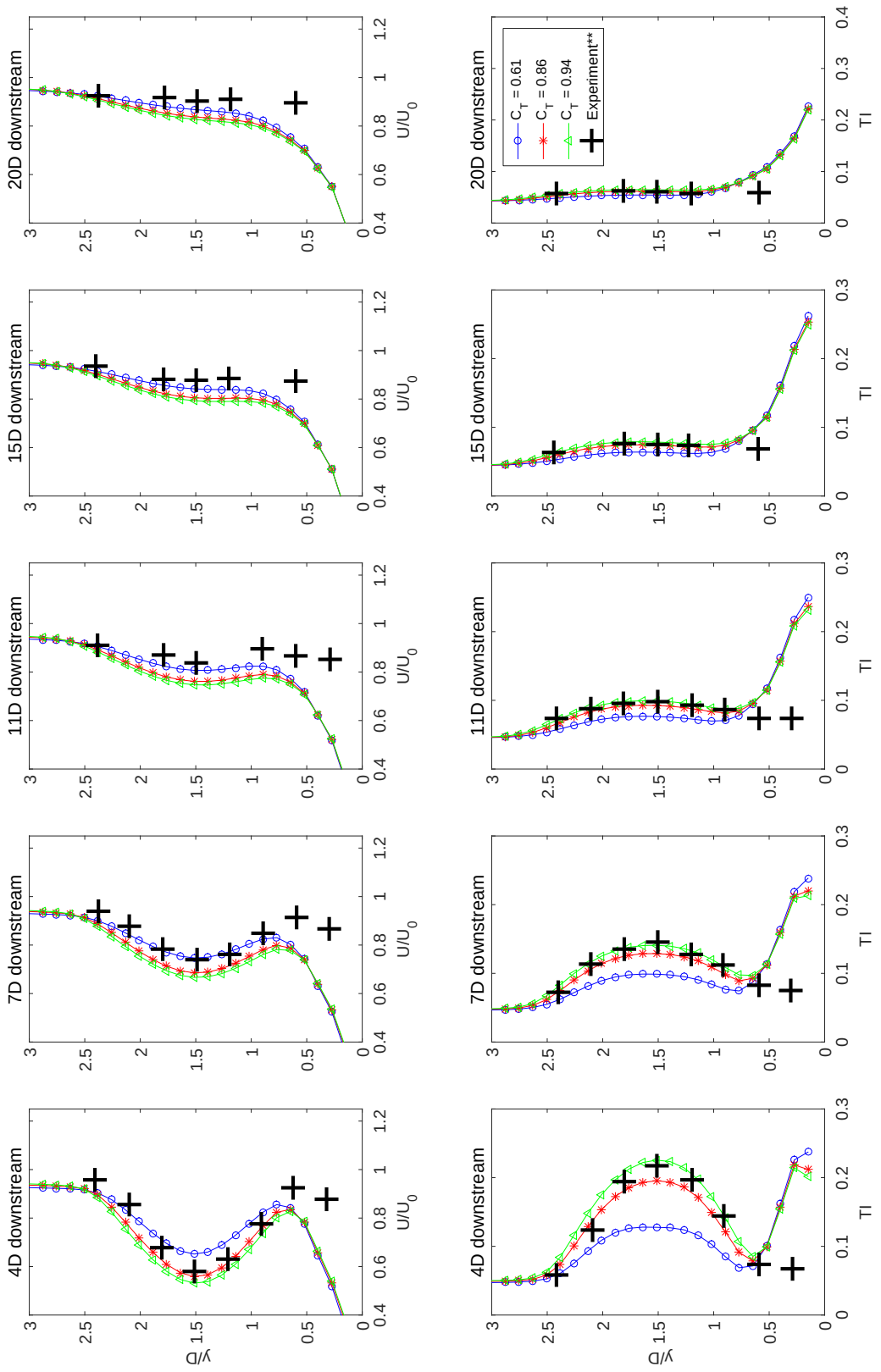

Figure 5.14: The validity of resistance coefficient parameter in imitating the thrust force exerted by a single turbine for a non-hydrostatic model. The experimental data points used in the plots are for $C_T = 0.86$ from the work published by Harrison et al.[23].

also employed in the study conducted by Harrison et al. [23] to examine the wake characteristic due to variation of the disc porosity (i.e. changing the thrust force acting on the disc).

Figure 5.14 shows the comparison results for the three tested K values, in which the experimental data points used in the plots are from the C_T = 0.86 porous disc set up. In theory, lower C_T means faster flow passing through the disc (i.e. less thrust force exerted by the disc), hence lower velocity deficit when compared with a higher C_T value. From the velocity plots presented in Figure 5.14, it can be seen that this phenomenon has been successfully reproduced by the model. The smallest velocity deficit (30%) is shown by the model imposed with C_T = 0.61 at 4D downstream of the disc, while the largest deficit (~40%) is recorded by the C_T = 0.98 model.

This behaviour continues to persist up to a distance of 20D behind the disc, albeit with decreasing velocity retardation as the flow recovers to match the free-stream velocity. In addition to this, the output from the models replicating C_T = 0.86 and C_T = 0.98 also display an almost analogous velocity profiles. This is to be expected since the magnitude of the thrust force imposed on both models are very close to one another. Nonetheless, while the shape of wake profile from the three models perfectly follows the measurement data, the model-experiment comparison invites further examination. At 4D location, both C_T = 0.86 and C_T = 0.98 models closely matched the data point, which should be anticipated since the measurement data points are from a rather similar C_T value.

Further downstream from 7D to 20D, however, the closest predicted velocity to the experimental data is shown by the model with minimal thrust force (C_T = 0.61), while the output from the other two models demonstrate slight velocity overestimation. This dissimilarity may be attributed to the mean turbulence intensity imposed on the model, which is just an approximation based upon the information gathered from the work in conducted in [23], and thus might slightly influence the model output. The TI plots in Figure 5.14 further corroborate the U_{def} results observed before. Lower C_T means slower fluid bypassing the disc, hence less turbulences behind the disc as illustrated by the C_T = 0.61 model. Similarly, higher C_T (0.98) enhances the blockage effect experienced by the disc, thus the bypass flow through the turbine contains more energy in general. This in turn translates into a highly turbulent region behind the disc due to the trailing vortices from the disc edges, as well as intense flow mixing.

Each of the tested resistance coefficients manages to reproduce the expected turbulence characteristic in the wake, where the discrepancy between the models can be clearly

seen in the 4D and 7D TI plots. At 4D location, K value of 0.91 (C_T = 0.61) registers a very low turbulence regime, at just about 10%. Conversely, both K = 2 (C_T = 0.86) and K = 3 (C_T = 0.98) exhibit a higher turbulence profile at around 18% and 20% respectively. Beyond 7D behind the disc, distinction between the models' turbulence profile are less prominent as the turbulence begins to dissolve, prompting the flow to reach equilibrium. In essence, the three resistance coefficient values tested in this study are able to simulate a range of C_Ts, where the replicated flow characteristic downstream of the actuator disc demonstrated excellent agreement with experimental data.

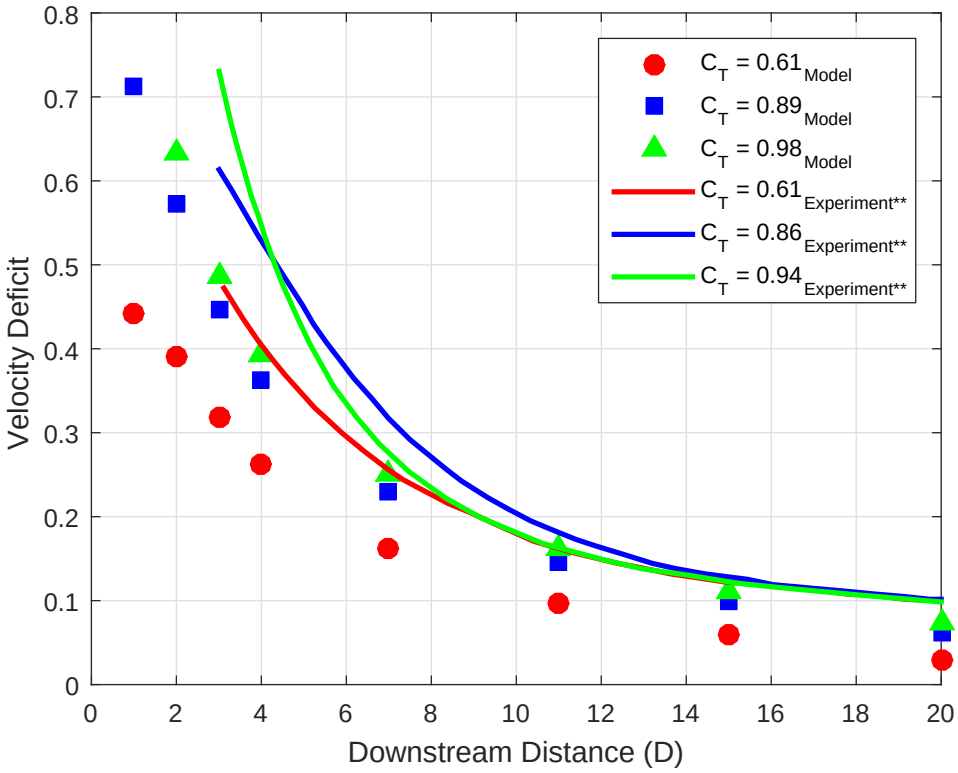

Figure 5.15: Comparison of three thrust coefficient values along the longitudinal distance for single actuator disc study using the non-hydrostatic assumption. The experimental data used in the plots are from the work published by Harrison et al.[23].

To further understand the models' performance against the measurement data, the downstream centreline velocity deficits for all three models are plotted and displayed in Figure 5.15. This plot clearly illustrates the capability of the numerical model in replicating the wake region, via the actuator disc approach, in which interchangeable trends as observed from published literature are clearly manifested. Equally important, the tested rate of change of resistance over the disc thickness, $K/\Delta x_t$ also signifies the anticipated thrust impact on the flow. A higher C_T value (i.e. K = 3) caused more

thrust force to be introduced, hence resulted in higher velocity deficit in the immediate vicinity behind the disc. Comparatively, a lower C_T (i.e. K = 0.93) resulted in smaller velocity deficit, as evidenced from Figure 5.15.

Nonetheless, the predicted velocity displays a notable underestimation when compared with the published literature, especially in the near wake region. This is to be expected since the K values are only an approximation, based upon the C_T measured experimentally. The flow converging points were also slightly different between the models and data points. Figure 5.15 shows that the flow from the experimental set up began to converge past the 14D location, whereas the predicted flow still shows sign of wake recovery at that particular position. Once again, this could be attributed to the estimated mean turbulence intensity rate imposed in the numerical model which was about 5%. As wake recovery is largely driven by free stream turbulence [22], imposing a slightly higher TI rate should push the converging point further upstream.

5.7 Discussion

A study to examine the validity of the RANS actuator disc approach in simulating a full scale tidal turbine has been presented by comparing the predicted velocities and computed turbulence intensities against laboratory measurement data sourced from literature. Numerical simulations were conducted using Telemac3D, and a detailed methodology in the implementation of the momentum source term was introduced and elaborated upon.The parameters investigated in this study include: the influence of (i) unstructured mesh sizes used in the computational domain, (ii) change in the turbine thickness (Δx_t), (iii) variation in the structured grid resolutions (Δx and Δy) used to represent the turbine's enclosure, (iv) resolution of vertical layers (Δz), and (v) the effect of hydrostatic and non-hydrostatic formulations on model output parameters.

The findings highlighted that the numerical model was highly sensitive to the mesh refinement upstream and downstream of the turbine, where the low resolution model had failed to properly represent the flow-device interactions. Besides, altering the disc's thickness (Δx_t) was found to have negligible impact on the downstream wakes and turbulence mixing, which was somewhat unexpected. Additionally, model accuracy was shown to be very susceptible to changes in the grid density of the turbine enclosure (i.e. the structured grid). However, poor correlation against the published data was shown by model imposed with the highest grid resolution (i.e. Δx,Δy = 0.5 m), where it produced the greatest velocity deficit. This was attributed to the uneven distribution

of nodes across the disc swept area, causing the computed source term to be applied predominantly at the mid section of the turbine surface.

In particular, the relationship between vertical resolution (Δz) and grid density in y-direction (Δy) in representing the the disc's features was thoroughly investigated. First, it has been demonstrated that the optimal structured grid density was obtained using Δx,Δy = 2 m, where its outputs compared well against the experimental data. Furthermore, the study on the impact of vertical resolutions (Δz) on the flow characteristics indicated that appropriate adjustment on both the horizontal and vertical planes must be performed to accomplish the optimal ratio between the nodes resolution in both z and y orientation. In fact, refining the structured grid density without taking into consideration the positioning of the nodes across the disc swept would certainly have caused the applied thrust force to be inaccurate. Specifically, this study has highlighted the importance of finding a balance between computational efficiency and numerical accuracy.

Uniquely, the impact of the hydrostatic and non-hydrostatic pressure assumptions on the predicted output were also examined, where both models exhibit nearly indistinguishable flow retardation characteristics behind the simulated disc. However, for the turbulence characteristics, only the non-hydrostatic model was able to accurately match the experimental result, while the hydrostatic solver failed to properly resolve the bottom turbulence mixing in the wake regions between 4D and 15D downstream positions. These observations might have been caused by three factors: (a) the applied slip criterion for the bottom boundary condition could not resolve the turbulence properties near the channel bed. (b) due to the inherent limitations of the hydrostatic solver itself, which neglects the vertical velocity components. (c) the ratio of the vertical to horizontal length scale used for the computational domain might not be large enough to warrant the hydrostatic solver effectively to determine the required properties.

To summarise, this study provided a preliminary demonstration of the applicability of the RANS actuator disc approach for a full size tidal device in a simple channel. The efficacy and robustness of the applied momentum source term have been thoroughly examined, and highlighted the model's capability to accurately replicate the wake profiles and turbulence characteristics downstream of the disc upon validation against the published experimental data. Naturally, the next step of this research work will look at the simulations of several full size tidal turbines in an array to observe the model's accuracy in replicating the flow interactions involved.

Chapter 6

Implementation of the Actuator Disc Approach in an Idealised Channel. Part II: Multiple Turbines and Flow Interactions

This chapter explores the validity of the actuator disc method in imitating the interactions of multiple tidal turbines using the 3D-RANS finite element model - Telemac3D[1]. More importantly, the work undertaken here is a continuation of the previous study in Chapter 5, where the implementation of a single actuator disc in an idealised channel was discussed. In particular, this chapter also employs comparable methodology in the application of actuator disc momentum source term and construction of the computational domain as demonstrated in Chapter 5.

Detailed set up on the arrays arrangement is presented and elaborated. The flow interactions between multiple turbines are examined, specifically for the two and three turbine set ups that are arranged into a single row array and a two row array. Mesh dependency study has also been carried out to ensure robustness of the models. Findings from this study are primarily represented using two plots - the models' predicted velocity in both lateral and longitudinal distances and also the contour of the simulated flow/turbulence. Also, in an effort to thoroughly validate the applied actuator disc source term in the numerical model, the models' output parameters have been compared with published data from the literature.

1. Part of the contents from this chapter had been presented at two international conferences, and was also used in writing up a manuscript for journal publication. Please refer to Appendix B for details.

6.1 Benchmarking and Data Validation

Data from experimental investigations are often required to validate the output parameters from any numerical models. In this study, the models are compared with published data from the two-row array interaction study conducted by Myers and Bahaj in [69]. For reference, similar experimental rig was also used by Harrison et al. in [23, 165] to study the wake characteristics of a single actuator disc. Highlights from the experimental work by Myers and Bahaj are as follows:

- The experiment was performed in a flume with the following dimensions: 21 meter long, 1.35 meter wide and tank depth of 0.3 meter.
- The wake structure and its recovery in the downstream region was produced using perforated disc with diameter and thickness of 0.1 meter and 0.001 meter respectively, where the disc porosities (ratio of open to close area) were kept constant at 0.48.
- The measured disc thrust coefficients, C_T varies from 0.91 - 1.08 depending on lateral separations.
- Additionally, the vertical velocity profile in the flume was developed to closely match the $1/7^{\text{th}}$ power law, where the maximum flow speed was observed at 0.3 m/s.
- Flume's turbulence intensity was in the range of 6% to 8% and is isotropic in nature. It is worth mentioning that this is a relatively low level of ambient turbulence intensity compared with field measurements taken at real sites, where an intensity as high as 30% had been reported in [180].

6.2 Model set up for array study

The methodology in setting up the actuator discs to be used for arrays configuration in a simple channel follows closely with the guidelines described in Section 5.4.1 in Chapter 5, and are summarised as follows:

(a) The configurations of the numerical domain used in this study are given in both Figures 6.1 and 6.2, where the channel length, width and depth was set to 1400 meter, 250 meter, and 60 meter respectively. More importantly, the dimension of this domain was properly scaled up so that it would have a blockage ratio that is close with the one employed by Myers and Bahaj in [69].

(b) The first row (which contains two turbines) were positioned 250 meter from the channel inlet, where its z and y axes centreline were fixed at 30 meter mid

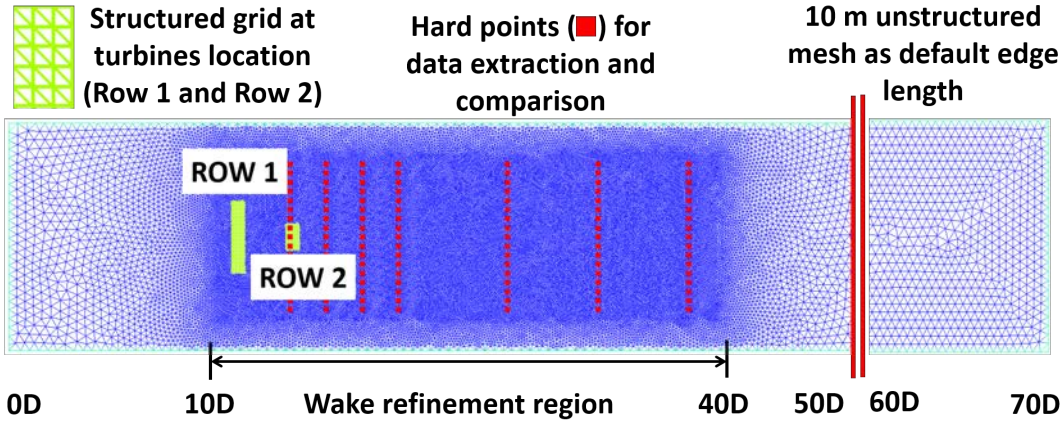

Figure 6.1: Geometry of the computational domain mesh used in the multiple actuator discs study. The extraction points for the model's outputs are denoted by the red nodes.

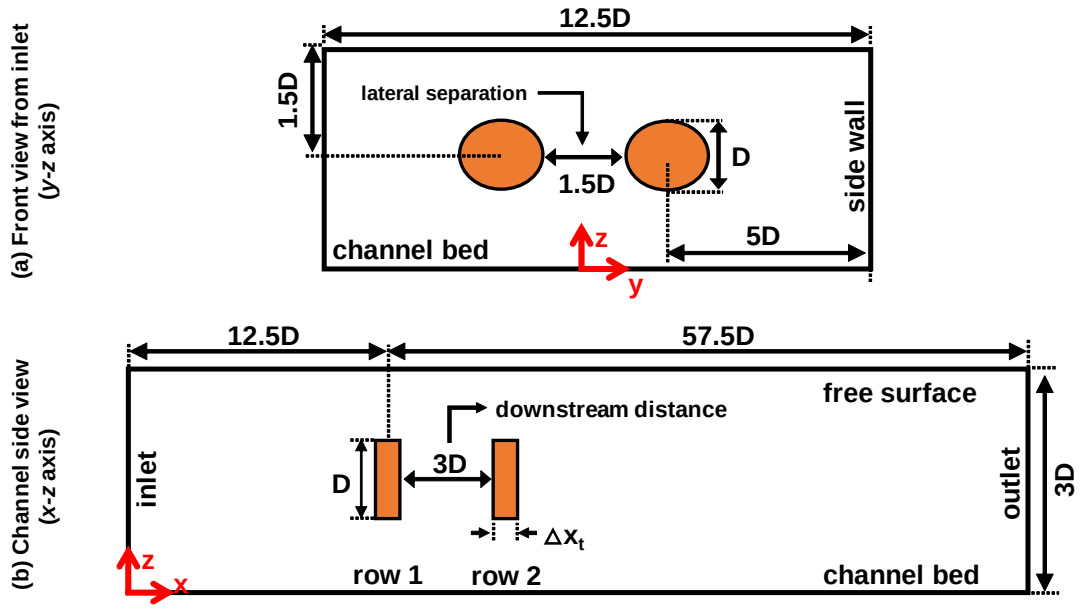

Figure 6.2: Schematic diagram for the simple channel study illustrating the arrangement of the actuator discs in their respective rows. Note that D corresponds to the diameter of the disc.

depth and 100 meter from the side wall (refer to Figure 6.2). The second row (consisting of one turbine), meanwhile, was located 3D downstream from the middle spacing of the front row as shown in Figure 6.1. Figure 6.3 illustrates the position of the turbine centreline adopted in this work for both single and two-row configurations.

(c) Similar with the single turbine study, structured grid was specifically used to define the enclosure of the turbine (i.e. turbine location) as this would facilitate in maintaining the turbine's features, while unstructured grid (with maximum edge length of 10 meter) was enforced elsewhere on the domain.

(d) The size of the structured grid were deliberately set to be larger than the turbine diameter, D (where D = 20 meter) and its width (Δx_t = 4 meter) to allow for numerical tolerance upon the execution of the momentum sink. Illustration on the implementation of structured grid as the turbine enclosure is given in Figure 5.2 in Chapter 5.

(e) Equally important, the vertical mesh resolution, Δz employed in this work was also represented by 24 σ layers, which is identical to the one used previously in Chapter 5 for the single turbine study.

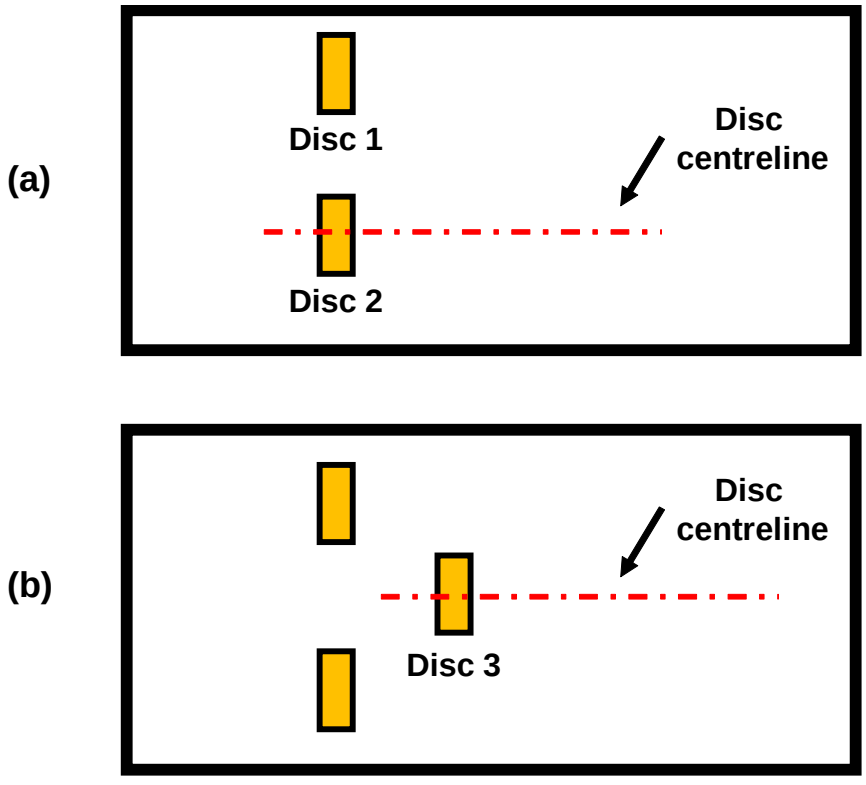

Figure 6.3: Illustration on the position of the turbine centreline adopted in this work. (a) Single row arrangement. (b) Two rows configuration.

The inlet of the computational domain shown in Figure 6.1 was imposed using a constant volume flow rate, Q = 39000 m^3/s, while the outlet was set to using water depth of 60 meter. Note that higher flow rate was imposed in this study to account for the increase in computational domain width (250 meter vs 140 meter previously). In an open flow, velocity at a certain point above the channel bed can be conveyed in terms of power function using depth ratio, given by the following expression:

$$\frac{U}{U_y} = \left(\frac{d}{y}\right)^{\frac{1}{n_p}} \tag{6.1}$$

where U is the stream wise velocity of 3 m/s, d is the channel depth (i.e. 60 meter), and U_y is the velocity at point y above the seabed. In this study, the value of n_p is set to 7. The turbulence at the inlet boundary was imposed using the $k-\varepsilon$ model, in which the turbulent kinetic energy, k and energy dissipation, ε were approximated using Equations 5.8 and 5.9 respectively. Also, both hydrostatic and non-hydrostatic codes were tested in this study, and their findings are discussed in Section 6.4. In particular, apart from the inlet boundary condition, similar numerical parameters as summarised in Table 5.2 were also employed in modelling the turbines and flow interactions within the idealised channel.

6.3 Models' sensitivity and validation

6.3.1 Mesh dependency test for single row configuration

Since the models' variables and parameters are approximated by the RANS equations, the size as well as the number of cells in any given CFD domain can directly affect the results of a numerical model. Accurate solution may be achieved by increasing the mesh density, although the drawback involves greater processing time and increase in computational requirement. To verify the robustness of the mesh used in the model, three domains with varying unstructured mesh resolutions were examined; 2 meter, 5 meter and 10 meter. The refinement zone begins at 10D from the channel inlet, till 40D downstream, as illustrated in Figure 6.1. The single row configurations are given as follows:

- The front row consists of two turbines.
- Separation distance between the turbine is set at 1.5D.
- The turbines are positioned 250 meter from the inlet.

Table 6.1: Mesh dependence study for single row array.

Mesh refinement	Mesh elements	4D down-stream	20D down-stream	Simulation run-time (approximated)
		Centreline velocity (m/s)		
2 meter	889,008	1.650	2.482	11 hours
5 meter	232,080	1.754	2.542	7 hours
10 meter	176,592	1.814	2.578	5 hours

In addition, rotor velocity deficit, U_{def} was used to characterise the wake recovery of the actuator disc (refer to Equation 5.10). Pertinent model outputs for the three refinement values are given in Table 6.1 From the table, it can be seen that the predicted velocity increases as the mesh density decreases, which corroborates previous findings in Section 5.5.2 in Chapter 5. The highest velocity variation (~9%) is observed in the near wake region (4D behind the disc) where the impact of turbulence is more pronounced due to vortices and wake mixing. Conversely, further downstream, only small velocity disparity of about 4% is observed as the flow begins to converge. These observations are corroborated by Figure 6.4a which displays the mid-depth lateral centreline velocity deficit of the three refinement values at 3D downstream position from the disc. Figure 6.4b on the other hand shows the velocity deficit across the longitudinal distances for similar disc set up.

From these two plots, it can be clearly seen that the velocity drop due to the presence of both discs can be modelled using the actuator disc approach, where the appropriate trend and expected velocity reduction are reasonably replicated by the applied source term. Additionally, although Figure 6.4a exhibits no apparent differences between the cell resolutions, a model utilising the 2 meter mesh refinement seems to perform marginally better in the near wake than the coarser models. A better presentation on the influence of the mesh resolution on the predicted velocity drop behind the discs is given in Figure 6.4b. In the near wake region (3D to 4D downstream distances), the velocity differences between the models are almost negligible.

Further downstream, however, the models' resolutions display immense influence on the flow wake, particularly in the regions between 5D to 15D downstream of the disc. Out of the three resolutions examined in this study, the 2 meter model exhibits the closest agreement with experimental result, while the coarser models (5 meter and 10 meter) significantly overestimate the velocity drop in the wake region. Finally, at 25D

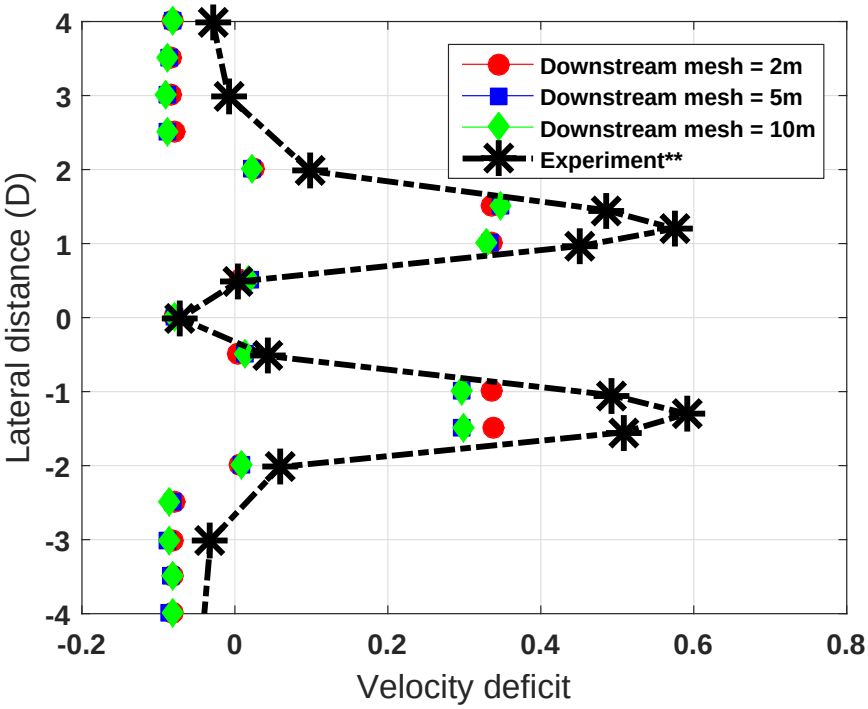

(a) Mid-depth lateral centreline velocity deficit at 3D downstream position.

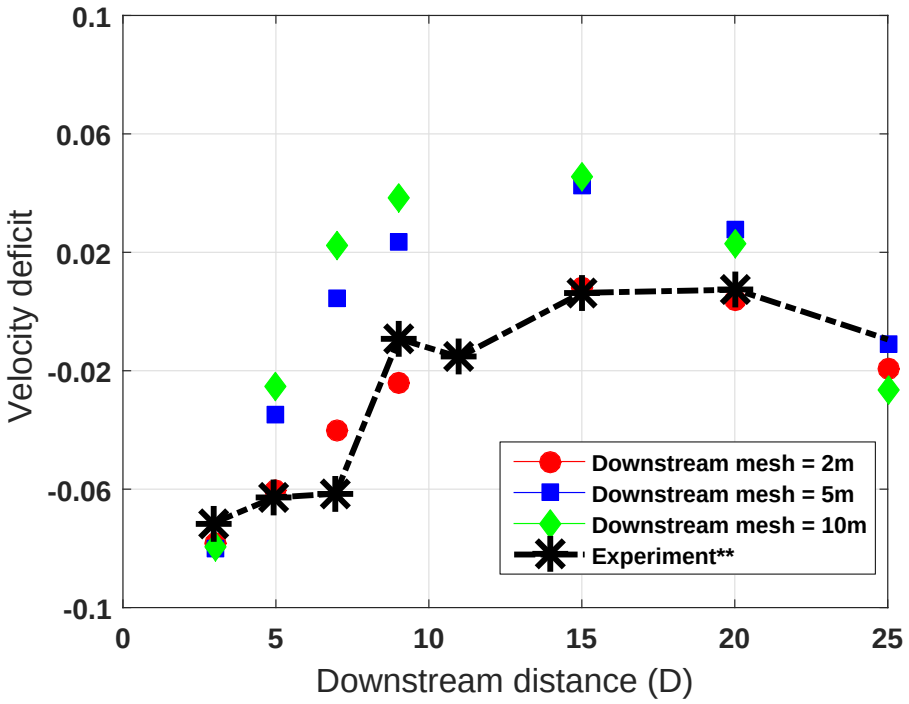

(b) Longitudinal centreline at increasing downstream distance.

Figure 6.4: Lateral and longitudinal centreline velocity deficits observed from the mesh dependency study for the dual actuator disc arrangements. The turbines are set at 1.5D apart and the outputs shown are from y/d = 0.5 (mid-channel depth). The experimental data used in the plots are from the work published by Myers and Bahaj [69].

downstream of the turbine, distinction between the models begin to disappear as the wake dissipates and the flow reaches homogeneity. Based on the results presented, model employing the 2 meter unstructured mesh refinement is used in the following simulations.

6.3.2 Velocity contours of lateral spacing for single row configuration

Following the experimental work conducted by Myers and Bahaj [69], three lateral turbine separations are simulated using the following intervals; 0.5D, 1.0D and 1.5D. Lateral separation is defined as the gap between the turbine's innermost edges, as illustrated in Figure 6.2. The velocity contour for each of the separation distances is shown in Figure 6.5, with reference to the mid-channel depth of the z plane slices (i.e. at 30 meter depth). For the shortest disc gap (0.5D), the flow immediately converges as soon it passes the discs (<3D behind the turbine) and forms a narrow wake that persists up to 48D downstream, as displayed by Figure 6.5(a). Conversely, Myers and Bahaj had reported that the flow from their 0.5D test only merged in the region of about 4D downstream of the fences.

Meanwhile for the 1.0D spacing, the individual wake from the turbine merges close to 7D downstream of the discs, as evidenced from Figure 6.5(b). The wake for the 1.0D separation also shows quicker recovery compared to the 0.5D spacing, where it fully dissipates before reaching 42D longitudinal distance. Finally, full wake separation is produced by the model with furthest disc span (1.5D) as illustrated in Figure 6.5(c). The model with 1.5D spacing clearly shows how the individual wake from each turbine is distinctly formed and does not merge until the flows reaches homogeneity near 25D region downstream of the two discs.

Figure 6.6 further highlights the influence of the disc inter-space on the flow passing through the devices. Plots of the velocity reduction across the lateral distance at 3D behind the disc is presented in Figure 6.6a, where the 1.5D spacing accurately produced the wake behaviour as observed from the experiment. However, the velocity drop between the turbine inter-space behaves quite differently from the published data. The measurement results demonstrate that at 3D downstream of the disc, the velocity between the turbine gap has been reduced by almost 20%, signifying that the flow has already begun to merge.

The predicted velocity, however, illustrates that the wake of the individual turbine is

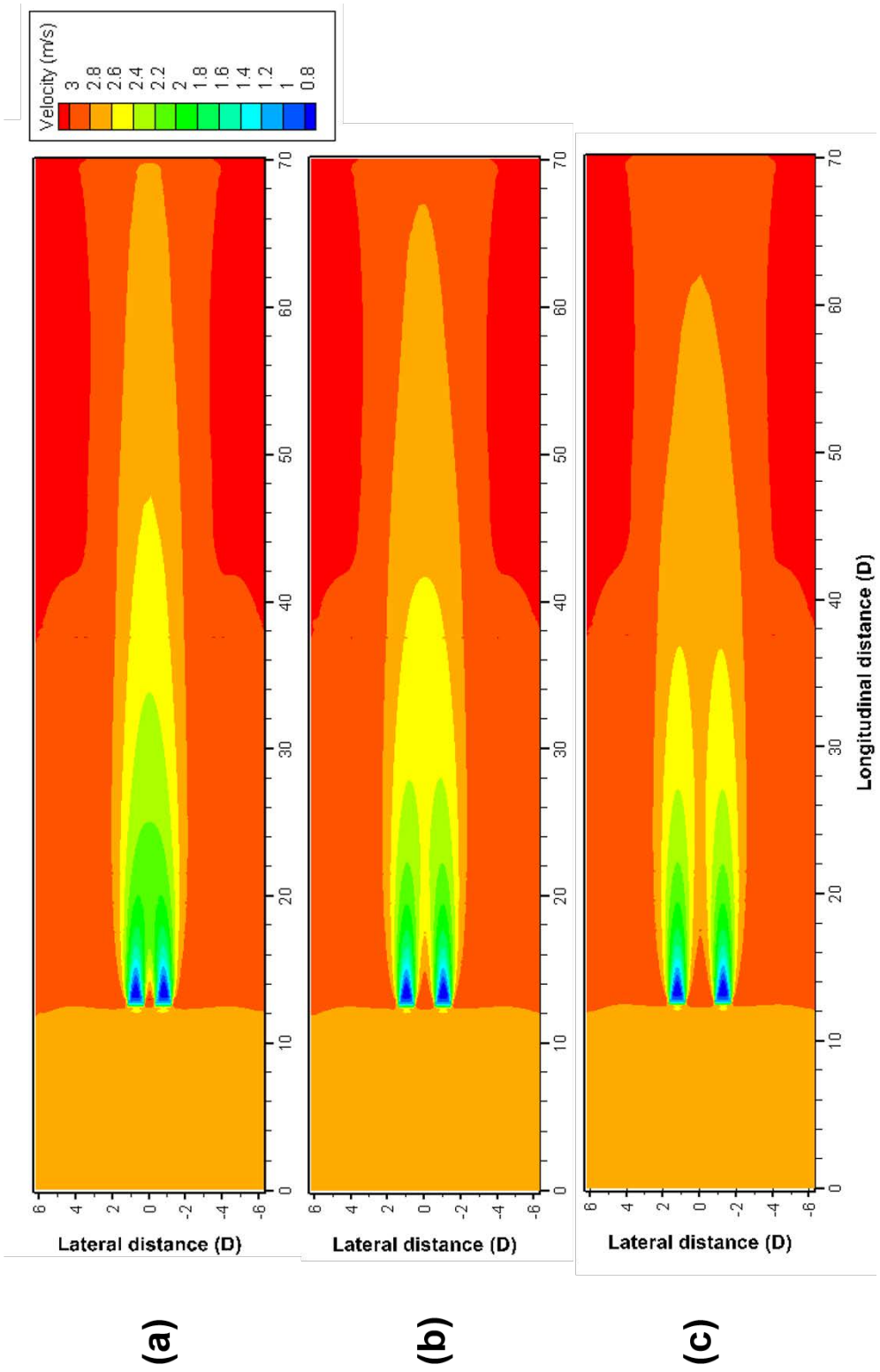

Figure 6.5: Velocity contour (z-plane slices) at mid-channel depth for single row array configuration at varying lateral separations. (a) 0.5D. (b) 1.0D. (c) 1.5D.

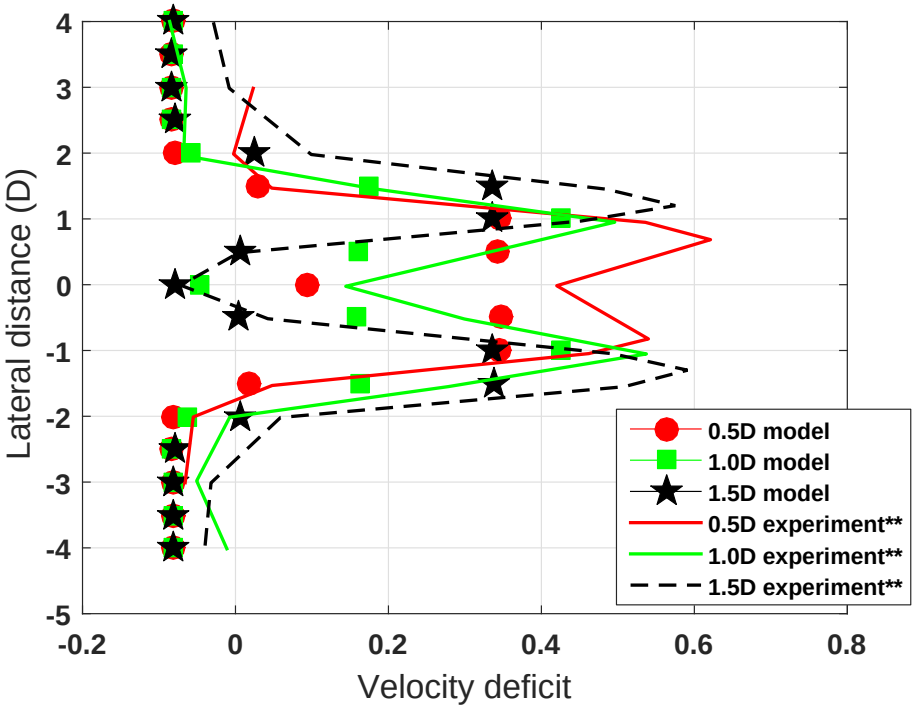

(a) Mid-depth lateral centreline velocity deficit at 3D downstream position.

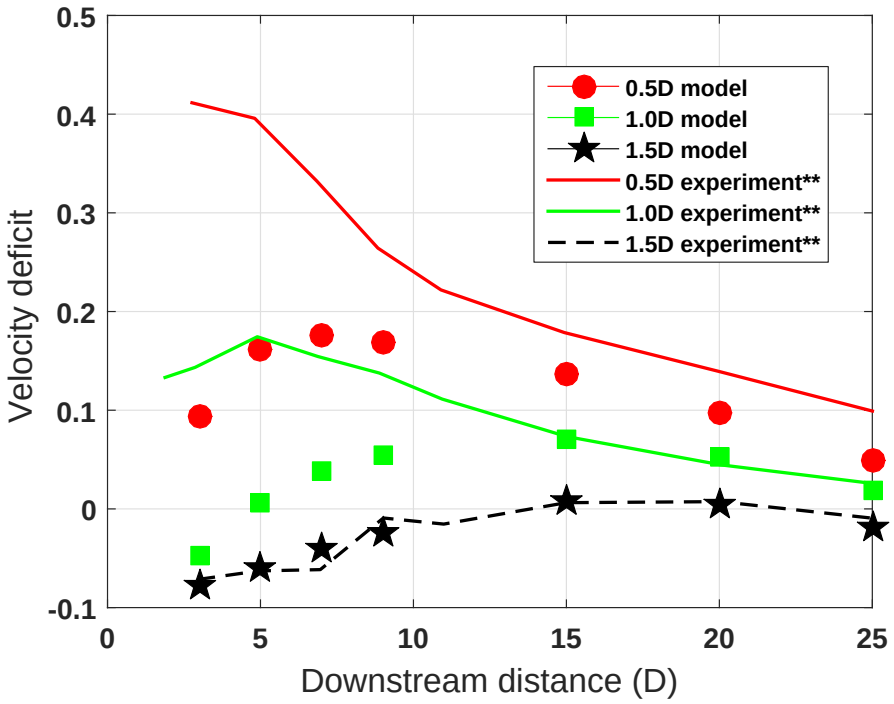

(b) Longitudinal centreline at increasing downstream distance.

Figure 6.6: Lateral and longitudinal centreline velocity deficits observed for various lateral separations used in the dual actuator disc arrangements. The outputs shown are from y/d = 0.5 (mid-channel depth). The experimental data used in the plots are from the work published by Myers and Bahaj [69].

yet to converge at that particular distance. Similar discrepancy is also shown by 0.5D model (closest gap). While the flow passing the turbine outer edges shows accurate correlation with the measurement data, the opposite is exhibited by the progressing flow between the turbine inner space. At 3D downstream of the disc, the 0.5D model shows a deficit of about 10%, indicating that the wake is just beginning to merge. Conversely, the experimental result displays a flow deficit of almost 40%, suggesting that the turbine wake has fully converged at this point.

Next, Figure 6.6b illustrates the velocity deficit for the three models along the longitudinal centreline downstream of the turbines. Once again, the model with the largest disc proximity (1.5D) gives the best comparison against the measurement data, while the other two models severely underestimate the velocity reduction in the region less than 10D downstream of the disc. Moreover, the model with 1.0D spacing experiences short flow acceleration at $3 < D < 5$, before the wakes from the two turbines merge at 5D downstream. On the other hand, flow for the 0.5D model quickly merges right after passing through the disc, as indicated by the positive velocity deficit in the near wake region.

Furthermore, it can also be observed from Figure 6.6b that the wakes for both 1.0D and 0.5D models are still recovering past 25D positions. Two remarks can be made upon this observation. First, models utilising the 0.5D and 1.0D spacing cannot accurately replicate the near wake characteristics since the increased ambient turbulence intensity aids the wake recovery, hence preventing wakes from merging until further downstream. Secondly, assuming that staggered array configuration is used, putting the upstream turbines too close to each other will cause huge flow retardation between the inter-space of the discs. This in turn will cause longer wake recovery, which ultimately may affect the performance of downstream turbine(s).

6.3.3 Configuration of two rows array

In this section, the inter-space between the first row turbines was set to 1.5D, while the single disc in the second row was located 3D downstream from the middle spacing of the front row. The influence of upstream turbines on the wake formation due from the downstream disc is highlighted in Figure 6.7, where velocity reduction across the lateral distance is plotted for several downstream locations. Once again, results from the models portray excellent conformity against the experimental set up in [69].

Crucially, the presence of a downstream turbine has a noticeable impact on the upstream wake, where it causes slight velocity reduction of about 5%. This observation

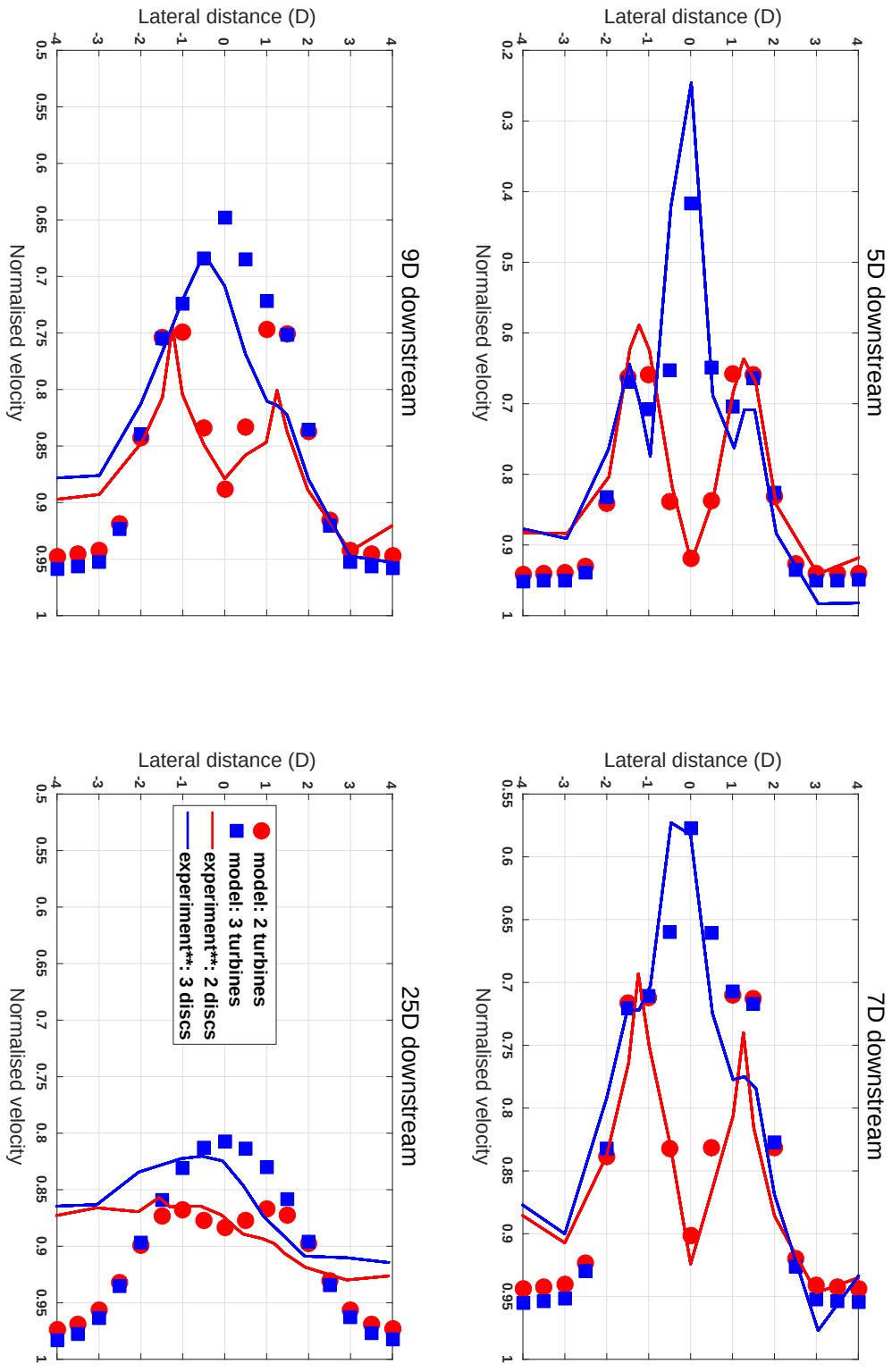

Figure 6.7: Comparison of lateral mid-channel depth velocity reduction between two and three discs arrangement at increasing downstream distances. The experimental data used in the plots are from the work published by Myers and Bahaj [69].

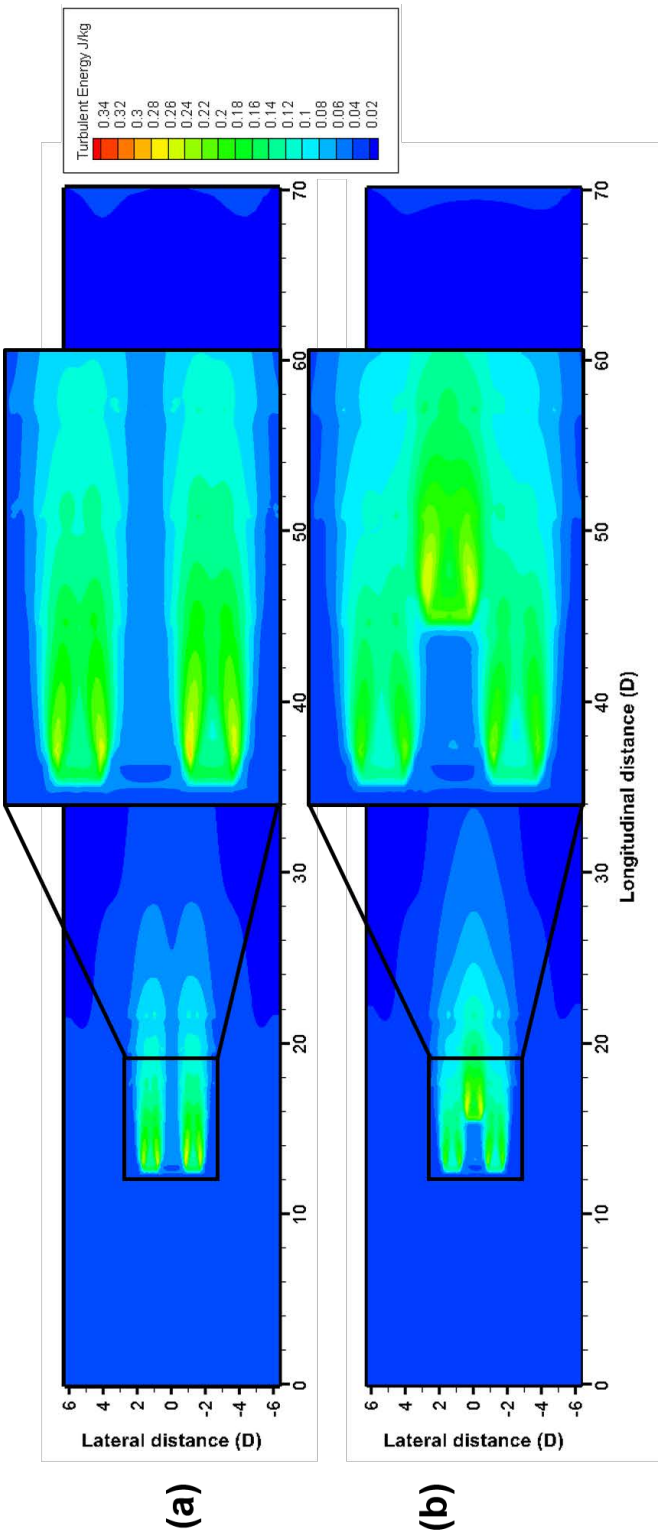

Figure 6.8: Horizontal contour plot for turbulent kinetic energy at mid-channel depth showing a diminishing flow return by the upstream turbines due to the presence of a downstream disc. (a) single row set up (b) two rows configuration.

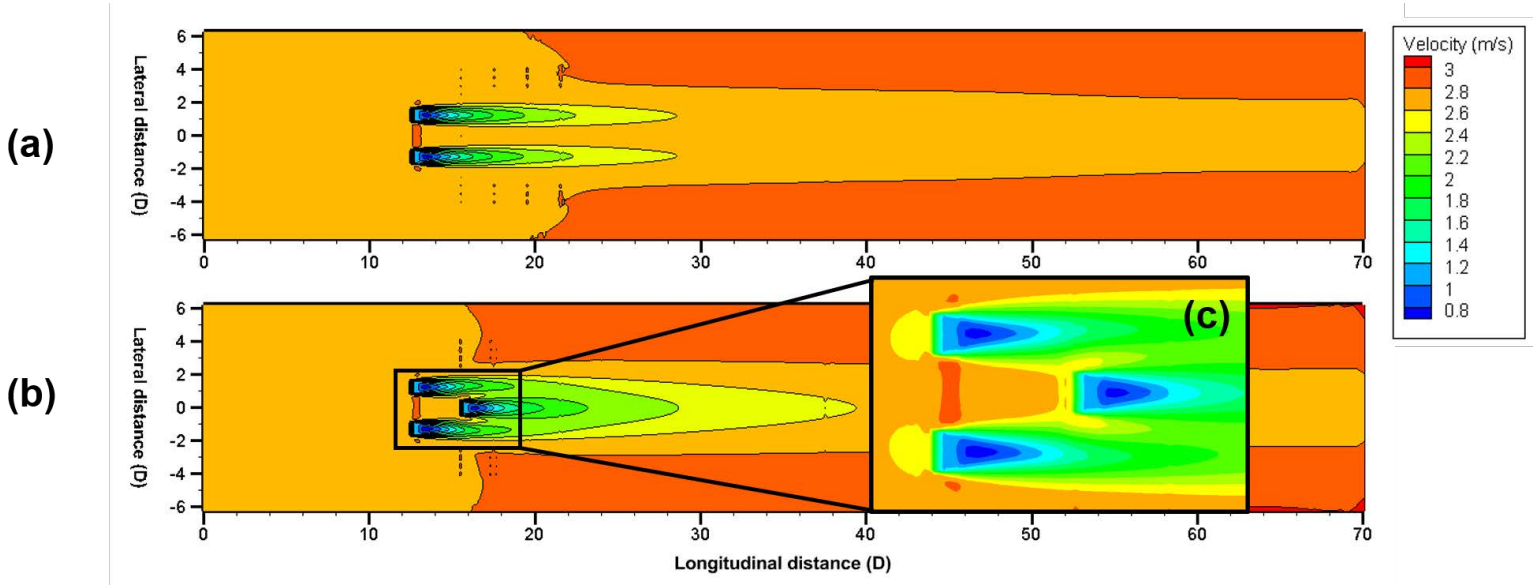

Figure 6.9: Horizontal contour plot for stream wise velocity at mid-channel depth. (a) single row set up. (b) two rows configuration. (c) magnified view of flow interactions caused by the three discs arrangement.

is also corroborated by the turbulent energy contour shown in Figure 6.8 for both two and three discs arrangement. In particular, the addition of a single device in the second row has visibly reduced the fluid kinetic energy that passes through the edges of the front row turbines, as demonstrated by Figure 6.8(b). Nonetheless, the influence of the downstream disc on the upstream wake is becoming less apparent in the region between 7D and 9D, as evidenced from Figure 6.7.

Further clarification on the impact of adding additional row in the arrays is provided by Figure 6.9. As expected, the presence of the downstream device causes the upstream wake to converge and expand further downstream, as demonstrated by the 25D downstream plot in Figure 6.7 as well as the contour plot in Figure 6.9(b). Furthermore, the use of 1.5D spacing (as per experimental set up) apparently helps to accelerate the flow passing through the downstream disc due to the localised duct-effect (i.e. blockage effects)[85, 163], and is clearly indicated by both contour plots in Figure 6.8(b) and Figure 6.9(b).

6.3.4 Large spacing configurations

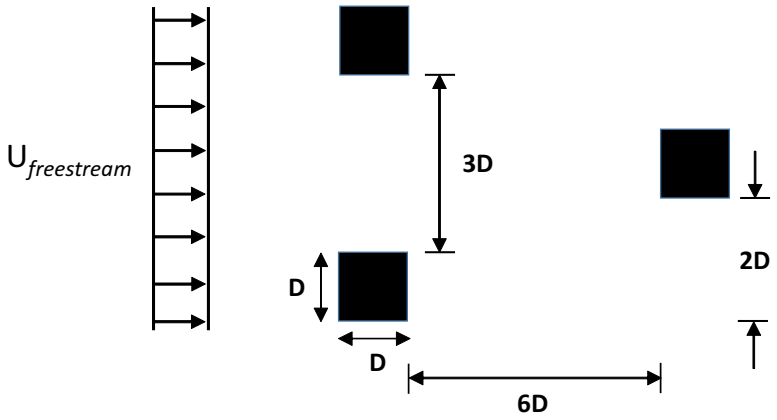

Figure 6.10: Turbines' inter-space for a more realistic arrays configuration.

In most experimental set up, the arrangement of the porous discs will be constrained by the size of the physical flume, meaning that the spacing between the turbines is relative to the width and length of the channel. This is unavoidable since certain properties must be conserved to ensure the experiment behaves in a realistic manner, and is usually parameterised by two dimensionless variables – the Froude number and the Reynolds number. The Froude number is used when gravitation forces are predominant in the channel flow, whereas the Reynolds number is adopted when viscous forces are

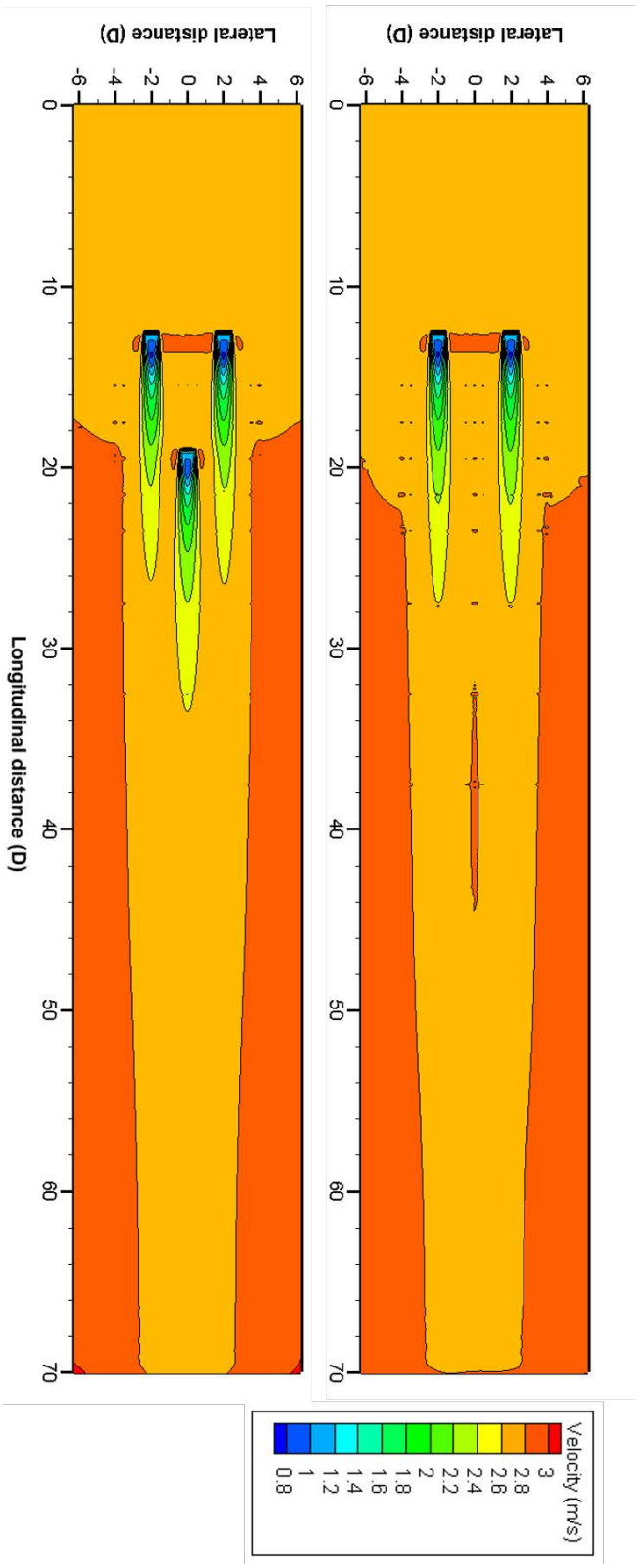

Figure 6.11: Horizontal contour plot for stream wise velocity at mid-channel depth for large turbines spacing (3D lateral and 6D longitudinal). (a) single row set up. (b) two rows configuration.

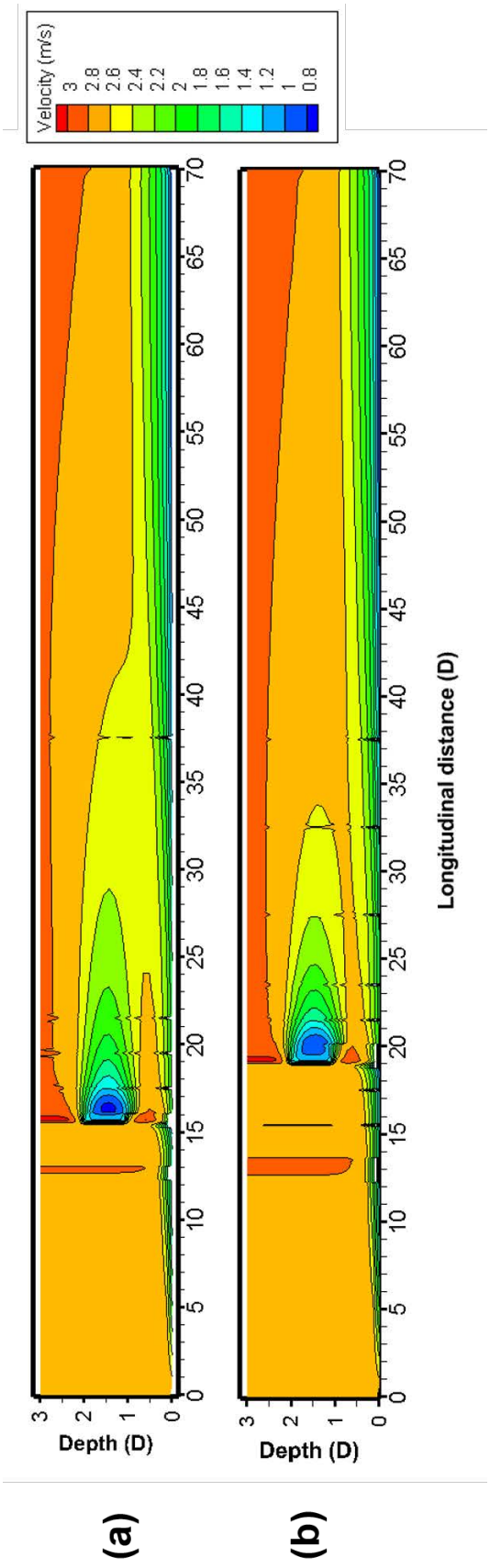

Figure 6.12: Velocity contour plot (y-slices) of the downstream device at mid-channel width for (a) close turbine proximity (1.5D lateral and 3D longitudinal) (b) larger turbine spacing (3D lateral and 6D longitudinal).

predominant in the channel flow.

Since it is almost impossible to make Froude number and Reynolds number identical in model and prototype, the use of these dimensionless parameters should be judged on a case by case basis. Moreover, discrepancy between the model and full scale Reynolds number is generally acceptable so long as both the model and full scale Reynolds numbers lie within the same turbulence classification, and the Froude similarity is maintained [181].

To examine a case of a more realistic turbine inter-space, an arrangement used by Christian and Vennell [182], as illustrated by Figure 6.10, is simulated. The lateral and longitudinal distance between the turbines are set to 3D and 6D respectively, which is doubled than the gap used previously (refer to Section 6.3.3). Figure 6.11 displays the velocity contour plot for both single and two rows arrangements of this new arrays layout. The larger lateral spacing (3D) in the first row shows similar wake recovery region as previously demonstrated by the close turbine proximity (1.5D), where individual wake from each turbine can be clearly seen in Figure 6.11(a).

Nonetheless, the dissimilarity between longitudinal distance of 3D and 6D are very apparent. Shorter lengthwise gap caused the upstream wake to merge with downstream turbine, hence forcing the flow to reach homogeneity further downstream (see Figure 6.9(b)) as a result of momentum conservation. Conversely, when using a much larger longitudinal spacing (i.e. 6D), the wake convergence happens at a much shorter distance since downstream turbine does not interfere (i.e. does not merge) with the upstream wakes as demonstrated by Figure 6.11(b).

In addition, Figure 6.12 presents a better wake convergence comparison (y-slices velocity contour) between the two-tested longitudinal distance at the downstream device position. The model with 3D length-wise gap shows an extended wake region (Figure 6.12(a)), where the flow only showing sign of homogeneity approaching the 44D region. On the contrary, the 6D spacing (Figure 6.12(b)) accurately illustrates a much shorter wake region, in which the flow fully recovers as it reaches the 34D point. Faster wake convergence is desirable for two reasons. First, it allows more power to be extracted from the downstream turbine due to a higher stream-wise velocity caused by the non-merging upstream wake. Secondly, as more power per turbine can be removed from the flow, the number of devices in the arrays can also be reduced, hence presenting a more attractive economics value for the developers.

6.4 Non-hydrostatic models for multiple turbines set up

6.4.1 Two row arrays configuration

Now that the wake characteristics from the hydrostatic models have been successfully simulated and validated, this section will then examine the outputs produced using the non-hydrostatic solvers in modelling the flow interactions of the devices in the first row with a downstream disc. A similar array arrangement as discussed in Section 6.3.3 is once again used for the simulation, in which the lateral distance between the first row turbines is fixed at 1.5D, while the single disc in the second row is located 3D downstream from the middle spacing of the front row. Figure 6.13 illustrates the comparison plots between the non-hydrostatic models and experimental data for several lateral velocity profiles (at 5D, 7D, 9D and 25D positions relative to the upstream row), where the effects of inserting a downstream disc can be clearly seen.

Similar to what was observed from the hydrostatic model, at 5D downstream, the centreline velocity of the upstream wakes is slightly accelerated by the presence of the downstream disc, and this is matched perfectly by the actuator disc model. However, the three-disc model shows quite a dramatic overestimation of about 15% when compared with the experimental data, signifying that the model predicted a faster moving flow in the area directly behind the actuator fence. Next, at 7D downstream, the generated wake due to the presence of downstream disc agreed closely with the measured data, except for the upstream flow profile. At this location, the centreline wake acceleration shown by the measurement data for three-disc set up it is no longer apparent to the numerical model.

This trend is also apparent further at 9D location, where the presence of downstream device no longer has significant influence on the upstream centreline wake velocity and is correctly predicted by the numerical model. Nevertheless, from the 9D plot, it can be seen that the actuator disc model for the three-disc arrangement overestimates the downstream wake velocity by about 5%. Furthermore, the persistence of the wake generated by the two row arrays is more pronounced further downstream, as highlighted by the 25D plot. Because the wake from the upstream and downstream devices eventually merged to form a single wake that is wider and longer, the recovery distance will also be extended before it reaches ambient velocity.

This observation agrees with findings in [183], which also showed an expanded overall

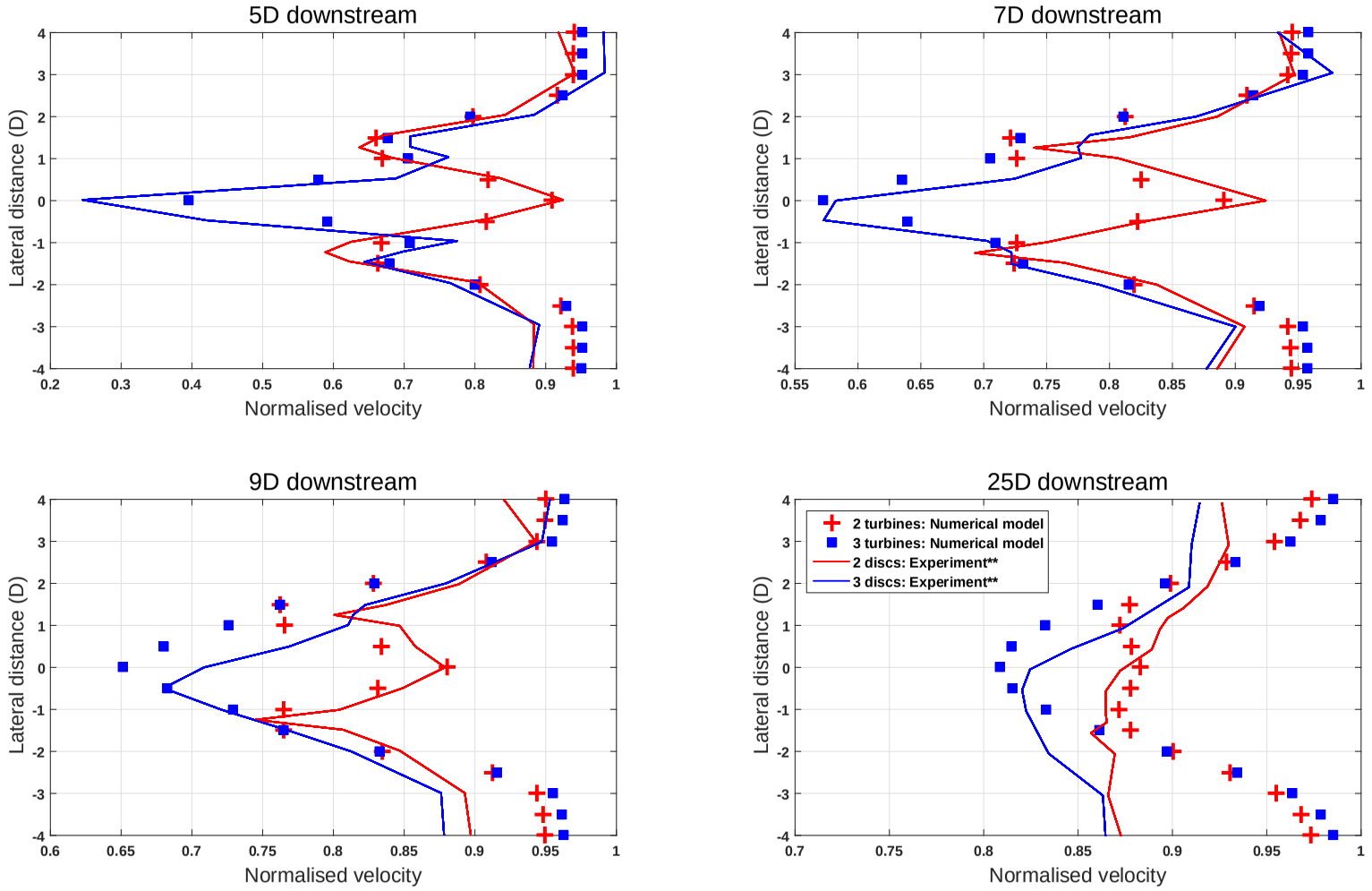

Figure 6.13: Comparison of lateral mid-channel depth velocity reduction between two and three discs arrangement at increasing downstream distances (non-hydrostatic models). The experimental data used in the plots are from the work published by Myers and Bahaj [69].

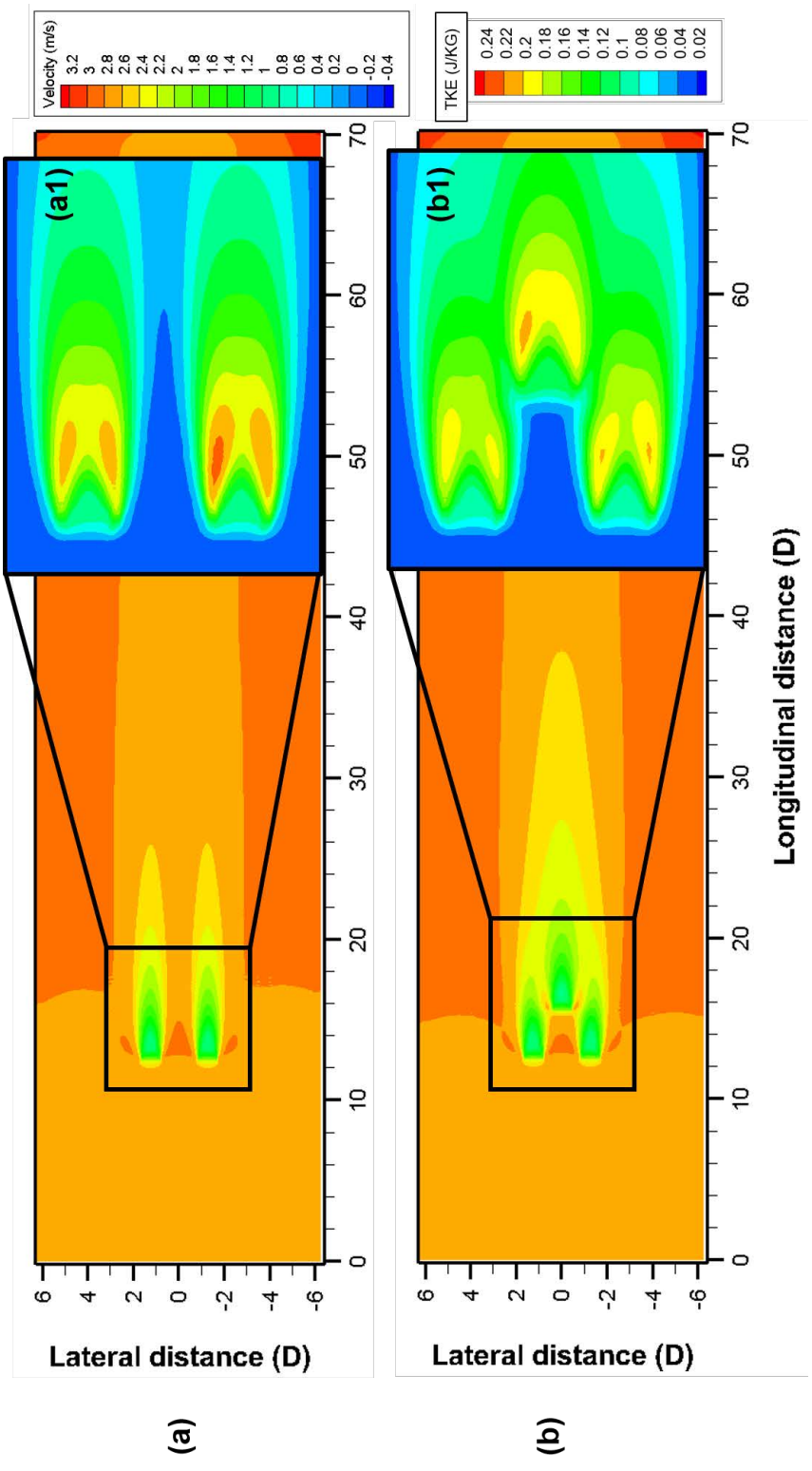

Figure 6.14: Horizontal contour plot (z-plane slices) at mid-channel depth for stream wise velocity and turbulent kinetic energy (TKE). (a) two turbines set up with lateral distance of 1.5D. (b) three turbines configuration with one staggered downstream disc. (a1) magnified view of the TKE contour for single row arrangement. (a2) magnified view of the TKE contour for three turbines configuration (non-hydrostatic models).

wake region due to mixing with the wake of adjacent turbines. In general, the numerical model manages to reasonably replicate this flow characteristic, in which the simulated wake from the two-disc arrangement already showing sign of flow recovery at 25 downstream. Despite the good agreement observed with the measured data, the simulated three-disc arrays still shows signs of slightly larger velocity deficit (about 5% more) than the experimental set up.

Another obvious disparity that can be observed from the plots in Figure 6.13 is for the near wall velocity data, specifically between -2 < D < -4. This imbalance shown by the experimental data is clearly visible from the 5D plot, and can be seen gradually increasing until far downstream at 25D region. Nonetheless, this is a common phenomenon for any wide circulating flumes, and is attributed to a non-uniform lateral flow distribution [23, 69, 164].

Moreover, the effect of a downstream disc on the wakes formed by the upstream discs can be better presented using the horizontal contour plots in Figure 6.14. The wake from the two-turbine arrangement (i.e. single row) displays full recovery upon reaching 26 longitudinal distance, as shown by Figure 6.14(a). Conversely, for a similar configuration using the hydrostatic solvers, the recovery distance was slightly longer by about 2D length. As for the three discs arrangement (Figure 6.14(b)), once again the hydrostatic model demonstrated a slightly longer recovery distance than the non-hydrostatic model (40D vs 30D).

Nevertheless, both hydrostatic and non-hydrostatic models are able to characterise the localised duct-effect [34] experienced by the downstream device due to enhanced flows through the gap. The blockage effect causes the solitary device to experience accelerated flows as it intercepts faster moving fluids induced by adjacent discs, meaning more energy is captured from the flow compared with the upstream devices [184]. This observation is accurately replicated by the numerical model, as demonstrated by the magnified turbulence kinetic energy plots in Figures 6.14(a1) and (a2). By comparison with the single row arrangement, the presence of the downstream device visibly reduces the kinetic energy from the flow that passes through the edges of the front row turbines, while at the same time increasing the turbulent kinetic energy of the flow bypassing the single disc in subsequent row.

All things considered, the non-hydrostatic models examined in this section demonstrate an almost indistinguishable outputs from the default hydrostatic models, which ratifies findings from the single turbine study. Not only that, both models have also illustrated excellent numerical output which matched closely with the experimental

results, and give credence to the applied source term in this study.

6.5 Discussion

A preliminary study to examine the effectiveness of the RANS actuator disc approach for simulating flow interactions within a small tidal arrays has been presented, where the modelled output was validated with experimental data from literature. The main findings from this chapter are summarized as follows:

- It has been demonstrated that the applied actuator disc source term was sufficiently accurate to simulate the complex interactions between multiple tidal devices, where the wake characteristics from a physical scale set up have been accurately replicated for both two and three disc arrangements.
- As with the single turbine set up discussed previously in Chapter 5, it has been illustrated that the model's outputs were highly susceptible to changes in the density of the mesh. The use of coarser unstructured meshes within the array's deployment region tended to underestimate the predicted velocity drop behind the disc. This could be due to the approximations and averaging used in the RANS equations, where the size as well as the number of cells in any given CFD domain can directly affect the outputs of a numerical model.
- Further, a diminishing flow return has also been successfully exhibited by the upstream turbines upon the addition of a downstream device. This confirms findings from literature, where the presence of downstream turbine is known to have an influence on both the flow condition as well as the wake formation experienced by the upstream devices [77].
- Similarly, the model has also been able to reproduce the blockage effect experienced by the downstream disc, where an increase in the turbulent energy around the edges of the device was accurately simulated.
- While both hydrostatic and non-hydrostatic assumptions have been tested, the lateral velocity outputs from the two models were found to be rather comparable to one another. Similar occurrence was also observed in the single turbine study, although it has been confirmed that the influence of non-hydrostatic solvers was more prominent in solving the turbulent properties close to the channel bed.
- In general, although the outputs from the models have demonstrated excellent comparison against the experimental data, some small variations can still be seen from plots. However, this is to be anticipated since some of the input parameters for the numerical models (e.g. turbulent levels) were approximated based on

the results presented in the published literature. Consequently, some margin of uncertainty and inaccuracy was introduced into the model.

- Furthermore, there are also some limitation for any numerical model to reproduce the exact characteristic of the flow within any experimental flume. For instance, the non-uniform lateral flow distribution observed from the published data is recognised as one of the inherent characteristics of a wide circulating flume is, hence was not feasible be emulated by the numerical model used in current study.

In brief, the studies conducted in Chapters 5 and 6 have provided evidence on the capability and robustness of the applied momentum source term in simulating the presence of tidal turbines using the actuator disc approach in an idealised channel. Naturally, the step would involve implementing the (adapted) momentum source term into an ocean scale model and examining the sensitivity of the numerical parameters involved. However, based upon the findings documented for the small channel studies, two concluding remarks can be made.

While it has been presented that the model outputs are susceptible to changes in mesh sizes used in the domain, it remains to be seen whether such a refined unstructured grid density (~2 meter) can be used in a regional scale simulation. Identically, the size of structured grid to be employed as enclosure for the actuator discs are also of interest in this research. Although implementing a 2 meter grid in this simple channel study was possible considering the scale of the domain involved, questions remain whether similar grid size can still be employed in a substantially large ocean scale domain.

Chapter 7

Implementation of the Actuator Disc Approach in a Regional Scale Model

The work presented here translates the knowledge and experiences gained from conducting the small scale actuator disc studies as elaborated in Chapters 5 and 6 into the simulation of an actual size tidal turbine at a commercial deployment site within the Inner Sound region of the PFOW. More importantly, the methodology and model set up in this chapter also follows the guidelines provided by EMEC [26] in an effort to provide realistic working and hydrodynamic conditions experienced by the devices in operation.

The primary aim of this chapter is to examine the robustness, as well as the sensitivity of the applied momentum source term in representing a 16 meter rotor diameter tidal turbine in a 3D ocean scale model. Criteria used in deciding the deployment locations of the turbines are presented, along with the detailed set up for the actuator disc models. Besides, some of the constraints faced in this research work are also discussed.

To facilitate data interpretation, the models' outputs are presented as velocity contours, plots of velocity deficit, as well as graphs of normalised velocity in lateral direction. Since published material on the implementation of actuator disc approach within a regional scale model is still scarce, it is hoped that this study could provide some evidence, guidance and examples of suggested best practice in effort to fill the research gap.

7.1 Study area

At the time of writing, the MeyGen tidal turbine array, planned for the Inner Sound region in the PFOW is likely to be the first commercial tidal energy array to be installed anywhere in the world. With current speeds up to 6 m/s recorded during spring tide, the MeyGen project is espected to extract up to 400 MW of energy resources available in the region [113]. With imminent deployment of tidal turbines and marine energy devices in general at the location, various studies have examined the potential environmental impact upon the deployment of large numbers of tidal devices - be it on ecological, socio-economics or sediment transport [12, 19, 159, 185, 186]. Consequently, it is also imperative to look at how the tidal turbines are represented in such models, which is the aim of this study.

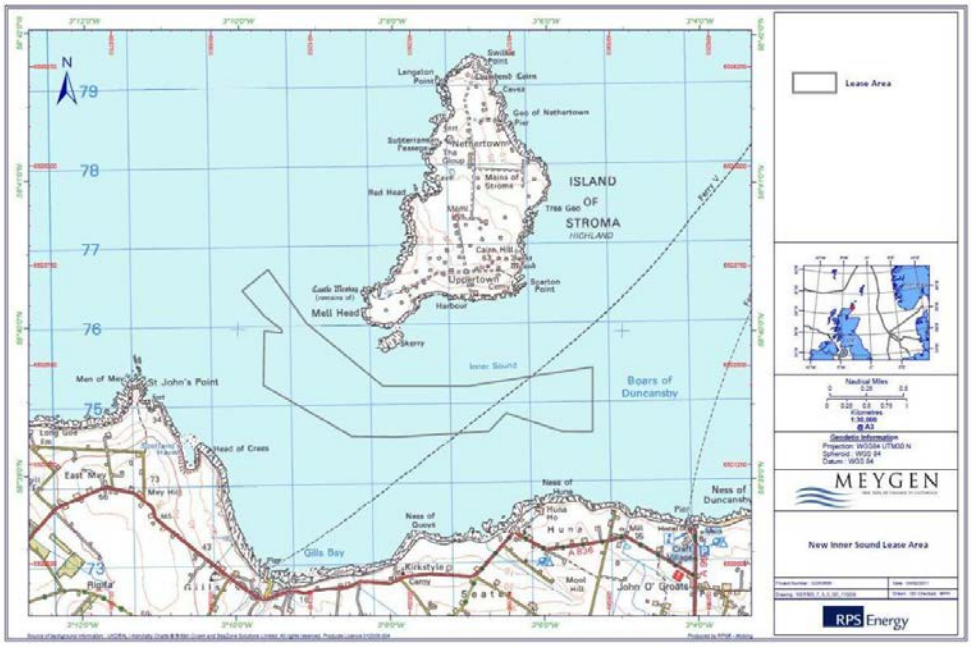

Figure 7.1: The Crown Estate's Inner Sound lease area as published in the Environmental Impact Assessment Scoping Report for the MeyGen Tidal Energy Project [14].

Deployment location for tidal devices examined in this study (i.e. in the Inner Sound) was estimated based upon the following criteria:

(a) Firstly from the Environmental Impact Assessment Scoping Report for the MeyGen Tidal Energy Project, where the updated Inner Sound lease area from The Crown Estate is shown in Figure 7.1.

(b) Instead of conducting numerical simulations for the whole tidal farm as planned

by the MeyGen, the purpose of this study is to demonstrate the methodology in representing a full size tidal turbine in 3D model within a very small array. As such, only small footprint within the Inner Sound domain is required to represent the turbines. Figure 7.2 illustrates the mean velocity contours of the Inner Sound region from Telemac3D model, from which the highest mean velocity is found to occur just south of the Stroma island. In particular, this observation agrees with the proposed location for tidal stream energy extraction in the Inner Sound as reported in [16, 187, 188]. For this reason, the turbines will be implemented at the location with highest velocity as displayed in Figure 7.2.

(c) Apart from fast current flow, local topography also plays significant role in deciding the exact deployment of the devices. From the guideline provided by EMEC [26], a minimum of 5 meter top and bottom (or 25% of the water depth, whichever is greater) clearance for the capture area is recommended for the following reasons:

- to allow for recreational activities
- to minimize turbulence and wave loading effects on the TECs
- to minimise damage from floating, as well as damaging materials that are moved along the seabed by the currents
- to reduce shear loading from the bottom boundary layer on the TECs

Alternatively, Nova Innovation Ltd has recommended that the minimum clearance of the turbine from Mean Low Water Springs (MLWS) to be 15 meter [189]. Hence, it becomes clear that finding a spot with suitable water depth is crucial in getting an accurate representation of the devices across water column.

More significantly, the chosen location must be able to accommodate the proposed tidal turbine design by MeyGen, as displayed in Figure 7.3. According to the diagram, the radius of the proposed turbine design is between 8 - 10 meter, with minimum top clearance of 8 meter. The height of the hub from the seabed meanwhile is between 13.5 - 16 meter. Moreover, since the average depth in the Inner Sound is about 30 meter, shown by both the sea floor elevation contours and the z-direction slicing of the bathymetry at the area of interest in Figure 7.4, it can then be approximated that the hub of the turbine will be located at the center of the water column (~15 meter depth).

Using this information, the subsequent task is to find the optimal location that satisfy the deployment criteria (i.e. currents speed and topography), as well as the proposed

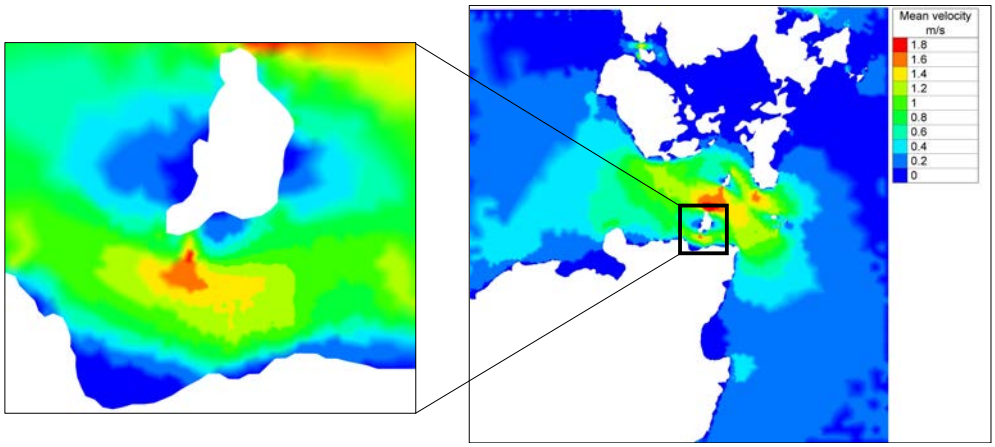

Figure 7.2: Mean velocity contour of the Pentland Firth and Orkney Waters produced using Telemac3D model. The inset displays a closer view of the predicted mean velocity in the Inner Sound region.

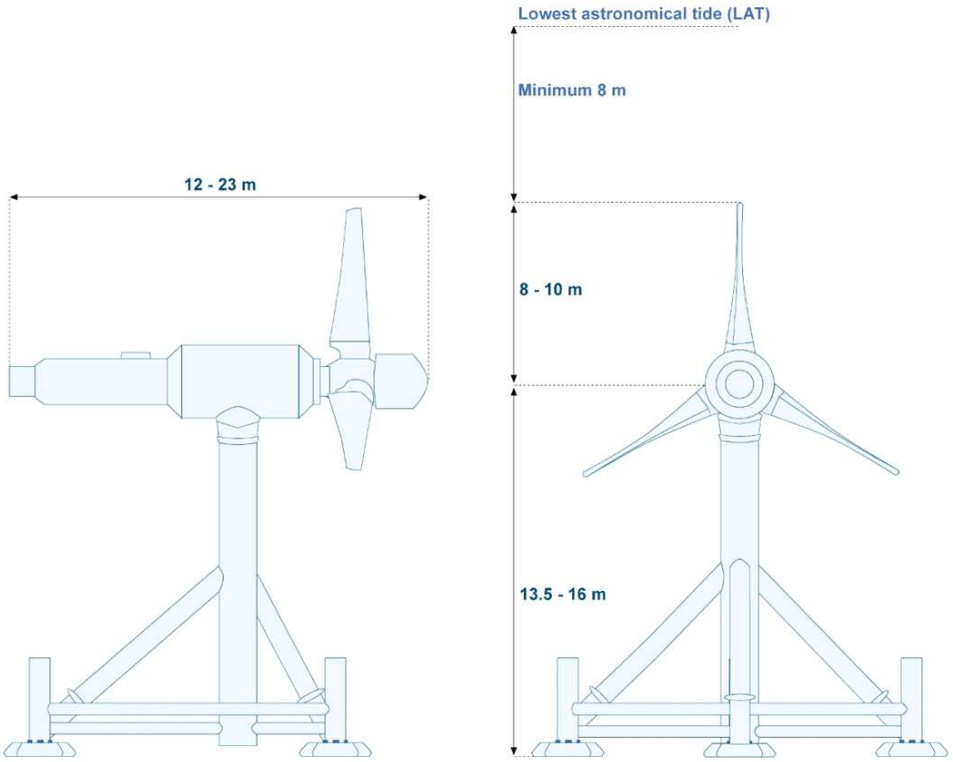

Figure 7.3: Dimension of the proposed tidal turbine design by MeyGen [190] to be deployed in the Inner Sound of the Pentland Firth. This turbine diagram is developed by way of collaboration between MeyGen and turbine technology developers - Atlantis Resources Limited (ARL) and Andritz Hydro Hammerfest (AHH). This diagram was reproduced from the MeyGen webpage [191].

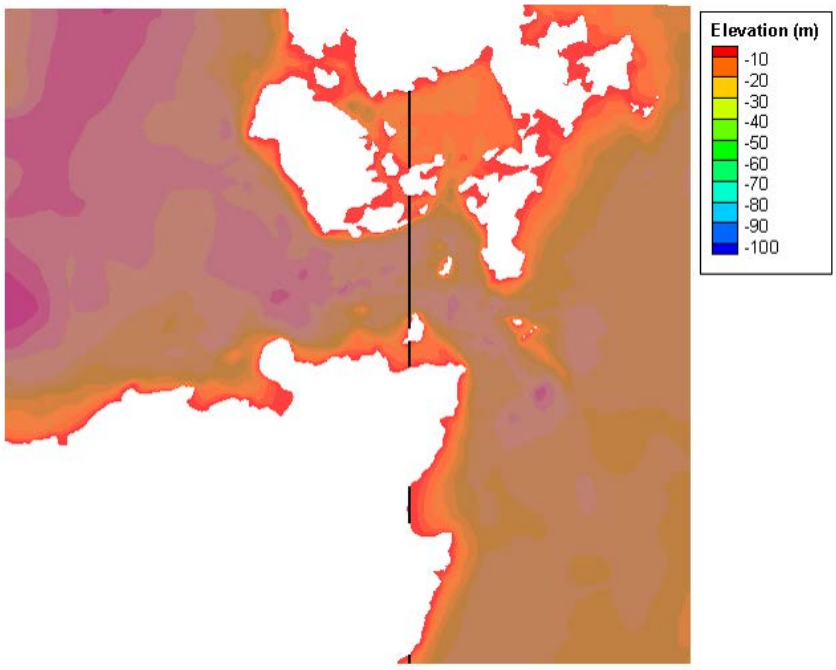

(a) Elevation contour for the PFOW using bathymetric dataset supplied by the TeraWatt consortium [133].

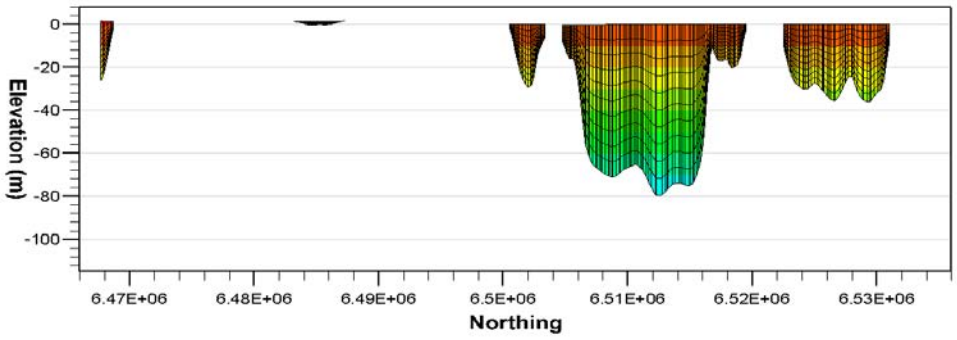

(b) Bathymetric slicing (z-direction) for the line shown above. Water depth for the Inner Sound region is depicted by the elevation contour in the upper left hand corner.

Figure 7.4: Sea floor elevation contours and bathymetric slicing across the Pentland Firth and Orkney Waters.

tidal turbine design (i.e. suitable depth to fit the devices with enough top and bottom clearance). More importantly, based on the information available, it is decided that the size of the tidal turbines to be simulated in this study is 16 meter in diameter, instead of the commonly cited 20 meter dimension in literature (e.g. [192]).

The rationale behind this decision is as follows: firstly, with an average water depth of 30 meter at the Inner Sound region, simulating a turbine with 20 meter rotor diameter implies that the top and bottom clearance of the device's capture area to be 5 meter or less. Combined with a highly uneven and complex topography in the area [193], it is highly possible that simulating a device of this size (i.e. 20 meter) can contribute to numerical instability due to how the actuator disc and vertical layers are defined in the model.

Section 7.2 provides details of the actuator disc representation and mesh transformation. Additionally, a small bottom clearance margin may also have an adverse effect on the numerical outputs due to the influence of the bottom boundary layer. Consequently, this might cause the computation of the wake characteristics of the model, which is the main focus of this chapter, to be rendered as fruitless. Above all, the chosen rotor diameter (i.e. 16 meter) to be used in this study is well within the range of the proposed dimension for the MeyGen devices, as illustrated in Figure 7.3.

To narrow down the exact deployment sites to be used in the model that matched the previously discussed requirement, bathymetric slicing was performed at several areas across the region with highest mean velocity as shown in Figure 7.5. In total, five positions were investigated in finding the optimal spots with suitable depth for implementing several 16 meter diameter tidal devices. For ease of illustration, three lines were employed in the bathymetric plots. The single vertical line (i.e. south to north alignment) was used to display the topography's cross section at each of the selected sites.

Conversely, the two horizontal lines (i.e. east to west alignment) was utilised to denote localities that falls within the minimum 30 meter depth requirement. Using Figure 7.2 as guide, which shows the mean velocity contour in the area of interest, Positions 1, 4 and 5 can then be eliminated from potential deployment sites to be used in the model since they demonstrated the lowest average velocity (i.e. about 1.4 m/s) among the five spots inspected.

In deciding between Positions 2 and 3, it is essential to properly examine the bathymetry gradient at each locations. From experience, it is recommended to avoid implementing

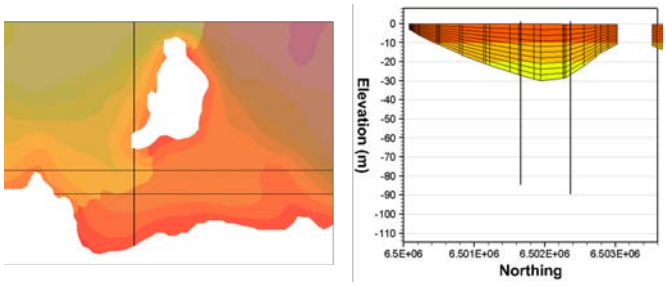

(a) Position 1

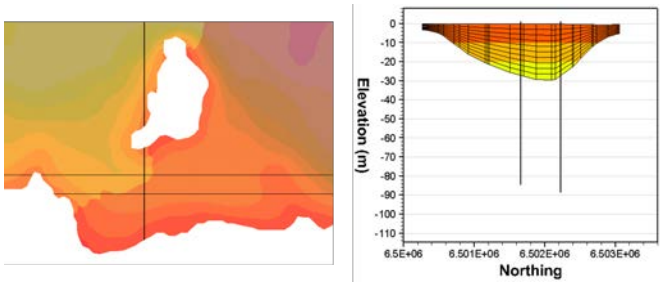

(b) Position 2

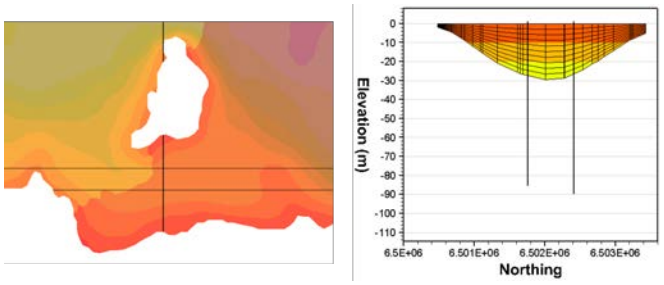

(c) Position 3

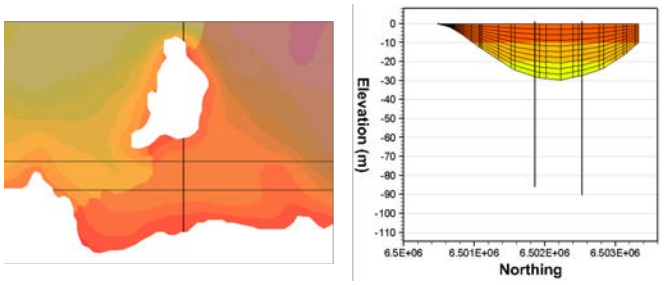

(d) Position 4

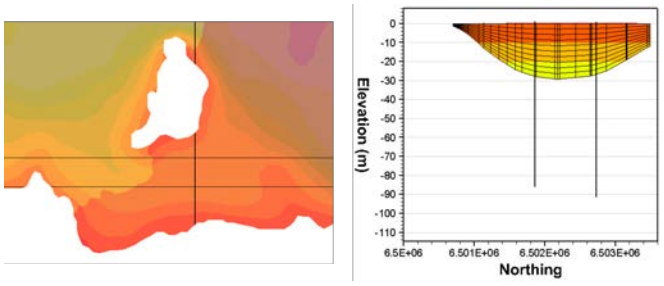

(e) Position 5

Figure 7.5: Bathymetric slicing performed at several locations across the Inner Sound region to find the optimal location for implementing the actuator disc.

an actuator disc at a locality with steep topography gradient since it may contribute to a number of problems. First, it limits where a disc can be placed, especially if the device swept area is located too close to the bank of the channel. This in turn may potentially induce numerical instability into the applied source term, more so if the actuator disc's swept area accidentally touches/crosses the channel edge. Secondly, the sharp gradient that is adjacent to one of the turbine's edges will most likely accelerate the flow passing through the device, albeit unevenly, hence influencing the numerical outputs.

For these reasons, Position 3 was chosen as the optimal spot for implementing the actuator disc in this study since it demonstrates a slightly better gradient distribution on both sides of the Inner Sound banks, as exemplified by Figure 7.5c, when compared with Position 2. For reference, Position 3 can accommodate a maximum of 11 tidal turbines in each rows, using the staggered configuration as suggested by Christian and Vennell [182].

7.2 Model set up

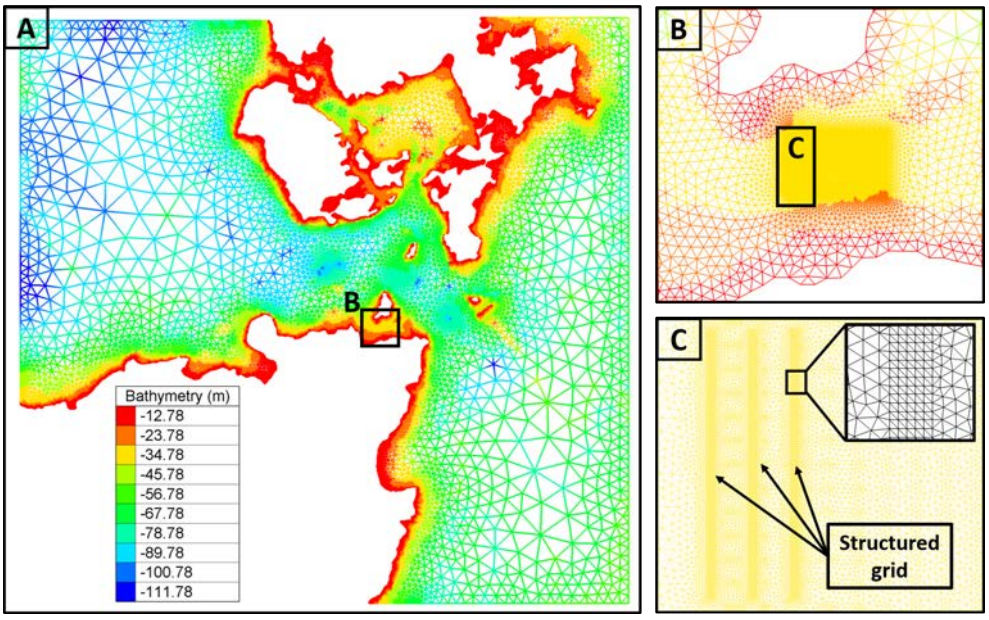

Figure 7.6: (A) Computational domain of the PFOW used in the application of the actuator disc source term. (B) Close up view of the location for deployment of turbines within the Inner Sound. (C) Arrangement of the imposed structured grid (three rows) within the numerical domain. Mesh integration between the structured and unstructured grid is illustrated by the inset in diagram (C). For ease of illustration, the colour of the mesh within the inset is changed to black.

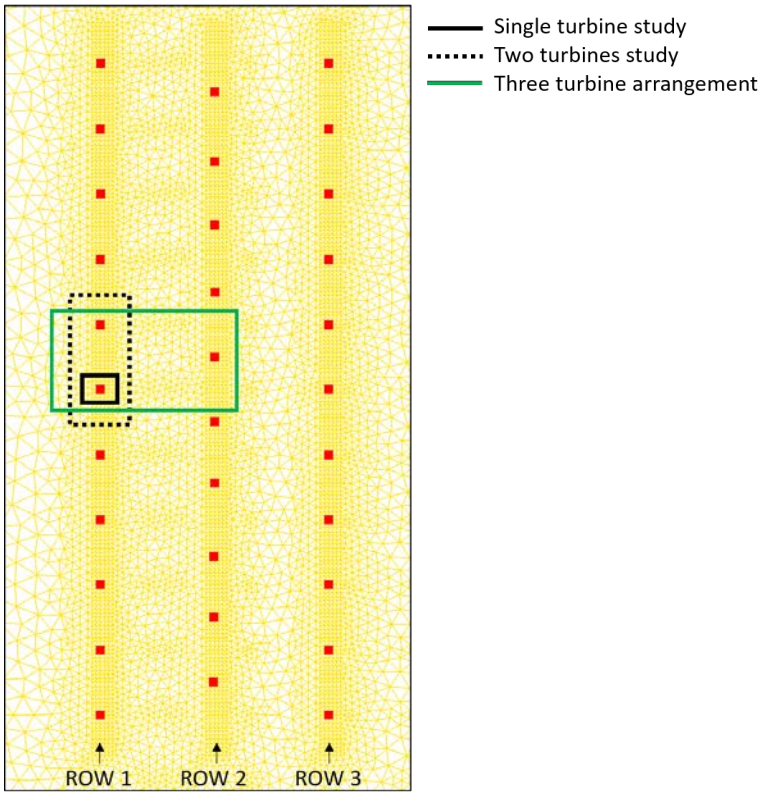

Figure 7.7: Configuration of tidal devices within the structured grid that are used in the regional scale study. The red square represents the centre of the disc/turbine hub.

Figure 7.6 illustrates the numerical domain developed for implementing the actuator disc source term in this study, containing 27,100 nodes for a single mesh plane. Additionally, a close up view of the location for turbine deployments within the Inner Sound region is clearly depicted in Figure 7.6(B), which is based on the bathymetric slicing and topography analysis conducted in Section 7.1. Using the staggered turbine layout as exhibited by Figure 6.10 in Chapter 6, a total of 32 turbines can be simulated within the prepared numerical boundary - 11 turbines in rows 1 and 3, and 10 turbines in row 2 respectively.

Figure 7.7, which is an extension from Figure 7.6(C), is then used to exemplify the arrangement of the 32 turbines within the structured grid area. The hub of the turbines (or the discs' centrelines in the momentum source application), are clearly shown in the diagram by red coloured squares. Moreover, from this figure, approximate locations for the single, two, and three turbines set up, which will be utilised in analysing the wake characteristics of the devices involved in this study, can be clearly identified.

As previously discussed in Chapters 5 and 6, the momentum source term utilised in

simulating the presence of tidal devices was implemented by modifying the TRISOU subroutine from Telemac3D (version 7) directory. A sample of the code adapted for use in this study is available in Appendix C (page 238). The simulation period of the models was set to 35 days, and were mostly run on The University of Edinburgh's Linux Computers Cluster (VLX), using 10 parallel processors. The computation time (i.e. time taken for the model to complete the task) ranged between 25 to 30 days, which depended on the case being studied, as well as computational load of the VLX system.

Additionally, outputs from the models were saved at 10-minute intervals. Numerical parameters used in the steering file to model the presence of tidal turbines are summarised in Table 7.1, which was based upon the outputs from the parametric studies conducted in Chapters 3. Nonetheless, there are a few discrepancies in the numerical set up between the hydrodynamic models of the PFOW conducted in Chapters 3, and present model. A few of the notable differences between the two models are highlighted as follows:

(a) Previously, tidal harmonic database TPXO version 7 was used in calibrating and validating the hydrodynamic models. However, the present study utilised TPXO8, which is the latest version available from the provider (refer to [194]). Interestingly, although the latest TPXO model combines a basic global solution (TPXO8, obtained at $1/6^{o}$ resolution) and high resolution local solutions ($1/30^{o}$ resolution where data are available), the comparison between the two tidal harmonic database revealed almost identical outputs, as demonstrated by the scatter plots and statistical analysis in Figure A.9 and Table A.2 respectively in Appendix A.

(b) As displayed in Figure 7.6(C), three rows of structured grid were imposed in the numerical domain for facilitating the implementation and computation of the momentum source term. The size of the structured grid, $\Delta x, \Delta y$, was set to 4 meter each. Significantly, the use of a grid size smaller than 4 meter is just not feasible due to the combination of computational constraint, as well as the time available for the author to complete this project. In fact, the sole reason for constructing only three rows of structured grid, instead of covering the whole area of interest with the same grid element, was to reduce the number of unnecessary nodes in the domain to speed up the computation process. Likewise, since the aim of this research is to explore the methodology and validity of representing 3D actuator disc approach in a regional scale model, the author

is impartial in looking at a full size tidal farm that contains hundreds of tidal devices. As such, only three rows of structured grid were imposed within the numerical domain to study the wake characteristics, as well as flow interactions due to the presence of tidal devices from the actuator disc simulation.

(c) In particular, since the smallest grid size used in the present study was 4 meter, the model time step was consequently set to 2 seconds to satisfy the CFL criterion. In fact, this time step was significantly smaller than the one employed in previous hydrodynamic models (i.e. 10 seconds).

(d) Besides, 10 σ layers were imposed on all of the models developed and used in the parametric study in Chapter 3. Conversely, to improve accuracy of the source term computation, it is imperative that sufficient number of nodes are made available across the disc swept area, as highlighted by Figure 5.3 in Chapter 5. Due to this reason, instead of using the default σ layers, 13 horizontal planes were manually fixed at the pertinent depths to properly define the shape of the disc. Details of this mesh transformation will be discussed in the following section.

Table 7.1: Numerical parameters adopted in the simulation of the actuator disc within a regional scale model.

Numerical parameters	Input / Values
Time step	2 seconds
Simulation start date	12/09/2011
Simulation period	35 days (1,512,000 seconds)
Graphic printout period (10 minutes interval)	300 seconds
Law of the bottom friction and friction coefficient	Chezy (44)
Initial condition	TPXO Satellite Altimetry
Option for liquid boundaries	Thompson method
Tidal database	TPXO 8
Horizontal turbulence model	Smagorinsky
Vertical turbulence model	Constant viscosity
Number of horizontal levels	13
Mesh transformation	Horizontal fixed planes
Coriolis input	No
Hydrostatic assumption	Yes

7.2.1 Regional scale actuator disc approach

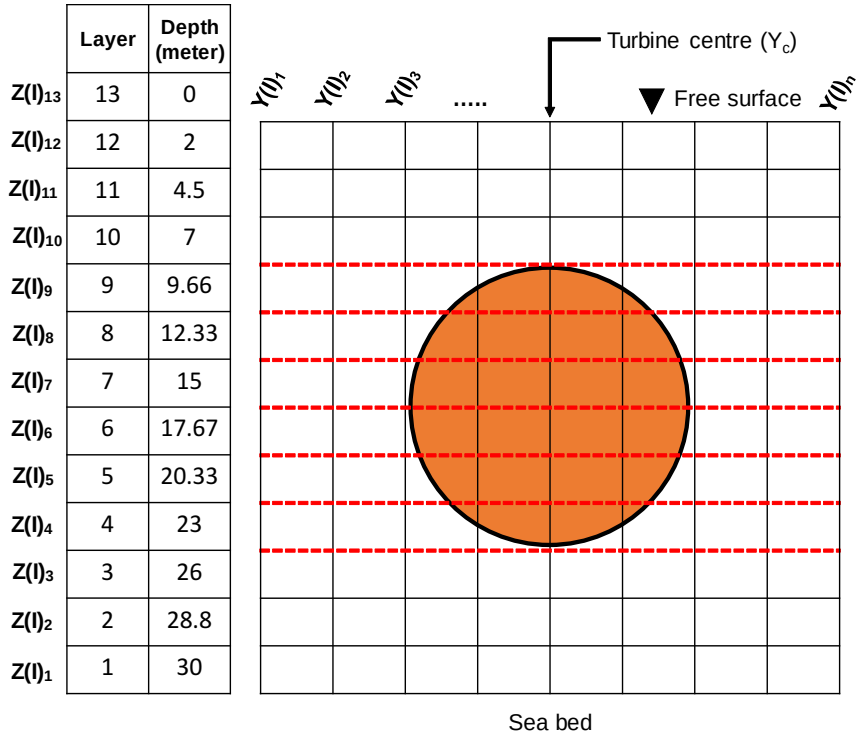

Figure 7.8: Configuration of the model's vertical layers for defining the turbine swept area used in the source code. Horizontal fixed planes option is preferred against the commonly used σ layers as it gives greater flexibility in arranging the planes' intersection across the disc capture area.

This section provides an overview of the implementation of the momentum source term into the model. As mentioned before, 13 horizontal planes were fixed at specific depths to define the vertical mesh transformation. This option was adopted instead of the commonly used σ layers as it allows greater flexibility in characterising the swept area of the disc. Detailed arrangement of the fixed planes and their corresponding depths is portrayed in Figure 7.8, where the hypothetical turbine hub was placed at a depth of 15 meter (i.e. close to the centre of water column at deployment region).

In total, the swept area of the actuator disc was represented by seven horizontal planes in the z-direction, and four Δy intervals (i.e. with Δy equal to 4 meter) in the y-direction that act as an enclosure for the 16 meter rotor diameter turbine used in this study. Δz between the planes that crossed the disc swept area was set to be about 2.66 meter, while slightly larger intervals were used for the remaining planes (i.e. layers positioned above and below the disc's edges).

Moreover, although the were only seven horizontal planes employed in representing the

disc swept area in present study, it should be sufficient to provide an even distribution of nodes across the actuator disc, as illustrated by the intersecting lines of Δy and Δz in Figure 7.8. In comparison, the small scale actuator disc study in Chapter 5 had nine intersecting planes. However, in deciding the optimal combination between Δz and Δy, two crucial parameters need to be taken under consideration:

(a) As previously discussed and demonstrated in Chapter 5, increasing the number of horizontal planes itself would not necessarily contribute to a better representation of tidal turbine in the model. Instead, both Δz and Δy must be examined to avoid having uneven nodes distribution across the disc swept area (as exemplified by Figure 5.3c). In particular, adding more planes in attempt to decrease the interval in the z-direction was just not feasible in this study, since it would require the enclosure of the disc (i.e. Δx and Δy) to be smaller than the default 4 meter grid size employed in present study.

(b) Ultimately, it all depends upon the computational resources available, since increasing the number of horizontal planes, as well as refining the mesh of turbine enclosure will undoubtedly contribute to longer calculation time. To highlight, the regional scale domain used in this study (Figure 7.6) contains 352,300 nodes and 615,432 elements for the 13-fixed depth mesh transformation planes.

With regard to simulating tidal turbines, the two parameters of interest are the power and thrust (drag) produced by the turbine. Power, P_w as well as thrust, T_r may be expressed using the following equations:

$$\mathrm{P} = \frac{1}{2} C_p \rho A U^3 \tag{7.1}$$

$$\mathrm{T} = \frac{1}{2} C_T \rho A U^3 \tag{7.2}$$

where A is the device swept area, U is the incoming flow velocity, ρ is the water density, C_p and C_T are the power and thrust coefficient respectively. Both C_p and C_T are influenced by parameters such as the blade pitch, yaw and tip speed ratio. On the other hand, since the actuator disc approach approximates the thrust forces exerted by the device onto the flow over a disc with the same rotor diameter, detailed analysis of those design factors are not relevant in the present study. Moreover, in an attempt to reduce the complexity of numerical computation, the turbine being simulated in this project was assumed to have fixed orientation, with its hub facing towards the western

side of the PFOW.

Following Equation 5.3, the computation of the actuator disc momentum source term requires two important parameters, namely the the resistance coefficient (K) and disc thickness (Δx_t). For the small scale idealised channel study discussed in Chapters 5 and 6, a constant (approximated) value of K was utilised to match the experimental data/set up from literature. Nonetheless, for a regional scale study, it was essential that operational characteristic of the simulated tidal turbine be as close as possible to the one in operation.

This relates to the relationship between C_T and flow velocity, where for any generic turbine design, the thrust coefficient is influenced by the minimum working velocity (or cut-in velocity, U_{cut-in}) and maximum working flow speed (or rated velocity, U_{rated}). Following the procedure established by Bahaj et al. [195] and Plew and Stevens [196], the thrust coefficient could then be parametrised as:

$$C_T(U) = \begin{cases} 0 & \text{if } U \leq U_{cut-in} \\ \overline{C}_T & \text{if } U_{cut-in} \leq U \leq U_{rated} \\ \overline{C}_T \dfrac{U_{rated}^3}{U^3} & \text{if } U \geq U_{rated} \end{cases} \tag{7.3}$$

where U is the velocity of the incoming flow, and $\overline{C}_T = 0.8$ (using design value as suggested by Bahaj et al. [195], which corresponds to K = 1.53). Additionally, the values of U_{cut-in} and U_{rated} employed in this study were set to 1 m/s and 2.5 m/s respectively, approximated upon published values from commercial devices in operation (refer to [171, 192, 197, 198]). Meanwhile, the default actuator disc thickness was consigned to 8 meter, based upon the results from Section 5.5.3 that indicated Δx_t had very little influence on the wake characteristic.

Bearing this in mind, although it was possible to use a smaller Δx_t value (i.e. 4 meter, because it was the smallest Δx interval employed in this study), it might be prudent to include as many nodes as possible (while maintaining a reasonable width of disc) in the computation of the momentum source term to avoid potential numerical uncertainty and vulnerability. All in all, information on the domain's mesh and actuator disc set up for this work is underlined in Table 7.2, while the influence of Δx_t on a regional scale model will be examined in the following section.

Table 7.2: Information on the domain's mesh and actuator disc set up employed in the simulation of a full size tidal turbine in the regional scale model.

Numerical parameters	Input / Values
Node counts	352,300
Element counts	615,432
Resistance coefficient, K	1.53
Size of structured grid ($\Delta x, \Delta y$)	4 meter
Actuator disc diameter, D	16 meter
Disc thickness (Δx_t)	8 meter
Disc z-centreline (e.g. turbine centre)	15 meter
Turbine design/alignment	Fixed orientation

7.2.2 Limitations of current study

Several limiting aspects associated with the use of actuator disc methods have been presented and discussed in Section 5.2.1. Nonetheless, while the idealised channel study in Chapters 5 and 6 had data from published literature that were used in the comparative studies, very few research articles are available concerning the implementation of the disc within a regional scale model. For this reason, the following restricting factors have been identified:

(a) Since in-situ measurement data from an operational tidal turbine are not available, it proved to be a challenge to examine properly and validate the accuracy of the applied actuator disc source term. Hence, the results presented in this chapter should be approached with respectful uncertainty.

(b) Accordingly, sound judgement based on the experience gained when conducting the idealised channel study is critical in evaluating the numerical outputs. For instance, the plotted velocity deficit contour from the models can only be examined by visual inspection to ensure that the wake produced by the actuator disc followed the expected behaviour as reported in literature (e.g. distance taken for the wake to recover or the flow characteristics due to the interactions between upstream and downstream devices).

(c) Unlike the idealised channel study where $k-\varepsilon$ model was applied, this study utilised Smagorinsky and constant viscosity for the turbulent models since they were able to improve substantially the models' calculation time. Nevertheless, because these models have no turbulence component (k) as one of the outputs,

the computation of turbulence intensity (TI) using Equation 5.11 is no longer valid. More significantly, the applied turbulent option caused the model's turbulent viscosity to be imposed (rather than being modelled when using $k-\varepsilon$ model) and constant in space (even in the wakes of the turbines). This might present complications in analysing the overall impact of the actuator disc in a regional model since this method strongly depends on turbulent viscosity.

Nonetheless, in an attempt to characterise the turbulence level, the TI was computed following its very basic interpretation - ratio of the Root Mean Square (RMS), or standard deviation, of turbulent velocity fluctuations at a particular location over a specific period of time to the average of the velocity at the same location over same time period. The following statistical approach was employed in computing the turbulent intensity in the x-direction [199–201]:

$$\text{Mean velocity: } \overline{u} = \frac{1}{N}\sum_{1}^{N} u_i \tag{7.4}$$

$$\text{Turbulent fluctuation: } u_i^{'} = u_i - \overline{u} \tag{7.5}$$

$$\text{Turbulent strength: } u_{rmse} = \sqrt{\frac{1}{N}\sum_{i=1}^{N}(u_i^{'})^2} \tag{7.6}$$

$$\text{Turbulent intensity: TI} = \frac{u_{rmse}}{\overline{u}} \tag{7.7}$$

The sample size N used in this analysis corresponds to the velocity data points from 15 September 2001 until 20 September 2001 (i.e. N = 720), which coincide with the spring tide period. $\overline{u}$ meanwhile is the mean longitudinal velocity for each horizontal plane. The TI can then be calculated by dividing u_{rmse}, which is the standard deviation of the random velocity fluctuation, with the mean velocity at each respective layers. Velocity fluctuation component $u_i^{'}$ used in the computation of the turbulent strength corresponds to the difference between velocity component (u_i) and the mean velocity ($\overline{u}$) of the chosen sample size. Larger u_{rmse} implies a stronger turbulence regime within the flow, and vice versa.

However, the computed TI using Equation 7.7 needs to be approached with caution. Any formula that employs turbulent fluctuation components is only feasible to be

implemented if the fluctuating motions can be resolved (e.g. when using LES or Direct Numerical Simulation (DNS) models). Consequently, since the velocities computed in Telemac3D were already time-averaged because it solves the RANS equations, Equation 7.7 may not be able to provide the best representation of the turbulent attributes from this actuator disc study.

To check this hypothesis, Figure A.10 in Appendix A is used to examine the computed TI from 4D till 20D downstream distances for the single disc arrangement. As evidenced from the plots, abnormally high values of TI were obtained from the model outputs, ranging from 400% - 1000%, which clearly contradicted the reported turbulence values between 3% to 25% from literatures (e.g. [179, 202–205]).

In brief, as Equation 7.7 is ill-suited to be used on a RANS-based model (such as Telemac3D) to help quantify the turbulence level, only the velocity deficit plots will be presented in this study to help analyse the wake characteristics caused by the implementation of the actuator disc momentum source term in the regional scale simulation.

7.3 Velocity contour at the deployment location

Before examining the overall impact of implementing tidal devices in the Inner Sound, it is sensible to look at the hydrodynamic condition at the area of interest. Current pattern at the deployment region for the whole simulation period (i.e. 35 days) can be examined using the depth-averaged velocity rose for the selected nodes, as illustrated in Figure 7.9. Looking at the plotted velocity roses, the flood flow enters the Inner Sound from the north west, and subsequently follows a rather curved path propagating through north east of the Stroma island. Conversely, during the ebb tide, the flows enter the Inner Sound from the north east and pass through the channel towards north westerly direction.

According to the tidal rose plots, the current speed ratio between spring and neap tides in the Pentland Firth is about 2:1. This ratio agrees with the one mentioned by Easton et al. [188], and is further validated using the time series plots of the U and V velocity components at the deployment area (refer to Figure 7.10). From this figure, it is evident that at spring tide, the maximum value of the U-velocity component at mid-depth of node 6390 (which is very close to the deployment area) is just about 4 m/s, while during neap tide the speed is almost halved, as indicated by the computed u_{rmse}.

Nonetheless, since this study excluded meteorological input (such as wave induced currents and wind forcing) which may have greater influence during the weaker neap

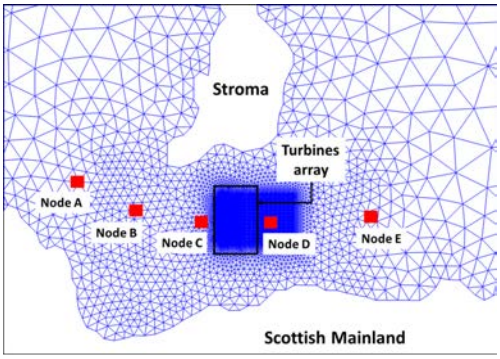

(a) Selected nodes for plotting tidal current rose.

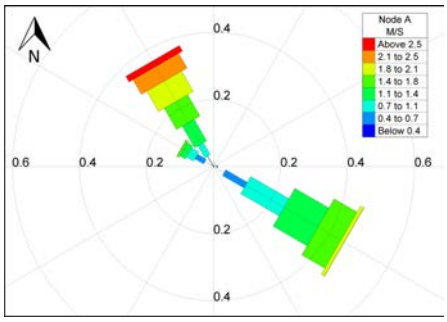

(b) Node A

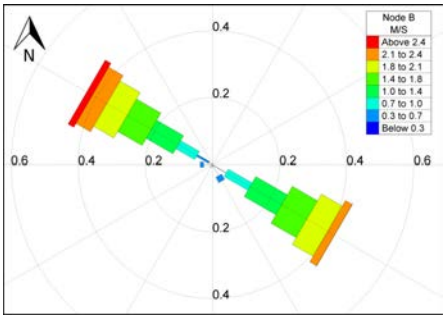

(c) Node B

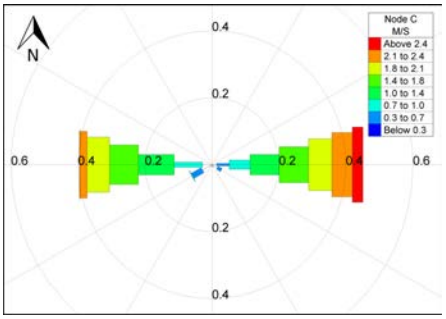

(d) Node C

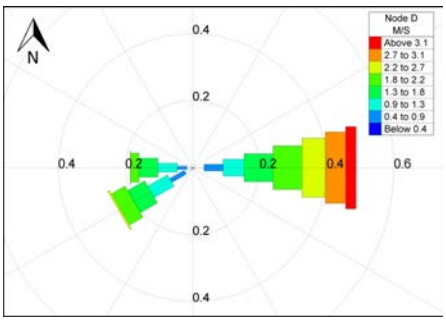

(e) Node D

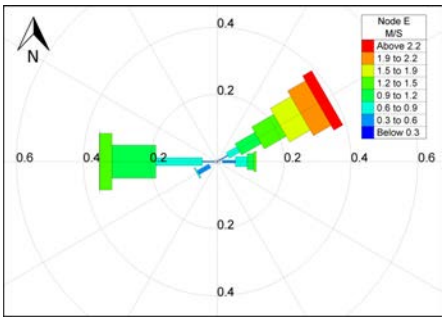

(f) Node E

Figure 7.9: Depth-averaged velocity tidal rose for the Inner Sound region illustrating the variation and current direction for the nodes shown in (a).

tide, the mentioned spring-neap tide ratio may possibly be inaccurate. Moreover, since tidal asymmetry in the PFOW forces the currents to be non bi-directional, there is a clear misalignment between the flood and ebb direction in the region [206]. All in all, since the observations in Figures 7.9 and 7.10 matched well with the general pattern of currents in the PFOW as reported in literatures (e.g. [187, 207]), they gave confidence to the numerical model to move forward with computation of the actuator disc momentum source term.

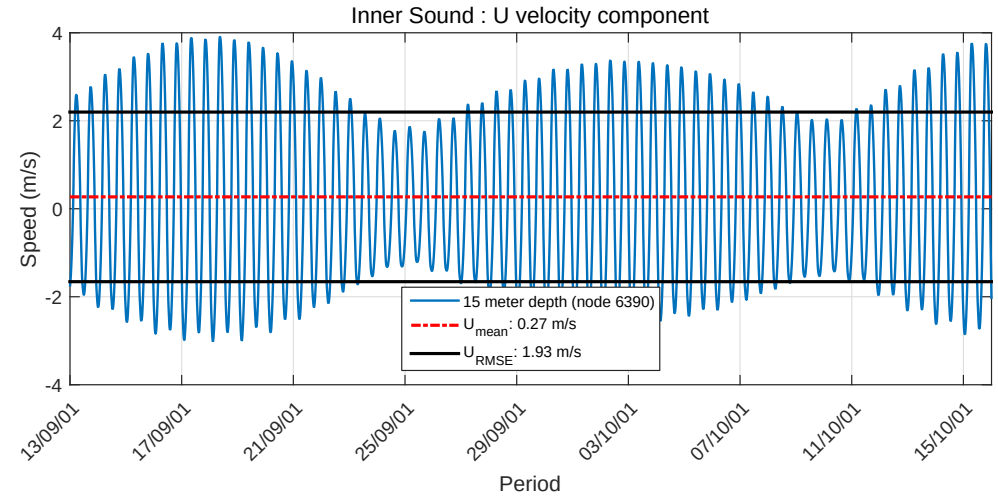

(a) U velocity component.

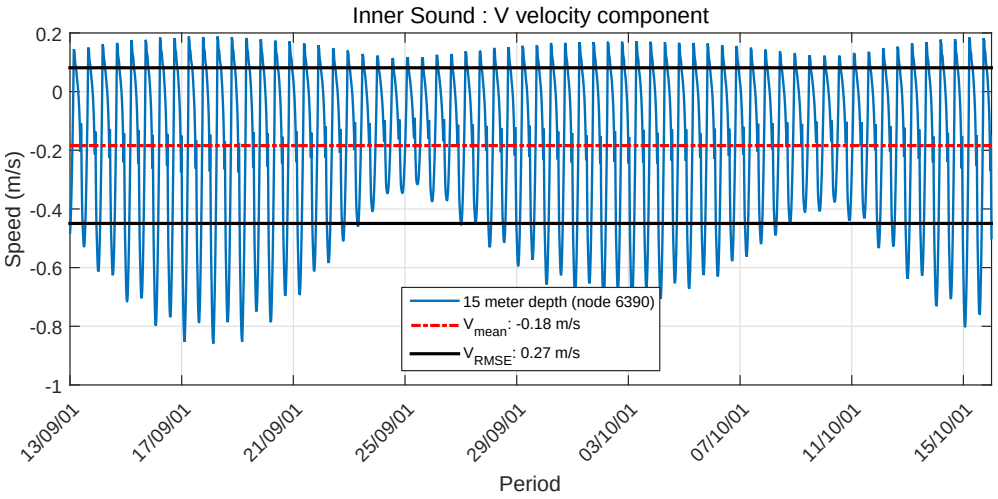

(b) V velocity component

Figure 7.10: Time series plot at the deployment area at mid-depth (15 meter) for node 6390 (20 meter upstream from the location used in the single turbine study - refer to Figure 7.7).

Overall configurations of the simulated tidal turbines in this study are summarised in Table 7.3. Please note, however, that this table does not provide details on the modelling parameters employed for individual set up (e.g. variation in disc thickness and resolution of the vertical layers). Such set up will be presented in the subsequent section that discusses the sensitivity study for selected turbine arrangements. To examine velocity contour at the area of interest, the output from the actuator disc models were compared with a base model (i.e. model without turbine(s)).

Table 7.3: Turbine arrangement that was simulated in this study using the default numerical parameters.

Turbine configuration	Structured grid / row set up
Single turbine	Row 1
Two turbines	Row 1
Three turbines	Row 1 & 2
Eleven turbines	Row 1
Twenty one turbines	Row 1 & 2
Thirty two turbines	Row 1, 2 & 3

From this exercise, not only velocity deficit (U_{def}) caused by the presence of tidal devices can be analysed, but more significantly, the validity of the actuator disc source term employed in representing those devices can also be inspected. Some indicators that could be used in checking the soundness of the simulated models include the length of the wake being produced (i.e. wake from a single row turbines should be shorter than the one produced by three rows of turbines), as well as the extent of velocity reduction in the immediate vicinity downstream of the devices.

The screen shot of the velocity contours shown in this section corresponds to the spring tide that occurred on 18 September 2001. These velocity contours were used as a reference point in checking the accuracy as well as the feasibility of the momentum source code applied in the regional scale actuator disc model. More significantly, the model must be able to produce similar flow attributes as observed in the idealised channel study, such as the wake formation and flow interactions. Figure 7.11a displays the velocity difference caused by the presence of a single tidal turbine at the area of interest, where the expected flow characteristics upstream and downstream of the device were satisfactorily produced.

Firstly, the thrust exerted by the disc caused the upstream flow to slow down (between 0.1 - 0.2 m/s) when approaching the disc, before the flow accelerated up to 0.4 m/s when passing through the disc. Appropriate velocity reduction in the immediate vicinity behind the turbine can also be seen, where it shows greatest flow reduction of about 0.6 m/s. Finally, further downstream of the disc, the value of velocity difference slowly diminished, from 0.3 m/s to 0.1 m/s before the flow completely recovered about 420 meter from device position.

Additionally, comparison between two Δx_t values (default 8 meter vs 4 meter) demon-

strates that the size of disc thickness employed in the source term has a notable influence on the numerical outputs. As shown in Figure 7.11b, the largest velocity difference (of about 0.25 m/s) occurred directly behind the disc. Nonetheless, as the flow travels further downstream of the device, the discrepancy between the two tested Δx_t seems to be dramatically reduced. To further understand this observation, a sensitivity study on Δx_t has been conducted and discussed in Section 7.4.2.

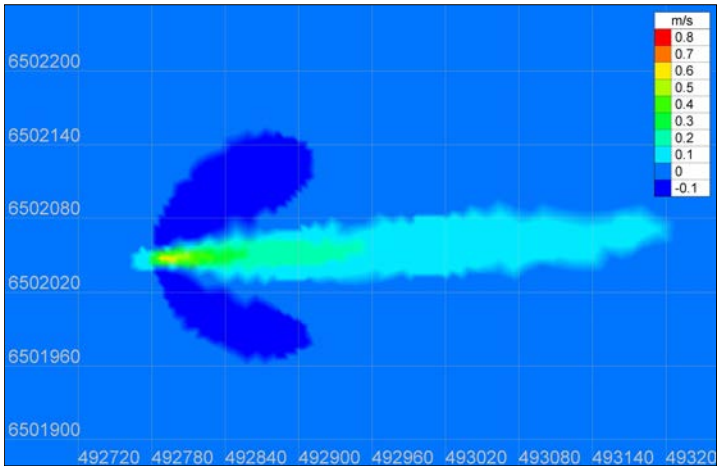

(a) Velocity difference due to the presence of a single turbine (using default Δx_t = 8 meter).

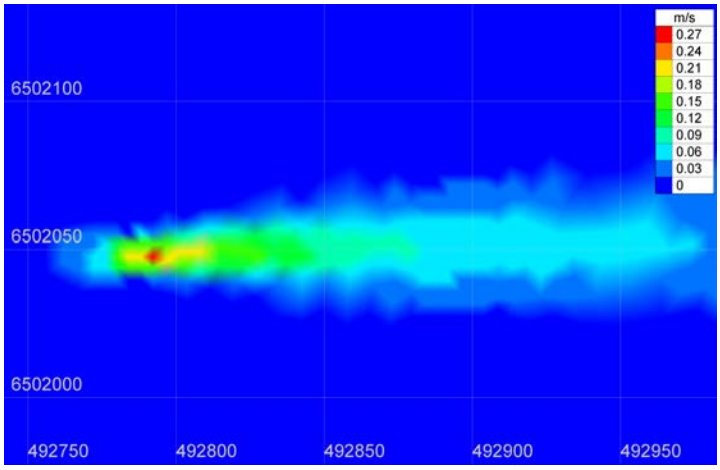

(b) Comparison of velocity difference between Δx_t = 8 meter and 4 meter.

Figure 7.11: Velocity contours showing the impact of a single turbine configuration on the flow in Inner Sound.

In addition, similar flow features are also evident for the two turbines configuration as shown in Figure 7.12. Interestingly, the wake formation between the two simulated turbines shows slight dissimilarities, with the bottom disc having a longer wake that curved upwards at the end. However, it is not of immediate concern since this occur-

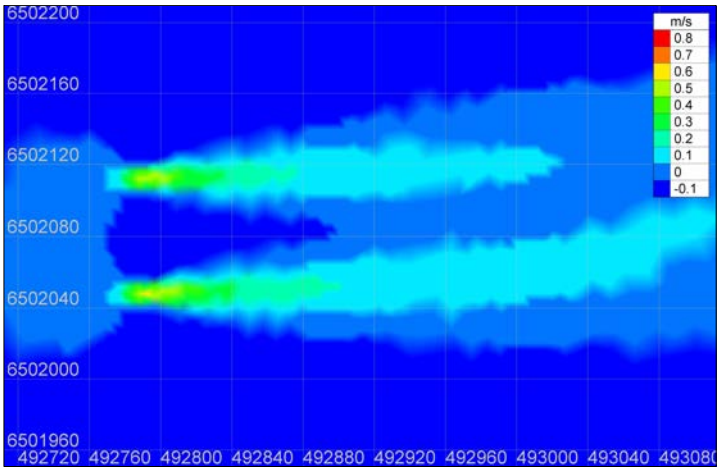

Figure 7.12: Velocity contours showing the impact of two turbines configuration on the flow in Inner Sound.

rence could be attributed to the complex geometry of the Inner Sound area. Bathymetry is known to have a huge influence in dictating the direction, as well the speed of the currents. While the turbines are laterally positioned up to 3D from each other, the wake formation observed in Figure 7.12 seems to persist for more than 300 meter downstream of the turbine, at which point the bathymetry may have drastically changed from where the turbines are located.

This observation is further exemplified using the 11-turbine configuration as displayed in Figure 7.13a, where the collective wake formation path from all the devices are heading towards the north easterly direction. This also signifies the distance required before the flow completely recovered, as the wake advancing pass the island of Stroma. Figures 7.13b and 7.13c then provide better perspectives on the velocity deficit recorded for the 11 turbines within the first row, where a few remarks can be made.

For example, the wake generated from the top three turbines in Figure 7.13b is isolated from the remaining eight devices, indicating that they faced an upstream velocity that is (a) slower, hence the shorter wake, and (b) coming at an angle, hence the upward curved path. As previously discussed, point (a) could be credited to the local topography that is somewhat shallow (refer to Figure 7.5). Nonetheless, point (b) seems to slightly contradict the plotted velocity rose in Figure 7.9, which indicates that the flow direction at the selected nodes across the deployment area is perpendicular to the disc (i.e. facing the incoming flow).

However, it is also plausible that these individual nodes (used in plotting the tidal rose) are not portraying the general hydrodynamic condition surrounding the area of

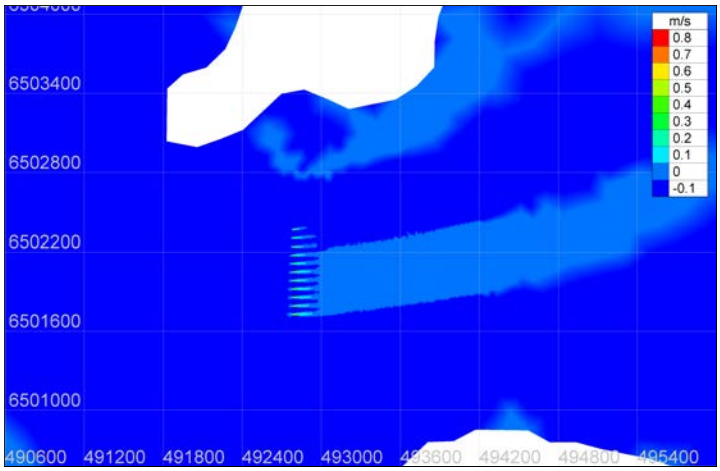

(a) Wake influence due to the presence of 11 devices.

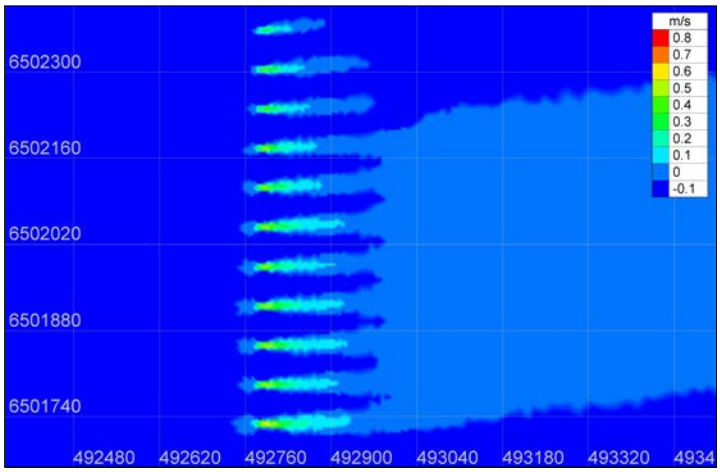

(b) Velocity difference due to the presence of 11 devices.

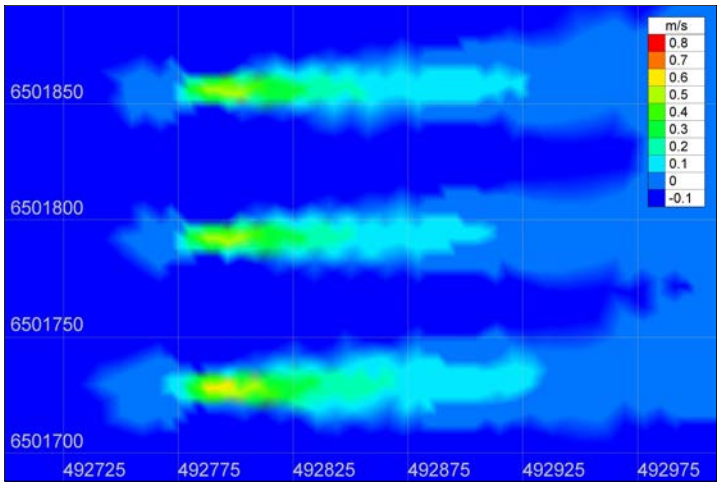

(c) Close up view of the 11 turbines arrangement highlighting the velocity deficit in the wake.

Figure 7.13: Velocity contours showing the impact of 11-turbine configuration on the flow in Inner Sound.

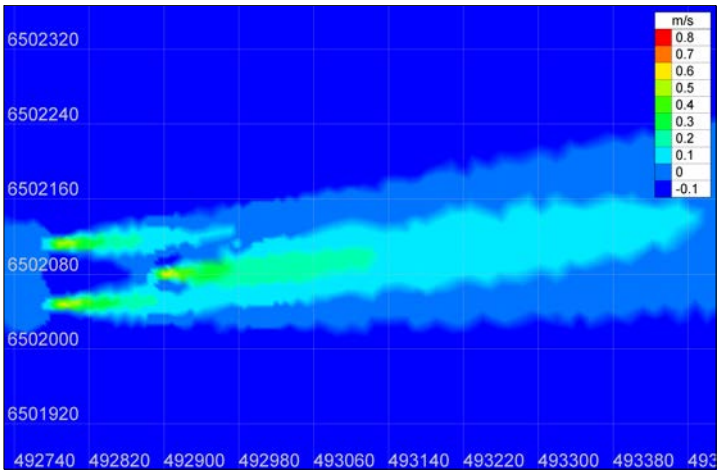

Figure 7.14: Velocity contours showing the impact of three-turbine arrangement on the flow in Inner Sound.

interest. Finally, the wake characteristics are unique and vary from one disc to another. For instance, the close up view in Figures 7.13c highlights how the wake formation, as well as the velocity reduction directly behind the discs varies in length and value. In contrast to the middle disc, the one at the bottom exhibits a slightly longer wake formation, with U_{def} of 0.7 m/s immediately behind the turbine.

Next, Figure 7.14 illustrates numerical output for the three turbine arrangement. The lateral distance between the upstream turbine was set to 3D, while the downstream turbine was positioned at 7D behind the front row devices. The output from the three-disc configuration is essential in inspecting the accuracy of the actuator disc' approach in modelling the interaction between upstream and downstream devices. As previously discussed in Chapter 6, the presence of a downstream turbine is known to have an influence on both the flow condition as well as the wake formation experienced by the upstream devices.

From the velocity difference shown by the contour plot in Figure 7.14, it can be concluded that the output from the regional scale model demonstrates similar flow characteristics as previously observed in the idealised channel study. As the wake from the upstream and downstream devices eventually merged, the flow recovery for the three-disc arrangement also becomes more pronounced further downstream, forming a single wake that is wider and longer.

In comparison, wake formation from the two disc arrangement persists up to only 300 meter downstream, while for the three turbine arrangement, the wake is yet to reach the ambient velocity even after 700 meter from the upstream turbines. More importantly,

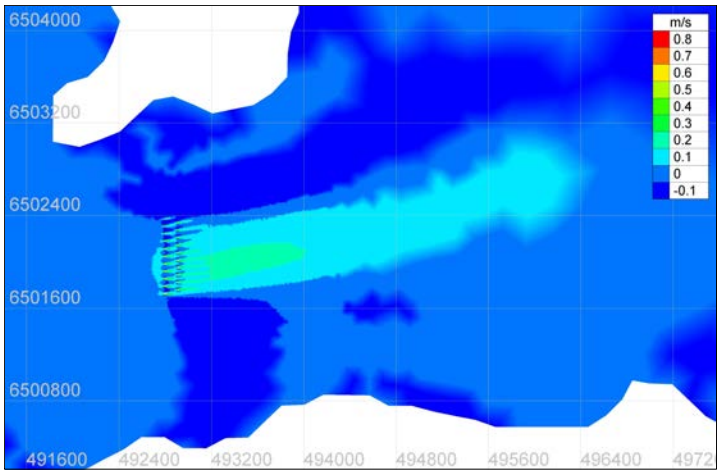

(a) Wake influence due to the presence of 21 devices.

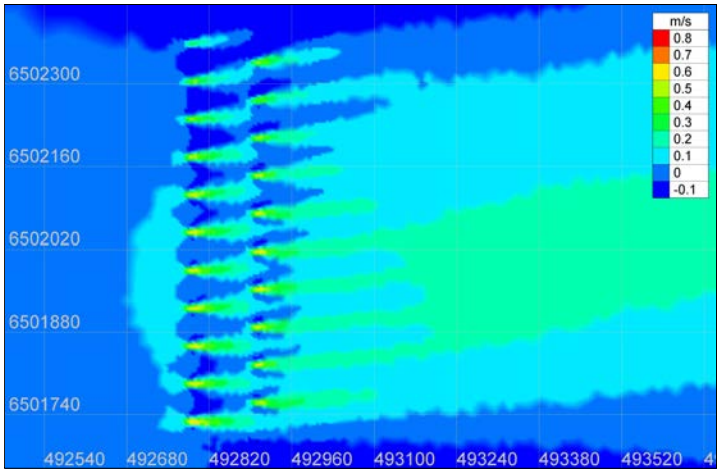

(b) Velocity difference due to the presence of 21 devices.

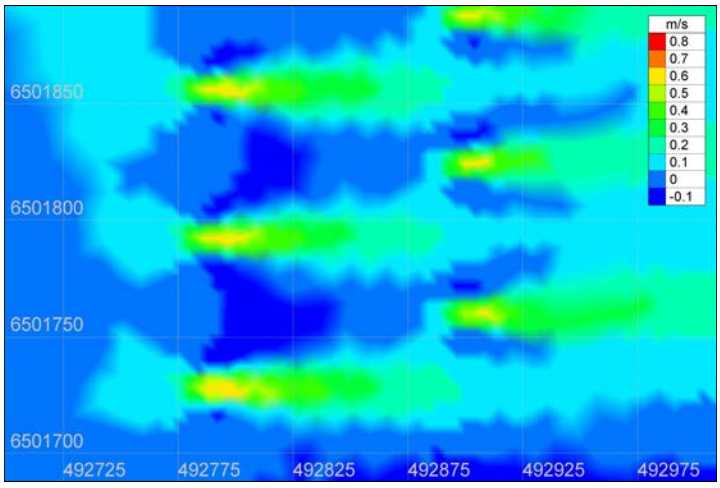

(c) Close up view of the 21 turbines arrangement highlighting the velocity deficit in the wake.

Figure 7.15: Velocity contours showing the impact of 21 turbines configuration on the flow in Inner Sound.

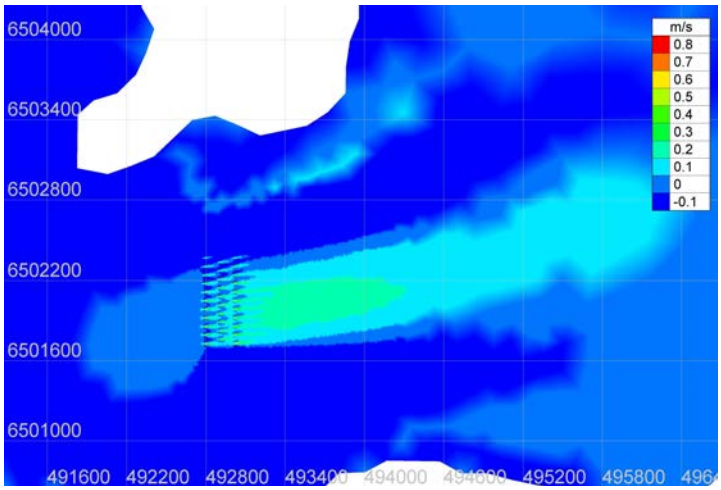

(a) Wake influence due to the presence of 32 devices.

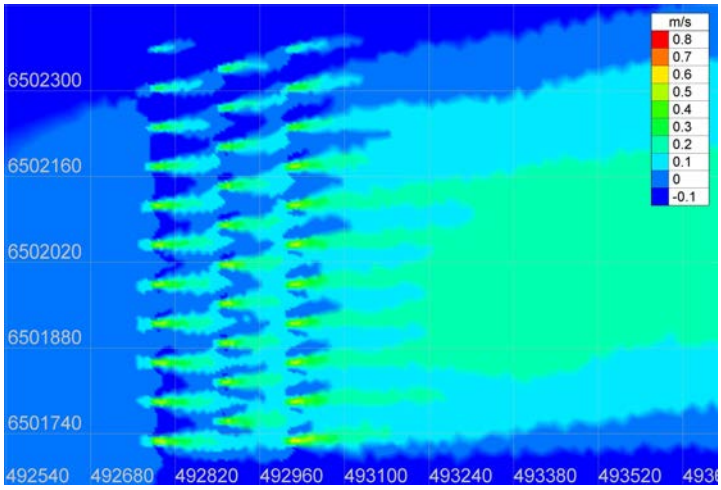

(b) Velocity difference due to the presence of 32 devices.

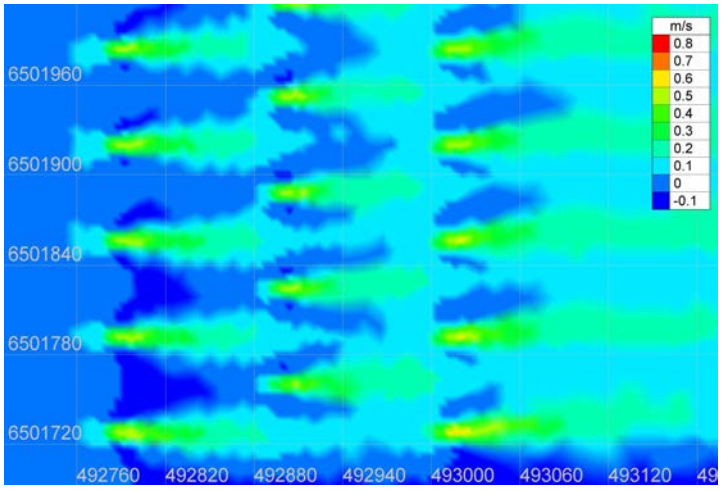

(c) Close up view showing higher velocity reduction behind the turbines in the third row.

Figure 7.16: Velocity contours showing the impact of 32 turbines configuration on the flow in Inner Sound.

the blockage effect which caused the downstream device to experience greater U_{def} than the front row devices, has also been appropriately simulated. From Figure 7.14, the downstream turbine experiences a velocity deficit of up to about 0.7 m/s, while the U_{def} for the upstream turbines is almost 0.5 m/s.

Since the validity of the actuator disc in simulating the flow and device interactions for three turbines set up at the regional scale have been established, next is to look at the velocity contour for the 21 (two rows) and 32 (three rows) arrangements. Figures 7.15a and 7.16a demonstrate the extent of the wake formation generated from the 21 and 32 turbines arrangement respectively. As more devices were added to the tidal farm, the wake region from the 32-disc configuration exhibits greater overall deficit coverage than the 21 disc configuration, which the models had properly predicted.

Moreover, both configurations also exhibit similar flow behaviour as previously observed for the 11 device set up, in which several of the discs that are located close to the Stroma island displays shorter wake formation. Consequently, it can be suggested that the incoming flows towards the deployment area were greatly influenced by the seabed features (i.e. steep channel slopes near Stroma island.), causing the uneven wake development as displayed in Figures 7.15b and 7.16b.

Significantly, the choice of both lateral and downstream spacing used in this study was also justified, since the wake developed by upstream devices did not interfere with the downstream devices. This means that more power could be extracted from the downstream turbine due to a higher stream-wise velocity caused by the non-merging upstream wake. Furthermore, Figure 7.16c also confirms that turbines in the last row of any array configuration will experience the highest U_{def}.

In brief, the applied actuator disc momentum source term has successfully demonstrated its capability in simulating the presence of tidal turbines within a regional scale model by generating the appropriate wake and flow characteristics to be expected from the devices. The next section will then explore the sensitivity of actuator disc parameters to further comprehend their influence on the numerical outputs.

7.4 Models' sensitivity and validation

To further examine the sensitivity of the regional scale actuator disc models, focus will be placed on the models' predicted velocity reduction along the water column. Similar to the idealised channel study, hard points were applied into the geometry mesh during pre-processing stage to establish positions of the fixed nodes within the domain. These nodes are imposed at various turbines' downstream distances and are essential in facilitating data extraction from the numerical model.

To support models' analyses, wake behaviours across the water columns for several downstream distances were plotted, with x and y axes of the plots corresponding to the velocity reduction due to the momentum source term and water depth respectively. Specifically, longitudinal velocity data from the 18th of September 2001 (time - 00:00) were employed to characterise the downstream velocity deficit experienced by the devices. This date was chosen since it signified the period where the highest (modelled) velocity was recorded as displayed in Figure 7.10. Additionally, a brief comparison of the model's velocity outputs for different time steps is shown in Figure A.11 in Appendix A, highlighting the capability of the applied momentum source term to reproduce appropriate wake characteristics depending on the flow conditions.

7.4.1 Single turbine set up

Figure 7.17 shows the flow characteristics over the water depth, due to the presence of a single turbine in the Inner Sound, where the top plots display the predicted velocity deficit from 4D till 20D downstream of the device. These plotting positions (i.e. 4D to 20D downstream of the disc) were initially established as the default data extraction locations to maintain consistency with the charted results from the idealised channel studies in previous chapters. The outputs from the actuator disc models were plotted together with results from a model that disregarded the momentum source term (i.e. model with no turbine, represented by the (+) red markers) to help provide some evidence on the efficacy of the applied actuator disc source term.

From Figure 7.17a, the model without the actuator disc (i.e. no turbine plots) clearly exhibits that the highest current velocity at the deployment location was about 4 m/s (close to the water surface), then gradually decreased to 3.5 m/s at the middle of the water column (~15 meter depth), before plummeting further to just about 1 m/s close to the seabed. As shown in the 4D plot, the greatest velocity reduction (of about 0.5 m/s) due to existence of the actuator disc happens near the turbine centreline at the

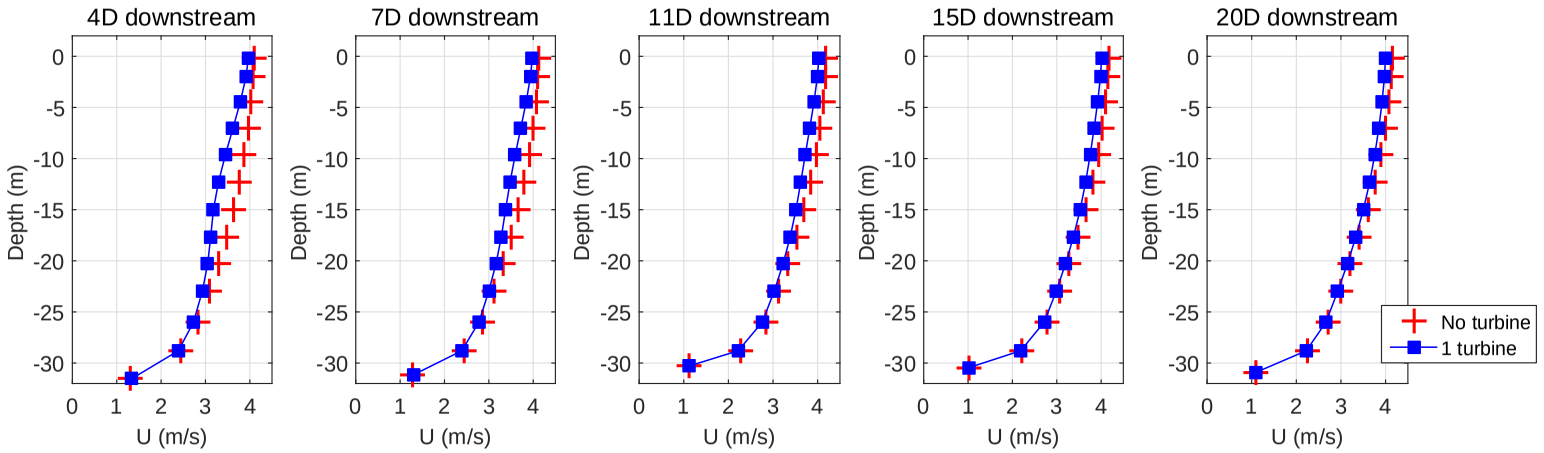

(a) Velocity reduction across the water column for various downstream distances.

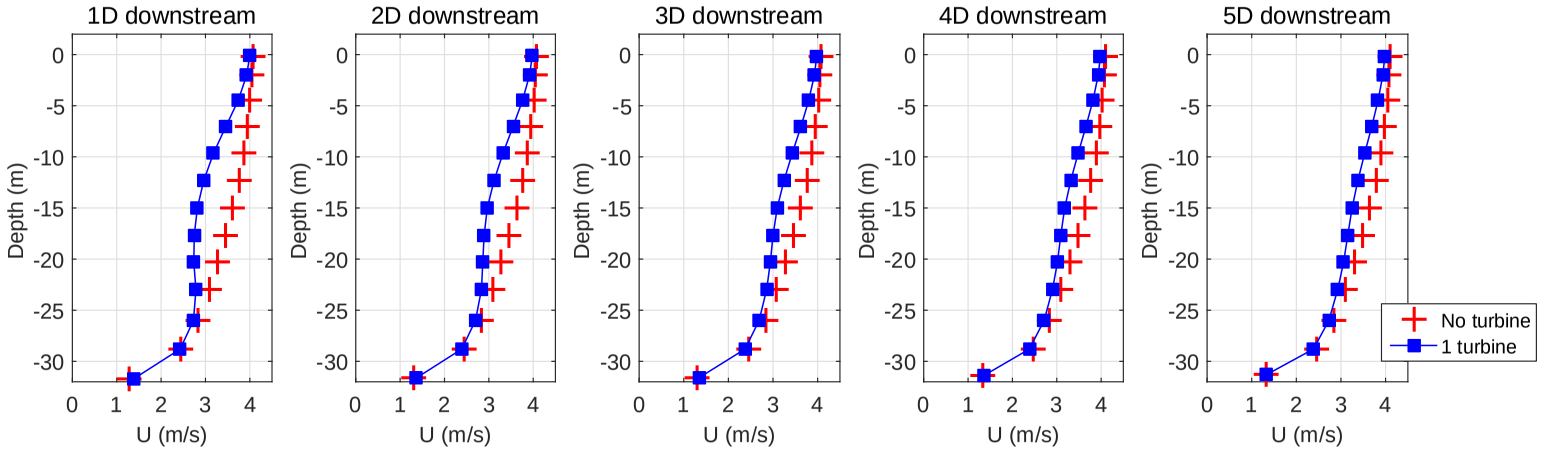

(b) Velocity reduction across the water column for shorter downstream distances.

Figure 7.17: Velocity deficit from the single turbine arrangement during spring tide for various downstream distances.

middle of the water column, while the top and bottom edges of the disc (at depths of about 7 meter and 23 meter respectively) demonstrate very small velocity deviation.

Moreover, velocity profiles from the actuator disc model at 7D and 11D downstream positions also exhibit minuscule divergence from the no turbine model, indicating that the energy from the flow is nearly recovered at these points. Finally, by the time the flow reaches the 15D position, the wake has completely recovered to attain its ambient velocity, as evidenced from the graph.

Several remarks can be made following the results presented in this figure. Firstly, although outputs for both small and regional scale models demonstrated that the flow has or nearly recovered by the time it reached 15D downstream of the disc, wake profiles between the two models prior to the mentioned distance were in stark contrast. As a case in point, for similar downstream distances, the plotted velocity reduction for the regional scale actuator disc model illustrates a much smaller deviation from the original velocity profile (i.e no turbine model) when compared against the small scale idealised channel model.

For example, at 4D location in the idealised channel actuator disc model, the largest velocity deficit at the disc centreline was discovered to be about 1.2 m/s (refer to Figure 5.5), which was more than double the value observed in Figure 7.17. Besides, the 7D and 11D downstream plots from the small scale study also demonstrated a more apparent velocity variation due to the applied momentum source term, contrary to the regional scale results. Significantly, the disparity observed in the current profiles across the water column between the two models can be attributed to rate of wake recovery experienced by the actuator discs.

Since the velocity profile at the deployment region in current study is much higher than the one used in the simple channel (i.e. ~4 m/s compared to ~3 m/s respectively), it increases the rate of far wake re-energisation [164, 208]. Consequently, this translates into a much smaller velocity deficit as depicted in Figure 7.17. Nonetheless, since the purpose of this study is to validate the effectiveness of the applied actuator disc momentum source term, the minuscule velocity variation observed from the 4D - 20D plots may not be ideal for conducting a thorough sensitivity study.

Due to this reason, in anticipation of seeing a much greater velocity reduction at a shorter downstream distance (i.e. from 1D till 5D positions), Figure 7.17b was subsequently plotted to facilitate data comparison. The plots show that the model has successfully produces appropriate wake profiles as expected from the actuator disc,

where the greatest centreline velocity reduction of about 0.8 m/s was observed in the 1D graphs. The flow then exhibits rapid recovery towards the ambient velocity, as evidenced from 2D - 5D graphs, where the model's velocity deficit steadily declined further downstream from the disc.

All in all, Figure 7.17 demonstrates that the implemented momentum source term was able to successfully predict the wake profiles due to the presence of a tidal turbine (in the form of a disc) in a regional scale simulation. Moreover, since this figure also corroborates the findings presented in Section 7.3 (i.e. plots of velocity contours) on the validity of the actuator disc set up, it gave further confidence in the models' outputs for conducting the sensitivity analysis. From here onwards, the top plots will displays the velocity deficit experienced by the disc at a shorter downstream distances (i.e. 1D - 5D), while the bottom plots are used for illustrating the wake profiles across longer downstream distance (i.e. 4D - 20D).

7.4.2 Influence of disc thickness

In this sensitivity exercise, three actuator disc thicknesses were tested; $\Delta x_t = 4$ meter, 8 meter, and 12 meter. Meanwhile, the structured grid interval Δx and Δy, was maintained using the default density of 4 meter by 4 meter. For example, when simulating a disc with thickness of 12 meter, the flow will progress through three Δx grid intervals/cells that act as width of the device being modelled. Comparison plots for the three Δx_t examined in this study are displayed in Figure 7.18. All models, regardless of the Δx_t, show orderly wake profiles where the greatest reduction is observed at 1D downstream of the disc, before the flow gradually showed sign of recovery as it progressed further away from the disc.

However, from Figure 7.18a, it can be seen that Δx_t has a greater impact on the implemented momentum source term at a shorter downstream distances. From 1D till 4D downstream positions, the actuator disc model with disc thickness of 4 meter demonstrates the largest velocity deviation when compared with the other two models. Conversely, the smallest velocity variation is shown by $\Delta x_t = 12$ meter, followed by $\Delta x_t = 8$ meter. Additionally, it can also be seen from the plots that wake profile deviation between $\Delta x_t = 8$ meter and 12 meter models are almost indistinguishable from one another, beginning from the 1D position until they finally reached the ambiance velocity.

Nonetheless, the influence of changing Δx_t is no longer apparent after the 7D downstream positions, as highlighted by the 7D graph. This implies that the disc thickness

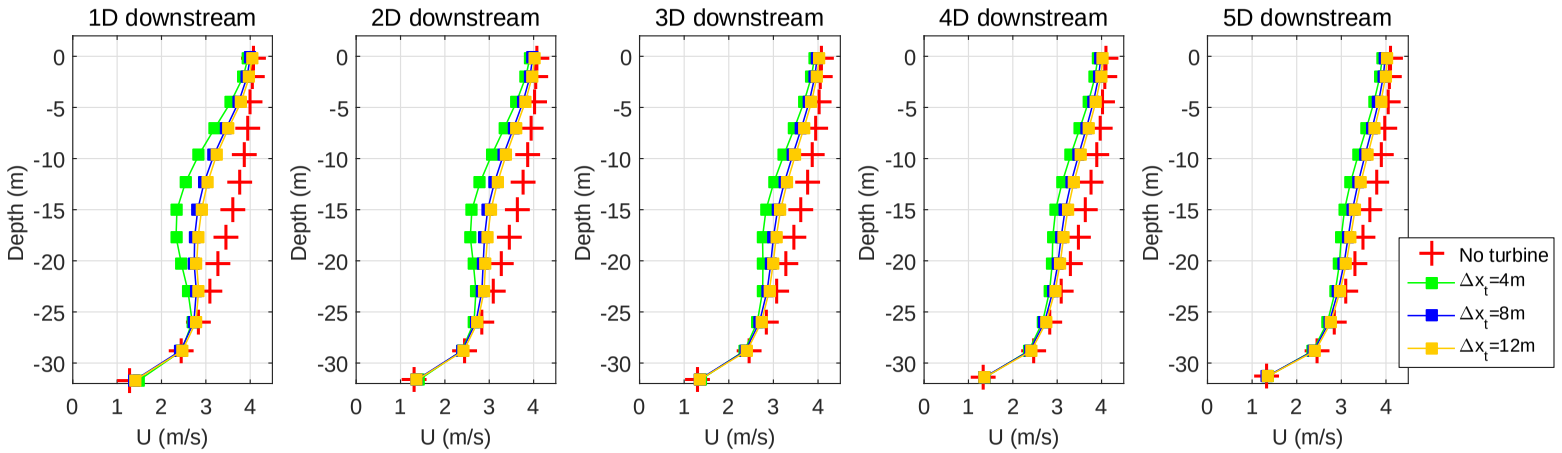

(a) Velocity reduction across shorter downstream distances for three distincts Δx_t.

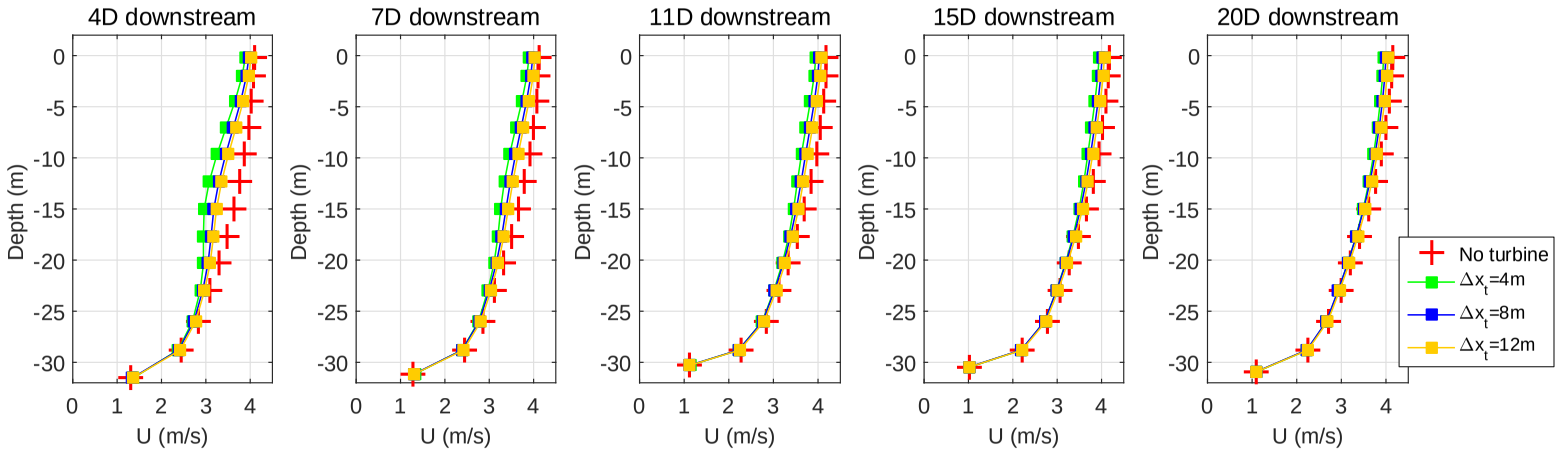

(b) Velocity reduction across longer downstream distances for three distincts Δx_t.

Figure 7.18: Velocity deficit caused by the presence of a single turbine during the spring tide for different turbine thickness.

parameter could very well be sensitive when subjected to highly turbulent regimes such as the regions immediately behind the disc. As the turbulent levels/intensity gradually decrease further from the disc, distinctions between flow profiles observed for the three tested Δx_t also slowly diminished. More significantly, the results presented in Figure 7.18 are consistent with the trend observed from the idealised channel study (refer to Figure 5.6), where the largest velocity deviation was caused by model utilising the smallest disc thickness.

Notwithstanding, these observations calls for another investigation on the importance of this parameter (i.e. Δx_t) on the 3D actuator disc model. In the small scale study, the best results against the published data were obtained using a model that was imposed with the largest disc thickness, although the outputs from the inspected models were very close to one another. However, since the plots examined in that study were for far wake distances, the shape of its near wake profiles are not known. Correspondingly, without in situ measurement data, it is almost impossible to ratify which of the Δx_t values is the most suitable to be employed in a regional scale actuator disc simulation.

To put it differently, near wake profiles are especially crucial when conducting resource assessment studies, or investigating the performance of a turbine. Regardless, since the focus of this study is on examining the sensitivity of a regional scale actuator disc approach, as well as the flow interactions between devices within a small array, less emphasis is placed on validating the near wake characteristics (between 1D - 5D downstream distances). As illustrated by the 7D plot in Figure 7.18b, although there are still slight velocity variations between the three tested Δx_t, the distinctions between the models are no longer apparent at this location.

Besides, since the downstream turbines in this study will be placed at about 7D downstream from the upstream devices, it means that the choice of an actuator disc thickness employed in the momentum source term has a very small impact on the outcome of wake produced by discs in subsequent rows. Hence, in the following sections, default $\Delta x_t = 8$ meter was employed as a compromise for the applied source term, since the grid intervals imposed using $\Delta x_t = 4$ meter may possibly be too small to ensure numerical stability, while setting Δx_t to 12 meter could be considered as too substantial for an actual turbine width in operation.

7.4.3 Two or three-turbine configuration

This section examines the validity of regional scale actuator disc in predicting flow interactions between the upstream and downstream devices for both two and three-disc configurations. The centreline gap between the two upstream devices was set to 4D, while the single downstream disc was located 7D behind the upstream devices in a staggered configurations as previously illustrated in Figure 6.10. Further, plots for the idealised channel study from Chapter 6 (refer to Figure 6.7) were used as the baseline in scrutinising the outputs from this ocean scale-three turbines set up. Comparison of lateral mid-channel depth velocity reduction between the two and three-turbine configurations in an array at four increasing downstream distances (5D, 9D, 15D and 25D) is demonstrated in Figure 7.19.

To better inspect the lateral velocity deficit, the normalised velocity (with U_∞ set to 4 m/s) was used in the x axis, while lateral offset in terms of turbine diameter (D) was utilised in the y axis. Influence of the downstream turbine in the array set up is already apparent in the 5D plot, where subtle velocity differences can be seen between the two and three turbines set up. Besides, the applied source term seems sufficient to correctly produce the anticipated flow behaviour from the disc's interactions, where the presence of downstream device has caused the speed of wake propagation from upstream devices to be slightly diminished.

However, these reductions observed for the regional scale model are extremely small, to the point they are almost negligible. While the velocity deficit between two and three-discs configurations in the idealised channel study was shown to be at about 5%, the variation for this large scale study was observed to be less than 3%. Additionally, while the wake from three turbine set up was clearly detectable at 5D downstream distance for the channel study, wake profile from the same device configuration in this study is yet to develop at this position.

These differences could be explained as follows; Firstly, the array configurations (i.e. lateral and downstream distances) employed in plotting Figure 6.7 are smaller than used in this study, hence explaining why the wake from the three turbine set up is not visible from the 5D plot in Figure 7.19. Secondly, the smaller velocity reduction observed for this large scale study could also be attributed to a faster flow current experienced by the disc, which increases the rate of wake recovery.

Moreover, the model outputs for the 5D plot also indicate the asymmetrical nature of the flow at this location, where the top turbine (y axis centreline lateral offset

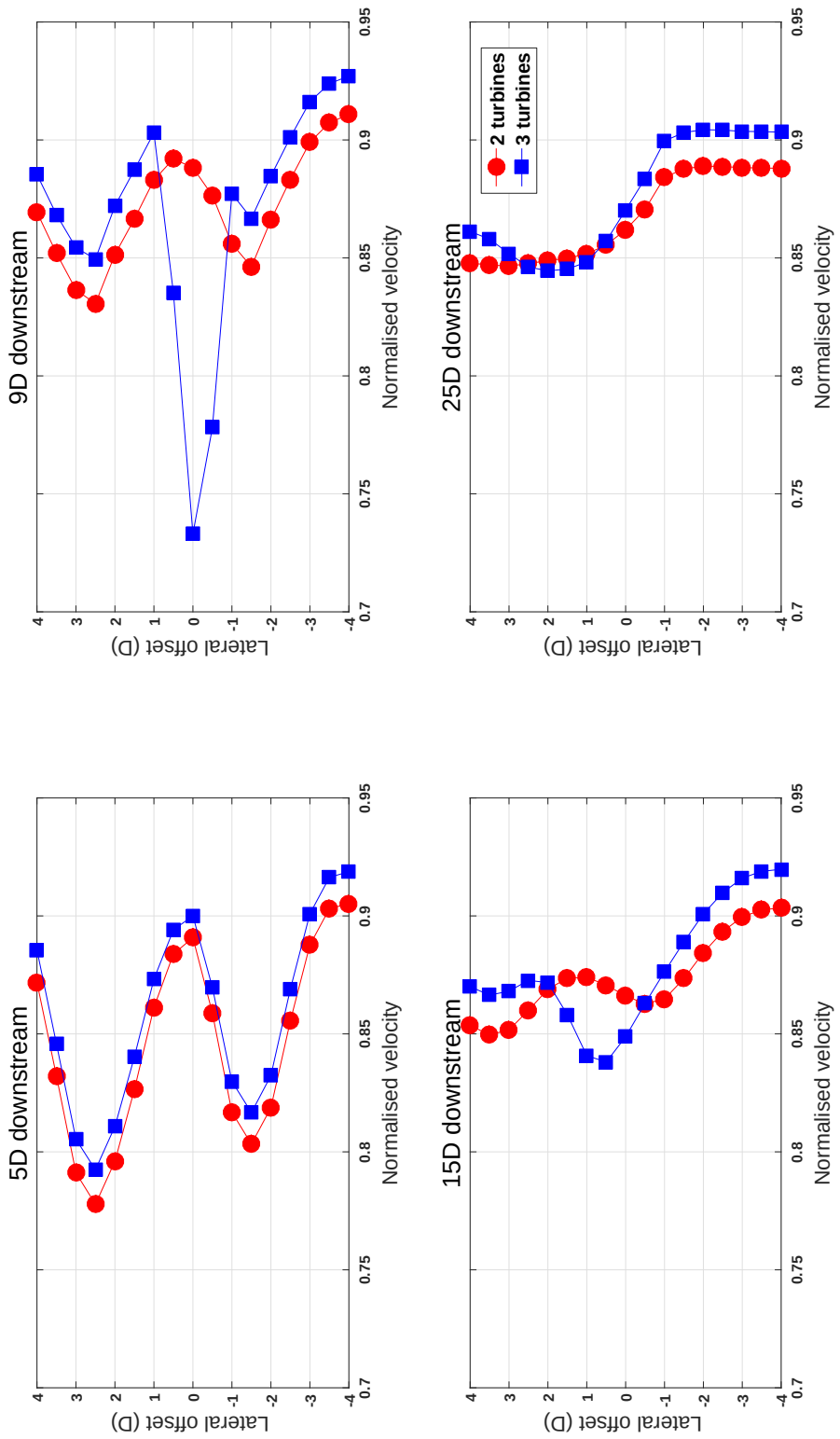

Figure 7.19: Comparison of lateral mid-channel depth velocity reduction between two and three turbines arrangement at increasing downstream distances.

between 2D and 3D) experiencing slightly faster current than the other device. In fact, this observation further complements the initial actuator disc assessment carried out in Section 7.3 that analysed the velocity flow contours generated from the devices' interaction in the small arrays. Next, for the three device arrangement at 9D position, the flow behind third disc undergoes a velocity reduction of approximately 25%, while the wake deficit experienced by the upstream devices is about 10%.

Further downstream at 15D location, although the wake from the three turbine set up is still visible from the plots, it bears close resemblance to the two turbine configuration, indicating close wake recovery rate for both arrangements at this point. Finally, disparities between the two models are no longer distinguishable by the 25D downstream distance, which implies that the flow has completely recovered and achieved the ambient velocity at this position.

To sum up, flow interactions due to the presence of two and three devices in a regional scale study have been successfully demonstrated, where the existence of a downstream disc has a noticeable impact on the general wake formation, albeit the difference is rather imperceptible. Notably, using the current array configuration, wake interference between the upstream and downstream devices has been greatly minimised. As a result, the downstream device will experience higher incoming flow velocity, hence producing more power per device within the arrays. Henceforth, this turbine's configuration/spacing has proven to be reliable and could be used for any array-related research in future.

7.4.4 Sensitivity of the vertical resolution

The sensitivity of the applied vertical resolution for the ocean scale model is explored in this section. The source code was appropriately altered to update the position of vertical layers to be used in current simulation, where the number of horizontal planes were reduced from 13 to just 9 layers. Graphical information for the modified horizontal planes is displayed in Figure 7.20, with the position of each fixed plane and its corresponding depth is clearly portrayed. In contrast with the default 13-layer model where the disc swept area was represented by seven planes, the model used here only has three horizontal planes that intersected with the disc's features.

From the figure, it can be seen that the disc is practically confined within layers four and six, while another solitary plane is fixed at the centre of the disc. Furthermore, reducing the number of model's layers also translates into a significantly smaller node

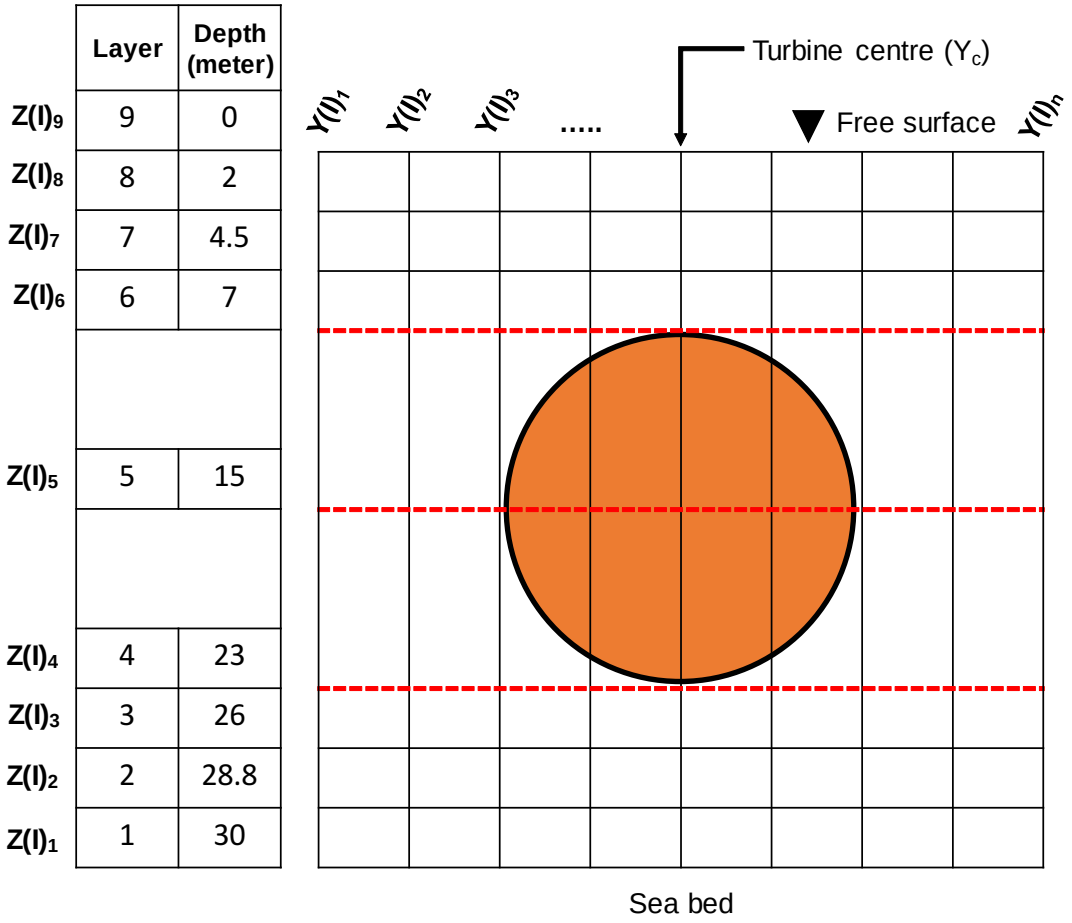

Figure 7.20: Graphical information exhibiting the modified horizontal planes (9 planes instead of the default 13 layers) used in the numerical model. The corresponding planes that crossed the disc surface area are clearly displayed. Note that this figure is not drawn to scale.

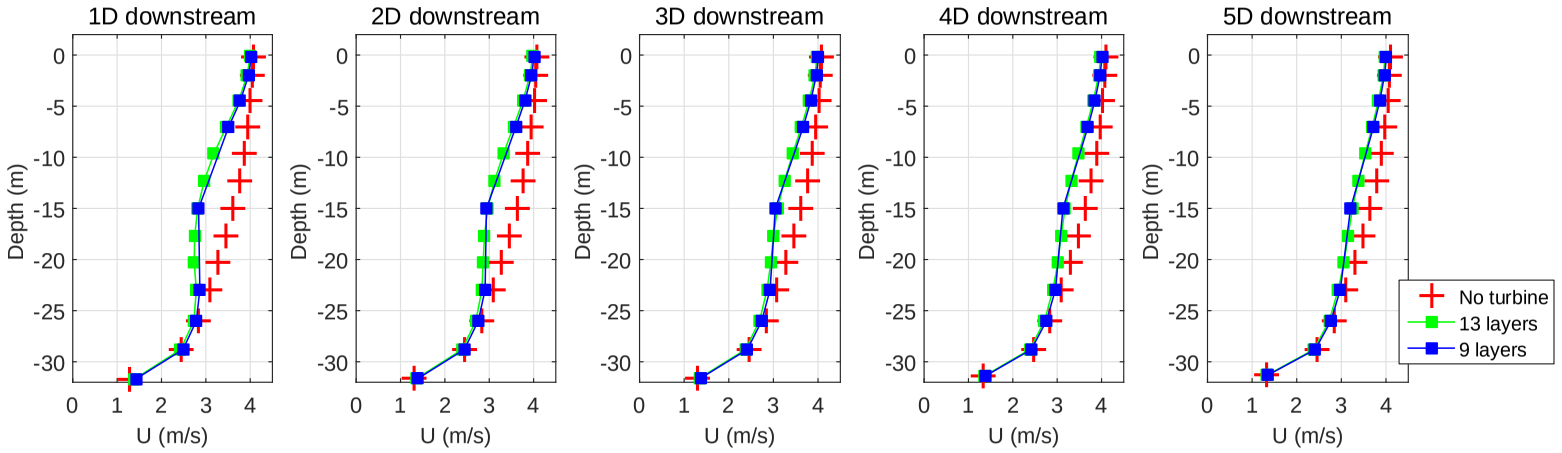

(a) Velocity reduction across shorter downstream distances for different σ layers.

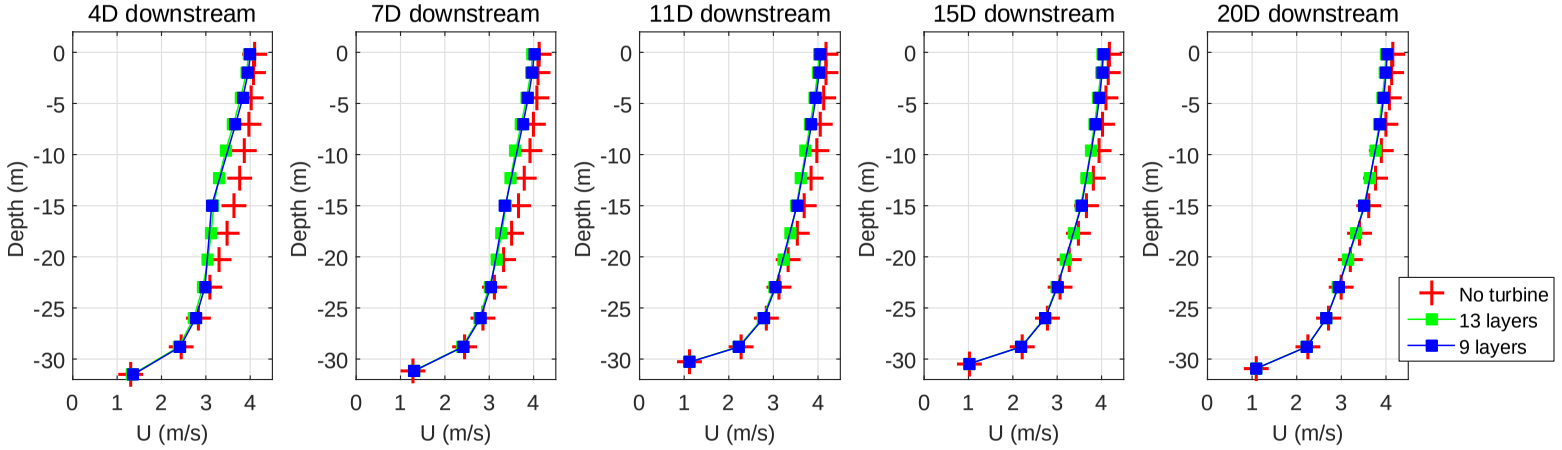

(b) Velocity reduction across longer downstream distances for different σ layers.

Figure 7.21: Influence of the vertical resolution (9 vs default 13 layers) on the modelled actuator disc. The results shown here are for the single turbine configuration.

counts within the domain. For instance, the model utilising the 9 horizontal planes comprised 243,900 nodes - about 100,000 less than the default 13-layer domain. This in turn improved the model computation time because of the reduced load on the processing unit. Nevertheless, other parameters such as structured grid density, resistance coefficient of the disc, hub/centreline depth etc. are maintained using the default parameters presented in Section 7.2.

The comparison between the two models (9 vs default 13 layers) for a single turbine set up is illustrated in Figure 7.21, where outputs from the model using 9 vertical layers consistently matched the velocity profile shown by the default model at all downstream distances. Although this observation seems to be in accordance with the findings presented in the idealised channel study (Section 5.5.6), it still comes as a surprise considering the substantially larger margin imposed between the vertical planes across the disc swept area.

As demonstrated in both Figures 7.20 and 7.21, for the 9-layer model, horizontal planes positioned on the top and bottom of the disc's edges were set to be at the same depth as used in the 13-layer model. This signifies that the spacing between the three intersected layers across the actuator disc features is about 8 meter apart, which is a very substantial margin for depicting a 16 diameter circular disc. As a result, the number of nodes that are available within the disc swept area for computing the momentum source term are also greatly reduced, as aptly represented by the intersecting y and z planes in Figure 7.20. Nonetheless, as shown by the plots in Figure 7.21, even under this circumstance (i.e. less nodes across disc swept area), the applied actuator disc momentum source term has proven to be very resilient and robust in imitating the force exerted by the device on the flow.

With this in mind, however, it is still imperative to approach the results presented in Figure 7.21 with caution. As demonstrated by Figure 5.9 in the idealised channel study, the impact of varying vertical layers was more evident on the turbulent intensity plots rather than the wake profile graphs. For that reason, assuming that turbulent profiles for the regional scale study are also sensitive to the changes in vertical resolution, it is imperative to avoid using horizontal interval that is too wide when defining the disc's surface area/features. This aspect will be considered in a future study, where it is hoped that the TI from the actuator disc can be properly calculated and analysed.

Figure 7.22 is then plotted to further understand the impact of varying the vertical resolution on the flow interactions for the 3-turbine configuration. The results shown are for the lateral velocity reduction experienced by the device at mid-channel depth for

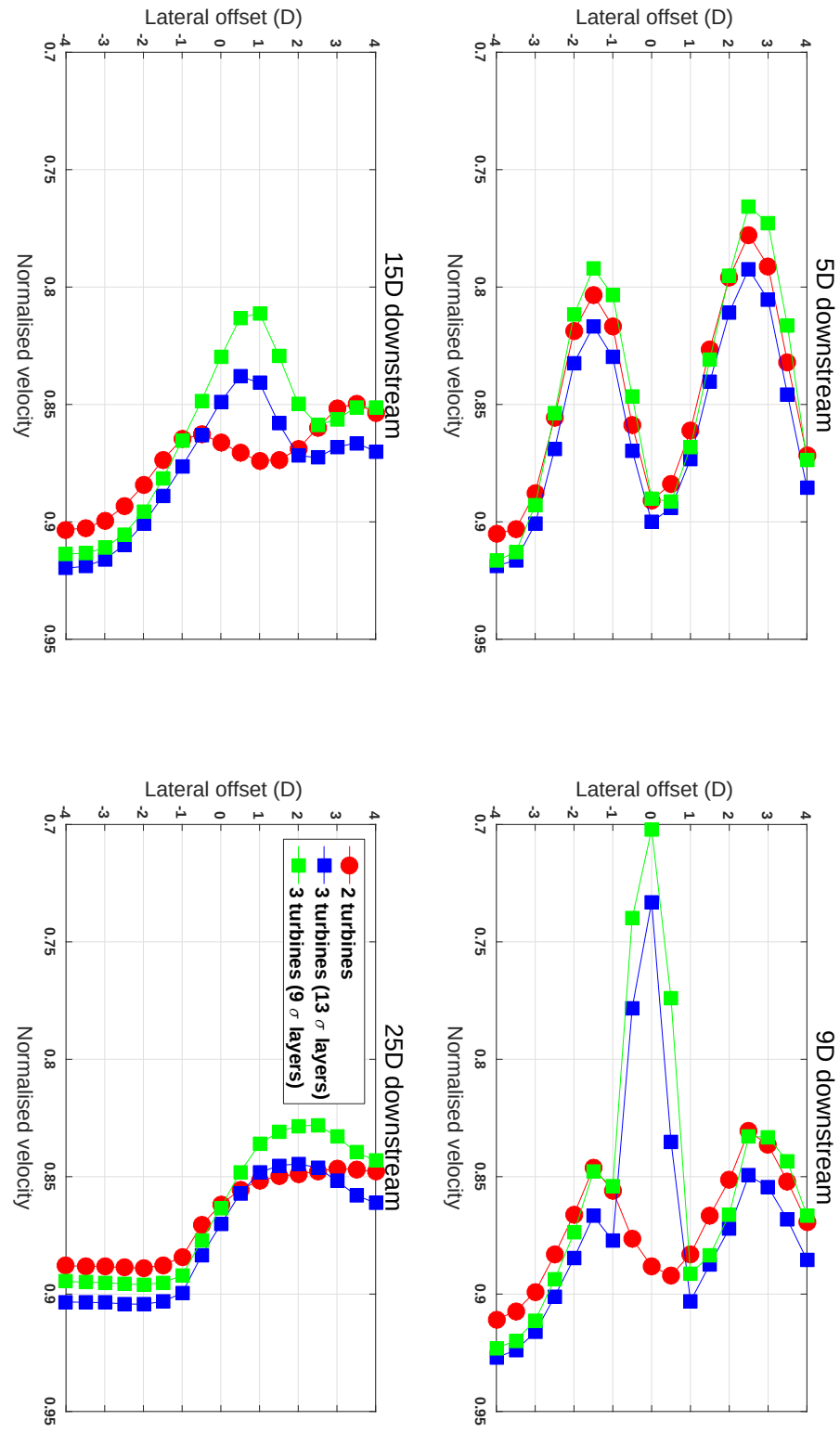

Figure 7.22: Comparison of lateral mid-channel depth velocity reduction between two and three-turbine configurations (13 vs 9-layer) at increasing downstream distances.

three distinct models - 2 and 3-disc configurations using 13 planes, and 3-disc configuration using 9 planes. Interestingly, although both models demonstrate similar lateral wake profiles from 5D till 25D downstream distances, very small velocity variations are detected between the 9 and 13-layer models. These discrepancies (between 3% to 5% at most) seem to vary from one position to another, and are not that obvious from the plotted wake profiles across the water depth in Figure 7.21.

To better illustrate the influence of the vertical profiles on the model outputs, flow contours of the mean velocity difference between the two distinct horizontal planes for the single and three disc arrangements are generated. Figure 7.23 provides a clearer graphical information on the disparity observed between the models, where it can now be firmly concluded that the vertical resolution used in defining the disc features does have an influence on the model's outputs. Both Figures 7.23a and 7.23b, for the single and three turbine set up respectively, display a slightly smaller average current velocity of about 0.1 m/s from model using the 9 vertical planes. Crucially, this observation also confirms the findings on lateral wake characteristics shown previously in Figure 7.21.

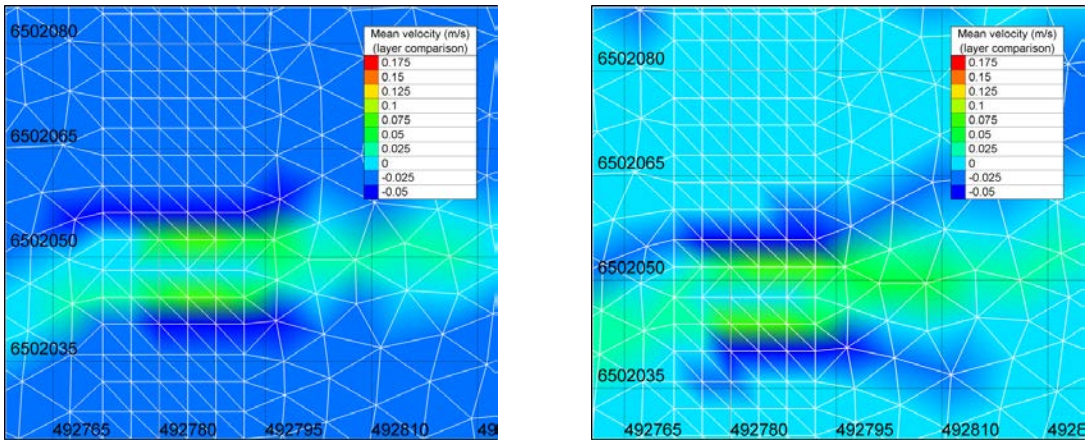

(a) Single turbine set up.

(b) Three turbines set up.

Figure 7.23: Comparison of the mean velocity difference for two distincts horizontal planes (9 vs default 13 layers) for the single and three turbine configurations.

In short, this particular study has demonstrated that the model's vertical resolution does have an influence on the outputs for a regional scale simulation, although its impression on the wake profile characteristics (both laterally and longitudinally) is rather minuscule. Nevertheless, the results shown in this section are also rather inconclusive. For instance, although the tested model with smaller number of vertical layers has consistently followed the wake profiles trend shown by the default model set up, its velocity deficit seems to vary from one downstream position to another. However, this

could probably be due to the inherent limitations of the RANS model which provides an averaged-numerical output during the stipulated time step.

Additionally, although it is evident from this study that the 9-layer model could yield an excellent agreement against the predicted wake velocity from that using the default horizontal planes, similar observations cannot be confidently applied to its turbulence profiles. Since the idealised channel studies in Chapters 5 and 6 have demonstrated that the impact of varying the vertical layers was more evident on the computed turbulent intensity rather than on the predicted wake profiles, this highlights the importance of finding optimal/suitable margins for the horizontal planes used specifically in defining the actuator disc swept area.

7.5 Models' sensitivity and validation: 2 meter structured grid

Influence of Δx and Δy used in the ocean scale model is scrutinised in this section. As previously discussed, increasing the grid density for the disc enclosure may help provide more accurate model outputs, since this will increase the number of nodes available to refine the actuator disc's swept area features. However, depending on the vertical resolution of any particular 3D model, increasing the grid density will also undoubtedly increase the required processing power and a computation time. Considering these two obvious constraints, only one other structured grid size can be tested within the current research frame - the 2 meter structured grid size (which will be referred to as $\Delta 2m$ henceforth).

At the time of models' simulation, this is the smallest structured grid size that could be used on the numerical domain using the default parameters as given in Section 7.2. The models were run on the VLX cluster using 10 parallel processors. Nonetheless, since the simulation for the $\Delta 2m$ model requires huge computational resources and is extremely time consuming, its running period was set to 14 days instead of 35 days employed previously for the 4 meter structured grid size models (which will be referred to as $\Delta 4m$ henceforth). For reference, it took about 30 days in average to finish the model's computation, highlighting the limitation to prolong the simulation time.

Comparison between the two domains/mesh sizes is presented in Table 7.4, and just like before, results shown on the plots were extracted during spring tide period. To ensure model's stability, the time step used for the $\Delta 2m$ model was reduced by 1 second.

Additionally, it also used similar actuator disc set up as discussed in Section 7.2.1, albeit Δx and Δy intervals that are now twice as smaller as before. Consequently, node counts for the $\Delta 2m$ domain also increased substantially by more than 350,000 than the one used previously for $\Delta 4m$ studies.

Table 7.4: Comparison of simulation parameters and domain properties between the 4 meter and 2 meter structured grid density.

	4 meter structured grid	**2 meter structured grid**
Time step	2 second	1 second
Graphic printout period	10 minutes	10 minutes
Simulation period	35 days (1,512,000 seconds)	14 days (1,209,600 seconds)
Node counts	352,300	549,432
Element count	615,432	979,368

7.5.1 4 meter vs 2 meter grid density

Figure 7.24 examines the relationship between the two tested grid densities and their influence on the predicted wake. This figure used the outputs from the three turbines configuration from both $\Delta 4m$ and $\Delta 2m$ models, with Δx_t set to 8 meter. Interestingly, both models only show subtle and almost indistinguishable differences on the plotted wake profiles at shorter downstream distances (Figure 7.24a), although the $\Delta 2m$ model seems to demonstrate a slightly lower reduction in the plotted velocity. Further downstream, pass the 11D position, discrepancies in the generated wake profiles are no longer noticeable once the wake fully recovers as shown in Figure 7.24b.

These results are consistent with the one observed in the small channel study, where both 4 meter and 2 meter structured grid models displayed nearly identical outputs. This proves that there is very little to differentiate between $\Delta 4m$ and $\Delta 2m$ outputs, provided that the models' numerical parameters (e.g. vertical resolution) are consistent to one another. Next, Figure 7.25 is plotted to inspect the lateral mid-channel depth velocity reduction for both grid sizes.

From the graphs, $\Delta 2m$ model can be seen to have a slightly lower velocity deficit than the 4 meter grid size at all downstream positions, which is consistent with the flow profiles exemplified in Figure 7.24. Besides, the normalised velocity variation between

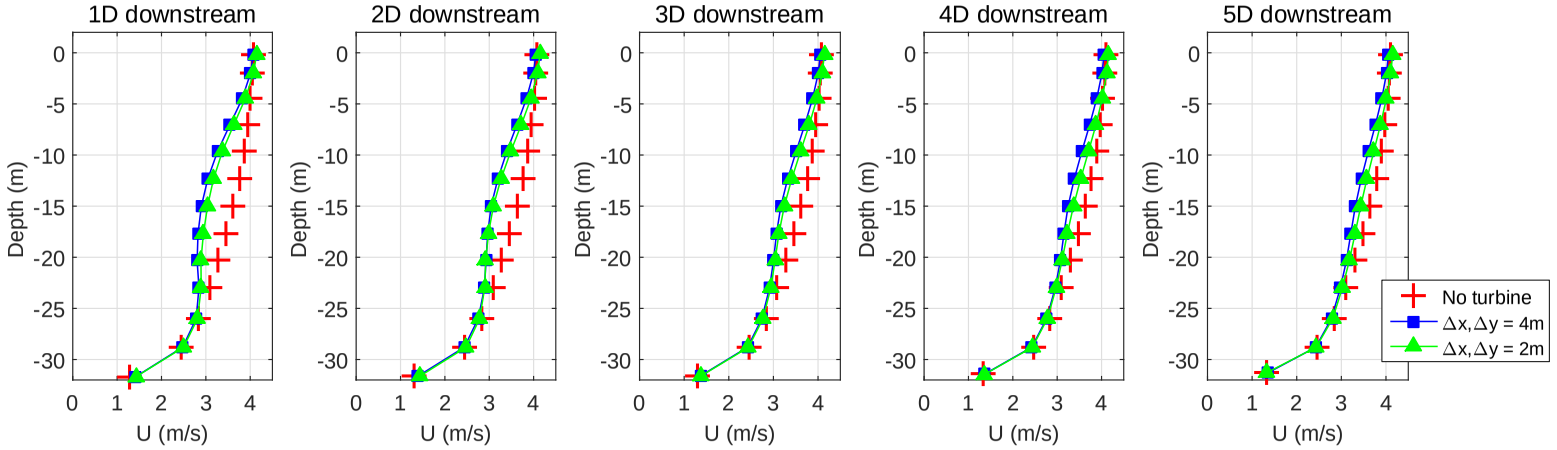

(a) Velocity reduction across shorter downstream distances for different grid densities.

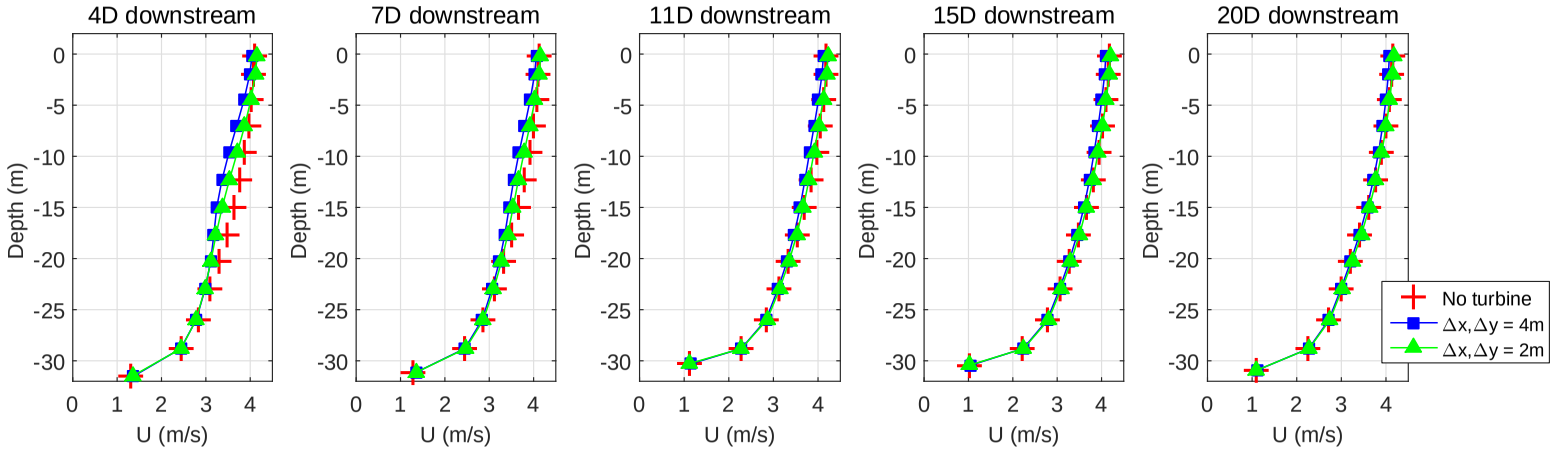

(b) Velocity reduction across longer downstream distances for different grid densities.

Figure 7.24: Comparison of the wake characteristics between 4 meter and 2 meter structured grids ($\Delta x, \Delta y$) for various downstream distances. The plotted velocity reduction are from the single downstream turbine positioned in the second row of the three-turbines arrangement.

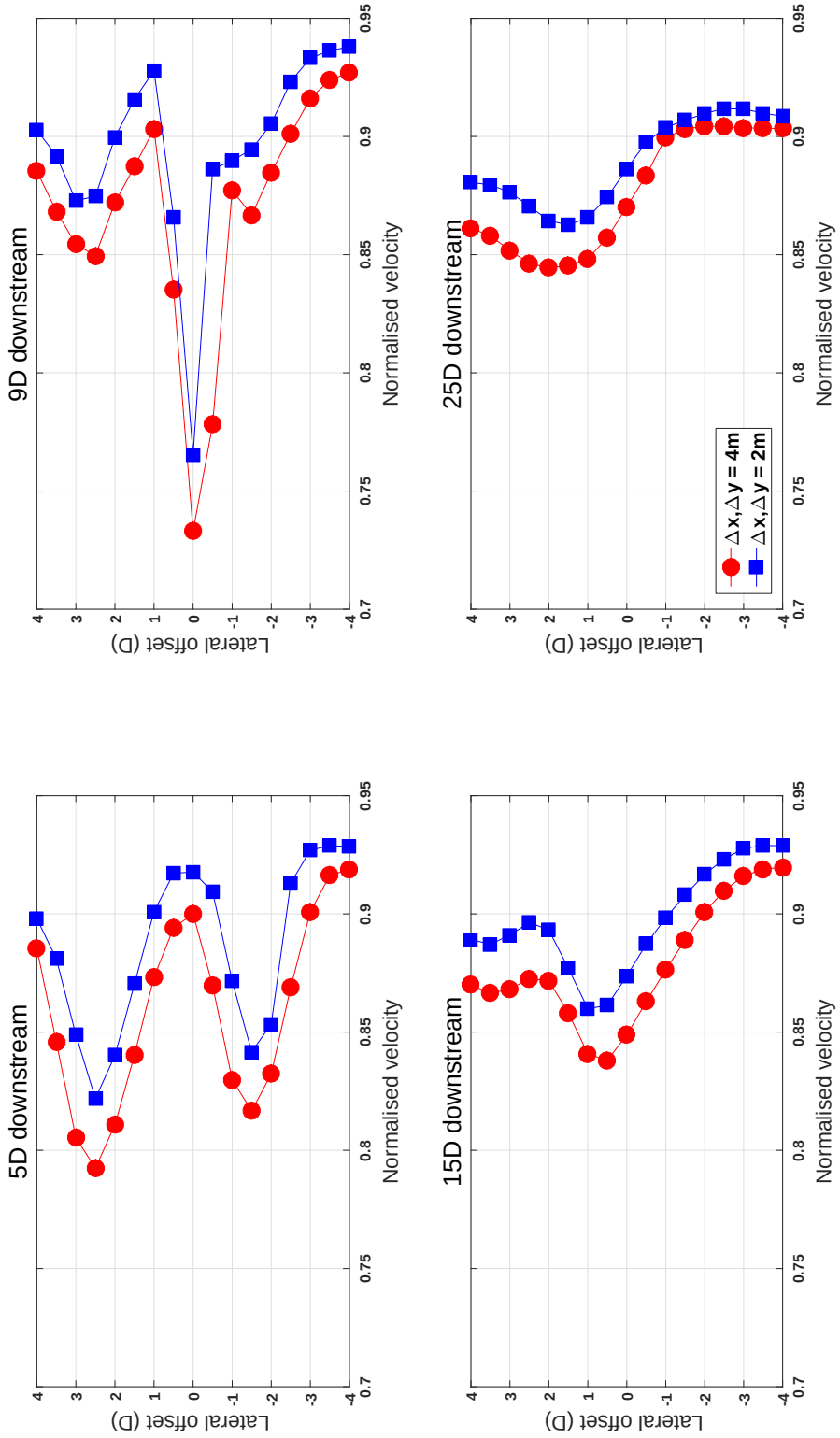

Figure 7.25: Comparison of lateral mid-channel depth velocity reduction for models employing $\Delta x, \Delta y$ = 4 meter and 2 meter at increasing downstream distances. The plotted velocity reduction are from the single downstream turbine positioned in the second row of the three-turbines arrangement.

the two models are also rather small, at about 0.025 (~0.1 m/s), and is uniform from the near until far wake distances.

Nevertheless, the outputs observed from these two figures seem to contradict the findings from the idealised channel study (refer to Figure 5.7), where the use of a smaller structured grid density had caused more energy to be extracted from the flow. Indeed, this resulted in a significant overestimation of the predicted velocity reduction of the models. Besides, this finding was attributed to the considerable number of node counts available within the disc swept area when a highly refined grid density was employed, causing the applied source term to be very receptive to changes in current velocity.

Hence, it is rather unexpected when the largest velocity reduction in this regional scale model is caused by the $\Delta 2m$ model instead of $\Delta 4m$. More significantly, without TI plots, no definite basis can be provided to explain this disparity observed between the small and large scale studies. On the positive side, implementing such a small grid size (e.g. 2 meter or lower) in order to define the turbine enclosure is probably not suited for the regional scale actuator disc approach for two reasons.

First, the purpose of this method is to speed up the process of approximating the flow and array interactions, where the the focus area is mostly in the far wake region, and not at the exact location of the devices. Secondly, utilising a highly refined domain mesh when running any 3D regional scale model would certainly require access to the computer clusters. Even so, the resources needed to handle such computational load would be rather extreme and impractical to say the least.

Thus, from the results presented here, $\Delta 4m$ model has demonstrated to be the optimal grid size in implementing the actuator disc within a regional scale simulation, where it was able to replicate the anticipated wake characteristics. Equally important, this grid density has also been proven to be computationally efficient in both small and large scale studies. With that in mind, based on the presented results (from previous and current studies), it is recommended to use the $\Delta 4m$ as the baseline grid size in the application of actuator disc source term for regional scale modelling.

7.5.2 Influence of disc thickness

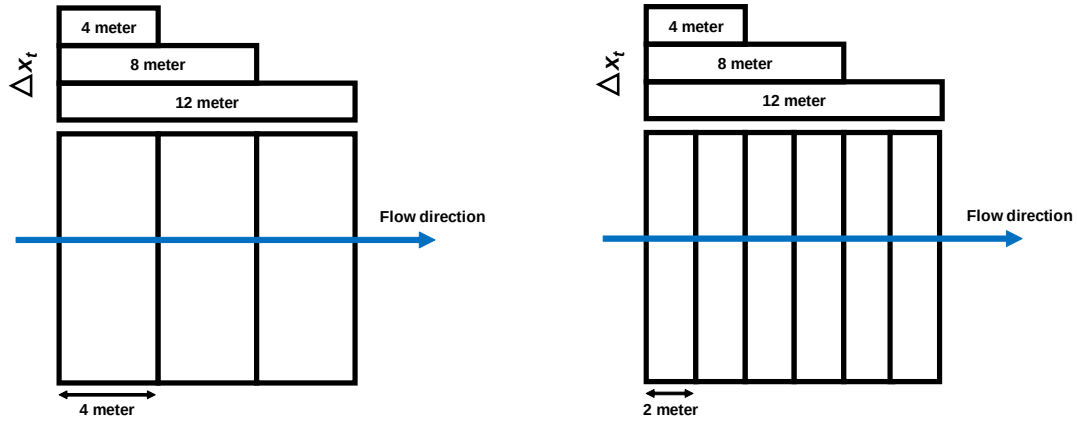

(a) Δx = 4 meter. **(b)** Δx = 2 meter.

Figure 7.26: Graphical illustration of the disc thickness and their corresponding grid sizes for both 4 meter and 2 meter structured grid density.

For this test, the $\Delta 2m$ model was then run using three distinct turbine thickness values - Δx_t = 4 meter, 8 meter and 12 meter. For clarification, when Δx_t is set to 8 meter, the flow will have to pass through four Δx grid cells (each cell interval is 2 meter in the x direction where the momentum source terms will determine the forces exerted by the turbine). Figure 7.26 provides graphical illustration of the disc thicknesses and their corresponding grid sizes for both 4 meter and 2 meter structured grid density. Next, the comparison plots of the three tested Δx_t are illustrated in Figure 7.27. Interestingly, the results show that the thickness of the actuator disc used on $\Delta 2m$ model has an almost negligible impact on the formation of downstream wake, albeit Δx_t = 4 meter showing minuscule overestimation at 1D till 3D distances.

Nonetheless, the findings from both $\Delta 4m$ and $\Delta 2m$ disc thickness studies offer interesting insights for discussions. While the three Δx_t values tested on the $\Delta 2m$ model demonstrate an almost identical output that is consistent across the downstream distances, the $\Delta 4m$ model exhibits varying velocity outputs for similar Δx_t values. As shown in Figure 7.18, the greatest variation on $\Delta 4m$ model was caused by disc thickness of 4 meter, while outputs from model using Δx_t equal to 8 meter and 12 meter displayed an almost identical plots as observed on $\Delta 2m$ model.

This distinction shown by Δx_t = 4 meter for both $\Delta 4m$ and $\Delta 2m$ models could perhaps be elaborated using Figure 7.26. For the 4 meter structured grid domain, only a single grid cell is involved when Δx_t is set to 4 meter. On the other hand, the 2 meter structured

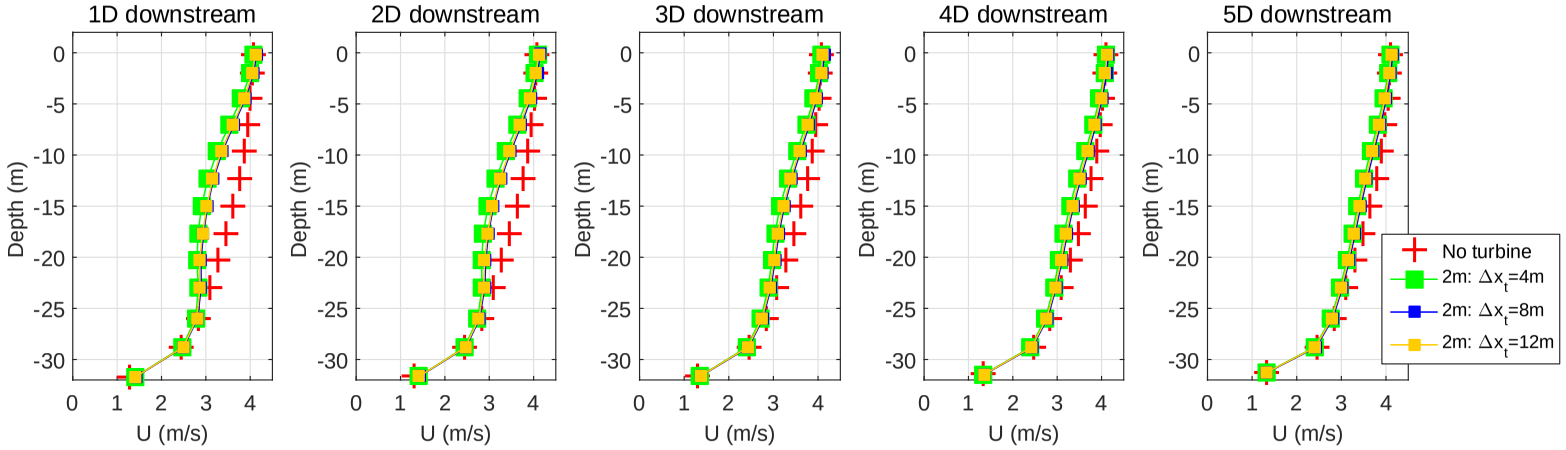

(a) Velocity reduction across shorter downstream distances for three distincts Δx_t .

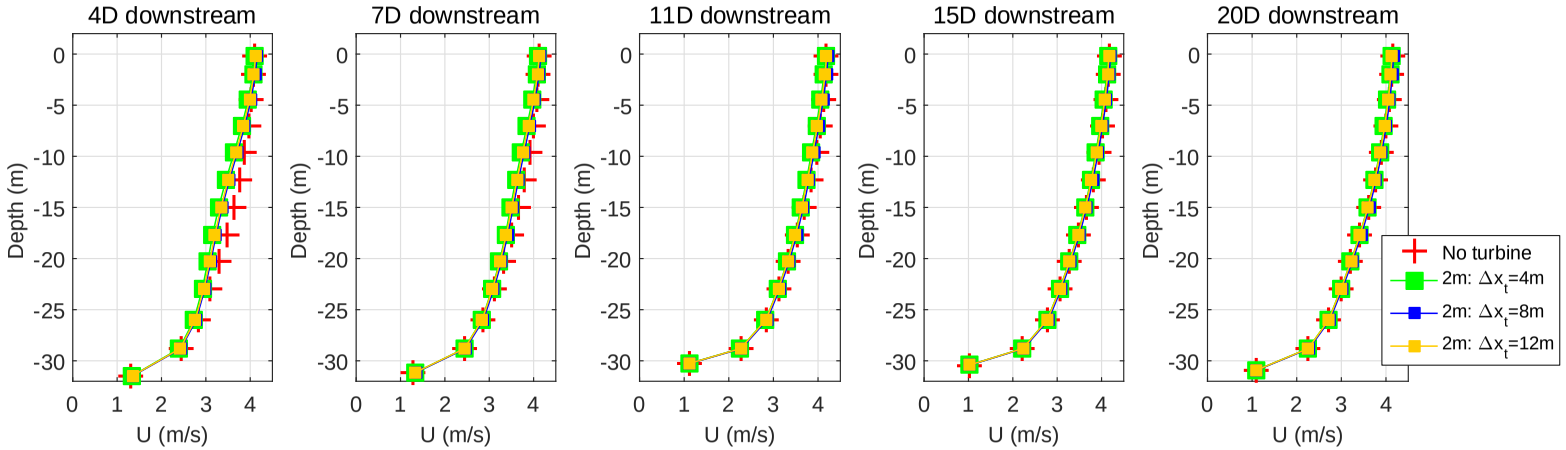

(b) Velocity reduction across longer downstream distances for three distincts Δx_t .

Figure 7.27: Comparison of the wake characteristics between distinct actuator disc thickness for various downstream distances. The plotted velocity reductions are from the single downstream turbine positioned in the second row of the three-turbines arrangement ($\Delta x, \Delta y$ = 2 meter).

grid domain requires two cell intervals for similar Δx_t value. Hence, this proves that the resistance loss coefficient (K / Δx_t) and structured grid density (Δx,Δy) are two parameters that are interdependent in imitating the force experience by tidal turbine.

From the results presented here, it can be deduced that the value of Δx_t applied in the programming code must at least be twice the size of Δx employed at the actuator disc locations to ensure that the disc's thickness would cover a minimum of two cell sizes in computing the momentum source term. This is crucial to make certain that the flow crosses at least two mesh cells to correctly represent the pressure drop created by the actuator disc. To conclude, the sensitivity analyses conducted for both small and large scale actuator disc studies have shown that the results in the far wake are fairly independent of the applied turbine thickness as long as the flow crosses at least two mesh/grid cells (i.e. Δx intervals that constitute the width of an actuator disc).

7.6 Discussion

A study to examine the sensitivity of parameters involved in the implementation of the RANS actuator disc approach in a 3D regional scale model has been discussed and presented. The actuator discs were implemented at an actual deployment site within the Inner Sound region of the PFOW following the methodology introduced in previous chapters. Guidelines provided by EMEC was also followed in setting up a 16 meter in diameter actuator disc model to provide realistic working and hydrodynamic conditions experienced by tidal devices in operation.

Notable limitations in this study include the absence of any in situ measurement data to be used for comparison purposes; hence the wake profiles and flow characteristics from published literature for the idealised channel study were utilised as the baseline in analysing outputs from the regional scale model. Additionally, since the use of $k-\varepsilon$ model requires more computational power and processing time, a combination of Smagorinsky and constant viscosity turbulent models was instead used. Consequently, the turbulent characteristics (in terms of its intensity) could not be computed and presented as the chosen models have no turbulence components.

An examination of the generated velocity difference contours for a number of turbines/arrays configurations highlighted the robustness of the applied momentum source code using the TRISOU subroutine, where appropriate wake characteristics and flow interactions have been successfully reproduced. Further, a comparison between two distinct Δx_t illustrated that the size of disc thickness employed in the source have

an obvious influence on the numerical outputs. Not only that, the presented velocity contours also confirmed the asymmetrical nature of the tidal currents observed in the PFOW [193] due to the complex topography in the area. Whereas the present study only scrutinised the flow conditions during spring tide period, it was safe to assume that the model should also be able to properly imitate the forces exerted by the device on the flow during neap tide.

In general, the plotted velocity reductions from the regional scale actuator disc model illustrated a much smaller deviation from the original velocity profile (i.e no turbine model) when compared against the small scale idealised channel model. While the largest velocity reduction observed in the small scale study was about 1.2 m/s, the greatest flow deficit shown by the regional scale model was only close to 0.5 m/s. Nonetheless, this could be due to the fact that the regional scale actuator disc model was experiencing a much larger free-stream velocity, hence increasing its rate of far wake re-energisation.

Comparison of the velocity deficit for three Δx_t values showed that there was noticeable impact when varying the turbine width, proving the initial observation from the plotted velocity contours. Nonetheless, its influence was only apparent in the near wake regions (1D-5D downstream distances), chiefly by model imposed with the smallest thickness possible (i.e. $\Delta x_t = 4$ meter). Next, although it was anticipated that resolution of the vertical layers would have an affect on the numerical outputs, its impression on the wake profile characteristics (both laterally and longitudinally) was rather minuscule. More significantly, without TI plots to corroborate these findings, the presented results were rather inconclusive.

It has also been demonstrated that using a smaller structured grid density (i.e. 2 meter grid) for the disc enclosure resulted in smaller reduction in current flow (~0.1 m/s), although this contradicted the findings from the idealised channel study. Nonetheless, the sensitivity study conducted on $\Delta 2m$ model for the influence of Δx_t has highlighted that the applied disc thickness in the momentum source term should cover a minimum of two Δx grid intervals to ensure that pressure drop created by the actuator disc is properly accounted. In fact, even with access to computer cluster, it was suggested that the optimal structured grid density (Δx,Δy) for implementing the actuator disc to be 4 meter, with the device width (Δx_t) set to 8 meter. Employing grid density smaller than 4 meter not only would require extreme computational power, but also inducing longer simulation time.

Chapter 8

Summary and Suggestions for Future Work

The research project described in this thesis is primarily aimed at exploring the methodology on implementation of the 3D actuator disc-RANS model for an ocean scale simulation. Of particular interest was the robustness, as well as the sensitivity of the applied momentum source term and its validity in representing a full-size tidal turbine. To achieve the intended objectives, the outputs from this work were grouped into three classes - (a) hydrodynamic analyses of the PFOW region using two distinct and free-to-use software, namely Telemac3D and Delft3D; (b) small idealised channel studies to explore the sensitivity of the actuator disc momentum source term; (c) regional scale actuator disc simulations to inspect the validity and robustness of the applied momentum source term.

This chapter summarises the key findings of this research study, and suggests future work to be undertaken which would further deepen and widen knowledge and improve confidence in these findings.

8.1 Hydrodynamic simulations of the Pentland Firth

Appropriate methods in developing a 3D tidal flow model for the PFOW region using two commonly used hydrodynamic software, namely Telemac3D and Delft3D, were thoroughly highlighted since they were not described in detail in any previous studies. Great care was taken to ensure the robustness of the models, and the predicted values were validated against the observed data supplied by the TeraWatt project to give confidence to the model.

However, it is imperative to highlight that this field data suffered from 'knock-down' at times of peak current speed, which caused some uncertainty regarding the reliability

of the dataset. At the time of writing, new sources of data for the Pentland Firth and Orkney Waters, specifically for the Inner Sound region, have recently become available and were discussed in the following documents [134, 187].

Results from both Telemac3D and Delft3D models demonstrated that the physical and numerical parameters used for the simulations worked well. Among the tested bed friction values for Telemac3D models, Cd = 0.005 produced the best results. Conversely, Cd = 0.0086 provided the best agreement with the measured data for Delft3D models. The observed difference in the Cd values from the two models, as well as from the literature could be attributed to several factors, such as:

- choice of boundary conditions and the grid size.
- option of spatial resolution and bathymetry data employed by the model.
- choice of numerical approach - (i.e. unstructured mesh in Telemac3D (finite element model) and structured grid in Delft3D (finite difference approach)).

Constructing a proper tidal flow model for the Pentland Firth region was crucial as it provided preliminary analyses of the efficiency of both numerical models to produce accurate 3D flow characteristics. Furthermore, this study also prescribed the groundwork for the next stage of this research, which involved inserting tidal devices into the numerical models. For this purpose, Telemac3D was chosen as the preferred modelling tools in the implementation of tidal turbines in this region due to the model's capability to perform parallel computing, as well as its flexibility to employ both structured and unstructured mesh in its numerical domain.

8.2 Actuator disc approach in an idealised channel

The efficiency and robustness of the applied actuator disc momentum source code in representing a 20-meter diameter tidal turbine in a small idealised channel, for both single and multiple-turbine configurations, had been examined using the Telemac3D numerical model. Further, simulation outputs were compared against published experimental data from a small-scale flume in order to provide confidence in the numerical models. The non-dimensional parameters employed in the comparison of wake characteristics were the velocity deficit and turbulence intensity, and both had been successfully replicated by the actuator disc model across the lateral and longitudinal distances.

Both hydrostatic and non-hydrostatic assumptions were tested, and it was shown that the hydrostatic model failed to resolve the turbulence in the bottom third of the channel.

Nonetheless, overall influence of the non-hydrostatic model on the flow profiles was found to be rather marginal. One key difference in the implementation of a large scale actuator disc model was the inability to use the no-slip condition for the bottom wall, which required a highly refined vertical mesh, predominantly near the bottom to satisfy the wall function.

For the structured grid used in defining the enclosure of the actuator disc, coarser grid sizes were shown to be unable to accurately approximate the thrust force experienced by the disc. In particular, the study also illustrated the importance of finding a balance between computational efficiency and numerical accuracy by employing an optimal ratio between the nodes resolution in both lateral and longitudinal directions. Apart from that, the impact of the value of resistance coefficient, K in imitating the thrust force exerted by the physical device had also been positively reproduced by the model.

In like manner, excellent results were also obtained for the simulation of turbines' interaction in a small array, where the wake recovery profiles shown by the actuator disc model matched the characteristics observed experimentally. Two sets of arrays configurations were tested; the first involved a single row set up with only two turbines, while the other was for two rows arrangement, with a single-staggered device located 3D downstream of the upstream pairs. For the single row set up with largest disc separation, the lateral and longitudinal velocity deficits shown by the model reasonably matched the experimental data. On the other hand, noticeable discrepancies in the near wake region were observed for models using a smaller disc inter-space, highlighting some limitation of the 3D-RANS actuator disc model in simulating complex processes in the immediate proximity of the devices.

Next, the inclusion of a downstream turbine (in staggered position) in the array further demonstrated that capability and efficacy of the applied momentum source term. The models were able to accurately reproduce the wake profile that was comparable with published data, although a marginally slower flow across the longitudinal distance was exhibited by the actuator disc model. More importantly, interaction between the upstream and downstream discs was also satisfactorily simulated, in which the blockage effect experienced by the downstream disc, as well as the diminishing return of upstream wake profiles, were clearly manifested.

To emphasise, the findings from this research work clearly demonstrated the capability of the administered actuator disc momentum source term to successfully reproduce the wake characteristics and interactions between single and multiple turbines arrangement as shown by the experimental data, albeit with slight discrepancies in the predicted

velocity downstream of the disc. Nevertheless, the discrepancies observed in this study were to be expected for the following reasons:

- the comparisons were made between two contrasting scales – very small porous disc (0.1 meter in diameter) from the published experimental set up, and a 20-meter diameter disc for the numerical simulation.
- some of the model input parameters (e.g. inlet turbulent levels) adopted in this study were only an approximation based on the published flume set up.

All things considered, this study had provided clear understanding into the simulation of a full-size turbine via the actuator disc, where key numerical parameters involved in implementation of the source term were investigated and analysed. More importantly, this study also served as an important baseline in setting up the regional scale actuator disc model undertook in subsequent research work.

8.3 Actuator disc approach in a regional scale model

Using interchangeable methodology that was employed in setting up the idealised channel model, a modified actuator disc momentum source term was implemented into a regional scale simulation using the Telemac3D numerical model. The chosen location for the deployment of tidal turbines in this study was the Inner Sound region of the Pentland Firth, which is a commercial site for installations of tidal energy array. Notably, based on the guideline provided by EMEC and turbine design by the developers, actuator disc with a diameter of 16 meter was simulated in this study.

Four main constraints encountered in this study were; (a) the absence of measurement data for calibration and comparison purposes (b) inability to apply the $k-\varepsilon$ turbulent model since it requires tremendous computational power and extended simulation time (c) inability to compute and analyse the turbulence intensity levels due to the choice of turbulent models (d) extremely long computational time. Each simulations took over a month to finish, hence limiting the amount of parameters that could be examined in current study.

The default structured grid size employed to define the disc's enclosure was set to 4 meter, while the maximum number of turbines simulated was 32; 11 turbines in row 1 and 3, and 10 turbines in row 2 using staggered configuration. The turbine was assumed to be in a fixed position with no yaw capability. Additionally, the default device width/thickness was set to 8 meter. Using commonly used design values from

literature, the turbine's thrust coefficient was set to 0.8, while values of 1 m/s and 2.5 m/s were adopted for the device's cut-in and rated velocity respectively.

In the absence of in-situ measurement data, the task at hand was to ensure the validity and accuracy of the implemented momentum source term, and by extension - results produced from the numerical models. To achieve this, contour plots illustrating the difference in velocity caused by the actuator disc model were generated, along with plots of velocity deficit, as well as graphs of normalised velocity in lateral directions.

In general, the plotted velocity reduction for the regional scale actuator disc model illustrated a much smaller variation when compared against the small scale idealised channel model. While the largest velocity reduction observed in the small scale study was about 1.2 m/s, the greatest flow deficit shown by the regional scale model was only close to 0.5 m/s. Nevertheless, since current flow at the real deployment site is known to be highly turbulent and fast moving, this could have had an influence in increasing the rate of far wake re-energisation. Interestingly, although resolution of the vertical layers was predicted to have an impact on the outputs of numerical models, its impression on the wake profile characteristics (both laterally and longitudinally) was rather negligible.

Additionally, a comparison on the velocity deficit for three disc thickness values demonstrated that the turbine width had an apparent impact, corroborating the preliminary analysis from the plotted velocity contour. Nonetheless, its influence was only apparent in the near wake regions, chiefly by model imposed with the smallest thickness possible (i.e. 4 meter). Moreover, a brief overview on the comparison between 4 meter and 2 meter structured grid sizes was also provided in this study. However, the results seemed to contradict the findings from the idealised channel study, where the use of a smaller grid size for the disc's enclosure in a regional model had caused higher velocity deficit. To emphasise, without the turbulent intensity plots to corroborate these findings, no definite basis could be provided to explain this disparity observed between the small and large scale studies.

This research work had highlighted that the applied disc thickness in the momentum source term should cover a minimum of two cell intervals to ensure that pressure drop created by the actuator disc was properly accounted. Besides, it was also recommended that the optimal structured grid density for implementing the actuator disc to be 4 meter, with the device width set to 8 meter to ensure numerical stability. Smaller grid size may be used at the expense of extreme computational power, as well as longer simulation time.

All in all, this study had demonstrated the efficacy and robustness of the applied actuator disc momentum source term in representing full-size tidal turbines at a real deployment site, where crucial numerical parameters were inspected analysed. Since published material on the implementation of actuator disc approach within a regional scale model is still scarce, it was aspired that this study could provide some evidence, guidance and examples of suggested best practice in effort to fill the research gap.

8.4 Suggestions for further work

- The actuator disc approach used in this regional scale simulations was set to be at a fixed orientation, facing towards the west. Yaw capability should be introduced in the next simulations to imitate a realistic turbine working conditions for maximising power extraction.
- Actuator disc is known as one of the simplest models available to represent a tidal turbine. However, the model's accuracy can be improved by integrating a few additional parameters into the momentum source term to compensate for its limitations. Two of the parameters that can be considered to improve the realism of the actuator disc model include:
    - adding a turbulence source into the model by accounting for the turbulence generated by the turbine [177].
    - considering the force from the supporting structures as well as the effects of surface fouling.
- Future work should also look at the inter-comparison actuator disc study between unstructured (i.e. Telemac3D) and structured (e.g. Delft3D) grid models. Although Delft3D is currently limited to structured grid domain, it is hopeful that the unstructured mesh version will be made public (i.e. open source) soon.
- As demonstrated in Chapter 7, the use of turbulent models other than the $k-\varepsilon$ has posed several limitations in the analysis of the numerical outputs, notably the computation of the turbulent intensities. For this reason, it is imperative to look into the use of the $k-\varepsilon$ models to help clarify some of the indeterminate findings.
- Since the analyses from the regional scale simulation solely focused on the model's outputs during the spring tide period, it would be interesting to see how they compare with the outputs during the neap spring tide. Further investigation into this is warranted.

Appendix A

Numerical Modelling - Figures and Tables

A.1 Chapter 3

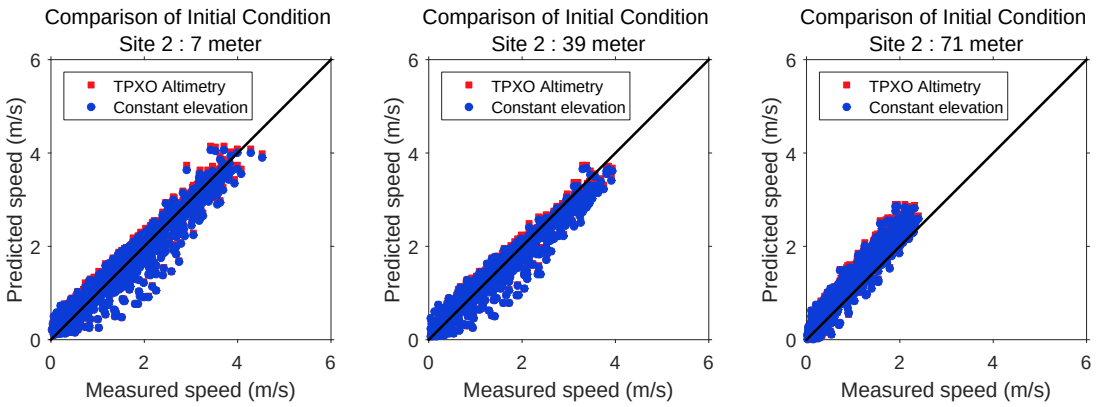

Figure A.1: Influence of the initial boundary conditions on the numerical model at Site 2.

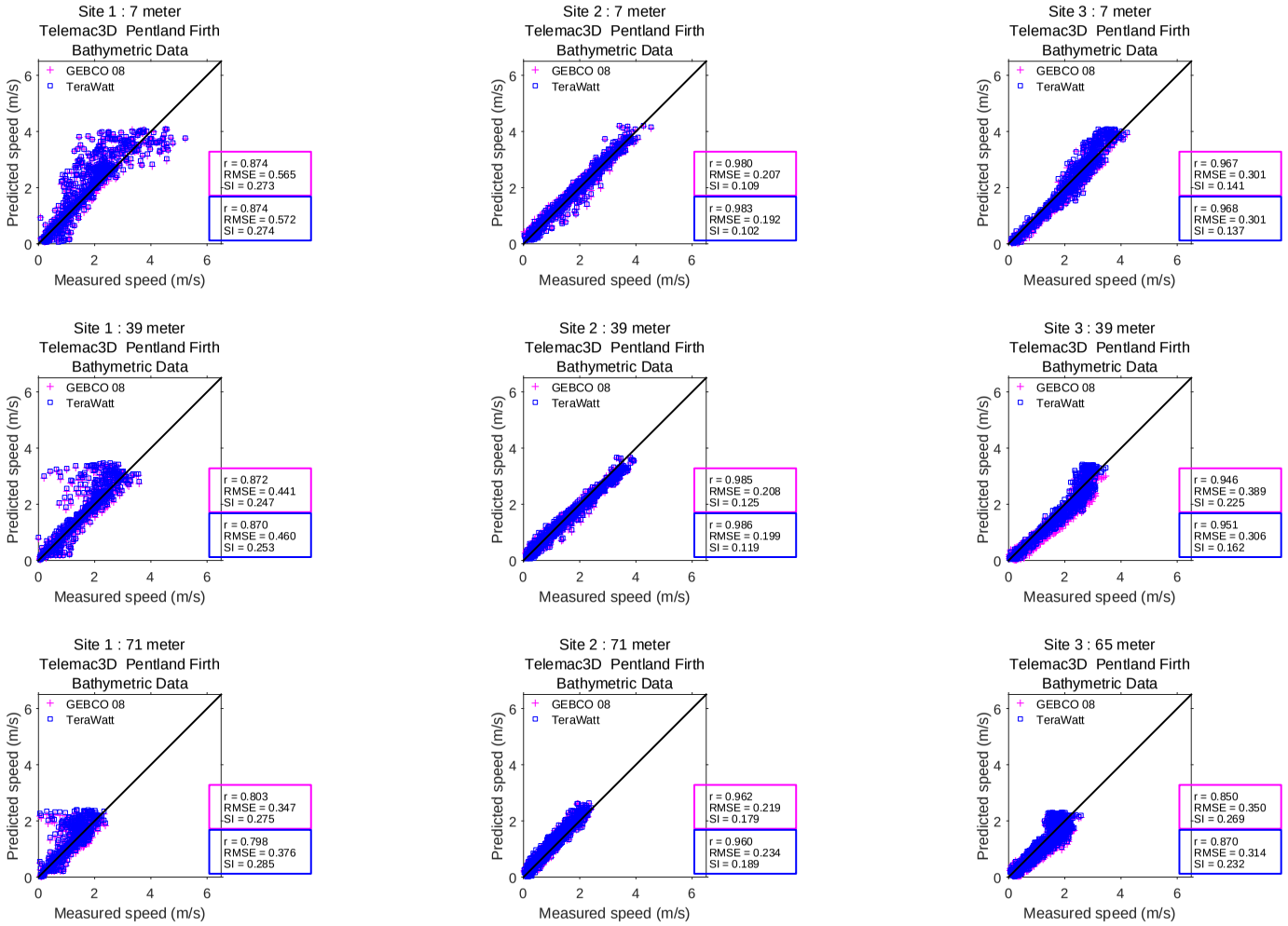

Figure A.2: Influence of the bathymetric input on Telemac3D models for Cd = 0.005.

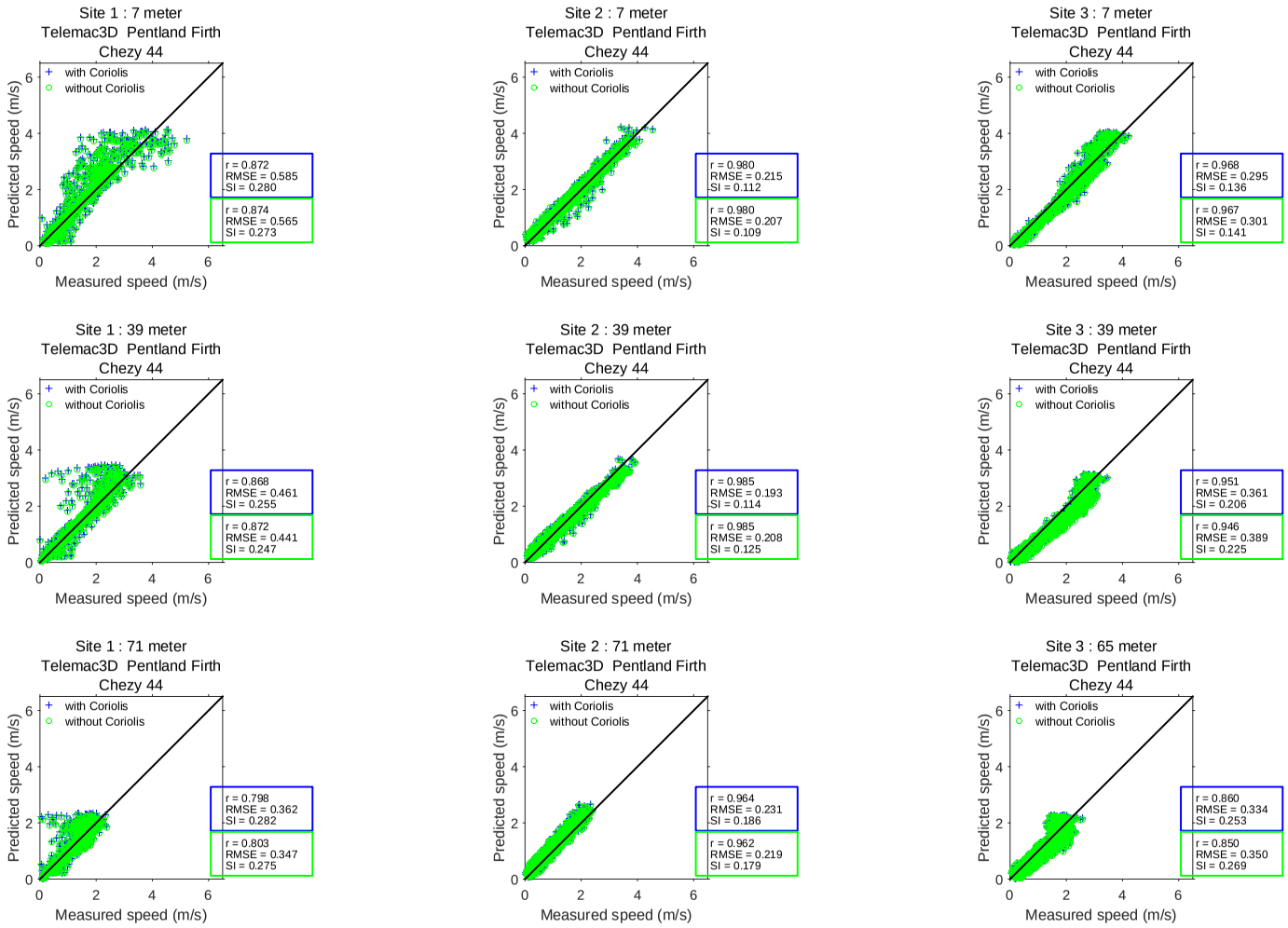

Figure A.3: Impact of the Coriolis force on Telemac3D models for Cd = 0.005.

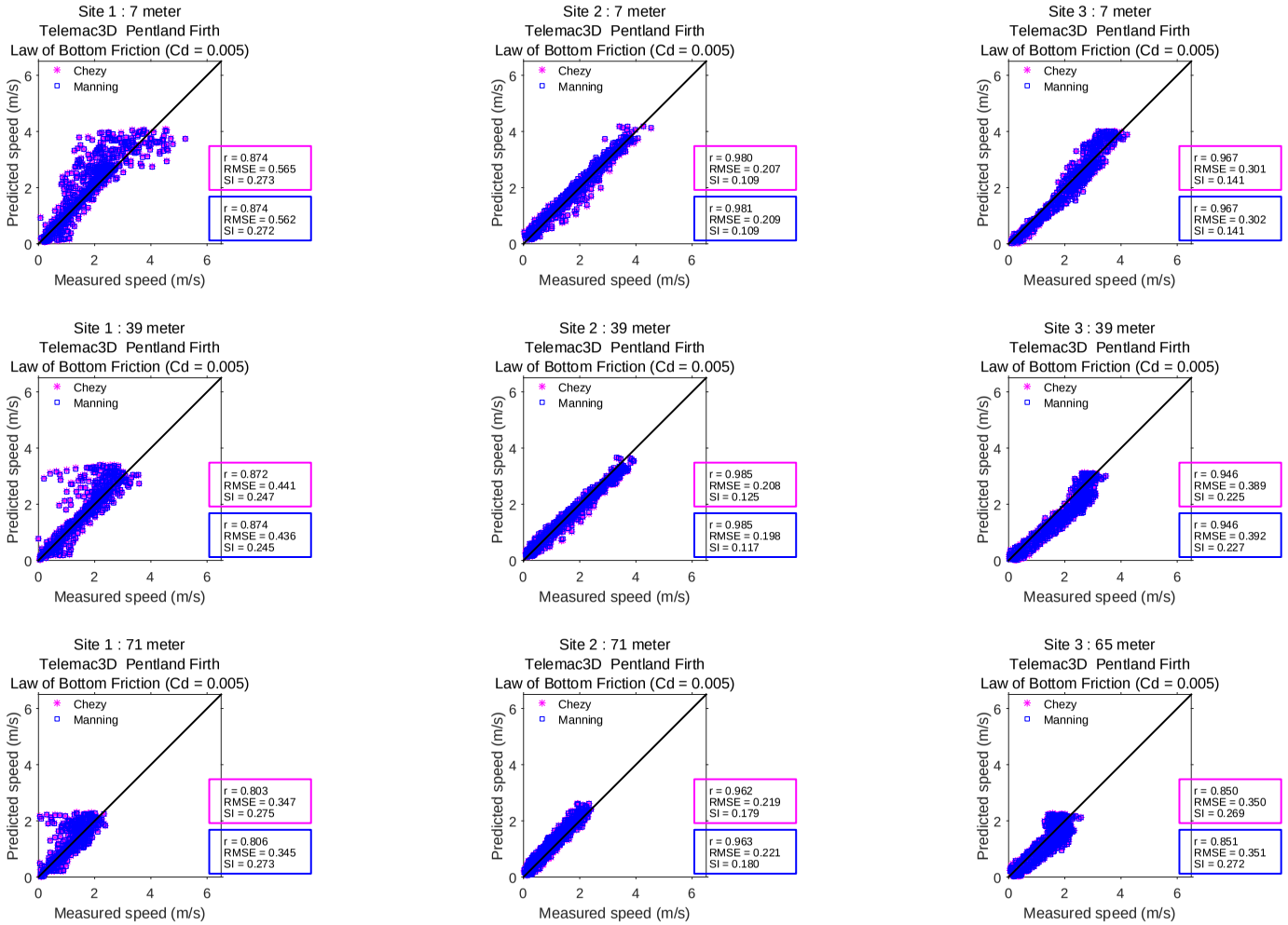

Figure A.4: Comparison of bottom roughness formulae (Manning and Chezy) for Telemac3D models using Cd = 0.005.

Table A.1: Performance indices for the comparison of initial boundary conditions at Site 2.

Depth (m)	Initial condition	Correlation coefficient, r	Root Mean Square Error, RMSE	Scatter Index, SI
7m	TPXO Altimetry	0.961	0.272	0.163
	Constant elevation	0.962	0.270	0.166
39m	TPXO Altimetry	0.971	0.234	0.153
	Constant elevation	0.972	0.243	0.163
71m	TPXO Altimetry	0.958	0.328	0.270
	Constant elevation	0.960	0.298	0.251

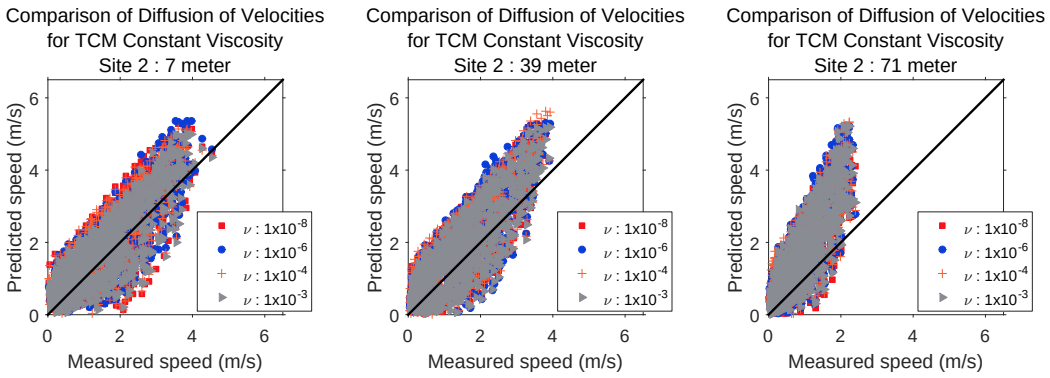

Figure A.5: Comparison of several additional viscosity coefficients values applied to Telemac3D models.

A.2 Chapter 4

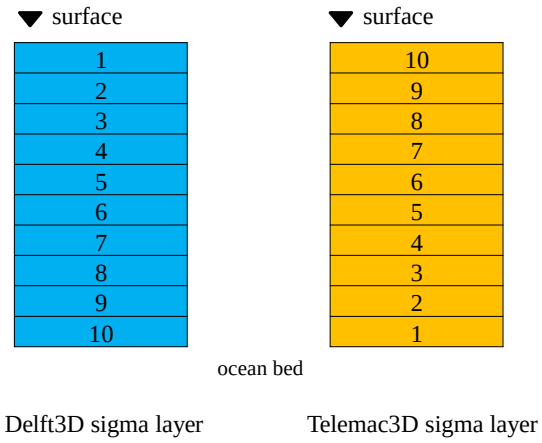

Figure A.6: Comparison between horizontal planes defined in Delft3D and Telemac3D.

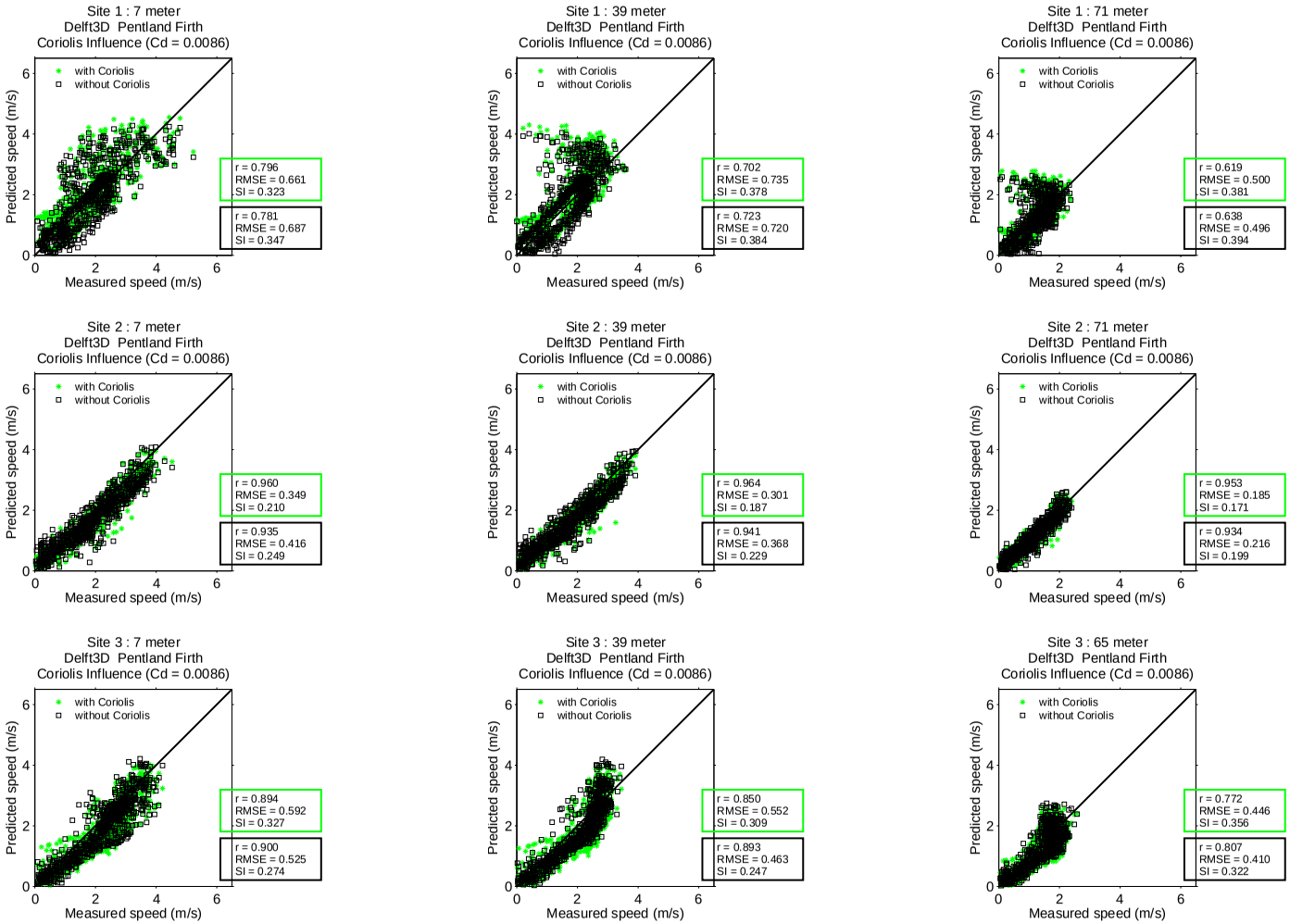

Figure A.7: Influence of the applied Coriolis force on Delft3D model using Cd = 0.0086.

A.3 Chapter 5

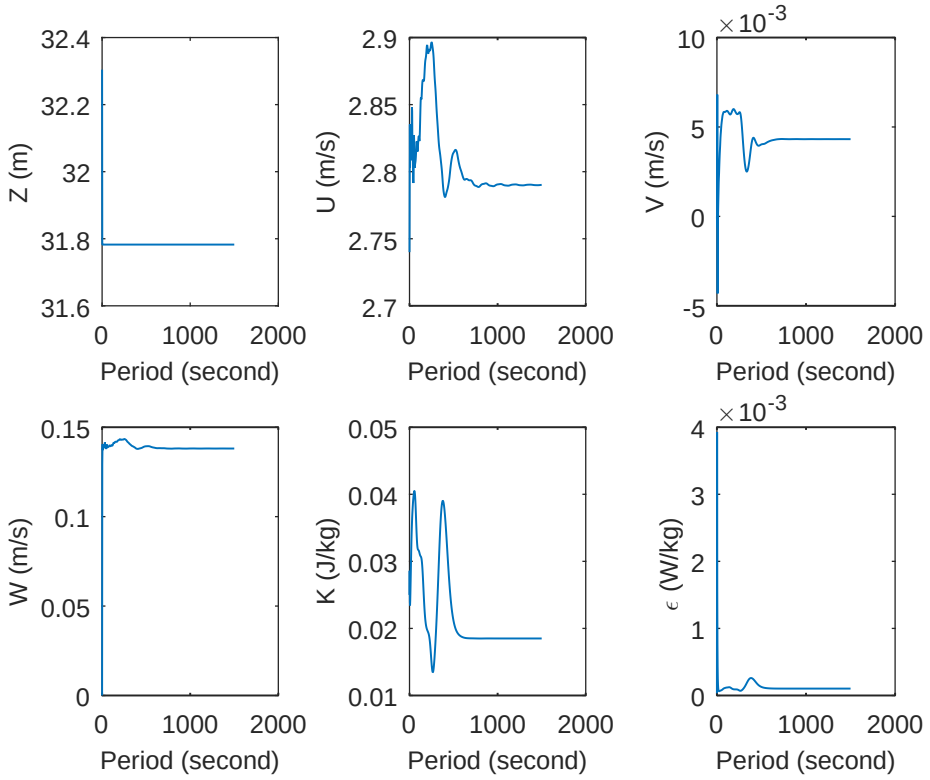

Figure A.8: Numerical outputs (refer to the Y axes) for the single actuator disc study in an idealised channel, illustrating that the model's steady state had been obtained for the selected simulation period. The outputs were extracted from the mid-depth node (i.e. layer 12) at the domain outlet.

A.4 Chapter 7

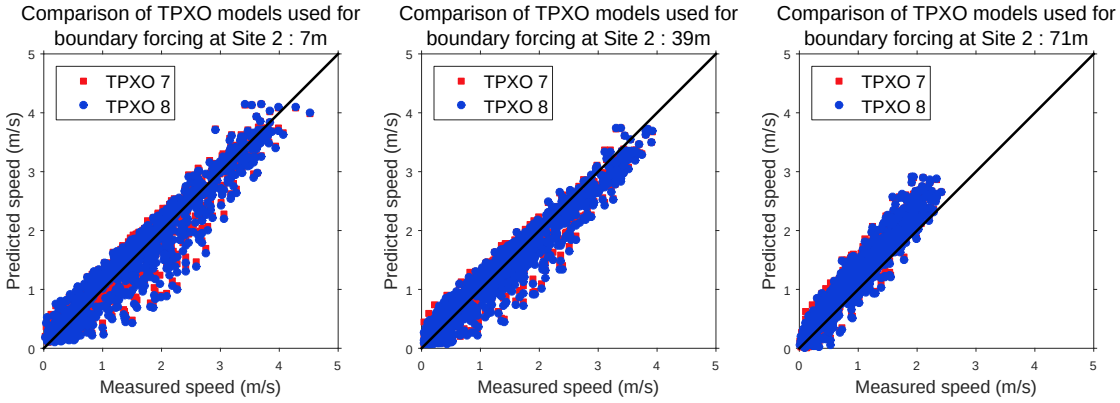

Figure A.9: Comparison between two tidal harmonic database (i.e. two different TPXO version) on the numerical model at Site 2.

Table A.2: Performance indices for the comparison of TPXO models used in the numerical models (i.e. boundary forcing) at Site 2.

Depth (m)	TPXO model	Correlation coefficient, r	Root Mean Square Error, RMSE	Scatter Index, SI
7m	TPXO 7	0.961	0.272	0.163
	TPXO 8	0.952	0.302	0.186
39m	TPXO 7	0.971	0.234	0.153
	TPXO 8	0.964	0.264	0.178
71m	TPXO 7	0.958	0.328	0.270
	TPXO 8	0.956	0.307	0.259

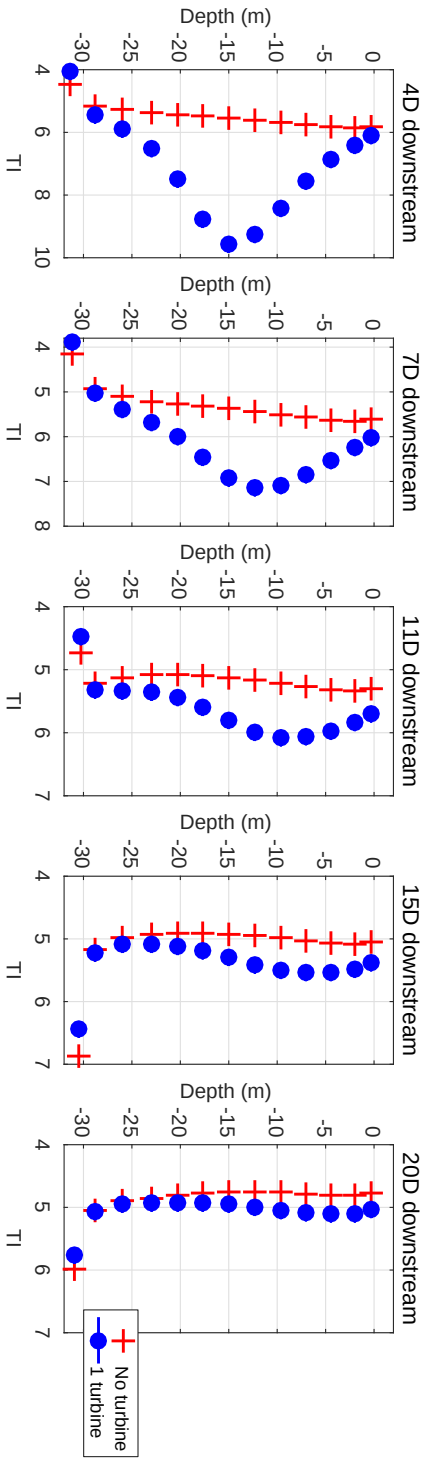

Figure A.10: Sample of computed turbulence intensity from the single turbine arrangement for various downstream distances.

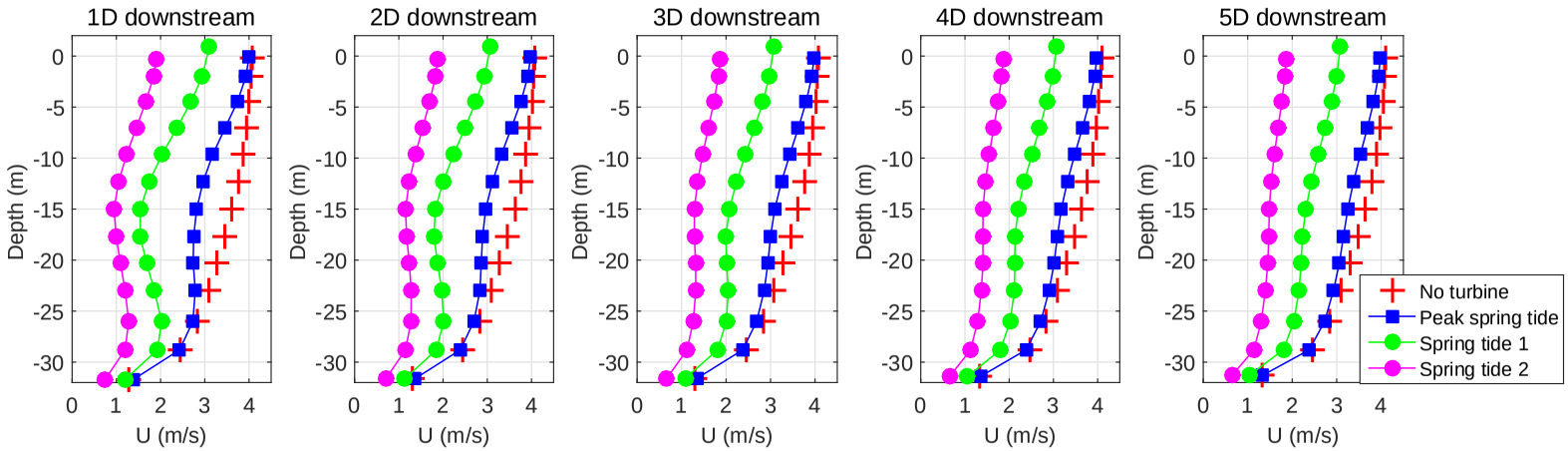

(a) Velocity reduction across the water column for shorter downstream distances.

Figure A.11: Velocity deficit from the single turbine arrangement at three distinct time steps. This figure demonstrates the capability of the applied momentum source term to accurately predict the force exerted by the actuator disc depending on the flow conditions.

Appendix B

Published Research Articles

Five conference papers had been published from this research work. Details of the published articles are listed below:

(a) Anas Rahman and Vengatesan Venugopal, 'On the Validation of Three-Dimensional Actuator Disc Approach for a Full Size Turbine', 3rd Asian Wave and Tidal Energy Conference (AWTEC), Singapore, 2016.

(b) Anas Rahman, Vengatesan Venugopal and David Ingram, 'Numerical Modelling of Full Scale Tidal Turbines and Flow Interactions Using a 3-Dimensional Actuator Disc Approach', 3rd Asian Wave and Tidal Energy Conference (AWTEC), Singapore, 2016.

(c) Anas Rahman and Vengatesan Venugopal, 'On The Validation of Three-Dimensional Hydrodynamic Models for The Pentland Firth Region', International Conference on Offshore Renewable Energy (CORE), Glasgow, Scotland, 2016.

(d) Anas Rahman and Vengatesan Venugopal, 'On The Challenges in Representing a Large Size Tidal Turbine Using the Actuator Disc Approach', International Conference on Offshore Renewable Energy (CORE), Glasgow, Scotland, 2016.

(e) Anas Rahman and Vengatesan Venugopal, 'Inter-Comparison of 3D Tidal Flow Models Applied To Orkney Islands and Pentland Firth', 11th European Wave and Tidal Energy Conference (EWTEC), Nantes, France, 2015.

Further, two manuscripts had been submitted for possible journal publications, and their status are as follows:

(a) Publication A
- Manuscript title : Parametric Analysis of Three Dimensional Flow Models Applied to Tidal Energy Sites in Scotland
- Submitted to : Estuarine, Coastal and Shelf Science (ECSS)
- Status : Accepted for publication

(b) Publication B
- Manuscript title : On the accuracy of three-dimensional actuator disc approach for a large size tidal turbine in simple channel
- Submitted to : Renewable and Sustainable Energy Reviews
- Status : With editor

Appendix C

Fortran Subroutines

Sample of FORTRAN subroutines adopted in the implementation of actuator disc method to represent tidal turbines for both small scale (i.e. idealised channel) as well as regional scale models are given here.

Subroutines for the idealised channel study: Page 230

Subroutines for the regional scale model: Page 238

```
!=====================================================================
! Implementation of the actuator disc in idealised channel
!                   (small scale study)
!=====================================================================
!
!                    *****************
                     SUBROUTINE CONDIM
!                    *****************
!
!
!***********************************************************************
! TELEMAC3D   V6P3                                   21/08/2010
! Edited AR  20/2/16
!***********************************************************************
!~~~~~~~~~~~~~~~~~~~~~~~~~~~~~~~~~~~~~~~~~~~~~~~~~~~~~~~~~~~~~~~~~~~~~~~
!~~~~~~~~~~~~~~~~~~~~~~~~~~~~~~~~~~~~~~~~~~~~~~~~~~~~~~~~~~~~~~~~~~~~~~~
!
      USE BIEF
      USE INTERFACE_TELEMAC3D, EX_CONDIM => CONDIM
      USE DECLARATIONS_TELEMAC
      USE DECLARATIONS_TELEMAC3D
      USE TPXO
!
      IMPLICIT NONE
      INTEGER LNG,LU
      COMMON/INFO/LNG,LU
!
!-----------------------------------------------------------------------
!
      INTEGER IPLAN, I,J
!
!++++++++++++++++++++++++++++++++++++++++++++
!
! EDITED AR
      DOUBLE PRECISION velprof(44)
! FIN AR
!++++++++++++++++++++++++++++++++++++++++++++
!
!***********************************************************************
!
!     ORIGIN OF TIME
!
      IF(.NOT.SUIT2) AT  = 0.D0
!
!     INITIALISES H, THE WATER DEPTH
!
      IF(.NOT.SUIT2) THEN
!
      IF(CDTINI(1:10).EQ.'COTE NULLE'.OR.
     &   CDTINI(1:14).EQ.'ZERO ELEVATION') THEN
        CALL OS( 'X=C     ' ,X=H,C=0.D0)
        CALL OV( 'X=X-Y   ' , H%R , Z , Z , 0.D0 , NPOIN2 )
      ELSEIF(CDTINI(1:14).EQ.'COTE CONSTANTE'.OR.
     &       CDTINI(1:18).EQ.'CONSTANT ELEVATION') THEN
        CALL OS( 'X=C     ' ,X=H,C=COTINI)
        CALL OV( 'X=X-Y   ' , H%R , Z , Z , 0.D0 , NPOIN2 )
      ELSEIF(CDTINI(1:13).EQ.'HAUTEUR NULLE'.OR.
     &       CDTINI(1:10).EQ.'ZERO DEPTH') THEN
        CALL OS( 'X=C     ' ,X=H,C=0.D0)
      ELSEIF(CDTINI(1:17).EQ.'HAUTEUR CONSTANTE'.OR.
     &       CDTINI(1:14).EQ.'CONSTANT DEPTH') THEN
        CALL OS( 'X=C     ' ,X=H,C=HAUTIN)
      ELSEIF(CDTINI(1:25).EQ.'ALTIMETRIE SATELLITE TPXO'.OR.
     &       CDTINI(1:24).EQ.'TPXO SATELLITE ALTIMETRY') THEN
        CALL OS('X=-Y     ',X=H,Y=ZF)
        CALL CONDI_TPXO(NPOIN2,MESH2D%NPTFR,MESH2D%NBOR%I,
     &                  X2%R,Y2%R,H%R,U2D%R,V2D%R,
     &                  LIHBOR%I,LIUBOL%I,KENT,KENTU,
     &                  GEOSYST,NUMZONE,LATIT,LONGIT,
     &                  T3D_FILES,T3DBB1,T3DBB2,
     &                  MARDAT,MARTIM,INTMICON,MSL)
      ELSEIF(CDTINI(1:13).EQ.'PARTICULIERES'.OR.
     &       CDTINI(1:10).EQ.'PARTICULAR'.OR.
     &       CDTINI(1:07).EQ.'SPECIAL') THEN
!     USER INPUT :
!     PROGRAM HERE SPECIAL INITIAL CONDITIONS ON DEPTH
!
!++++++++++++++++++++++++++++++++++++++++++++
!
! Edited AR
        CALL OS( 'X=C     ' ,X=H,C=60.D0)
! FIN AR
!
!++++++++++++++++++++++++++++++++++++++++++++
!
!     END OF SPECIAL INITIAL CONDITIONS
!     END OF USER INPUT
      ELSE
        IF(LNG.EQ.1) THEN
        WRITE(LU,*) 'CONDIM : CONDITION INITIALE NON PREVUE : ',CDTINI
        ENDIF
        IF(LNG.EQ.2) THEN
        WRITE(LU,*) 'CONDIM: INITIAL CONDITION UNKNOWN: ',CDTINI
        ENDIF
        STOP
      ENDIF
      ELSE
        IF(LNG.EQ.1) WRITE(LU,*) 'HAUTEUR LUE DANS LE FICHIER BINAIRE 1'
        IF(LNG.EQ.2) WRITE(LU,*) 'DEPTH IS READ IN THE BINARY FILE 1'
      ENDIF
!
!     CLIPS H
!
      DO I=1,NPOIN2
        H%R(I)=MAX(H%R(I),0.D0)
      ENDDO
!
      CALL OS ('X=Y     ',X=HN,Y=H)
!
!-----------------------------------------------------------------------
! Edited AR
! 24 sigma layers
!
      DO IPLAN = 1,NPLAN
        TRANSF_PLANE%I(IPLAN)=1
      ENDDO
!
!***********************************************************************
!
!     COMPUTES ELEVATIONS
!     IF IT IS A CONTINUATION, WILL BE DONE AFTER CALLING 'SUITE'
!
      IF(DEBU) CALL CALCOT(Z,H%R)
!
!***********************************************************************
!
!     INITIALISES VELOCITIES
!
      IF(SUIT2) THEN
        DO I=1,NPLAN
          DO J=1,NPOIN2
            U%R((I-1)*NPOIN2+J)=U2D%R(J)
            V%R((I-1)*NPOIN2+J)=V2D%R(J)
          ENDDO
        ENDDO
      ELSEIF(CDTINI(1:25).EQ.'ALTIMETRIE SATELLITE TPXO'.OR.
     &       CDTINI(1:24).EQ.'TPXO SATELLITE ALTIMETRY') THEN
        DO I=1,NPLAN
          DO J=1,NPOIN2
            U%R((I-1)*NPOIN2+J)=U2D%R(J)
            V%R((I-1)*NPOIN2+J)=V2D%R(J)
          ENDDO
        ENDDO
      ELSE
        CALL OS( 'X=0     ' , X=U )
        CALL OS( 'X=0     ' , X=V )
      ENDIF
!
!++++++++++++++++++++++++++++++++++++++++++++
!
! EDITED AR
! -->
      OPEN(unit=27,form='formatted',file=
     & '../../../04_input_files/b_constant_KEPS/0_v24.dat')
      READ(27,*) velprof
      CLOSE(27)
!
      DO I=1,NPLAN
        DO J=1,NPOIN2
          U%R((I-1)*NPOIN2+J)=velprof(I)
        ENDDO
      ENDDO
! <--
!!      CALL OS( 'X=0     ' , X=U )
! FIN AR
      CALL OS( 'X=0     ' , X=V )
      CALL OS( 'X=0     ' , X=W )
!
```

```
!
!+++++++++++++++++++++++++++++++++++++++++++++
!
!-----------------------------------------------------------------------
!
!     INITIALISES TRACERS
!
      IF(NTRAC.GT.0) THEN
        DO I=1,NTRAC
          CALL OS( 'X=C     ', X=TA%ADR(I)%P, C=TRAC0(I))
        ENDDO
      ENDIF
!
!
!-----------------------------------------------------------------------
!   INITIALISES THE K-EPSILON MODEL (OPTIONAL)
!   WHEN DONE: AKEP = .FALSE.
!
!+++++++++++++++++++++++++++++++++++++++++++++
!
      AKEP=.TRUE.
!
!      IF(ITURBV.EQ.3) THEN
!
!      ENDIF
!
!+++++++++++++++++++++++++++++++++++++++++++++
!
!-----------------------------------------------------------------------
!
! INITIALISES THE PRESSURE FIELDS TO 0.0
!
      IF(NONHYD) THEN
        CALL OS('X=C     ',X=DP,C=0.D0)
        WRITE (LU,*) 'CONDIM: DYNAMIC PRESSURE INITIALISED TO ZERO'
        CALL OS('X=C     ',X=PH,C=0.D0)
        WRITE (LU,*) '         HYDROSTATIC PRESSURE INITIALISED TO ZERO.'
      ENDIF
!
!-----------------------------------------------------------------------
!
      RETURN
      END
!
!
!                     ***********************************
!                     DOUBLE PRECISION FUNCTION VEL PROF Z
!                     ***********************************
!
     &( I , IPOIN2 , TIME , LT , IPLAN , ENTET , IOPT )
!
!*********************************************************************
! TELEMAC3D   V6P1                                   21/08/2010
!*********************************************************************
!~~~~~~~~~~~~~~~~~~~~~~~~~~~~~~~~~~~~~~~~~~~~~~~~~~~~~~~~~~~~~~~~~~~~~
!
      USE BIEF
      USE DECLARATIONS_TELEMAC
      USE DECLARATIONS_TELEMAC3D
!
      IMPLICIT NONE
      INTEGER LNG,LU
      COMMON/INFO/LNG,LU
!
!+-+-+-+-+-+-+-+-+-+-+-+-+-+-+-+-+-+-+-+-+-+-+-+-+-+-+-+-+-+-+-+-+-+-+
!
      INTEGER          , INTENT(IN) :: I,IPOIN2,IPLAN,IOPT,LT
      DOUBLE PRECISION , INTENT(IN) :: TIME
      LOGICAL          , INTENT(IN) :: ENTET
!
!+-+-+-+-+-+-+-+-+-+-+-+-+-+-+-+-+-+-+-+-+-+-+-+-+-+-+-+-+-+-+-+-+-+-+
!
      DOUBLE PRECISION Y0,HH,DENOM,AUX,DELTAZ,DZ
!
!+++++++++++++++++++++++++++++++++++++++++++++
!
!
      DOUBLE PRECISION velprof(44)
!
!+++++++++++++++++++++++++++++++++++++++++++++
!
!-----------------------------------------------------------------------
!
      IF(IOPT.EQ.0) THEN
!
!+++++++++++++++++++++++++++++++++++++++++++++
!
! Edited AR
! -->
        OPEN(unit=27,form='formatted',file=
     & '../../../04_input_files/b_constant_KEPS/0_v24.dat')
     READ(27,*) velprof
        CLOSE(27)
        VEL_PROF_Z=velprof(IPLAN)
! FIN AR
!
!+++++++++++++++++++++++++++++++++++++++++++++
!
!
      ELSEIF(IOPT.EQ.2) THEN
!
!       FROM FRICTION COEFFICENT CF TO KS (NIKURADSE LAW...)
!
        AUX=KARMAN*SQRT(2.D0/CF%R(IPOIN2))
        HH=MAX( MESH3D%Z%R(IPOIN2+(NPLAN-1)*NPOIN2)
     &         -MESH3D%Z%R(IPOIN2)                    , 1.D-4)
!
! : Y0 = KS/30
!
        Y0=HH/EXP(1.D0+AUX)
!   EXP(1)= 2.71828182845D0
        DENOM=MAX(LOG(HH/Y0/2.71828182845D0),1.D-4)
!
        IF(IPLAN.EQ.1) THEN
!
!         VELOCITY AT THE BOTTOM IS TAKEN AT A HEIGHT IN THE
!         LOGARITHMIC PROFILE THAT ENSURES THAT THE FLUX OF THE
!         FIRST LAYER WILL BE CORRECT IF COMPUTED WITH A LINEAR
!         INTERPOLATION
!         NOTE: THE CRITERION OF STRESS INSTEAD OF FLUX WOULD
!         ALSO LEAD TO A DIVISION BY E**2
!
          DZ=(MESH3D%Z%R(IPOIN2+NPOIN2)-MESH3D%Z%R(IPOIN2))
          AUX=2.D0
          DELTAZ=DZ/EXP(AUX)
        ELSE
          DELTAZ=MESH3D%Z%R(IPOIN2+(IPLAN-1)*NPOIN2)-MESH3D%Z%R(IPOIN2)
        ENDIF
        DELTAZ=MAX(DELTAZ,Y0)
        VEL_PROF_Z=LOG(DELTAZ/Y0)/DENOM
!
!     ELSEIF(IOPT.EQ.3) THEN
!
!
      ELSE
!
        IF(LNG.EQ.1) THEN
          WRITE(LU,*) 'VEL_PROF_Z : OPTION INCONNUE POUR LE PROFIL'
          WRITE(LU,*) 'IOPT=',IOPT,' 0 ET 2 POSSIBLES SEULEMENT'
        ENDIF
        IF(LNG.EQ.2) THEN
          WRITE(LU,*) 'VEL_PROF_Z: UNKNOWN OPTION FOR THE PROFILE'
          WRITE(LU,*) 'IOPT=',IOPT,' 0 AND 2 ONLY ARE POSSIBLE'
        ENDIF
        CALL PLANTE(1)
        STOP
!
      ENDIF
!
!-----------------------------------------------------------------------
!
      RETURN
      END
!
!
!
!
!                     ****************
!                     SUBROUTINE KEPCL3
!                     ****************
!
     &(KBORF,EBORF,LIKBOF,LIEBOF,LIUBOF,
     & KBORL,EBORL,LIKBOL,LIEBOL,LIUBOL,RUGOL,
     & KBORS,EBORS,LIKBOS,LIEBOS,LIUBOS,
     & DISBOR,AK,U,V,H,Z,NBOR,NPOIN2,NPLAN,NPTFR,
     & DNUVIH,DNUVIV,KARMAN,CMU,LISRUF,LISRUL,
     & VIRT,KMIN,KMAX,EMIN,EMAX,KENT,KENTU,KSORT,KADH,KLOG,
     & UETCAR,UETCAL)
```

```
!
!~~~~~~~~~~~~~~~~~~~~~~~~~~~~~~~~~~~~~~~~~~~~~~~~~~~~~~~~~~~~~~~~~~~~~~~~~~~~
!
      USE DECLARATIONS_TELEMAC3D, ONLY : IPBOT,AEBORF,BEBORF,SIGMAE
!
      IMPLICIT NONE
!
      INTEGER LNG,LU
      COMMON/INFO/LNG,LU
!
!+-+-+-+-+-+-+-+-+-+-+-+-+-+-+-+-+-+-+-+-+-+-+-+-+-+-+-+-+-+-+-+-+-+-+-+-+
!
      INTEGER, INTENT(IN) :: NPTFR, NPLAN, NPOIN2,KENTU
      INTEGER, INTENT(IN) :: LISRUF,LISRUL,KENT,KSORT,KADH,KLOG
!
      INTEGER, INTENT(INOUT) :: LIKBOF(NPOIN2), LIKBOS(NPOIN2)
      INTEGER, INTENT(INOUT) :: LIKBOL(NPTFR,NPLAN)
      INTEGER, INTENT(INOUT) :: LIEBOF(NPOIN2), LIEBOS(NPOIN2)
      INTEGER, INTENT(INOUT) :: LIEBOL(NPTFR,NPLAN)
      INTEGER, INTENT(INOUT) :: LIUBOF(NPOIN2), LIUBOS(NPOIN2)
      INTEGER, INTENT(INOUT) :: LIUBOL(NPTFR,NPLAN)
!
      INTEGER, INTENT(IN) :: NBOR(NPTFR)
!
      DOUBLE PRECISION, INTENT(IN) :: U(NPOIN2,NPLAN), V(NPOIN2,NPLAN)
      DOUBLE PRECISION, INTENT(IN) :: Z(NPOIN2,NPLAN), AK(NPOIN2,NPLAN)
      DOUBLE PRECISION, INTENT(IN) :: H(NPOIN2)       , UETCAR(NPOIN2)
!
      DOUBLE PRECISION, INTENT(INOUT) :: KBORF(NPOIN2), KBORS(NPOIN2)
      DOUBLE PRECISION, INTENT(INOUT) :: KBORL(NPTFR,NPLAN)
      DOUBLE PRECISION, INTENT(INOUT) :: EBORF(NPOIN2), EBORS(NPOIN2)
      DOUBLE PRECISION, INTENT(INOUT) :: EBORL(NPTFR,NPLAN)
      DOUBLE PRECISION, INTENT(IN)    :: UETCAL(NPTFR,NPLAN)
!
      DOUBLE PRECISION, INTENT(IN)    :: DISBOR(NPTFR)
      DOUBLE PRECISION, INTENT(IN)    :: RUGOL(NPTFR,NPLAN)
!
      DOUBLE PRECISION, INTENT(IN) :: VIRT, DNUVIH, DNUVIV, KARMAN
      DOUBLE PRECISION, INTENT(IN) :: CMU
      DOUBLE PRECISION, INTENT(IN) :: KMIN, KMAX, EMIN, EMAX
!
!++++++++++++++++++++++++++++++++++++++++++++
!
! EDITED AR
! -->
      DOUBLE PRECISION kinput(44),einput(44)
! FIN AR
!
!++++++++++++++++++++++++++++++++++++++++++++
!
!+-+-+-+-+-+-+-+-+-+-+-+-+-+-+-+-+-+-+-+-+-+-+-+-+-+-+-+-+-+-+-+-+-+-+-+-+
!
      INTRINSIC EXP
!
!----------------------------------------------------------------------
!
      INTEGER IPTFR,IPLAN,IPOIN2,IP,IBOT
!
      DOUBLE PRECISION ESURF, HAUT
      DOUBLE PRECISION SSQCMU, DIST, PROPNU
      DOUBLE PRECISION DISTFOND
!                                    VINCENT BOYER'S CHOICE
      DOUBLE PRECISION, PARAMETER :: FICTIFUET = 2.D0
      DOUBLE PRECISION, PARAMETER :: FICTIFEPS = 2.D0
      DOUBLE PRECISION, PARAMETER :: NIVTURB = 0.005D0
      DOUBLE PRECISION, PARAMETER :: TESTREICH = 1.D-4
      INTEGER, PARAMETER :: MAXITEREICH = 30
!
      INTRINSIC SQRT,MAX,LOG
!
!----------------------------------------------------------------------
!
      SSQCMU = 1.D0 /SQRT(CMU)
      PROPNU = (2*DNUVIH + DNUVIV) /3.D0
!
!++++++++++++++++++++++++++++++++++++++++++++
!
! EDITED AR
! -->
      OPEN(unit=37,form='formatted',file=
     & '../../../04_input_files/b_constant_KEPS/01_k24_5.dat')
      READ(37,*) kinput
      CLOSE(37)
      OPEN(unit=38,form='formatted',file=
     & '../../../04_input_files/b_constant_KEPS/01_e24_5.dat')
      READ(38,*) einput
      CLOSE(38)
! FIN AR
!
!++++++++++++++++++++++++++++++++++++++++++++
!
!=======================================================================
!     BOTTOM
!=======================================================================
!
!      print*,'---'
      DO IPOIN2=1,NPOIN2
!
! Deb JT not important
        IF(IPBOT%I(IPOIN2).EQ.0) THEN
!         NORMAL CASE
          IF (IPOIN2.eq.35036) print*,'ue',sqrt(UETCAR(IPOIN2))
          IF (IPOIN2.eq.35236) print*,'ue',sqrt(UETCAR(IPOIN2))
          IF (IPOIN2.eq.35436) print*,'ue',sqrt(UETCAR(IPOIN2))
          IF (IPOIN2.eq.35636) print*,'ue',sqrt(UETCAR(IPOIN2))
          IF (IPOIN2.eq.35836) print*,'ue',sqrt(UETCAR(IPOIN2))
          IF (IPOIN2.eq.36036) print*,'ue',sqrt(UETCAR(IPOIN2))
          DIST =(Z(IPOIN2,2)-Z(IPOIN2,1))/FICTIFUET
          IF(LIEBOF(IPOIN2).EQ.KENT) THEN
            EBORF(IPOIN2)=MAX(UETCAR(IPOIN2)*
     &      SQRT(UETCAR(IPOIN2))/(KARMAN*DIST),EMIN)
          ENDIF
          IF(LIKBOF(IPOIN2).EQ.KENT) THEN
            KBORF(IPOIN2) = MAX(SSQCMU*UETCAR(IPOIN2),KMIN)
          ENDIF
        ELSE
!         RISK OF SMASHED PLANES OR TIDAL FLATS
          IPLAN=IPBOT%I(IPOIN2)+1
          IF(IPLAN.EQ.NPLAN) THEN
!           CASE OF TIDAL FLATS
            IF(LIEBOF(IPOIN2).EQ.KENT) THEN
              EBORF(IPOIN2)=EMIN
            ENDIF
!           IN THIS CASE KBORF COMPUTED ABOVE MAY YIELD
!           ABNORMAL VALUES OF VISCOSITY
            IF(LIKBOF(IPOIN2).EQ.KENT) KBORF(IPOIN2)=KMIN
          ELSE
!           CASE OF SMASHED PLANES : DIST COMPUTED ON FIRST FREE LAYER
            DIST =(Z(IPOIN2,IPLAN+1)-Z(IPOIN2,IPLAN))/FICTIFUET
            IF(LIEBOF(IPOIN2).EQ.KENT) THEN
              EBORF(IPOIN2)=MAX(UETCAR(IPOIN2)*
     &                          SQRT(UETCAR(IPOIN2))/(KARMAN*DIST),EMIN)
            ENDIF
            IF(LIKBOF(IPOIN2).EQ.KENT) THEN
              KBORF(IPOIN2) = MAX(SSQCMU*UETCAR(IPOIN2),KMIN)
            ENDIF
          ENDIF
        ENDIF
!
      ENDDO
!
! FIN AR
!=======================================================================
!     FREE SURFACE
!=======================================================================
!
      DO IPOIN2=1,NPOIN2
!
!       DIRICHLET ON EPSILON
!       --------------------
!
        IF(LIEBOS(IPOIN2).EQ.KENT) THEN
!
!         NEZU & NAKAGAWA: TURBULENCE IN OPEN CHANNEL FLOWS
!
!         SEE KEPICL: THIS VALUE IS NOT USED IF CONDITION
!                     IS NOT SET TO KENT ON EPSILON
          HAUT = MAX(H(IPOIN2),1.D-7)
          ESURF = SQRT(AK(IPOIN2,NPLAN)**3) / (0.18D0*HAUT)
!
!         5.9
!         ESURF = CMU**0.75D0 / KARMAN
!    &          * AK(IPOIN2,NPLAN)**1.5D0 / (VIRT*HAUT)
          EBORS(IPOIN2) = MAX(ESURF,EMIN)
!
        ENDIF
!
      ENDDO
```

```
!
!=====================================================================
!     LATERAL BOUNDARIES
!=====================================================================
!
      DO IPTFR=1,NPTFR
!
         IPOIN2 = NBOR(IPTFR)
         DIST   = DISBOR(IPTFR) / FICTIFUET
         HAUT   = MAX(H(IPOIN2),1.D-7)
!
         DO IPLAN=1,NPLAN
!
            IP=MAX(IPLAN,2)
            IBOT=MIN(IPBOT%I(IPOIN2)+1,NPLAN-1)
!           DISTANCE TO BOTTOM (WILL BE 0 WITH TIDAL FLATS)
            DISTFOND =  (Z(IPOIN2,IP)-Z(IPOIN2,IBOT))
!
!           DIRICHLET ON K
!           --------------
!
            IF(LIKBOL(IPTFR,IPLAN).EQ.KENT) THEN
!           -----------------------------------
!
!              ***********************************
               IF(LIUBOL(IPTFR,IPLAN).EQ.KENT.OR.
     &            LIUBOL(IPTFR,IPLAN).EQ.KENTU.OR.
     &            LIUBOL(IPTFR,IPLAN).EQ.KSORT     ) THEN
!              ***********************************
!
!              THEORY BY VINCENT BOYER (SEE ALSO KEPINI)
!
!              KBORL(IPTFR,IPLAN) = MAX(NIVTURB*U(IPOIN2,IPLAN)**2,KMIN)
!
!              NO TURBULENCE
!
               KBORL(IPTFR,IPLAN) = KMIN
!
!+++++++++++++++++++++++++++++++++++++++++++++
!
! EDITED AR
! -->
             IF ((IPTFR.eq.1).OR.(IPTFR.ge.215)) THEN
           KBORL(IPTFR,IPLAN)=kinput(IPLAN)
             ENDIF
! FIN AR
!
!+++++++++++++++++++++++++++++++++++++++++++++
!
!              ***************************************
               ELSEIF(LIUBOL(IPTFR,IPLAN).EQ.KLOG .OR.
     &                LIUBOL(IPTFR,IPLAN).EQ.KADH) THEN
!              ***************************************
!
                 WALL
!
                 KBORL(IPTFR,IPLAN)=MAX(SSQCMU*UETCAL(IPTFR,IPLAN),KMIN)
                 KBORL(IPTFR,IPLAN)=KMIN
!
!              ****
               ELSE
!              ****
!
                 IF (LNG.EQ.1) WRITE(LU,111) IPTFR,LIUBOL(IPTFR,IPLAN)
                 IF (LNG.EQ.2) WRITE(LU,112) IPTFR,LIUBOL(IPTFR,IPLAN)
                 CALL PLANTE(1)
                 STOP
!
!              *****
               ENDIF
!              *****
!
            ENDIF
!           -----
!
!           DIRICHLET ON EPSILON
!           --------------------
!
            IF(LIEBOL(IPTFR,IPLAN).EQ.KENT) THEN
!           ------------------------------------
!
!              ***********************************
               IF(LIUBOL(IPTFR,IPLAN).EQ.KENT.OR.
     &            LIUBOL(IPTFR,IPLAN).EQ.KENTU.OR.
     &            LIUBOL(IPTFR,IPLAN).EQ.KSORT     ) THEN
!              ***********************************
!
!                COMING IN THE DOMAIN: TURBULENCE DUE TO THE
!                BOTTOM AS IN KEPINI; COMPUTES EBORL ACCORDING
!                TO KBORL AT THE BOTTOM
!
!+++++++++++++++++++++++++++++++++++++++++++++
!
! EDITED AR
! -->
                 IF ((IPTFR.eq.1).OR.(IPTFR.ge.215)) THEN
               EBORL(IPTFR,IPLAN)=einput(IPLAN)
             ENDIF
! FIN AR
!
!+++++++++++++++++++++++++++++++++++++++++++++
!
!              ***************************************
               ELSEIF(LIUBOL(IPTFR,IPLAN).EQ.KLOG .OR.
     &                LIUBOL(IPTFR,IPLAN).EQ.KADH) THEN
!              ***************************************
!
                 WALL
!
                 EBORL(IPTFR,IPLAN) =
     &           MAX(UETCAL(IPTFR,IPLAN)*SQRT(UETCAL(IPTFR,IPLAN))/
     &           (KARMAN*DIST*FICTIFUET/FICTIFEPS),EMIN)
                 EBORL(IPTFR,IPLAN)=EMIN
!
!              ****
               ELSE
!              ****
!
                 OTHER
!
                 IF (LNG.EQ.1) WRITE(LU,121) IPTFR,LIUBOL(IPTFR,IPLAN)
                 IF (LNG.EQ.2) WRITE(LU,122) IPTFR,LIUBOL(IPTFR,IPLAN)
                 CALL PLANTE(1)
                 STOP
!
!              *****
               ENDIF
!              *****
!
             ENDIF
!            -----
!
          ENDDO
        ENDDO
!
!-----------------------------------------------------------------------
!
101   FORMAT(' KEPCL3 : REGIME DE TURBULENCE INCONNU : ',I6)
102   FORMAT(' KEPCL3 : UNKNOWN TURBULENCE MODEL : ',I6)
111   FORMAT(' KEPCL3 : POINT DE BORD',I6,
     &       ' - CAS NON PREVU POUR KBOR : LIUBOR =',I6)
112   FORMAT(' KEPCL3 : BOUNDARY NODE',I6,
     &       ' - UNEXPECTED CONDITION FOR KBOR : LIUBOR =',I6)
121   FORMAT(' KEPCL3 : POINT DE BORD',I6,
     &       ' - CAS NON PREVU POUR EBOR : LIUBOR =',I6)
122   FORMAT(' KEPCL3 : BOUNDARY NODE',I6,
     &       ' - UNEXPECTED CONDITION FOR EBOR : LIUBOR =',I6)
!
!-----------------------------------------------------------------------
!
      RETURN
      END
!
!
!
!                     *****************
                      SUBROUTINE KEPINI
!                     *****************
!
     &(AK,EP,U,V,Z,ZF,NPOIN2,NPLAN,DNUVIH,DNUVIV,KARMAN,CMU,KMIN,EMIN)
!
!***********************************************************************
! TELEMAC3D   V6P1                                   21/08/2010
!***********************************************************************
!~~~~~~~~~~~~~~~~~~~~~~~~~~~~~~~~~~~~~~~~~~~~~~~~~~~~~~~~~~~~~~~~~~~~~~~
!
      IMPLICIT NONE
      INTEGER LNG, LU
```

```
      COMMON/INFO/ LNG, LU
!
!+-+-+-+-+-+-+-+-+-+-+-+-+-+-+-+-+-+-+-+-+-+-+-+-+-+-+-+-+-+-+-+-+-+-+-+-+
!
      INTEGER, INTENT(IN)             :: NPOIN2,NPLAN
      DOUBLE PRECISION, INTENT(INOUT):: AK(NPOIN2,NPLAN)
      DOUBLE PRECISION, INTENT(INOUT):: EP(NPOIN2,NPLAN)
      DOUBLE PRECISION, INTENT(IN)    :: U(NPOIN2,NPLAN), V(NPOIN2,NPLAN)
      DOUBLE PRECISION, INTENT(IN)    :: Z(NPOIN2,NPLAN)
      DOUBLE PRECISION, INTENT(IN)    :: ZF(NPOIN2)
      DOUBLE PRECISION, INTENT(IN)    :: KARMAN, DNUVIH, DNUVIV
      DOUBLE PRECISION, INTENT(IN)    :: CMU
      DOUBLE PRECISION, INTENT(IN)    :: KMIN, EMIN
!
!+-+-+-+-+-+-+-+-+-+-+-+-+-+-+-+-+-+-+-+-+-+-+-+-+-+-+-+-+-+-+-+-+-+-+-+-+
!
      INTEGER IPOIN2,IPLAN
!
      INTRINSIC LOG, SQRT, MAX
!
      DOUBLE PRECISION, PARAMETER :: FICTIFEPS = 2.D0
!
!++++++++++++++++++++++++++++++++++++++++++++
!
! EDITED AR
!
      DOUBLE PRECISION kinput(44),einput(44)
!
!++++++++++++++++++++++++++++++++++++++++++++
!
!-----------------------------------------------------------------------
!
!-----------------------------------------------------------------------
!
!     HERE: NO INITIAL TURBULENCE
!
!++++++++++++++++++++++++++++++++++++++++++++
!
! EDITED AR
      OPEN(unit=37,form='formatted',file=
     & '../../../04_input_files/b_constant_KEPS/01_k24_5.dat')
      READ(37,*) kinput
      CLOSE(37)
      OPEN(unit=38,form='formatted',file=
     & '../../../04_input_files/b_constant_KEPS/01_e24_5.dat')
      READ(38,*) einput
      CLOSE(38)
!
!      DO IPOIN2 = 1,NPOIN2
!        DO IPLAN = 1,NPLAN
!          AK(IPOIN2,IPLAN) = KMIN
!          EP(IPOIN2,IPLAN) = EMIN
!        ENDDO
!      ENDDO
!
      DO IPLAN = 1,NPLAN
        DO IPOIN2=1,NPOIN2
          AK(IPOIN2,IPLAN) = kinput(IPLAN)
          EP(IPOIN2,IPLAN) = einput(IPLAN)
        ENDDO
      ENDDO

! FIN AR
!++++++++++++++++++++++++++++++++++++++++++++
!
!-----------------------------------------------------------------------
!
      RETURN
      END
!
!                     *****************
                      SUBROUTINE TRISOU
!                     *****************
!
     & (CV1, CV2, SCV1, SCV2, UN3, VN3, TA, X, Y, Z, ZS,
     &  DELTAR,MESH3,FCOR,CORIOL,NTRAC,LT,AT,DT,SURFAC,
     &  T1,ST1, W1, W2, W3, SEDI, GRAV, NPOIN3, NELEM3, NPOIN2,
     &  NELEM2, NPLAN, NETAGE, IKLE3, PRIVE, LV, MSK, MASKEL, INCHYD,
     &  SVOLU,VOLU,SVIDE,IELM3,SMASKEL,NREJEU,ISCE,KSCE,QSCE,USCE,VSCE,
     &  IELM2H,GRADZSX,GRADZSY,Z3,TRAV2,FU2,MESH2D, ST2,T2,ST3,T3,
     &  LATIT, LONGIT, NORD,SMU,SMV,YASEM3D,SCHCVI,DENLAW,FXH,FYH,
     &  COUROU,NPTH,T3D_FILES,T3DBI1)
!
!***********************************************************************
```

```
! TELEMAC3D   V6P3                                   21/08/2010
!***********************************************************************
!~~~~~~~~~~~~~~~~~~~~~~~~~~~~~~~~~~~~~~~~~~~~~~~~~~~~~~~~~~~~~~~~~~~~~~~~~~~
!
      USE BIEF
      USE DECLARATIONS_TELEMAC
      USE INTERFACE_TELEMAC3D, EX_TRISOU => TRISOU
      USE DECLARATIONS_TELEMAC3D, ONLY : SPHERI
!
      IMPLICIT NONE
      INTEGER LNG,LU
      COMMON/INFO/LNG,LU
!
!+-+-+-+-+-+-+-+-+-+-+-+-+-+-+-+-+-+-+-+-+-+-+-+-+-+-+-+-+-+-+-+-+-+-+-+-+
!
      INTEGER, INTENT(IN) :: NPOIN3,NELEM3,NPOIN2,NELEM2
      INTEGER, INTENT(IN) :: NPLAN,NETAGE,NTRAC,NPTH,T3DBI1
      INTEGER, INTENT(IN) :: LV,LT,IELM2H,NREJEU,IELM3,SCHCVI,DENLAW
!
      INTEGER, INTENT(IN) :: IKLE3(NELEM3,6)
!
      DOUBLE PRECISION, INTENT(IN)    :: MASKEL(NELEM3)
      DOUBLE PRECISION, INTENT(IN)    :: LATIT,LONGIT,NORD
!
      DOUBLE PRECISION, INTENT(INOUT) :: CV1(NPOIN3),CV2(NPOIN3)
      TYPE(BIEF_OBJ),   INTENT(INOUT) :: SCV1,SCV2,FXH,FYH
!
      DOUBLE PRECISION, INTENT(IN)    :: UN3(NPOIN3), VN3(NPOIN3)
      DOUBLE PRECISION, INTENT(IN)    :: SURFAC(NELEM2)
      DOUBLE PRECISION, INTENT(IN)    :: X(NPOIN3), Y(NPOIN3), Z(NPOIN3)
      DOUBLE PRECISION, INTENT(INOUT) :: ZS(NPOIN3)
      DOUBLE PRECISION, INTENT(INOUT) :: W1(NELEM3,6), W2(NELEM3,6)
      DOUBLE PRECISION, INTENT(INOUT) :: W3(NELEM3,6)
      DOUBLE PRECISION, DIMENSION(NPOIN2,NPLAN), INTENT(INOUT) :: VOLU
!
      DOUBLE PRECISION, INTENT(INOUT) :: T1(NPOIN3)
      DOUBLE PRECISION, INTENT(INOUT) :: T2(NPOIN3), T3(NPOIN3)
      TYPE(BIEF_OBJ),   INTENT(INOUT) :: ST1, ST2, ST3
      TYPE(BIEF_OBJ),   INTENT(INOUT) :: TA
      TYPE(BIEF_OBJ),   INTENT(INOUT) :: PRIVE
      TYPE(BIEF_OBJ),   INTENT(INOUT) :: DELTAR
      TYPE(BIEF_MESH),  INTENT(INOUT) :: MESH3
      TYPE(BIEF_OBJ),   INTENT(INOUT) :: GRADZSX
      TYPE(BIEF_OBJ),   INTENT(INOUT) :: GRADZSY
      TYPE(BIEF_MESH),  INTENT(INOUT) :: MESH2D
      TYPE(BIEF_OBJ),   INTENT(IN)    :: Z3
      TYPE(BIEF_OBJ),   INTENT(IN)    :: SMASKEL
      TYPE(BIEF_OBJ),   INTENT(INOUT) :: SVIDE
      TYPE(BIEF_OBJ),   INTENT(INOUT) :: TRAV2, FU2
      TYPE(BIEF_OBJ),   INTENT(INOUT) :: SVOLU,SMU,SMV
!
!                                  * = NSCE
      INTEGER, INTENT(IN) :: ISCE(*),KSCE(*)
      DOUBLE PRECISION, INTENT(IN) :: QSCE(*),USCE(*),VSCE(*)
!
      DOUBLE PRECISION, INTENT(IN) :: GRAV, DT, AT, FCOR
      LOGICAL, INTENT(IN) :: CORIOL, SEDI, MSK, INCHYD,COUROU
      LOGICAL, INTENT(INOUT) :: YASEM3D
      TYPE(BIEF_FILE), INTENT(IN) :: T3D_FILES(*)
!
!+-+-+-+-+-+-+-+-+-+-+-+-+-+-+-+-+-+-+-+-+-+-+-+-+-+-+-+-+-+-+-+-+-+-+-+-+
!
      INTEGER IELEM3,IPLAN,IETAGE,IZ,IZM,IZS,ERR,NP,I3D
      DOUBLE PRECISION A,OMEGA,PI,CORI
!
      INTEGER I,OPTFLO
      CHARACTER(LEN=15) FORMUL
!
      INTEGER I1,I2,I3,I4,I5,I6
      DOUBLE PRECISION DX1,DX2,DX3,DY1,DY2,DY3
      DOUBLE PRECISION DZ1,DZ2,DZ3,DR1,DR2,DR3
      DOUBLE PRECISION SZ1,SZ2,SZ3,SR1,SR2,SR3
      DOUBLE PRECISION DZSUDX,DZSUDY,DRSUDX,DRSUDY
      DOUBLE PRECISION DZ123,C,ATH
!
!++++++++++++++++++++++++++++++++++++++++++++
! EDITED AR
      DOUBLE PRECISION DIST,FORCEH,XSOM(4),YSOM(4),X4,Y4
      DOUBLE PRECISION compt,deltad,K,THICK
!     DOUBLE PRECISION, PARAMETER :: THICK = 4.D0
!++++++++++++++++++++++++++++++++++++++++++++
!
!     FOR WAVE DRIVEN CURRENTS
!
```

```
      CHARACTER*16 NOMX,NOMY
      LOGICAL DEJALU,OKX,OKY,HYDROLIENNE
      DATA DEJALU /.FALSE./
      REAL, ALLOCATABLE :: W(:)
      SAVE W
!
!***********************************************************************
!
! INITIALISES
!
!     CALL OS( 'X=C     ' , X=SCV1 , C=0.D0 )
!     CALL OS( 'X=C     ' , X=SCV2 , C=0.D0 )
!
      SCV1%TYPR='0'
      SCV2%TYPR='0'
!
!-----------------------------------------------------------------------
!  BUOYANCY SOURCE TERMS
!-----------------------------------------------------------------------
!
      YASEM3D=.FALSE.
!
      IF(DENLAW.NE.0.AND.NTRAC.GT.0) THEN
!
      SCV1%TYPR='Q'
      SCV2%TYPR='Q'
      CALL OS( 'X=0     ' , X=SCV1 )
      CALL OS( 'X=0     ' , X=SCV2 )
!
!     VOLUME OF TEST FUNCTIONS
!
      CALL VECTOR(ST1, '=', 'MASBAS          ',IELM3, 1.D0,
     &            SVIDE, SVIDE,
     &            SVIDE, SVIDE, SVIDE, SVIDE, MESH3,.FALSE.,SMASKEL)
      IF(NCSIZE.GT.1) CALL PARCOM(ST1,2,MESH3)
!
!     1 : BUOYANCY IN REAL MESH
!     2 : BUOYANCY IN TRANSFORMED MESH
!
!     OPTFLO CHANGED FROM 2 INTO 1 BY JMH ON 03/10/2002
!     ENABLES TREATMENT WITH TETRAHEDRONS
!     WHO CAN TELL WHICH IS BEST WITH PRISMS ?
!
      OPTFLO=1
!
      IF(OPTFLO.EQ.1) THEN
!
      YASEM3D=.FALSE.
!
! - G DENSITY GRADIENTS
!     WITH TREATMENT OF HYDROSTATIC INCONSISTENCIES IF NEEDED
!     THIS IS AVAILABLE ONLY FOR PRISMS !!!!!!!!!!!!
!
      FORMUL='GRADF          '
      IF(IELM3.EQ.41.AND.INCHYD) FORMUL(6:6)='2'
!
!     ================================================
!     BETTER FILTERING OF HYDROSTATIC INCONSISTENCIES
!     ================================================
!
!     3 OR 4 IMPLIES THAT 2 IS ALSO APPLIED
!
!     RECOMMENDED : FILTER 4
!
!     FILTER 3
!     IF(INCHYD) FORMUL(6:6)='3'
!     FILTER 4
!     IF(INCHYD) FORMUL(6:6)='4'
!
!
      CALL VECTOR(ST2, '=',FORMUL//'X',IELM3,-GRAV,DELTAR,SVIDE,
     &            SVIDE,SVIDE,SVIDE,SVIDE,MESH3,MSK,SMASKEL)
!
      CALL VECTOR(ST3, '=',FORMUL//'Y',IELM3,-GRAV,DELTAR,SVIDE,
     &            SVIDE,SVIDE,SVIDE,SVIDE,MESH3,MSK,SMASKEL)
!
      IF(NCSIZE.GT.1) THEN
        CALL PARCOM(ST2,2,MESH3)
        CALL PARCOM(ST3,2,MESH3)
      ENDIF
!
! NODAL VALUE
!
      CALL OVD('X=Y/Z   ',T2,T2,T1,0.D0,NPOIN3,2,0.D0,1.D-9)
      CALL OVD('X=Y/Z   ',T3,T3,T1,0.D0,NPOIN3,2,0.D0,1.D-9)
!
! SIMPSON INTEGRATION
!
      DO IPLAN = NPLAN, 2, -1
        DO I = 1, NPOIN2
          IZ  =(IPLAN-1)*NPOIN2+I
          IZM =(IPLAN-2)*NPOIN2+I
          A = 0.5D0 * (Z(IZ)-Z(IZM))
          CV1(IZM) = CV1(IZ) + (T2(IZ)+T2(IZM)) * A
          CV2(IZM) = CV2(IZ) + (T3(IZ)+T3(IZM)) * A
        ENDDO
      ENDDO
!
! TERMS WITH FREE SURFACE GRADIENT (NODAL VALUES)
!
      DO IPLAN = 1, NPLAN-1
!
        DO I = 1, NPOIN2
          IZ  = (IPLAN-1)*NPOIN2+I
          IZS = (NPLAN-1)*NPOIN2+I
          A = GRAV*(DELTAR%R(IZ)-DELTAR%R(IZS))
!
          CV1(IZ) = CV1(IZ) + A * GRADZSX%R(I)
          CV2(IZ) = CV2(IZ) + A * GRADZSY%R(I)
!
        ENDDO
!
      ENDDO
!
      ELSEIF(OPTFLO.EQ.2) THEN
!
      YASEM3D = .FALSE.
!
! TRANSFORMED MESH
!
! COMPUTES ZS: OPPOSITE OF WATER DEPTH AT CONSIDERED POINT
!
       I2 = NPOIN3 - NPOIN2 + 1
       I4 = NPOIN3
       DO IPLAN = 1,NPLAN
         I1 = NPOIN2*(IPLAN-1) + 1
         I3 = NPOIN2* IPLAN
         CALL OV( 'X=Y-Z   ', ZS(I1:I3), Z(I1:I3), Z(I2:I4), C, NPOIN2)
       END DO
!
       BYELEMENT: DO IELEM3 = 1 , NELEM3
!
          I1 = IKLE3(IELEM3,1)
          I2 = IKLE3(IELEM3,2)
          I3 = IKLE3(IELEM3,3)
          I4 = IKLE3(IELEM3,4)
          I5 = IKLE3(IELEM3,5)
          I6 = IKLE3(IELEM3,6)
!
          DX1 = X(I3) - X(I2)
          DX2 = X(I1) - X(I3)
          DX3 = X(I2) - X(I1)
          DY1 = Y(I2) - Y(I3)
          DY2 = Y(I3) - Y(I1)
          DY3 = Y(I1) - Y(I2)
!
          DR1 = DELTAR%R(I4) - DELTAR%R(I1)
          DR2 = DELTAR%R(I5) - DELTAR%R(I2)
          DR3 = DELTAR%R(I6) - DELTAR%R(I3)
          DZ1 = ZS(I4) - ZS(I1)
          DZ2 = ZS(I5) - ZS(I2)
          DZ3 = ZS(I6) - ZS(I3)
          DZ123 = DZ1 + DZ2 + DZ3
!
          SZ1 = ZS(I4) + ZS(I1)
          SZ2 = ZS(I5) + ZS(I2)
          SZ3 = ZS(I6) + ZS(I3)
          SR1 = DELTAR%R(I4) + DELTAR%R(I1)
          SR2 = DELTAR%R(I5) + DELTAR%R(I2)
          SR3 = DELTAR%R(I6) + DELTAR%R(I3)
!
          IF(MAX(ZS(I1),ZS(I2),ZS(I3)).GT.
     &       MIN(ZS(I4),ZS(I5),ZS(I6)).AND.INCHYD) THEN
            DR1 = 0.D0
            DR2 = 0.D0
            DR3 = 0.D0
            SR1 = 0.D0
            SR2 = 0.D0
```

```
                SR3 = 0.D0
              ENDIF
!
              DZSUDX = SZ1 * DY1 + SZ2 * DY2 + SZ3 * DY3
              DZSUDY = SZ1 * DX1 + SZ2 * DX2 + SZ3 * DX3
              DRSUDX = SR1 * DY1 + SR2 * DY2 + SR3 * DY3
              DRSUDY = SR1 * DX1 + SR2 * DX2 + SR3 * DX3
!
              W1(IELEM3,1) = DR1 * DZSUDX - DZ1 * DRSUDX
              W1(IELEM3,2) = DR2 * DZSUDX - DZ2 * DRSUDX
              W1(IELEM3,3) = DR3 * DZSUDX - DZ3 * DRSUDX
              W2(IELEM3,1) = DR1 * DZSUDY - DZ1 * DRSUDY
              W2(IELEM3,2) = DR2 * DZSUDY - DZ2 * DRSUDY
              W2(IELEM3,3) = DR3 * DZSUDY - DZ3 * DRSUDY
              W3(IELEM3,1) = DZ1 + DZ123
              W3(IELEM3,2) = DZ2 + DZ123
              W3(IELEM3,3) = DZ3 + DZ123
!
            END DO BYELEMENT
!
            IF (NETAGE.NE.1) THEN
!
               BYETAGE: DO IETAGE = NETAGE-1 , 1 , -1
                  I2 = NELEM2*IETAGE + 1
                  I1 = I2 - NELEM2
                  CALL OV('X=X+Y    ' , W1(I1,1) , W1(I2,1) , Z , C , NELEM2)
                  CALL OV('X=X+Y    ' , W1(I1,2) , W1(I2,2) , Z , C , NELEM2)
                  CALL OV('X=X+Y    ' , W1(I1,3) , W1(I2,3) , Z , C , NELEM2)
                  CALL OV('X=X+Y    ' , W2(I1,1) , W2(I2,1) , Z , C , NELEM2)
                  CALL OV('X=X+Y    ' , W2(I1,2) , W2(I2,2) , Z , C , NELEM2)
                  CALL OV('X=X+Y    ' , W2(I1,3) , W2(I2,3) , Z , C , NELEM2)
               END DO BYETAGE
!
               I2 = NELEM2 + 1
               I1 = NELEM3 - NELEM2
               CALL OV('X=Y      ' , W1(1,4) , W1(I2,1) , Z , C , I1)
               CALL OV('X=Y      ' , W1(1,5) , W1(I2,2) , Z , C , I1)
               CALL OV('X=Y      ' , W1(1,6) , W1(I2,3) , Z , C , I1)
               CALL OV('X=Y      ' , W2(1,4) , W2(I2,1) , Z , C , I1)
               CALL OV('X=Y      ' , W2(1,5) , W2(I2,2) , Z , C , I1)
               CALL OV('X=Y      ' , W2(1,6) , W2(I2,3) , Z , C , I1)
!
            ENDIF
!
            I1 = NELEM3 - NELEM2 + 1
            CALL OV('X=C      ' , W1(I1,4) , Y , Z , 0.D0 , NELEM2)
            CALL OV('X=C      ' , W1(I1,5) , Y , Z , 0.D0 , NELEM2)
            CALL OV('X=C      ' , W1(I1,6) , Y , Z , 0.D0 , NELEM2)
            CALL OV('X=C      ' , W2(I1,4) , Y , Z , 0.D0 , NELEM2)
            CALL OV('X=C      ' , W2(I1,5) , Y , Z , 0.D0 , NELEM2)
            CALL OV('X=C      ' , W2(I1,6) , Y , Z , 0.D0 , NELEM2)
!
            CALL OV('X=XY     ' , W1(1,1) , W3 , Z , C , 3*NELEM3)
            CALL OV('X=XY     ' , W1(1,4) , W3 , Z , C , 3*NELEM3)
            CALL OV('X=XY     ' , W2(1,1) , W3 , Z , C , 3*NELEM3)
            CALL OV('X=XY     ' , W2(1,4) , W3 , Z , C , 3*NELEM3)
!
            DO IETAGE = 1 , NETAGE
              I1 = NELEM2*(IETAGE-1) + 1
              CALL OV('X=XY     ' , W3(I1,1) , SURFAC , Z , C , NELEM2)
              CALL OV('X=XY     ' , W3(I1,2) , SURFAC , Z , C , NELEM2)
              CALL OV('X=XY     ' , W3(I1,3) , SURFAC , Z , C , NELEM2)
            ENDDO
            CALL OV('X=Y      ' , W3(1,4) , W3 , Z , C , 3*NELEM3)
!
            CALL ASSVEC(CV1,IKLE3,NPOIN3,NELEM3,NELEM3,41,W1,.FALSE.,
     &                  LV,MSK,MASKEL,6)
            CALL ASSVEC(CV2,IKLE3,NPOIN3,NELEM3,NELEM3,41,W2,.FALSE.,
     &                  LV,MSK,MASKEL,6)
            CALL ASSVEC(T1,IKLE3,NPOIN3,NELEM3,NELEM3,41,W3,.TRUE. ,
     &                  LV,MSK,MASKEL,6)
!
            IF(NCSIZE.GT.1) THEN
              CALL PARCOM(SCV1,2,MESH3)
              CALL PARCOM(SCV2,2,MESH3)
              CALL PARCOM(ST1,2,MESH3)
            ENDIF
!
            CALL OVD('X=CY/Z  ',CV1,CV1,T1,0.25D0*GRAV,NPOIN3,2,0.D0,1D-9)
            CALL OVD('X=CY/Z  ',CV2,CV2,T1,0.25D0*GRAV,NPOIN3,2,0.D0,1D-9)
!
          ENDIF
!
!     IF(NTRAC.GT.0)
```

```
          ENDIF
!
!-----------------------------------------------------------------------
!  CORIOLIS FORCE
!
!  NOTE JMH : THERE ARE ADDITIONAL TERMS IF W IS TAKEN INTO ACCOUNT
!
!-----------------------------------------------------------------------
!
          IF(CORIOL) THEN
!
            IF(SCV1%TYPR.EQ.'0') THEN
              CALL OS( 'X=0     ' , X=SCV1 )
              CALL OS( 'X=0     ' , X=SCV2 )
              SCV1%TYPR='Q'
              SCV2%TYPR='Q'
            ENDIF
!
!           HERE THE VERTICAL VELOCITY IS NEGLECTED
!
            IF(SPHERI) THEN
!
              PI=ACOS(-1.D0)
              OMEGA=2.D0*PI/86164.D0
!
              DO IPLAN=1,NPLAN
                DO I=1,NPOIN2
                  CORI=2.D0*OMEGA*MESH2D%SINLAT%R(I)
                  I3=(IPLAN-1)*NPOIN2+I
                  CV1(I3)=CV1(I3)+VN3(I3)*CORI
                  CV2(I3)=CV2(I3)-UN3(I3)*CORI
                ENDDO
              ENDDO
!
            ELSE
!
              CALL OV('X=X+CY   ',CV1,VN3,VN3,  FCOR,NPOIN3)
              CALL OV('X=X+CY   ',CV2,UN3,UN3,-FCOR,NPOIN3)
!
            ENDIF
!
          ENDIF
!
!*********************************************************************
!
!     * WITH WAVE DRIVEN CURRENTS
!       -------------------------
!
!       FORCING TERMS FROM A TOMAWAC RESULTS FILE
!
!       BEWARE :    1. MESHES MUST BE THE SAME
!       ---------
!                   2. TAKES THE LAST TIMESTEP FROM TOMAWAC FILE
!
          IF(COUROU) THEN
!
            IF(.NOT.DEJALU.AND..NOT.INCLUS(COUPLING,'TOMAWAC')) THEN
!
              ALLOCATE(W(NPOIN2),STAT=ERR)
              IF(ERR.NE.0) THEN
                IF(LNG.EQ.1) THEN
                  WRITE(LU,*) 'ERREUR D''ALLOCATION DE W DANS TRISOU'
                ENDIF
                IF(LNG.EQ.2) THEN
                  WRITE(LU,*) 'MEMORY ALLOCATION ERROR OF W IN TRISOU'
                ENDIF
              ENDIF
!
!             T3DBI1 : BINARY DATA FILE 1
              NOMX='FORCE FX        '
              NOMY='FORCE FY        '
              CALL FIND_IN_SEL(FXH,NOMX,T3D_FILES(T3DBI1)%LU,
     &                         T3D_FILES(T3DBI1)%FMT,
     &                         W,OKX,NPTH,NP,ATH)
              CALL FIND_IN_SEL(FYH,NOMY,T3D_FILES(T3DBI1)%LU,
     &                         T3D_FILES(T3DBI1)%FMT,
     &                         W,OKY,NPTH,NP,ATH)
!
              IF(.NOT.OKX.OR..NOT.OKY) THEN
                IF(LNG.EQ.1) WRITE(LU,5)
                IF(LNG.EQ.2) WRITE(LU,6)
 5              FORMAT(1X,'TRISOU : FORCE FX OU FY NON TROUVES',/,1X,
     &                  '         DANS LE FICHIER DE HOULE')
 6              FORMAT(1X,'TRISOU: FORCE FX OR FY NOT FOUND',/,1X,
```

```
      &                    '        IN THE WAVE RESULTS FILE')
                CALL PLANTE(1)
                STOP
              ENDIF
              IF(NP.NE.NPOIN2) THEN
                IF(LNG.EQ.1) WRITE(LU,95)
                IF(LNG.EQ.2) WRITE(LU,96)
 95             FORMAT(1X,'TRISOU : SIMULATION DES COURANTS DE HOULE.',/,
     &                 1X,'LES MAILLAGES HOULE ET COURANTS SONT ',/,
     &                 1X,'DIFFERENTS : PAS POSSIBLE POUR LE MOMENT.')
 96             FORMAT(1X,'TRISOU: WAVE DRIVEN CURRENTS MODELLING.',/,
     &                 1X,'WAVE AND CURRENT MODELS MESHES ARE ',/,
     &                 1X,'DIFFERENT : NOT POSSIBLE AT THE MOMENT.')
!
                CALL PLANTE(1)
                STOP
              ENDIF
!             WRITES OUT TO LISTING
              IF(LNG.EQ.1) WRITE(LU,115) ATH
              IF(LNG.EQ.2) WRITE(LU,116) ATH
115           FORMAT(1X,/,1X,'TRISOU : COURANTS DE HOULE',/,
     &                 1X,'          LECTURE AU TEMPS ',F10.3,/)
116           FORMAT(1X,/,1X,'TRISOU: WAVE DRIVEN CURRENTS MODELLING',/,
     &                 1X,'          READING FILE AT TIME ',F10.3,/)
              DEJALU = .TRUE.
!
            ENDIF
!
!           ADDS TO SOURCE TERMS
!
            IF(SCV1%TYPR.EQ.'0') THEN
              DO I=1,NPOIN2
                DO IPLAN=1,NPLAN
                  I3D=((IPLAN-1)*NPOIN2)+I
!                 CV1(I3D)=1.5D0*FXH%R(I)   (SOGREAH-PECHON-TEISSON VERSION)
                  CV1(I3D)=FXH%R(I)
                  CV2(I3D)=FYH%R(I)
                ENDDO
              ENDDO
              SCV1%TYPR='Q'
              SCV2%TYPR='Q'
            ELSE
              DO I=1,NPOIN2
                DO IPLAN=1,NPLAN
                  I3D=((IPLAN-1)*NPOIN2)+I
!                 CV1(I3D)=CV1(I3D)+1.5D0*FXH%R(I)   (SOGREAH-PECHON-TEISSON VERSION)
                  CV1(I3D)=CV1(I3D)+FXH%R(I)
                  CV2(I3D)=CV2(I3D)+FYH%R(I)
                ENDDO
              ENDDO
            ENDIF
!
          ENDIF
!
!+++++++++++++++++++++++++++++++++++++++++++++++
!
! EDITED AR
!
!+++++++++++++++++++++++++++++++++++++++++++++

          IF(SCV1%TYPR.EQ.'0') THEN
            CALL OS( 'X=0     ' , X=SCV1 )
            CALL OS( 'X=0     ' , X=SCV2 )
            SCV1%TYPR='Q'
            SCV2%TYPR='Q'
          ENDIF
!
! EDITED AR

!+++++++++++++++++++++++++++++++++++++++++++++
!-------------     400m  ----------------------!
!         deltad = 0.3D0
!         XSOM(1) = 400.D0-deltad
!         XSOM(2) = 404.D0+deltad
!         XSOM(3) = 404.D0+deltad
!         XSOM(4) = 400.D0-deltad
!         YSOM(1) = 60.D0-deltad
!         YSOM(2) = 60.D0-deltad
!         YSOM(3) = 80.D0+deltad
!         YSOM(4) = 80.D0+deltad
!
!+++++++++++++++++++++++++++++++++++++++++++++++
!-------------     250m  ----------------------!
          deltad = 1.D0
          XSOM(1) = 250.D0-deltad
          XSOM(2) = 254.D0+deltad
          XSOM(3) = 254.D0+deltad
          XSOM(4) = 250.D0-deltad
          YSOM(1) = 60.D0-deltad
          YSOM(2) = 60.D0-deltad
          YSOM(3) = 80.D0+deltad
          YSOM(4) = 80.D0+deltad
!
         THICK = 4.D0
!-------------------------------------------------------------
!
          HYDROLIENNE = .true.
          compt=0
          K = 2.D0
          IF (HYDROLIENNE) THEN
            DO I=1,NPOIN2
           IF(INPOLY(X(I),Y(I),XSOM,YSOM,4)) THEN
                 DO IPLAN=1,NPLAN
                   I3D=((IPLAN-1)*NPOIN2)+I
                   IF(LT.EQ.1)THEN
                     WRITE(41,*) I3D
                   ENDIF
                   DIST = SQRT((Y(I)-70.D0)**2 + (Z(I3D)-30.D0)**2)
                   IF (DIST.LE.10.D0) THEN
            FORCEH = -(0.5D0*K/THICK)*(UN3(I3D)**2+VN3(I3D)**2)
         print*,'FORCEH = ', FORCEH
            IF(LT.LE.100) FORCEH = FORCEH*LT/1.D2
            CV1(I3D)=CV1(I3D)+FORCEH
                     compt=compt+1
!                    IF(MOD(LT,500).eq.0) print*,X(I),Y(I),Z(I3D),FORCEH
                   ENDIF
             ENDDO
               ENDIF
             ENDDO
            ENDIF
!   IF(MOD(LT,500).eq.0) print*,'-----------',compt
!
! Fin AR
!
!---------------------------------------------------------------------
!
! TAKES THE VELOCITY OF SOURCES INTO ACCOUNT
!
! NOTE : IF USCE AND VSCE ARE NOT GIVEN, CONSIDERS THAT
!        USCE=UN3 AND VSCE=VN3
!
         IF(NREJEU.GT.0.AND.SCHCVI.NE.ADV_NSC.AND.SCHCVI.NE.ADV_PSI
     &                .AND.SCHCVI.NE.ADV_LPO.AND.SCHCVI.NE.ADV_NSC_TF
     &                .AND.SCHCVI.NE.ADV_LPO_TF) THEN
!
           IF(SCV1%TYPR.EQ.'0') THEN
             CALL OS( 'X=0     ' , X=SCV1 )
             CALL OS( 'X=0     ' , X=SCV2 )
             SCV1%TYPR='Q'
             SCV2%TYPR='Q'
           ENDIF
!
!          WITH DISTRIBUTIVE SCHEMES AND FINITE VOLUME SCHEMES
!          THIS IS DONE DIRECTLY INTO SUBROUTINE MURD3D, AND NOT WITH CV1
!
           DO I=1,NREJEU
             IF(ISCE(I).GT.0) THEN
               CV1((KSCE(I)-1)*NPOIN2+ISCE(I))=
     &         CV1((KSCE(I)-1)*NPOIN2+ISCE(I))
     &         +(USCE(I)-UN3((KSCE(I)-1)*NPOIN2+ISCE(I)))*
     &                                        QSCE(I)/VOLU(ISCE(I),KSCE(I))
               CV2((KSCE(I)-1)*NPOIN2+ISCE(I))=
     &         CV2((KSCE(I)-1)*NPOIN2+ISCE(I))
     &         +(VSCE(I)-VN3((KSCE(I)-1)*NPOIN2+ISCE(I)))*
     &                                        QSCE(I)/VOLU(ISCE(I),KSCE(I))
             ENDIF
           ENDDO
!
         ENDIF
!
!---------------------------------------------------------------------
!
         RETURN
         END
!
!
```

```
!=====================================================================
! Implementation of the actuator disc in the regional scale model
!=====================================================================
!
!                     *****************
                      SUBROUTINE CONDIM
!                     *****************
!
!
!***********************************************************************
! TELEMAC3D   V6P3                                   21/08/2010
! Edited AR  27/9/16
!***********************************************************************
!
!~~~~~~~~~~~~~~~~~~~~~~~~~~~~~~~~~~~~~~~~~~~~~~~~~~~~~~~~~~~~~~~~~~~~~~~
!~~~~~~~~~~~~~~~~~~~~~~~~~~~~~~~~~~~~~~~~~~~~~~~~~~~~~~~~~~~~~~~~~~~~~~~
!
      USE BIEF
      USE INTERFACE_TELEMAC3D, EX_CONDIM => CONDIM
      USE DECLARATIONS_TELEMAC
      USE DECLARATIONS_TELEMAC3D
      USE TPXO
!
      IMPLICIT NONE
      INTEGER LNG,LU
      COMMON/INFO/LNG,LU
!
!-----------------------------------------------------------------------
!
      INTEGER IPLAN, I,J
!
!***********************************************************************
!
!     ORIGIN OF TIME
!
      IF(.NOT.SUIT2) AT  = 0.D0
!
!     INITIALISES H, THE WATER DEPTH
!
      IF(.NOT.SUIT2) THEN
!
      IF(CDTINI(1:10).EQ.'COTE NULLE'.OR.
     &   CDTINI(1:14).EQ.'ZERO ELEVATION') THEN
        CALL OS( 'X=C     ' ,X=H,C=0.D0)
        CALL OV( 'X=X-Y   ' , H%R , Z , Z , 0.D0 , NPOIN2 )
      ELSEIF(CDTINI(1:14).EQ.'COTE CONSTANTE'.OR.
     &       CDTINI(1:18).EQ.'CONSTANT ELEVATION') THEN
        CALL OS( 'X=C     ' ,X=H,C=COTINI)
        CALL OV( 'X=X-Y   ' , H%R , Z , Z , 0.D0 , NPOIN2 )
      ELSEIF(CDTINI(1:13).EQ.'HAUTEUR NULLE'.OR.
     &       CDTINI(1:10).EQ.'ZERO DEPTH') THEN
        CALL OS( 'X=C     ' ,X=H,C=0.D0)
      ELSEIF(CDTINI(1:17).EQ.'HAUTEUR CONSTANTE'.OR.
     &       CDTINI(1:14).EQ.'CONSTANT DEPTH') THEN
        CALL OS( 'X=C     ' ,X=H,C=HAUTIN)
      ELSEIF(CDTINI(1:25).EQ.'ALTIMETRIE SATELLITE TPXO'.OR.
     &       CDTINI(1:24).EQ.'TPXO SATELLITE ALTIMETRY') THEN
        CALL OS('X=-Y    ',X=H,Y=ZF)
        CALL CONDI_TPXO(NPOIN2,MESH2D%NPTFR,MESH2D%NBOR%I,
     &                  X2%R,Y2%R,H%R,U2D%R,V2D%R,
     &                  LIHBOR%I,LIUBOL%I,KENT,KENTU,
     &                  GEOSYST,NUMZONE,LATIT,LONGIT,
     &                  T3D_FILES,T3DBB1,T3DBB2,
     &                  MARDAT,MARTIM,INTMICON,MSL,
     &                  TIDALTYPE,BOUNDARY_COLOUR,ICALHWG)
      ELSEIF(CDTINI(1:13).EQ.'PARTICULIERES'.OR.
     &       CDTINI(1:10).EQ.'PARTICULAR'.OR.
     &       CDTINI(1:07).EQ.'SPECIAL') THEN
!     USER INPUT :
!     PROGRAM HERE SPECIAL INITIAL CONDITIONS ON DEPTH
        IF(LNG.EQ.1) WRITE(LU,10)
        IF(LNG.EQ.2) WRITE(LU,11)
10      FORMAT(1X,'CONDIM : AVEC DES CONDITIONS INITIALES PARTICULIERES'
     &       ,/,1X,'         VOUS DEVEZ MODIFIER CONDIM')
11      FORMAT(1X,'CONDIM : WITH SPECIAL INITIAL CONDITIONS'
     &       ,/,1X,'         YOU HAVE TO MODIFY CONDIM')
        CALL PLANTE(1)
        STOP
!     END OF SPECIAL INITIAL CONDITIONS
!     END OF USER INPUT
      ELSE
        IF(LNG.EQ.1) THEN
        WRITE(LU,*) 'CONDIM : CONDITION INITIALE NON PREVUE : ',CDTINI
        ENDIF
        IF(LNG.EQ.2) THEN
        WRITE(LU,*) 'CONDIM: INITIAL CONDITION UNKNOWN: ',CDTINI
        ENDIF
        CALL PLANTE(1)
        STOP
      ENDIF
      ELSE
        IF(LNG.EQ.1) WRITE(LU,*) 'HAUTEUR LUE DANS LE FICHIER BINAIRE 1'
        IF(LNG.EQ.2) WRITE(LU,*) 'DEPTH IS READ IN THE BINARY FILE 1'
      ENDIF
!
!     CLIPS H
!
      DO I=1,NPOIN2
        H%R(I)=MAX(H%R(I),0.D0)
      ENDDO
!
      CALL OS ('X=Y     ',X=HN,Y=H)
!
!-----------------------------------------------------------------------
! Edited AR 30/11/16
!-----------------------------------------------------------------------
      DO IPLAN = 1,NPLAN
        TRANSF_PLANE%I(IPLAN)=3
      ENDDO
      TRANSF_PLANE%I(2)=3
      ZPLANE%R(2)=-28.8D0
      TRANSF_PLANE%I(3)=3
      ZPLANE%R(3)=-26.D0
      TRANSF_PLANE%I(4)=3
      ZPLANE%R(4)=-22.95D0
      TRANSF_PLANE%I(5)=3
      ZPLANE%R(5)=-20.33D0
      TRANSF_PLANE%I(6)=3
      ZPLANE%R(6)=-17.67D0
      TRANSF_PLANE%I(7)=3
      ZPLANE%R(7)=-15.D0
      TRANSF_PLANE%I(8)=3
      ZPLANE%R(8)=-12.33D0
      TRANSF_PLANE%I(9)=3
      ZPLANE%R(9)=-9.66D0
      TRANSF_PLANE%I(10)=3
      ZPLANE%R(10)=-7.05D0
      TRANSF_PLANE%I(11)=3
      ZPLANE%R(11)=-4.5D0
      TRANSF_PLANE%I(12)=3
      ZPLANE%R(12)=-2.D0
!
!
!***********************************************************************
!
!     COMPUTES ELEVATIONS
!     IF IT IS A CONTINUATION, WILL BE DONE AFTER CALLING 'SUITE'
!
      IF(DEBU) CALL CALCOT(Z,H%R)
!
!***********************************************************************
!
!     INITIALISES VELOCITIES
!
      IF(SUIT2) THEN
        DO I=1,NPLAN
          DO J=1,NPOIN2
            U%R((I-1)*NPOIN2+J)=U2D%R(J)
            V%R((I-1)*NPOIN2+J)=V2D%R(J)
          ENDDO
        ENDDO
      ELSEIF(CDTINI(1:25).EQ.'ALTIMETRIE SATELLITE TPXO'.OR.
     &       CDTINI(1:24).EQ.'TPXO SATELLITE ALTIMETRY') THEN
        DO I=1,NPLAN
          DO J=1,NPOIN2
            U%R((I-1)*NPOIN2+J)=U2D%R(J)
            V%R((I-1)*NPOIN2+J)=V2D%R(J)
          ENDDO
        ENDDO
      ELSE
        CALL OS( 'X=0     ' , X=U )
        CALL OS( 'X=0     ' , X=V )
      ENDIF
!
      CALL OS( 'X=0     ' , X=W )
!
!-----------------------------------------------------------------------
!
```

```
!     INITIALISES TRACERS
!
      IF(NTRAC.GT.0) THEN
        DO I=1,NTRAC
          CALL OS( 'X=C     ', X=TA%ADR(I)%P, C=TRAC0(I))
        ENDDO
      ENDIF
!
!
!-----------------------------------------------------------------------
!   INITIALISES THE K-EPSILON MODEL (OPTIONAL)
!   WHEN DONE: AKEP = .FALSE.
!
      AKEP=.TRUE.
!
!     IF(ITURBV.EQ.3) THEN
!
!       HERE INITIALISES K AND EPSILON
!
!       AKEP = .FALSE.
!     ENDIF
!
!-----------------------------------------------------------------------
!
! INITIALISES THE PRESSURE FIELDS TO 0.0
!
      IF(NONHYD) THEN
        CALL OS('X=C     ',X=DP,C=0.D0)
        WRITE (LU,*) 'CONDIM: DYNAMIC PRESSURE INITIALISED TO ZERO'
        CALL OS('X=C     ',X=PH,C=0.D0)
        WRITE (LU,*) '         HYDROSTATIC PRESSURE INITIALISED TO ZERO.'
      ENDIF
!
!-----------------------------------------------------------------------
!
      RETURN
      END
!
!                     *****************
                      SUBROUTINE TRISOU
!                     *****************
!
     & (CV1, CV2, SCV1, SCV2, UN3, VN3, TA, X, Y, Z, ZS,
     &  DELTAR,MESH3,FCOR,CORIOL,NTRAC,LT,AT,DT,SURFAC,
     &  T1,ST1, W1, W2, W3, SEDI, GRAV, NPOIN3, NELEM3, NPOIN2,
     &  NELEM2, NPLAN, NETAGE, IKLE3, PRIVE, LV, MSK, MASKEL, INCHYD,
     &  SVOLU,VOLU,SVIDE,IELM3,SMASKEL,NREJEU,ISCE,KSCE,QSCE,USCE,VSCE,
     &  IELM2H,GRADZSX,GRADZSY,Z3,TRAV2,FU2,MESH2D, ST2,T2,ST3,T3,
     &  LATIT, LONGIT, NORD,SMU,SMV,YASEM3D,SCHCVI,DENLAW,FXH,FYH,
     &  COUROU,NPTH,T3D_FILES,T3DBI1)
!
!***********************************************************************
! TELEMAC3D   V6P3                                   21/08/2010
! AR : version v7p1r1   5/9/16
!***********************************************************************
!
!~~~~~~~~~~~~~~~~~~~~~~~~~~~~~~~~~~~~~~~~~~~~~~~~~~~~~~~~~~~~~~~~~~~~~~~~
!
      USE BIEF
      USE DECLARATIONS_TELEMAC
      USE INTERFACE_TELEMAC3D, EX_TRISOU => TRISOU
      USE DECLARATIONS_TELEMAC3D, ONLY : SPHERI,MAREE,MARDAT,MARTIM,
     &                                   T2_01,T2_02
!
      IMPLICIT NONE
      INTEGER LNG,LU
      COMMON/INFO/LNG,LU
!
!+-+-+-+-+-+-+-+-+-+-+-+-+-+-+-+-+-+-+-+-+-+-+-+-+-+-+-+-+-+-+-+-+-+-+-+
!
      INTEGER, INTENT(IN) :: NPOIN3,NELEM3,NPOIN2,NELEM2
      INTEGER, INTENT(IN) :: NPLAN,NETAGE,NTRAC,NPTH,T3DBI1
      INTEGER, INTENT(IN) :: LV,LT,IELM2H,NREJEU,IELM3,SCHCVI,DENLAW
!
      INTEGER, INTENT(IN) :: IKLE3(NELEM3,6)
!
      DOUBLE PRECISION, INTENT(IN)    :: MASKEL(NELEM3)
      DOUBLE PRECISION, INTENT(IN)    :: LATIT,LONGIT,NORD
!
      DOUBLE PRECISION, INTENT(INOUT) :: CV1(NPOIN3),CV2(NPOIN3)
      TYPE(BIEF_OBJ),   INTENT(INOUT) :: SCV1,SCV2,FXH,FYH
!
      DOUBLE PRECISION, INTENT(IN)    :: UN3(NPOIN3), VN3(NPOIN3)
      DOUBLE PRECISION, INTENT(IN)    :: SURFAC(NELEM2)
      DOUBLE PRECISION, INTENT(IN)    :: X(NPOIN3), Y(NPOIN3), Z(NPOIN3)
      DOUBLE PRECISION, INTENT(INOUT) :: ZS(NPOIN3)
      DOUBLE PRECISION, INTENT(INOUT) :: W1(NELEM3,6), W2(NELEM3,6)
      DOUBLE PRECISION, INTENT(INOUT) :: W3(NELEM3,6)
      DOUBLE PRECISION, DIMENSION(NPOIN2,NPLAN), INTENT(INOUT) :: VOLU
!
      DOUBLE PRECISION, INTENT(INOUT) :: T1(NPOIN3)
      DOUBLE PRECISION, INTENT(INOUT) :: T2(NPOIN3), T3(NPOIN3)
      TYPE(BIEF_OBJ),   INTENT(INOUT) :: ST1, ST2, ST3
      TYPE(BIEF_OBJ),   INTENT(INOUT) :: TA
      TYPE(BIEF_OBJ),   INTENT(INOUT) :: PRIVE
      TYPE(BIEF_OBJ),   INTENT(INOUT) :: DELTAR
      TYPE(BIEF_MESH),  INTENT(INOUT) :: MESH3
      TYPE(BIEF_OBJ),   INTENT(INOUT) :: GRADZSX
      TYPE(BIEF_OBJ),   INTENT(INOUT) :: GRADZSY
      TYPE(BIEF_MESH),  INTENT(INOUT) :: MESH2D
      TYPE(BIEF_OBJ),   INTENT(IN)    :: Z3
      TYPE(BIEF_OBJ),   INTENT(IN)    :: SMASKEL
      TYPE(BIEF_OBJ),   INTENT(INOUT) :: SVIDE
      TYPE(BIEF_OBJ),   INTENT(INOUT) :: TRAV2, FU2
      TYPE(BIEF_OBJ),   INTENT(INOUT) :: SVOLU,SMU,SMV
!
!                                     * = NSCE
      INTEGER, INTENT(IN) :: ISCE(*),KSCE(*)
      DOUBLE PRECISION, INTENT(IN) :: QSCE(*),USCE(*),VSCE(*)
!
      DOUBLE PRECISION, INTENT(IN) :: GRAV, DT, AT, FCOR
      LOGICAL, INTENT(IN) :: CORIOL, SEDI, MSK, INCHYD,COUROU
      LOGICAL, INTENT(INOUT) :: YASEM3D
      TYPE(BIEF_FILE), INTENT(IN) :: T3D_FILES(*)
!
!+-+-+-+-+-+-+-+-+-+-+-+-+-+-+-+-+-+-+-+-+-+-+-+-+-+-+-+-+-+-+-+-+-+-+-+
!
      INTEGER IELEM3,IPLAN,IETAGE,IZ,IZM,IZS,ERR,NP,I3D
      DOUBLE PRECISION A,OMEGA,PI,CORI
!
      INTEGER I,OPTFLO
      CHARACTER(LEN=15) FORMUL
!
      CHARACTER(LEN=8) :: FFORMAT
      INTEGER :: FILE_ID, IERR
!
      INTEGER I1,I2,I3,I4,I5,I6
      DOUBLE PRECISION DX1,DX2,DX3,DY1,DY2,DY3
      DOUBLE PRECISION DZ1,DZ2,DZ3,DR1,DR2,DR3
      DOUBLE PRECISION SZ1,SZ2,SZ3,SR1,SR2,SR3
      DOUBLE PRECISION DZSUDX,DZSUDY,DRSUDX,DRSUDY
      DOUBLE PRECISION DZ123,C,ATH
!
!+++++++++++++++++++++++++++++++++++++++++++++
!+++++++++++++++++++++++++++++++++++++++++++++
! JT & AR
      DOUBLE PRECISION DIST,FORCEX,FORCEY,XSOM(4),YSOM(4),X4,Y4
      DOUBLE PRECISION deltad,THICK,K0,KN
      DOUBLE PRECISION XMID,YMID,ZMID,Xwest,Xeast,Ynorth,Ysouth
      DOUBLE PRECISION DISTwest,DISTeast
      DOUBLE PRECISION Ct0,Ct,cutin,cutoff
      DOUBLE PRECISION VupsWEST,VupsEAST,Vupstream
      DOUBLE PRECISION XTURB(12),YTURB(12)
      INTEGER, PARAMETER :: NTURB = 3
      INTEGER J,IPTwest,IPTeast,IPT,I3Dwest,I3Deast
!+++++++++++++++++++++++++++++++++++++++++++++
!+++++++++++++++++++++++++++++++++++++++++++++
!
!     FOR WAVE DRIVEN CURRENTS
!JT & AR - add HYDROLIENNE in logical
!
      CHARACTER*16 NOMX,NOMY
      LOGICAL DEJALU,OKX,OKY,HYDROLIENNE
      DATA DEJALU /.FALSE./
!
!***********************************************************************
!
! INITIALISES
!
!     CALL OS( 'X=C     ' , X=SCV1 , C=0.D0 )
!     CALL OS( 'X=C     ' , X=SCV2 , C=0.D0 )
!
      SCV1%TYPR='0'
      SCV2%TYPR='0'
!
!-----------------------------------------------------------------------
!  BUOYANCY SOURCE TERMS (ONLY WITH DENLAW NOT 0, EVEN FOR SEDIMENT !!)
!-----------------------------------------------------------------------
```

```
!
      YASEM3D=.FALSE.
!
      IF(DENLAW.NE.0.AND.NTRAC.GT.0) THEN
!
      SCV1%TYPR='Q'
      SCV2%TYPR='Q'
      CALL OS( 'X=0     ' , X=SCV1 )
      CALL OS( 'X=0     ' , X=SCV2 )
!
!     VOLUME OF TEST FUNCTIONS
!
      CALL VECTOR(ST1, '=', 'MASBAS          ',IELM3, 1.D0,
     &            SVIDE, SVIDE,
     &            SVIDE, SVIDE, SVIDE, SVIDE, MESH3,.FALSE.,SMASKEL)
      IF(NCSIZE.GT.1) CALL PARCOM(ST1,2,MESH3)
!
!     1 : BUOYANCY IN REAL MESH
!     2 : BUOYANCY IN TRANSFORMED MESH
!
!     OPTFLO CHANGED FROM 2 INTO 1 BY JMH ON 03/10/2002
!     ENABLES TREATMENT WITH TETRAHEDRONS
!     WHO CAN TELL WHICH IS BEST WITH PRISMS ?
!
      OPTFLO=1
!
      IF(OPTFLO.EQ.1) THEN
!
      YASEM3D=.FALSE.
!
! - G DENSITY GRADIENTS
!     WITH TREATMENT OF HYDROSTATIC INCONSISTENCIES IF NEEDED
!     THIS IS AVAILABLE ONLY FOR PRISMS !!!!!!!!!!!!
!
      FORMUL='GRADF          '
      IF(IELM3.EQ.41.AND.INCHYD) FORMUL(6:6)='2'
!
!     ================================================
!     BETTER FILTERING OF HYDROSTATIC INCONSISTENCIES
!     ================================================
!
!     3 OR 4 IMPLIES THAT 2 IS ALSO APPLIED
!
!     RECOMMENDED : FILTER 4
!
!     FILTER 3
!     IF(INCHYD) FORMUL(6:6)='3'
!     FILTER 4
!     IF(INCHYD) FORMUL(6:6)='4'
!
!
      CALL VECTOR(ST2, '=',FORMUL//'X',IELM3,-GRAV,DELTAR,SVIDE,
     &            SVIDE,SVIDE,SVIDE,SVIDE,MESH3,MSK,SMASKEL)
!
      CALL VECTOR(ST3, '=',FORMUL//'Y',IELM3,-GRAV,DELTAR,SVIDE,
     &            SVIDE,SVIDE,SVIDE,SVIDE,MESH3,MSK,SMASKEL)
!
      IF(NCSIZE.GT.1) THEN
        CALL PARCOM(ST2,2,MESH3)
        CALL PARCOM(ST3,2,MESH3)
      ENDIF
!
! NODAL VALUE
!
      CALL OVD('X=Y/Z   ',T2,T2,T1,0.D0,NPOIN3,2,0.D0,1.D-9)
      CALL OVD('X=Y/Z   ',T3,T3,T1,0.D0,NPOIN3,2,0.D0,1.D-9)
!
! SIMPSON INTEGRATION
!
      DO IPLAN = NPLAN, 2, -1
        DO I = 1, NPOIN2
          IZ  =(IPLAN-1)*NPOIN2+I
          IZM =(IPLAN-2)*NPOIN2+I
          A = 0.5D0 * (Z(IZ)-Z(IZM))
          CV1(IZM) = CV1(IZ) + (T2(IZ)+T2(IZM)) * A
          CV2(IZM) = CV2(IZ) + (T3(IZ)+T3(IZM)) * A
        ENDDO
      ENDDO
!
! TERMS WITH FREE SURFACE GRADIENT (NODAL VALUES)
!
      DO IPLAN = 1, NPLAN-1
!
        DO I = 1, NPOIN2
          IZ  = (IPLAN-1)*NPOIN2+I
          IZS = (NPLAN-1)*NPOIN2+I
          A = GRAV*(DELTAR%R(IZ)-DELTAR%R(IZS))
!
          CV1(IZ) = CV1(IZ) + A * GRADZSX%R(I)
          CV2(IZ) = CV2(IZ) + A * GRADZSY%R(I)
!
        ENDDO
!
      ENDDO
!
      ELSEIF(OPTFLO.EQ.2) THEN
!
      YASEM3D = .FALSE.
!
! TRANSFORMED MESH
!
! COMPUTES ZS: OPPOSITE OF WATER DEPTH AT CONSIDERED POINT
!
        I2 = NPOIN3 - NPOIN2 + 1
        I4 = NPOIN3
        DO IPLAN = 1,NPLAN
          I1 = NPOIN2*(IPLAN-1) + 1
          I3 = NPOIN2* IPLAN
          CALL OV( 'X=Y-Z   ', ZS(I1:I3), Z(I1:I3), Z(I2:I4), C, NPOIN2)
        END DO
!
        BYELEMENT: DO IELEM3 = 1 , NELEM3
!
          I1 = IKLE3(IELEM3,1)
          I2 = IKLE3(IELEM3,2)
          I3 = IKLE3(IELEM3,3)
          I4 = IKLE3(IELEM3,4)
          I5 = IKLE3(IELEM3,5)
          I6 = IKLE3(IELEM3,6)
!
          DX1 = X(I3) - X(I2)
          DX2 = X(I1) - X(I3)
          DX3 = X(I2) - X(I1)
          DY1 = Y(I2) - Y(I3)
          DY2 = Y(I3) - Y(I1)
          DY3 = Y(I1) - Y(I2)
!
          DR1 = DELTAR%R(I4) - DELTAR%R(I1)
          DR2 = DELTAR%R(I5) - DELTAR%R(I2)
          DR3 = DELTAR%R(I6) - DELTAR%R(I3)
          DZ1 = ZS(I4) - ZS(I1)
          DZ2 = ZS(I5) - ZS(I2)
          DZ3 = ZS(I6) - ZS(I3)
          DZ123 = DZ1 + DZ2 + DZ3
!
          SZ1 = ZS(I4) + ZS(I1)
          SZ2 = ZS(I5) + ZS(I2)
          SZ3 = ZS(I6) + ZS(I3)
          SR1 = DELTAR%R(I4) + DELTAR%R(I1)
          SR2 = DELTAR%R(I5) + DELTAR%R(I2)
          SR3 = DELTAR%R(I6) + DELTAR%R(I3)
!
          IF(MAX(ZS(I1),ZS(I2),ZS(I3)).GT.
     &       MIN(ZS(I4),ZS(I5),ZS(I6)).AND.INCHYD) THEN
            DR1 = 0.D0
            DR2 = 0.D0
            DR3 = 0.D0
            SR1 = 0.D0
            SR2 = 0.D0
            SR3 = 0.D0
          ENDIF
!
          DZSUDX = SZ1 * DY1 + SZ2 * DY2 + SZ3 * DY3
          DZSUDY = SZ1 * DX1 + SZ2 * DX2 + SZ3 * DX3
          DRSUDX = SR1 * DY1 + SR2 * DY2 + SR3 * DY3
          DRSUDY = SR1 * DX1 + SR2 * DX2 + SR3 * DX3
!
          W1(IELEM3,1) = DR1 * DZSUDX - DZ1 * DRSUDX
          W1(IELEM3,2) = DR2 * DZSUDX - DZ2 * DRSUDX
          W1(IELEM3,3) = DR3 * DZSUDX - DZ3 * DRSUDX
          W2(IELEM3,1) = DR1 * DZSUDY - DZ1 * DRSUDY
          W2(IELEM3,2) = DR2 * DZSUDY - DZ2 * DRSUDY
          W2(IELEM3,3) = DR3 * DZSUDY - DZ3 * DRSUDY
          W3(IELEM3,1) = DZ1 + DZ123
          W3(IELEM3,2) = DZ2 + DZ123
          W3(IELEM3,3) = DZ3 + DZ123
!
        END DO BYELEMENT
```

```
!
        IF (NETAGE.NE.1) THEN
!
           BYETAGE: DO IETAGE = NETAGE-1 , 1 , -1
              I2 = NELEM2*IETAGE + 1
              I1 = I2 - NELEM2
              CALL OV('X=X+Y   ' , W1(I1,1) , W1(I2,1) , Z , C , NELEM2)
              CALL OV('X=X+Y   ' , W1(I1,2) , W1(I2,2) , Z , C , NELEM2)
              CALL OV('X=X+Y   ' , W1(I1,3) , W1(I2,3) , Z , C , NELEM2)
              CALL OV('X=X+Y   ' , W2(I1,1) , W2(I2,1) , Z , C , NELEM2)
              CALL OV('X=X+Y   ' , W2(I1,2) , W2(I2,2) , Z , C , NELEM2)
              CALL OV('X=X+Y   ' , W2(I1,3) , W2(I2,3) , Z , C , NELEM2)
           END DO BYETAGE
!
           I2 = NELEM2 + 1
           I1 = NELEM3 - NELEM2
           CALL OV('X=Y     ' , W1(1,4) , W1(I2,1) , Z , C , I1)
           CALL OV('X=Y     ' , W1(1,5) , W1(I2,2) , Z , C , I1)
           CALL OV('X=Y     ' , W1(1,6) , W1(I2,3) , Z , C , I1)
           CALL OV('X=Y     ' , W2(1,4) , W2(I2,1) , Z , C , I1)
           CALL OV('X=Y     ' , W2(1,5) , W2(I2,2) , Z , C , I1)
           CALL OV('X=Y     ' , W2(1,6) , W2(I2,3) , Z , C , I1)
!
        ENDIF
!
        I1 = NELEM3 - NELEM2 + 1
        CALL OV('X=C     ' , W1(I1,4) , Y , Z , 0.D0 , NELEM2)
        CALL OV('X=C     ' , W1(I1,5) , Y , Z , 0.D0 , NELEM2)
        CALL OV('X=C     ' , W1(I1,6) , Y , Z , 0.D0 , NELEM2)
        CALL OV('X=C     ' , W2(I1,4) , Y , Z , 0.D0 , NELEM2)
        CALL OV('X=C     ' , W2(I1,5) , Y , Z , 0.D0 , NELEM2)
        CALL OV('X=C     ' , W2(I1,6) , Y , Z , 0.D0 , NELEM2)
!
        CALL OV('X=XY    ' , W1(1,1) , W3 , Z , C , 3*NELEM3)
        CALL OV('X=XY    ' , W1(1,4) , W3 , Z , C , 3*NELEM3)
        CALL OV('X=XY    ' , W2(1,1) , W3 , Z , C , 3*NELEM3)
        CALL OV('X=XY    ' , W2(1,4) , W3 , Z , C , 3*NELEM3)
!
        DO IETAGE = 1 , NETAGE
          I1 = NELEM2*(IETAGE-1) + 1
          CALL OV('X=XY    ' , W3(I1,1) , SURFAC , Z , C , NELEM2)
          CALL OV('X=XY    ' , W3(I1,2) , SURFAC , Z , C , NELEM2)
          CALL OV('X=XY    ' , W3(I1,3) , SURFAC , Z , C , NELEM2)
        ENDDO
        CALL OV('X=Y     ' , W3(1,4) , W3 , Z , C , 3*NELEM3)
!
        CALL ASSVEC(CV1,IKLE3,NPOIN3,NELEM3,NELEM3,41,W1,.FALSE.,
     &              LV,MSK,MASKEL,6)
        CALL ASSVEC(CV2,IKLE3,NPOIN3,NELEM3,NELEM3,41,W2,.FALSE.,
     &              LV,MSK,MASKEL,6)
        CALL ASSVEC(T1,IKLE3,NPOIN3,NELEM3,NELEM3,41,W3,.TRUE. ,
     &              LV,MSK,MASKEL,6)
!
        IF(NCSIZE.GT.1) THEN
          CALL PARCOM(SCV1,2,MESH3)
          CALL PARCOM(SCV2,2,MESH3)
          CALL PARCOM(ST1,2,MESH3)
        ENDIF
!
        CALL OVD('X=CY/Z  ',CV1,CV1,T1,0.25D0*GRAV,NPOIN3,2,0.D0,1D-9)
        CALL OVD('X=CY/Z  ',CV2,CV2,T1,0.25D0*GRAV,NPOIN3,2,0.D0,1D-9)
!
      ENDIF
!
!     IF(NTRAC.GT.0)
      ENDIF
!
!-----------------------------------------------------------------------
!  CORIOLIS FORCE
!-----------------------------------------------------------------------
!
      IF(CORIOL) THEN
!
        IF(SCV1%TYPR.EQ.'0') THEN
          CALL OS( 'X=0     ' , X=SCV1 )
          CALL OS( 'X=0     ' , X=SCV2 )
          SCV1%TYPR='Q'
          SCV2%TYPR='Q'
        ENDIF
!
!       HERE THE VERTICAL VELOCITY IS NEGLECTED
!
        IF(SPHERI) THEN
!
          PI=ACOS(-1.D0)
          OMEGA=2.D0*PI/86164.D0
!
          DO IPLAN=1,NPLAN
            DO I=1,NPOIN2
              CORI=2.D0*OMEGA*MESH2D%SINLAT%R(I)
              I3=(IPLAN-1)*NPOIN2+I
              CV1(I3)=CV1(I3)+VN3(I3)*CORI
              CV2(I3)=CV2(I3)-UN3(I3)*CORI
            ENDDO
          ENDDO
!
!         TAKES THE TIDE GENERATING FORCE INTO ACCOUNT
!
          IF(MAREE) THEN
            CALL CPSTVC(MESH2D%X,T2_01)
            CALL CPSTVC(MESH2D%Y,T2_02)
            CALL OS('X=0     ',X=T2_01)
            CALL OS('X=0     ',X=T2_02)
            CALL MARAST(MARDAT,MARTIM,LONGIT,NPOIN2,AT,
     &                  T2_01%R,T2_02%R,MESH2D%X%R,
     &                  MESH2D%SINLAT%R,MESH2D%COSLAT%R,GRAV)
            DO IPLAN=1,NPLAN
              DO I=1,NPOIN2
                I3=(IPLAN-1)*NPOIN2+I
                CV1(I3)=CV1(I3)+T2_01%R(I)
                CV2(I3)=CV2(I3)+T2_02%R(I)
              ENDDO
            ENDDO
          ENDIF
!
        ELSE
!
          CALL OV('X=X+CY   ',CV1,VN3,VN3,  FCOR,NPOIN3)
          CALL OV('X=X+CY   ',CV2,UN3,UN3,-FCOR,NPOIN3)
!
        ENDIF
!
      ENDIF
!
!***********************************************************************
!
!     * WITH WAVE DRIVEN CURRENTS
!       -------------------------
!
!       FORCING TERMS FROM A TOMAWAC RESULTS FILE
!
!       BEWARE :    1. MESHES MUST BE THE SAME
!       ---------
!                   2. TAKES THE LAST TIMESTEP FROM TOMAWAC FILE
!
      IF(COUROU) THEN
!
        IF(.NOT.DEJALU.AND..NOT.INCLUS(COUPLING,'TOMAWAC')) THEN
!
!
!         T3DBI1 : BINARY DATA FILE 1
          NOMX='FORCE FX        '
          NOMY='FORCE FY        '
          FFORMAT = T3D_FILES(T3DBI1)%FMT
          FILE_ID = T3D_FILES(T3DBI1)%LU
          CALL FIND_VARIABLE(FFORMAT, FILE_ID, NOMX, FXH%R, NPOIN2,
     &                       IERR,RECORD=NPTH,TIME_RECORD=ATH)
          OKX = IERR.EQ.0
          CALL FIND_VARIABLE(FFORMAT, FILE_ID, NOMY, FYH%R, NPOIN2,
     &                       IERR,RECORD=NPTH,TIME_RECORD=ATH)
          OKY = IERR.EQ.0
!
          IF(.NOT.OKX.OR..NOT.OKY) THEN
            IF(LNG.EQ.1) WRITE(LU,5)
            IF(LNG.EQ.2) WRITE(LU,6)
 5          FORMAT(1X,'TRISOU : FORCE FX OU FY NON TROUVES',/,1X,
     &             '         DANS LE FICHIER DE HOULE')
 6          FORMAT(1X,'TRISOU: FORCE FX OR FY NOT FOUND',/,1X,
     &             '        IN THE WAVE RESULTS FILE')
            CALL PLANTE(1)
            STOP
          ENDIF
!         WRITES OUT TO LISTING
          IF(LNG.EQ.1) WRITE(LU,115) ATH
          IF(LNG.EQ.2) WRITE(LU,116) ATH
115       FORMAT(1X,/,1X,'TRISOU : COURANTS DE HOULE',/,
     &           1X,'         LECTURE AU TEMPS ',F10.3,/)
116       FORMAT(1X,/,1X,'TRISOU: WAVE DRIVEN CURRENTS MODELLING',/,
```

```
673       &               1X,'         READING FILE AT TIME ',F10.3,/)
674            DEJALU = .TRUE.
675  !
676           ENDIF
677  !
678  !       ADDS TO SOURCE TERMS
679  !
680           IF(SCV1%TYPR.EQ.'0') THEN
681             DO I=1,NPOIN2
682               DO IPLAN=1,NPLAN
683                 I3D=((IPLAN-1)*NPOIN2)+I
684  !              CV1(I3D)=1.5D0*FXH%R(I)   (SOGREAH-PECHON-TEISSON VERSION)
685                 CV1(I3D)=FXH%R(I)
686                 CV2(I3D)=FYH%R(I)
687               ENDDO
688             ENDDO
689             SCV1%TYPR='Q'
690             SCV2%TYPR='Q'
691           ELSE
692             DO I=1,NPOIN2
693               DO IPLAN=1,NPLAN
694                 I3D=((IPLAN-1)*NPOIN2)+I
695  !              CV1(I3D)=CV1(I3D)+1.5D0*FXH%R(I)   (SOGREAH-PECHON-TEISSON VERSION)
696                 CV1(I3D)=CV1(I3D)+FXH%R(I)
697                 CV2(I3D)=CV2(I3D)+FYH%R(I)
698               ENDDO
699             ENDDO
700           ENDIF
701  !
702         ENDIF
703  !
704  !
705  !+++++++++++++++++++++++++++++++++++++++++++++
706  !
707  ! JT : HYDROLIENNES
708  ! EDITED AR  10/10/16
709  !
710  !+++++++++++++++++++++++++++++++++++++++++++++
711  !
712           IF(SCV1%TYPR.EQ.'0') THEN
713             CALL OS( 'X=0     ' , X=SCV1 )
714             CALL OS( 'X=0     ' , X=SCV2 )
715             SCV1%TYPR='Q'
716             SCV2%TYPR='Q'
717           ENDIF
718  !
719  ! JT Force hydroliennes en ms-2
720  ! EDITED AR
721  !
722           HYDROLIENNE = .true.
723  !-------------------------------------------------------------------------------
724  !        print*,'READ 2: HYDROLIENNE = TRUE'
725  !-------------------------------------------------------------------------------
726         IF (HYDROLIENNE) THEN
727  ! TURBINE - parameters
728           K0     = 1.53D0
729           Ct0    = 0.8D0
730           cutin  = 1.D0
731           cutoff = 2.5D0
732  ! TURBINE - Structured grid
733           THICK  = 8.D0
734           ZMID   = 15.D0
735           deltad = 1.D0
736  !  Indicate the position of each turbine (rectangle)
737  !--------------- ** ROW 1 ** ----------------------
738  !---------------- Turbine 1 -----------------------
739           XTURB(1) = 492780.D0-deltad
740           XTURB(2) = 492788.D0+deltad
741           XTURB(3) = 492788.D0+deltad
742           XTURB(4) = 492780.D0-deltad
743  !
744           YTURB(1) = 6502040.D0-deltad
745           YTURB(2) = 6502040.D0-deltad
746           YTURB(3) = 6502056.D0+deltad
747           YTURB(4) = 6502056.D0+deltad
748  !---------------- Turbine 2 -----------------------
749           XTURB(5) = 492780.D0-deltad
750           XTURB(6) = 492788.D0+deltad
751           XTURB(7) = 492788.D0+deltad
752           XTURB(8) = 492780.D0-deltad
753  !
754           YTURB(5) = 6502104.D0-deltad
755           YTURB(6) = 6502104.D0-deltad
756           YTURB(7) = 6502120.D0+deltad
757           YTURB(8) = 6502120.D0+deltad
758  !---------------- Turbine 3 -----------------------
759           XTURB(9)  = 492892.D0-deltad
760           XTURB(10) = 492900.D0+deltad
761           XTURB(11) = 492900.D0+deltad
762           XTURB(12) = 492892.D0-deltad
763  !
764           YTURB(9)  = 6502072.D0-deltad
765           YTURB(10) = 6502072.D0-deltad
766           YTURB(11) = 6502088.D0+deltad
767           YTURB(12) = 6502088.D0+deltad
768  !------------- END OF TURBINE -----------------
769          DO J=1,NTURB
770           XSOM(1) = XTURB(1+(J-1)*4)-deltad
771           XSOM(2) = XTURB(2+(J-1)*4)+deltad
772           XSOM(3) = XTURB(3+(J-1)*4)+deltad
773           XSOM(4) = XTURB(4+(J-1)*4)-deltad
774  !
775           YSOM(1) = YTURB(1+(J-1)*4)-deltad
776           YSOM(2) = YTURB(2+(J-1)*4)-deltad
777           YSOM(3) = YTURB(3+(J-1)*4)+deltad
778           YSOM(4) = YTURB(4+(J-1)*4)+deltad
779  !-------------------------------------------------------------------------------
780  !        print*,'READ 3: XSOM(4) YSOM(4) = ', XSOM(4),YSOM(4)
781  !-------------------------------------------------------------------------------
782           DO I=1,NPOIN2
783            IF(INPOLY(X(I),Y(I),XSOM(1:4),YSOM(1:4),4)) THEN
784  !         Compute upstream velocity
785            XMID =  ((XSOM(1)+XSOM(2))/2.D0)
786            YMID =  ((YSOM(1)+YSOM(4))/2.D0)
787  !         To find free stream velocity (Uf) for nodes
788  !         located 50m from the turbines
789            Xwest  = XMID - 50.D0
790            Xeast  = XMID + 50.D0
791            Ynorth = YMID + 8.D0
792            Ysouth = YMID - 8.D0
793  !         Find nearest nodes to Xwest & Xeast
794  !         MAX value for SQRT((x(IPT)-XMID)**2+(y(IPT)-YMID)**2)
795            DISTwest   = 50.636D0
796            DISTeast   = 50.636D0
797            IPTwest = 1
798            IPTeast = 1
799            DO IPT=1,NPOIN2
800             IF (SQRT((X(IPT)-Xwest)**2+(Y(IPT)-Ynorth)**2).le.
801       &     DISTwest) THEN
802              DISTwest=SQRT((X(IPT)-Xwest)**2+(Y(IPT)-Ynorth)**2)
803              IPTwest = IPT
804             ENDIF
805             IF (SQRT((X(IPT)-Xeast)**2+(Y(IPT)-Ynorth)**2).le.
806       &     DISTeast) THEN
807              DISTeast=SQRT((X(IPT)-Xeast)**2+(Y(IPT)-Ynorth)**2)
808              IPTeast = IPT
809             ENDIF
810            ENDDO
811  !-------------------------------------------------------------------------------
812  !       print*,'READ 4: IPTwest & IPTeast = ',  IPTwest , IPTeast
813  !-------------------------------------------------------------------------------
814  !         Upstream velocity for Xwest & Xeast
815  !         (averaged over the vertical speed)
816            VupsWEST =0.D0
817            VupsEAST =0.D0
818            DO IPLAN=1,NPLAN
819              I3Dwest =  ((IPLAN-1)*NPOIN2)+IPTwest
820              I3Deast =  ((IPLAN-1)*NPOIN2)+IPTeast
821              VupsWEST=VupsWEST+
822       &        SQRT(UN3(I3Dwest)*UN3(I3Dwest)+VN3(I3Dwest)*VN3(I3Dwest))
823              VupsEAST=VupsEAST+
824       &        SQRT(UN3(I3Deast)*UN3(I3Deast)+VN3(I3Deast)*VN3(I3Deast))
825            ENDDO
826            VupsWEST=VupsWEST/NPLAN
827            VupsEAST=VupsEAST/NPLAN
828            Vupstream=VupsWEST
829            IF(VupsEAST.GT.Vupstream) THEN
830              Vupstream=VupsEAST
831            ENDIF
832  !-------------------------------------------------------------------------------
833  !       print*,'READ 5: VupsWEST & VupsEAST = ',  VupsWEST , VupsEAST
834  !-------------------------------------------------------------------------------
835  !         Implementation of the momentum sink
836            DO IPLAN=1,NPLAN
837             I3D=((IPLAN-1)*NPOIN2)+I
838             DIST = SQRT((Y(I)-YMID)**2 + (ABS(Z(I3D))-ZMID)**2)
839  !-------------------------------------------------------------------------------
840  !     print*,'READ 6: plane Z(I3D) & calculated DIST = ',  Z(I3D) , DIST
```

```
!-----------------------------------------------------------------------
            IF (DIST.LE.8.3D0) THEN
!            for cut in velocity of (1m/s)
             IF (Vupstream.GE.cutin) THEN
!             for cut off velocity of (2.5m/s)
              IF (Vupstream.LE.cutoff) THEN
                    FORCEX = -(0.5D0*K0/THICK)*
     &           SQRT(UN3(I3D)*UN3(I3D)+VN3(I3D)*VN3(I3D))*UN3(I3D)
                    CV1(I3D)=CV1(I3D)+FORCEX
!
                    FORCEY = -(0.5D0*K0/THICK)*
     &           SQRT(UN3(I3D)*UN3(I3D)+VN3(I3D)*VN3(I3D))*VN3(I3D)
                    CV2(I3D)=CV2(I3D)+FORCEY
!-----------------------------------------------------------------------
!      print*,'READ 7a:FORCEX & FORCEY = ', FORCEX , FORCEY
!-----------------------------------------------------------------------
               ELSE ! for velocity greater than cut off (2.5m/s)
!-----------------------------------------------------------------------
                    Ct = (Ct0*cutoff**3) / (Vupstream**3)
                    KN = (16-8*Ct-16*(SQRT(1-Ct)))/(2*Ct)
!-----------------------------------------------------------------------
                    FORCEX = -(0.5D0*KN/Thick)*
     &           SQRT(UN3(I3D)*UN3(I3D)+VN3(I3D)*VN3(I3D))*UN3(I3D)
                    CV1(I3D)=CV1(I3D)+FORCEX
!
                    FORCEY = -(0.5D0*KN/Thick)*
     &           SQRT(UN3(I3D)*UN3(I3D)+VN3(I3D)*VN3(I3D))*VN3(I3D)
                    CV2(I3D)=CV2(I3D)+FORCEY
!-----------------------------------------------------------------------
!      print*,'READ 7b:FORCEX & FORCEY = ', FORCEX , FORCEY
!-----------------------------------------------------------------------
              ENDIF
             ENDIF
            ENDIF
           ENDDO
          ENDIF
         ENDDO
        ENDDO
       ENDIF
!
! Fin JT & AR
!
!-----------------------------------------------------------------------
!
! TAKES THE VELOCITY OF SOURCES INTO ACCOUNT
!
! NOTE : IF USCE AND VSCE ARE NOT GIVEN, CONSIDERS THAT
!        USCE=UN3 AND VSCE=VN3
!
      IF(NREJEU.GT.0.AND.SCHCVI.NE.ADV_NSC.AND.SCHCVI.NE.ADV_PSI
     &                  .AND.SCHCVI.NE.ADV_LPO.AND.SCHCVI.NE.ADV_NSC_TF
     &                  .AND.SCHCVI.NE.ADV_LPO_TF) THEN
!
        IF(SCV1%TYPR.EQ.'0') THEN
          CALL OS( 'X=0      ' , X=SCV1 )
          CALL OS( 'X=0      ' , X=SCV2 )
          SCV1%TYPR='Q'
          SCV2%TYPR='Q'
        ENDIF
!
!       ASSEMBLING THE VOLUMES IN PARALLEL
!
        CALL OS('X=Y     ',X=ST1,Y=SVOLU)
        IF(NCSIZE.GT.1) CALL PARCOM(ST1,2,MESH3)
!
!       WITH DISTRIBUTIVE SCHEMES AND FINITE VOLUME SCHEMES
!       THIS IS DONE DIRECTLY INTO SUBROUTINE MURD3D, AND NOT WITH CV1
!
        DO I=1,NREJEU
          IF(ISCE(I).GT.0) THEN
            I3D=(KSCE(I)-1)*NPOIN2+ISCE(I)
            A=MAX(ST1%R(I3D),1.D-6)
            CV1(I3D)=CV1(I3D)+(USCE(I)-UN3(I3D))*QSCE(I)/A
            CV2(I3D)=CV2(I3D)+(VSCE(I)-VN3(I3D))*QSCE(I)/A
          ENDIF
        ENDDO
!
      ENDIF
!
!-----------------------------------------------------------------------
!
      RETURN
      END
```

References

[1] IPCC, "Climate Change 2014. Synthesis Report. Summary Chapter for Policy-makers," Tech. Rep., 2014.

[2] International Energy Agency (IEA), "Key world energy statistics," Tech. Rep., 2016. [Online]. Available: www.iea.org

[3] Scottish Government, "Action on energy in Scotland," 2016. [Online]. Available: http://www.gov.scot/Topics/Business-Industry/Energy/Action

[4] House of Commons - Energy and Climate Change Commitee, "2020 renewable heat and transport targets," Parliament UK, Tech. Rep., 2016. [Online]. Available: https://publications.parliament.uk/pa/cm201617/cmselect/cmenergy/173/173.pdf

[5] Scottish Government, "2020 ROUTEMAP FOR RENEWABLE ENERGY IN SCOTLAND - UPDATE," Tech. Rep. September, 2011. [Online]. Available: http://www.gov.scot/Resource/0048/00485407.pdf

[6] BBC, "Scotland sets 50% renewable energy target," 2017. [Online]. Available: http://www.bbc.co.uk/news/uk-scotland-scotland-politics-38729869

[7] I. Johnston, "UK ranked 24th out of 28 EU member states for renewable energy," 2017. [Online]. Available: http://www.independent.co.uk/environment/uk-ranked-24-out-of-28-eu-member-states-renewable-energy-wind-farms-fossil-fuels-solar-p
html

[8] D. Boffey, "EU on track to meet renewable energy targets – but UK lags behind," 2017. [Online]. Available: https://www.theguardian.com/environment/2017/feb/01/eu-on-track-to-meet-renewable-energy-targets-but-uk-lags-behind

[9] Parliament UK, "Government to miss 2020 renewable energy targets," 2016. [Online]. Available: https://www.parliament.uk/business/committees/committees-a-z/commons-select/energy-and-climate-change-committee/news-parliament-2015/heat-transport-report-published-16-17/

[10] Parliament UK, "2020 renewable heat and transport targets," 2016. [Online]. Available: https://publications.parliament.uk/pa/cm201617/cmselect/cmenergy/173/17310.htm?utm{_}source=173{&}utm{_}medium=crbullet{&}utm{_}campaign=modulereports

[11] Scottish Government, "Energy in Scotland: Get the facts," 2017. [Online]. Available: http://www.gov.scot/Topics/Business-Industry/Energy/Facts

[12] M. A. A. Shields, L. J. J. Dillon, D. K. K. Woolf, and A. T. T. Ford, "Strategic priorities for assessing ecological impacts of marine renewable energy devices in the Pentland Firth (Scotland, UK)," *Marine Policy*, vol. 33, no. 4, pp. 635–642, 2009.

[13] S. Draper, "Tidal Stream Energy Extraction in Coastal Basins," Ph.D. dissertation, University of Oxford, 2011.

[14] MeyGen Ltd, "MeyGen Phase 1 EIA Scoping Document," 2011. [Online]. Available: http://www.meygen.com/the-project/pentland-firth-inner-sound/

[15] L. J. Dillon and D. K. Woolf, "An Initial Evaluation of Potential Tidal Stream Development Sites in Pentland Firth , Scotland," in *10th World Renewable Energy Congress*, 2008, pp. 1023–1029.

[16] R. B. O'Hara Murray and A. Gallego, "A modelling study of the tidal stream resource of the Pentland Firth, Scotland," *Renewable Energy*, vol. 102, pp. 326–340, 2017. [Online]. Available: http://dx.doi.org/10.1016/j.renene.2016.10.053

[17] T. Wang and Z. Yang, "A modeling study of tidal energy extraction and the associated impact on tidal circulation in a multi-inlet bay system of Puget Sound," *Renewable Energy*, vol. 114, pp. 204–214, 2017. [Online]. Available: http://dx.doi.org/10.1016/j.renene.2017.03.049

[18] A. Pérez-Ortiz, A. G. Borthwick, J. McNaughton, and A. Avdis, "Characterization of the tidal resource in Rathlin Sound," *Renewable Energy*, vol. 114, pp. 229–243, 2017.

[19] R. Martin-Short, J. Hill, S. C. Kramer, A. Avdis, and P. a. Allison, "Tidal resource extraction in the Pentland Firth , UK : potential impacts on flow regime and sediment transport in the Inner Sound of Stroma," *Renewable Energy*, vol. 76, pp. 596–607, 2015. [Online]. Available: http://dx.doi.org/10.1016/j.renene.2014.11.079

[20] Atlantis Resources Limited, "Meygen - Project Development and Operation," 2017. [Online]. Available: https://www.atlantisresourcesltd.com/projects/meygen/

[21] X. Sun, J. Chick, and I. Bryden, "Laboratory-scale simulation of energy extraction from tidal currents," *Renewable Energy*, vol. 33, no. 6, pp. 1267–1274, 2008. [Online]. Available: http://linkinghub.elsevier.com/retrieve/pii/S0960148107002340

[22] T. Daly, L. E. Myers, and a. S. Bahaj, "Modelling of the flow field surrounding tidal turbine arrays for varying positions in a channel." *The Royal Society A*, vol. 371, no. January, p. 20120246, feb 2013. [Online]. Available: http://www.ncbi.nlm.nih.gov/pubmed/23319708

[23] M. Harrison, W. Batten, L. Myers, and A. Bahaj, "Comparison between CFD simulations and experiments for predicting the far wake of horizontal axis tidal turbines," *Renewable Power Generation, IET*, vol. 4, no. 6, pp. 613–627, 2010. [Online]. Available: http://eprints.soton.ac.uk/73773/

[24] C. Lartiga and C. Crawford, "Actuator Disk Modeling in Support of Tidal Turbine Rotor Testing," in *3rd International Conference on Ocean Energy*, 2010, pp. 1–6.

[25] T. Roc, D. C. Conley, and D. Greaves, "Methodology for tidal turbine representation in ocean circulation model," *Renewable Energy*, vol. 51, pp. 448–464, 2013.

[26] EMEC, "Assessment of Tidal Energy Resource. Marine Renewable Energy Guides," Tech. Rep., 2009. [Online]. Available: file:///C:/Users/s1361364/Downloads/4AssessmentofTidalEnergyResource.pdf

[27] RenewableUK, "Wave and Tidal Energy in the UK - State of the industry report," Tech. Rep. March, 2011.

[28] UK Government, "Wave and tidal energy: part of the UK's energy mix," 2013. [Online]. Available: https://www.gov.uk/guidance/wave-and-tidal-energy-part-of-the-uks-energy-mix

[29] A. Thomas, R. Mason-Jones, D. Turner, P. Davies, T. O. Doherty, D. O'Doherty, and A. Mason-Jones, "Tidal and Marine Energy in the UK– Identifying the Future Challenges for Supply Chain Development," in *11th International Conference on Manufacturing Research*, no. September, pp. 655–660.

[30] Carbon Trust, Black & Veatch, and Npower, "UK Tidal Current Resource and Economics Study," Tech. Rep. July, 2011.

[31] Crown Estate Scotland, "Wave and tidal," 2017. [Online]. Available: http://www.crownestatescotland.com/the-assets/marine/asset/wave-and-tidal

[32] RenewableUK, "UK Marine Energy Database (UKMED)," 2017. [Online]. Available: http://www.renewableuk.com/page/UKMED2

[33] European Marine Energy Centre (EMEC) Ltd, "WAVE & TIDAL PROJECTS," 2017. [Online]. Available: http://www.emec.org.uk/marine-energy/wave-and-tidal-projects/

[34] Carbon Trust, "Accelerating marine energy," Tech. Rep. July, 2011.

[35] T. Delorm, "TIDAL STREAM DEVICES : RELIABILITY PREDICTION MODELS DURING THEIR CONCEPTUAL & DEVELOPMENT PHASES," Ph.D. dissertation, 2014.

[36] D. Magagna and A. Uihlein, "Ocean energy development in Europe: Current status and future perspectives," *International Journal of Marine Energy*, vol. 11, pp. 84–104, 2015. [Online]. Available: http://dx.doi.org/10.1016/j.ijome.2015.05.001

[37] European Marine Energy Centre (EMEC) Ltd, "TIDAL DEVELOPERS," 2017. [Online]. Available: http://www.emec.org.uk/marine-energy/tidal-developers/

[38] European Marine Energy Centre (EMEC) Ltd, "The European Marine Energy Centre (EMEC)," 2017. [Online]. Available: http://www.emec.org.uk/

[39] Atlantis Resources Limited, "Atlantis Resources Ltd," 2017. [Online]. Available: https://www.atlantisresourcesltd.com/

[40] DP Energy, "DP Energy," 2017. [Online]. Available: http://www.dpenergy.com/

[41] Nova Innovation Ltd, "Nova Innovation Ltd," 2017. [Online]. Available: https://www.novainnovation.com/

[42] A. Frangoul, "Nova Innovation explores tidal energy potential off north Wales coast," 2017. [Online]. Available: https://www.cnbc.com/2017/07/17/nova-innovation-explores-tidal-energy-potential-off-north-wales-coast.html

[43] Oceanflow Energy Ltd, "Oceanflow Energy Limited," 2017. [Online]. Available: http://www.oceanflowenergy.com/

[44] QED Naval Ltd, "QED Naval Limited," 2017. [Online]. Available: http://www.qednaval.co.uk/

[45] Scotrenewables Tidal Power Ltd, "Scotrenewables Tidal Power Limited," 2017. [Online]. Available: http://www.scotrenewables.com/

[46] Minesto, "Minesto - Technology," 2017. [Online]. Available: https://minesto.com/our-technology

[47] RenewableUK, "Ocean Energy Race - The UK ' s inside track," Tech. Rep., 2017. [Online]. Available: https://c.ymcdn.com/sites/renewableuk.site-ym.com/resource/resmgr/publications/OER{_}inside{_}track{_}final{_}-{_}onl.pdf

[48] NASA - Goddard Space Flight Center, "TOPEX/Poseidon: Revealing Hidden Tidal Energy," 2016. [Online]. Available: https://svs.gsfc.nasa.gov//stories/topex/tides.html

[49] H.-w. Liu, S. Ma, W. Li, H.-g. Gu, Y.-g. Lin, and X.-j. Sun, "A review on the development of tidal current energy in China," *Renewable and Sustainable Energy Reviews*, vol. 15, no. 2, pp. 1141–1146, feb 2011. [Online]. Available: http://linkinghub.elsevier.com/retrieve/pii/S1364032110004119

[50] M. Gorji-Bandpy, M. Azimi, and M. Jouya, "Tidal energy and main resources in the persian gulf," *Distributed Generation & Alternative Energy Journal*, vol. 28, no. 2, pp. 61–77, 2013. [Online]. Available: http://dx.doi.org/10.1080/21563306.2013.10677551

[51] H. Samani and M. R. Heidary, "Feasibility Study on Renewable Power Plants : Tidal Power Plants," vol. 3, no. 3, pp. 66–71, 2014.

[52] Ocean Energy Systems, "Annual Report: Implementing Agreement on Ocean Energy Systems," Tech. Rep. December, 2013.

[53] International Renewable Energy Agency (IRENA), "Tidal Energy: Technology Brief," IRENA Ocean Energy Technology, Tech. Rep. June, 2014.

[54] Parliament UK, "PUBLICATION OF THE HENDRY REVIEW INTO THE STRATEGIC ROLE OF TIDAL LAGOONS IN

THE UK," 2017. [Online]. Available: https://www.parliament.uk/business/publications/written-questions-answers-statements/written-statement/Commons/2017-01-12/HCWS404/

[55] C. Hendry, "THE ROLE OF FINAL LAGOONS," Tech. Rep. December, 2016. [Online]. Available: https://hendryreview.files.wordpress.com/2016/08/hendry-review-final-report-english-version.pdf

[56] S. Waters and G. Aggidis, "Tidal range technologies and state of the art in review," *Renewable and Sustainable Energy Reviews*, vol. 59, pp. 514–529, 2016.

[57] S. R. Waters, "Analysing the performance of the Archimedes Screw Turbine within tidal range technologies," no. November, 2015.

[58] S. Waters and G. Aggidis, "A world first: Swansea Bay tidal lagoon in review," *Renewable and Sustainable Energy Reviews*, vol. 56, pp. 916–921, 2016. [Online]. Available: http://dx.doi.org/10.1016/j.rser.2015.12.011

[59] J. R. Brammer, "Physical and Numerical Modelling of Marine Renewable Energy Technologies , with Particular Focus on Tidal Stream and Tidal Range Devices," Ph.D. dissertation, 2014.

[60] A. Cornett, J. Cousineau, and I. Nistor, "Assessment of hydrodynamic impacts from tidal power lagoons in the Bay of Fundy," *International Journal of Marine Energy*, vol. 1, pp. 33–54, apr 2013. [Online]. Available: http://linkinghub.elsevier.com/retrieve/pii/S2214166913000076

[61] T. J. Hammons, "Tidal power," *Proceedings of the IEEE*, vol. 81, no. 3, pp. 419–433, Mar 1993.

[62] European Marine Energy Centre (EMEC) Ltd, "TIDAL DEVICES," 2017. [Online]. Available: http://www.emec.org.uk/marine-energy/tidal-devices/

[63] Atlantis Resources Limited, "Ar1500 Tidal Turbine," Tech. Rep., 2017. [Online]. Available: https://www.atlantisresourcesltd.com/wp/wp-content/uploads/2016/08/AR1500-Brochure-Final-1.pdf

[64] ESRU - University of Strathclyde, "Technology: Vertical Axis Turbine." [Online]. Available: http://www.esru.strath.ac.uk/EandE/Web{_}sites/05-06/marine{_}renewables/technology/vertaxis.htm

[65] ESRU - University of Strathclyde, "Technology: Oscillating Hydrofoil," 2017. [Online]. Available: http://www.esru.strath.ac.uk/EandE/Web{_}sites/05-06/marine{_}renewables/technology/oschydro.htm

[66] Lunar Energy Ltd, "Lunar Energy - Technology," 2017. [Online]. Available: http://www.lunarenergy.co.uk/productOverview.htm

[67] New England Hydropower Company LLC, "Archimedes Screw Generators," 2017. [Online]. Available: http://www.nehydropower.com/screw-generators

[68] I. Renewable, *Offshore Renewable Energy: Accelerating the Deployment of Offshore Wind, Tidal, and Wave Technologies*. Taylor & Francis, 2013. [Online]. Available: https://books.google.co.uk/books?id=q_7IBQAAQBAJ

[69] L. Myers and A. Bahaj, "An experimental investigation simulating flow effects in first generation marine current energy converter arrays," *Renewable Energy*, vol. 37, no. 1, pp. 28–36, 2012. [Online]. Available: http://www.sciencedirect.com/science/article/pii/S0960148111001716

[70] E. Zangiabadi, M. Edmunds, I. A. Fairley, M. Togneri, A. J. Williams, I. Masters, and N. Croft, "Computational fluid dynamics and visualisation of coastal flows in tidal channels supporting ocean energy Development," *Energies*, vol. 8, no. 6, pp. 5997–6012, 2015.

[71] Mason-Jones, D. M. O'Doherty, C. E. Morris, T. O'Doherty, C. B. Byrne, P. W. Prickett, R. I. Grosvenor, I. Owen, S. Tedds, and R. J. Poole, "Non-dimensional scaling of tidal stream turbines," *Energy*, vol. 44, no. 1, pp. 820–829, 2012. [Online]. Available: http://dx.doi.org/10.1016/j.energy.2012.05.010

[72] S. Tatum, M. Allmark, C. Frost, D. O'Doherty, A. Mason-Jones, and T. O'Doherty, "CFD modelling of a tidal stream turbine subjected to profiled flow and surface gravity waves," *International Journal of Marine Energy*, vol. 15, pp. 156–174, 2016. [Online]. Available: http://dx.doi.org/10.1016/j.ijome.2016.04.003

[73] V. James, "Marine Renewable Energy: A Global Review of the Extent of Marine Renewable Energy Developments, the Developing Technologies and Possible Conservation Implications for Cetaceans," Whale and Dolphine Conservation, Tech. Rep. November, 2013. [Online]. Available: http://uk.whales.org/sites/default/files/2{_}-{_}wdc{_}marine{_}renewables{_}2013{_}lowres.pdf

[74] Farinia Group, "Tidal Turbine Ballast and Other Tidal Turbine Foundations," 2017. [Online]. Available: http://www.farinia.com/energy/tidal-turbine-counterweights/tidal-turbine-ballast-and-other-tidal-turbine-foundations

[75] Z. Zhou, F. Scuiller, J. F. Charpentier, M. Benbouzid, and T. Tang, "An up-to-date review of large marine tidal current turbine technologies," in *2014 International Power Electronics and Application Conference and Exposition*, 2014, pp. 480–484.

[76] 4C Offshore Ltd, "Tidal Projects," 2017. [Online]. Available: http://www.4coffshore.com/windfarms/tidals.aspx

[77] T. A. A. Adcock, S. Draper, and T. Nishino, "Tidal power generation - A review of hydrodynamic modelling," *Proceedings of the Institution of Mechanical Engineers, Part A: Journal of Power and Energy*, vol. 0, no. 0, pp. 1–17, 2015. [Online]. Available: http://pia.sagepub.com/lookup/doi/10.1177/0957650915570349

[78] R. F. Mikkelsen, "Actuator Disc Methods Applied to Wind Turbines by Robert Mikkelsen Dissertation submitted to the Technical University of Denmark in partial fulfillment of," Ph.D. dissertation, 2004.

[79] A. Creech, A. Borthwick, and D. Ingram, "Effects of Support Structures in an LES Actuator Line Model of a Tidal Turbine with Contra-Rotating Rotors," *Energies*, vol. 10, no. 6, p. 726, 2017. [Online]. Available: http://www.mdpi.com/1996-1073/10/5/726

[80] M. Visbal, "Three-Dimensional Flow Structure on a Heaving Low-Aspect-Ratio Wing," *49th AIAA Aerospace Sciences Meeting including the New Horizons Forum and Aerospace Exposition*, no. January, 2011. [Online]. Available: http://arc.aiaa.org/doi/10.2514/6.2011-219

[81] C. Garrett and P. Cummins, "The Power Potential of Tidal Currents In Channels," *Proceedings of the Royal Society A: Mathematical, Physical and Engineering Sciences*, vol. 461, no. 2060, pp. 2563–2572, aug 2005. [Online]. Available: http://rspa.royalsocietypublishing.org/cgi/doi/10.1098/rspa.2005.1494

[82] C. a. Consul, R. H. J. Willden, and S. C. McIntosh, "Blockage effects on the hydrodynamic performance of a marine cross-flow turbine." *Philosophical transactions. Series A, Mathematical, physical, and engineering sciences*, vol. 371, no. 1985, p. 20120299, 2013. [Online]. Available: http://www.ncbi.nlm.nih.gov/pubmed/23319712

[83] J. Whelan, M. Thomson, J. M. R. Graham, and J. Peiro, "Modelling of free surface proximity and wave induced velocities around a horizontal axis tidal stream turbine," in *Proceedings of the 7th European Wave and Tidal Energy Conference Porto Portugal*, 2007, pp. 11–14.

[84] J. N. Sørensen, "Aerodynamic aspects of wind energy conversion," *Annual Review of Fluid Mechanics*, vol. 43, pp. 427–448, 2011.

[85] R. Vennell, S. W. Funke, S. Draper, C. Stevens, and T. Divett, "Designing large arrays of tidal turbines: A synthesis and review," *Renewable and Sustainable Energy Reviews*, vol. 41, pp. 454–472, 2015. [Online]. Available: http://dx.doi.org/10.1016/j.rser.2014.08.022

[86] T. Nishino and R. H. J. Willden, "Effects of 3-D channel blockage and turbulent wake mixing on the limit of power extraction by tidal turbines," *International Journal of Heat and Fluid Flow*, vol. 37, pp. 123–135, 2012. [Online]. Available: http://dx.doi.org/10.1016/j.ijheatfluidflow.2012.05.002

[87] A. Olczak, T. Stallard, T. Feng, and P. Stansby, "Comparison of a RANS blade element model for tidal turbine arrays with laboratory scale measurements of wake velocity and rotor thrust," *Journal of Fluids and Structures*, vol. 64, pp. 87–106, 2016. [Online]. Available: http://linkinghub.elsevier.com/retrieve/pii/S088997461530058X

[88] J. F. Manwell, J. G. McGowan, and A. L. Rogers, *Wind Energy Explained: Theory, Design and Application*, 2nd ed. Wiley-Blackwell, 2009.

[89] Y. Shan, "2D Actuator Disk and Vertical Axis Rotor Model in the Wave- Current Unsteady Flow," Ph.D. dissertation, Delft University, 2013.

[90] S. Baston, S. Waldman, and J. Side, "Modelling energy extraction in tidal flows," Tech. Rep. June, 2014.

[91] C. Garrett and P. Cummins, "The efficiency of a turbine in a tidal channel," *Journal of Fluid Mechanics*, vol. 588, pp. 243–251, sep 2007. [Online]. Available: http://www.journals.cambridge.org/abstract{_}S0022112007007781

[92] J. I. Whelan, J. M. R. Graham, and J. Peiró, "A free-surface and blockage correction for tidal turbines," *Journal of Fluid Mechanics*, vol. 624, pp. 281–291, mar 2009. [Online]. Available: http://www.journals.cambridge.org/abstract{_}S0022112009005916

[93] G. T. Houlsby and S. Draper, "Application of Linear Momentum Actuator Disc Theory to Open Channel Flow," *OUEL*, p. 25, 2008.

[94] R. Vennell, "Exceeding the Betz limit with tidal turbines," *Renewable Energy*, vol. 55, pp. 277–285, 2013. [Online]. Available: http://dx.doi.org/10.1016/j.renene.2012.12.016

[95] S. R. Turnock, A. B. Phillips, J. Banks, and R. Nicholls-Lee, "Modelling tidal current turbine wakes using a coupled RANS-BEMT approach as a tool for analysing power capture of arrays of turbines," *Ocean Engineering*, vol. 38, no. 11-12, pp. 1300–1307, 2011. [Online]. Available: http://dx.doi.org/10.1016/j.oceaneng.2011.05.018

[96] R. Malki, A. J. Williams, T. N. Croft, M. Togneri, and I. Masters, "A coupled blade element momentum - Computational fluid dynamics model for evaluating tidal stream turbine performance," *Applied Mathematical Modelling*, vol. 37, no. 5, pp. 3006–3020, 2013. [Online]. Available: http://dx.doi.org/10.1016/j.apm.2012.07.025

[97] G. Ingram, "Wind Turbine Blade Analysis using the Blade Element Momentum Method. Version 1.1," Tech. Rep. c, 2011.

[98] M. E. Harrison, W. M. J. Batten, and a. S. Bahaj, "A blade element actuator disc approach applied to tidal stream turbines," in *OCEANS 2010*, 2010.

[99] W. Batten, M. Harrison, and A. Bahaj, "The accuracy of the actuator disc-RANS approach for predicting the performance and far wake of a horizontal axis tidal stream turbine," *Philosophical Transactions of the Royal Society of London A: Mathematical, Physical and Engineering Sciences*, vol. 371, no. 1985, 2013. [Online]. Available: http://rsta.royalsocietypublishing.org/content/371/1985/20120293.abstract

[100] R. Malki, A. J. Williams, T. N. Croft, M. Togneri, and I. Masters, "A coupled blade element momentum - Computational fluid dynamics model for evaluating tidal stream turbine performance," *Applied Mathematical*

Modelling, vol. 37, no. 5, pp. 3006–3020, 2013. [Online]. Available: http://dx.doi.org/10.1016/j.apm.2012.07.025

[101] C. Belloni, "Hydrodynamics of Ducted and Open-Centre Tidal Turbines," Ph.D. dissertation, University of Oxford, 2013.

[102] R. F. Nicholls-lee and S. Uk, "Simulation Based Optimisation of Marine Current Turbine Blades," in *7th International Conference on Computer and IT Applications in the Maritime Industries (COMPIT'08), Liège, Belgium*, 2008, pp. 314–328.

[103] N. Troldborg, "Actuator Line Modeling of Wind Turbine Wakes by Niels Troldborg Dissertation submitted to the Technical University of Denmark in partial fulfillment of," Ph.D. dissertation, 2008.

[104] L. Martinez, S. Leonardi, M. Churchfield, P. Moriarty, and L. a. Mart, "A Comparison of Actuator Disk and Actuator Line Wind Turbine Models and Best Practices for Their Use," in *50th AIAA Aerospace Sciences Meeting including the New Horizons Forum and Aerospace Exposition*, no. January, 2012, pp. 1–13. [Online]. Available: http://dx.doi.org/10.2514/6.2012-900

[105] R. E. Keck, "A numerical investigation of nacelle anemometry for a HAWT using actuator disc and line models in CFX," *Renewable Energy*, vol. 48, pp. 72–84, 2012. [Online]. Available: http://dx.doi.org/10.1016/j.renene.2012.04.004

[106] M. J. Churchfield, Y. Li, and P. J. Moriarty, "A large-eddy simulation study of wake propagation and power production in an array of tidal-current turbines." *Philosophical transactions. Series A, Mathematical, physical, and engineering sciences*, vol. 371, no. 1985, p. 20120421, 2013. [Online]. Available: http://www.ncbi.nlm.nih.gov/pubmed/23319713

[107] T. Burton, N. Jenkins, D. Sharpe, and E. Bossanyi, *Wind Energy Handbook*. John Wiley & Sons LTD, 2011. [Online]. Available: http://books.google.com/books?hl=en{&}lr={&}id=dip2LwCRCscC{&}pgis=1

[108] S. Draper, A. G. L. Borthwick, and G. T. Houlsby, "Energy potential of a tidal fence deployed near a coastal headland." *Philosophical transactions. Series A, Mathematical, physical, and engineering sciences*, vol. 371, no. January, p. 20120176, 2013. [Online]. Available: http://www.ncbi.nlm.nih.gov/pubmed/23319703

[109] S. Serhadlıoğlu, T. a.a. Adcock, G. T. Houlsby, S. Draper, and A. G. Borthwick, "Tidal stream energy resource assessment of the Anglesey Skerries," *International Journal of Marine Energy*, vol. 3-4, pp. e98–e111, dec 2013. [Online]. Available: http://linkinghub.elsevier.com/retrieve/pii/S2214166913000404

[110] T. S. Government, "Energy in Scotland: Get the facts," Available: http://www.gov.scot/Topics/Business-Industry/Energy/Facts, 2014, [Online; accessed 1-October-2014].

[111] T. A. A. Adcock, S. Draper, G. T. Houlsby, A. G. L. Borthwick, and S. Serhadlıoğlu, "The available power from tidal stream turbines in the Pentland Firth," *Proceedings of the Royal Society A: Mathematical, Physical and Engineering Science*, vol. 469, no. 2157, sep 2013. [Online]. Available: http://rspa.royalsocietypublishing.org/content/469/2157/20130072.abstract

[112] The Crown Estate, "Wave and tidal energy in the Pentland Firth and Orkney waters - Delivering the first phases of projects," Tech. Rep. September, 2013.

[113] MeyGen, "MeyGen Phase 1 EIA Scoping Document," no. May, p. 108, 2011.

[114] RenewableUK, "Wave & Tidal Energy," Available: http://www.renewableuk.com/en/renewable-energy/wave-and-tidal/, 2016, [Online; accessed 6-April-2016].

[115] A. M. Davies, S. C. M. Kwong, and J. C. Lee, "A Detailed Comparison of a Range of Three-Dimensional Models of the M2 Tide in the Faeroe – Shetland Channel and Northern North Sea," *Journal of Physical Oceanography*, vol. 31, no. 1995, pp. 1747–1763, 2001.

[116] A. Chatzirodou and H. Karunarathna, "Impacts of tidal energy extraction on sea bed morphology," in *Coastal Engineering Proceedings*, vol. 1, no. 34, 2014, p. 33. [Online]. Available: https://icce-ojs-tamu.tdl.org/icce/index.php/icce/article/view/7352

[117] S. Baston, R. E. Harris, D. K. Woolf, R. A. Hiley, and J. C. Side, "Sensitivity Analysis of the Turbulence Closure Models in the Assessment of Tidal Energy Resource in Orkney," in *10th European Wave and Tidal Energy Conference (EWTEC)*, 2013.

[118] V. Venugopal and R. Nemalidinne, "Marine Energy Resource Assessment for Orkney Waters with a Coupled Wave and Tidal Flow Model," in *33rd International Conference on Ocean, Offshore and Arctic Engineering (OMAE2014)*, 2014.

[119] M. C. Easton, D. K. Woolf, and P. a. Bowyer, "The dynamics of an energetic tidal channel, the Pentland Firth, Scotland," *Continental Shelf Research*, vol. 48, pp. 50–60, oct 2012. [Online]. Available: http://linkinghub.elsevier.com/retrieve/pii/S0278434312002233

[120] S. Baston and R. E. Harris, "Modelling the Hydrodynamic Characteristics of Tidal Flow in the Pentland Firth," in *9th European Wave and Tidal Energy Conference (EWTEC)*, 2010.

[121] P. Bowyer and G. Marchi, "Tidal Residual flows in the Pentland Firth," in *9th European Wave and Tidal Energy Conference (EWTEC)*, 2011. [Online]. Available: http://www.eri.ac.uk/files/downloads/download2152.pdf

[122] A. Pérez-Ortiz, J. Pescatore, and I. Bryden, "A Systematic Approach to Undertake Tidal Energy Resource Assessment with Telemac-2D," in *10th European Wave and Tidal Energy Conference (EWTEC)*, 2013.

[123] EDF, "TELEMAC-MASCARET," Available: http://www.opentelemac.org/, 2008, [Online; accessed 1-July-2014].

[124] J. M. Hervouet, *Hydrodynamics of Free Surface Flows: Modelling with the finite element method.* John Wiley and Sons, 2007.

[125] Deltares, "Delft3D Open Source Community," Available: http://oss.deltares.nl/web/delft3d, 2010, [Online; accessed 1-November-2013].

[126] EDF, "TELEMAC-3D Operating Manual," Tech. Rep. March, 2013.

[127] J. M. Hervouet and J. A. Jankowski, "Comparing numerical simulations of free surface flows using non-hydrostatic Navier-Stokes and Boussinesq equations," in *Proceedings of the 4th Conference on Hydroinformatics*, Iowa City, Iowa (USA), 2000.

[128] EDF, "TELEMAC-3D CODE," Tech. Rep. December, 2007.

[129] J. A. Jankowski, A. Malcherek, and W. Zielke, "Numerical modeling of sediment transport processes caused by deep sea mining discharges," in *OCEANS '94. 'Oceans Engineering for Today's Technology and Tomorrow's Preservation.' Proceedings*, vol. 3, Sep 1994, pp. III/269–III/277 vol.3.

[130] M. Serrer, "Blue Kenue: Software for the Hydraulic Modellers," Available: http://www.nrc-cnrc.gc.ca/eng/solutions/advisory/blue{_}kenue{_}index.html, 2012, [Online; accessed 10-May-2014].

[131] N. Clavreul, "Fudaa PreProcessor," Available: http://prepro.fudaa.fr/index.en.php, 2012, [Online; accessed 20-July-2014].

[132] B. O. D. C. (BODC), "GEBCO Grid Display Software," Available: http://www.gebco.net/about{_}us/news{_}and{_}events/grid{_}display{_}version{_}211.html, 2009, [Online; accessed 15-June-2014].

[133] TeraWatt, "Terrawatt consortium."

[134] P. A. Gillibrand, R. A. Walters, and J. McIlvenny, "Numerical simulations of the effects of a tidal turbine array on near-bed velocity and local bed shear stress," *Energies*, vol. 9, no. 10, 2016.

[135] A. J. Goward Brown, S. P. Neill, and M. J. Lewis, "Tidal energy extraction in three-dimensional ocean models," *Renewable Energy*, vol. 114, pp. 244–257, 2017. [Online]. Available: http://dx.doi.org/10.1016/j.renene.2017.04.032

[136] A. Rahman and V. Venugopal, "Parametric analysis of three dimensional flow models applied to tidal energy sites in scotland," *Estuarine, Coastal and Shelf Science*, vol. 189, pp. 17 – 32, 2017. [Online]. Available: http://www.sciencedirect.com/science/article/pii/S0272771417302123

[137] K. Gunn and C. Stock-Williams, "On validating numerical hydrodynamic models of complex tidal flow," *International Journal of Marine Energy*, vol. 3-4, pp. e82–e97, 2013. [Online]. Available: http://dx.doi.org/10.1016/j.ijome.2013.11.013

[138] EDF, "TOMAWAC Reference Manual," Tech. Rep. September, 2011.

[139] A. Jourieh, "Multi-dimensional Numerical Simulation of Hydrodynamics and Transport Processes in Surface Water Systems in Berlin," Ph.D. dissertation, 2014.

[140] M. J. Kreitmair, "Effect of bed roughness uncertainty on tidal stream power estimates," in *European Wave and Tidal Energy Conference 2017*, 2017.

[141] R. Soulsby, "Tidal-Current Boundary Layers," in *Ocean Engineering Science*, B. L. Mehaute and D. M. Hanes, Eds. Cambridge, Massachusetts and London: Harvard University Press, 1990, ch. 15, pp. 523–567.

[142] A. Rahman and V. Venugopal, "Inter-Comparison of 3D Tidal Flow Models Applied To Orkney Islands and Pentland Firth," in *11th European Wave and Tidal Energy Conference (EWTEC 2015)*, 2015.

[143] A. R. Campbell, J. H. Simpson, and G. L. Allen, "The Dynamical Balance of Flow in the Menai Strait," *Coastal and Shelf Science Estuarine*, no. February 1997, pp. 449–455, 1998.

[144] V. Venugopal, T. Davey, H. Smith, G. Smith, L. Cavaleri, L. Bertotti, and J. Lawrence, "Application of Numerical Models - EquiMAR Deliverable D2.3," Tech. Rep. June, 2010.

[145] A. M. Davies, S. C. M. Kwong, and J. C. Lee, "A Detailed Comparison of a Range of Three-Dimensional Models of the M2 Tide in the Faeroe – Shetland Channel and Northern North Sea," *Journal of Physical Oceanography*, vol. 31, no. 1995, pp. 1747–1763, 2001.

[146] J. Nikuradse, "Laws of Flow in Rough Pipes (Stromungsgesetze in Rauen Rohren), VDI-Forschungsheft) vol. 361, 1933. Beilage zu: Forschung auf dem Gebiete des Ingenieurwesens, Ausgabe B Band 4; English Translation NACA Tech. Mem. 1292," Tech. Rep. November, 1950.

[147] J. Kämpf, *Advanced Ocean Modelling Using Open-Source Software*. Springer, 2010. [Online]. Available: http://link.springer.com/content/pdf/10.1007/978-3-642-10610-1.pdf

[148] J. Smagorinsky, "General Circulation Experiments With the Primitive Equations," *Monthly Weather Review*, vol. 91, no. 3, pp. 99–164, 1963. [Online]. Available: http://journals.ametsoc.org/doi/abs/10.1175/1520-0493(1963)091{%}3C0099:GCEWTP{%}3E2.3.CO;2

[149] Y. Mensencal and C. Freissinet, "Sustainable Management of Scarce Resources in the Coastal Zone (SMART) : Hydrological simulation modelling system," Tech. Rep., 2003.

[150] T. J. Zitman and H. M. Schuttelaars, "Importance of cross-channel bathymetry and eddy viscosity parameterisation in modelling estuarine flow," *Ocean Dynamics*, vol. 62, no. 4, pp. 603–631, feb 2012. [Online]. Available: http://link.springer.com/10.1007/s10236-011-0513-5

[151] I. Nezu and H. Nakagawa, *Turbulence in Open-Channel Flows*. Rotterdam, Netherlands: Balkema Publishers, 1993.

[152] A. G. Borthwick and R. W. Barber, "River and reservoir flow modelling using the transformed shallow water equations," *International Journal for Numerical Methods in Fluids*, vol. 14, no. 10, pp. 1193–1217, 1992.

[153] P. Bonar, "Toward best practice in the design of tidal turbine arrays," PhD Thesis, University of Edinburgh, UK, 2017.

[154] M. Bijvelds, "Numerical Modelling of Estuarine Flow Over Steep Topography," Ph.D. dissertation, Delft University, 2001.

[155] Deltares, "Delft3D Flow User Manual," Tech. Rep. December, 2014.

[156] I. Fairley, I. Masters, and H. Karunarathna, "The cumulative impact of tidal stream turbine arrays on sediment transport in the Pentland Firth," *Renewable Energy*, vol. 80, pp. 755–769, 2015. [Online]. Available: http://dx.doi.org/10.1016/j.renene.2015.03.004

[157] T. Stiven, S. J. Couch, and A. S. Iyer, "Assessing the impact of ADCP resolution and sampling rate on tidal current energy project economics," in *OCEANS 2011 IEEE - Spain, Santander*, 2011, pp. 1–10.

[158] Deltares, "Problems Running Delft3D Simulation in Parallel on Linux Cluster," 2014. [Online]. Available: http://oss.deltares.nl/web/delft3d/coast-/-estuary/-/message{_}boards/view{_}message/474071;jsessionid=89DCF899C4075720FA6AEBA5CC4E22F8

[159] S. P. Neill, E. J. Litt, S. J. Couch, and A. G. Davies, "The impact of tidal stream turbines on large-scale sediment dynamics," *Renewable Energy*, vol. 34, no. 12, pp. 2803–2812, dec 2009.

[160] P. E. Robins, S. P. Neill, and M. J. Lewis, "Impact of tidal-stream arrays in relation to the natural variability of sedimentary processes," *Renewable Energy*, vol. 72, pp. 311–321, 2014. [Online]. Available: http://linkinghub.elsevier.com/retrieve/pii/S0960148114004352

[161] V. T. Nguyen, S. S. Guillou, J. Thiebot, and A. S. Cruz, "Modelling turbulence with an Actuator Disk representing a tidal turbine," *Renewable Energy*, 2016.

[162] G. Taylor, *The Scientific Papers of Sir Geoffrey Ingram Taylor*, Edited by G.K.Batchelor., Ed. Cambridge University Press, 1963.

[163] C. Belloni and R. H. J. Willden, "A computational study of a bi-directional ducted tidal turbine," in *3rd International Conference on Ocean Energy (ICOE), Bilbao*, no. 1, 2010.

[164] L. E. Myers and a. S. Bahaj, "Experimental analysis of the flow field around horizontal axis tidal turbines by use of scale mesh disk rotor simulators," *Ocean Engineering*, vol. 37, no. 2-3, pp. 218–227, 2010. [Online]. Available: http://dx.doi.org/10.1016/j.oceaneng.2009.11.004

[165] M. Harrison, W. Batten, L. Myers, and A. Bahaj, "A comparison between CFD simulations and experiments for predicting the far wake of horizontal axis tidal turbines," in *Proceedings of the 8th European Wave and Tidal Energy Conference*, vol. 4, no. 6, 2009, pp. 613–627. [Online]. Available: http://eprints.soton.ac.uk/73773/

[166] N. C. Scott, M. R. Smeed, A. C. McLaren, and Xero Energy Ltd, "Pentland Firth Tidal Energy Project Grid Options Study Prepared for : Highlands and Islands Enterprise," Tech. Rep. January, 2009.

[167] Carbon Trust, "PHASE II : UK TIDAL STREAM ENERGY RESOURCE ASSESSMENT," Tech. Rep. 0, 2005.

[168] A. Rahman and V. Venugopal, "On the Validation of Three-Dimensional Actuator Disc Approach for a Full Size Turbine," in *Proceedings of the 3rd Asian Wave and Tidal Energy Conference (AWTEC2016), Singapore - Vol 2*, no. 3. Singapore: Research Publishing, 2016, pp. 551–558. [Online]. Available: http://www.awtec.asia/awtec-2016/

[169] S. M. Salim and S. C. Cheah, "Wall y + Strategy for Dealing with Wall-bounded Turbulent Flows," in *International MultiConference of Engineers and Computer Scientists (IMECS)*, vol. II, 2009, pp. 1–6.

[170] G. Kalitzin, G. Medic, G. Iaccarino, and P. Durbin, "Near-wall behavior of RANS turbulence models and implications for wall functions," *Journal of Computational Physics*, vol. 204, no. 1, pp. 265–291, 2005.

[171] J. Macenri, M. Reed, and T. Thiringer, "Influence of tidal parameters on SeaGen flicker performance." *Philosophical Transactions of the Royal Society A: Mathematical, Physical and Engineering Sciences*, vol. 371, no. 1985, p. 20120247, 2013. [Online]. Available: http://www.ncbi.nlm.nih.gov/pubmed/23319709

[172] E. Osalusi, J. Side, and R. Harris, "Reynolds stress and turbulence estimates in bottom boundary layer of Fall of Warness," *International Communications in Heat and Mass Transfer*, vol. 36, no. 5, pp. 412–421, 2009. [Online]. Available: http://dx.doi.org/10.1016/j.icheatmasstransfer.2009.02.004

[173] E. Osalusi, J. Side, and R. Harris, "Structure of turbulent flow in EMEC's tidal energy test site," *International Communications in Heat and Mass Transfer*, vol. 36, no. 5, pp. 422–431, 2009. [Online]. Available: http://dx.doi.org/10.1016/j.icheatmasstransfer.2009.02.010

[174] IEC61400-21, "Wind turbines part 21: measurement and assessment of power quality characteristics of grid connected wind turbines." Tech. Rep., 2008.

[175] I. a. Milne, R. N. Sharma, R. G. J. Flay, and S. Bickerton, "The Role of Onset Turbulence on Tidal Turbine Blade Loads," in *17th Australasian Fluid Mechanics Conference Auckland New Zealand 59 December 2010*, no. December, 2010, pp. 1–8.

[176] A. Rohatgi, "WebPlotDigitizer," 2013. [Online]. Available: http://arohatgi.info/WebPlotDigitizer/

[177] T. Blackmore, W. Batten, M. Harrison, and A. Bahaj, "The Sensitivity of Actuator-Disc RANS Simulations to Turbulence Length Scale Assumptions," in *European Wave and Tidal Energy Conference 2011*, 2011, pp. 390–399. [Online]. Available: http://scholar.google.com/scholar?hl=en{&}btnG=Search{&}q=intitle:The+Sensitivity+of+Actuator-Disc+RANS+Simulations+to+Turbulence+Length+Scale+Assumptions{#}5

[178] S. H. Salter, "Correcting the Under-estimate of the Tidal-Stream Resource of the Pentland Firth," in *Proceedings of the 8th European Wave and Tidal Energy Conference*, Uppsala, Sweeden, 2009.

[179] P. Mycek, B. Gaurier, G. Germain, G. Pinon, and E. Rivoalen, "Experimental study of the turbulence intensity effects on marine current turbines behaviour. Part I: One single turbine," *Renewable Energy*, vol. 68, no. June, pp. 729–746, 2014. [Online]. Available: http://dx.doi.org/10.1016/j.renene.2013.12.048

[180] Y. Li, J. a. Colby, N. Kelley, R. Thresher, B. Jonkman, and S. Hughes, "Inflow measurement in a tidal strait for deploying tidal current turbines: lessons, opportunities and challenges," in *ASME 2010 29th International Conference on Ocean, Offshore and Arctic Engineering (OMAE2010), 6-11 June 2010, Shanghai, China. Volume 3*, 2010, pp. 1–8. [Online]. Available: http://proceedings.asmedigitalcollection.asme.org/proceeding.aspx?articleid=1617582

[181] A. S. Bahaj, L. E. Myers, M. D. Thomson, and N. Jorge, "Characterising the wake of horizontal axis marine current turbines," in *Proceedings of the 7th European Wave and Tidal Energy Conference (AWTEC), Porto, Portugal, 2007*, Porto, Portugal, 2007.

[182] C. Christian and R. Vennel, "Efficiency of tidal turbine farms," *Coastal Engineering Proceedings*, vol. 1, no. 33, p. 4, 2012. [Online]. Available: https://journals.tdl.org/icce/index.php/icce/article/view/6470

[183] T. Stallard, R. Collings, T. Feng, and J. Whelan, "Interactions betweem tidal turbine wakes: Experimental study of a group of 3-bladed rotors," *Philosophical Transactions of the Royal Society of London: A*, vol. 371, no. 1985, pp. 1471–2962, 2013.

[184] S. Nash, A. I. Olbert, and M. Hartnett, "Towards a low-cost modelling system for optimising the layout of tidal turbine arrays," *Energies*, vol. 8, no. 12, pp. 13 521–13 539, 2015.

[185] P. A. Bonar, I. G. Bryden, and A. G. Borthwick, "Social and ecological impacts of marine energy development," *Renewable and Sustainable Energy Reviews*, vol. 47, pp. 486–495, 2015. [Online]. Available: http://dx.doi.org/10.1016/j.rser.2015.03.068

[186] S. P. Neill, J. R. Jordan, and S. J. Couch, "Impact of tidal energy converter (TEC) arrays on the dynamics of headland sand banks," *Renewable Energy*, vol. 37, no. 1, pp. 387–397, jan 2012. [Online]. Available: http://linkinghub.elsevier.com/retrieve/pii/S0960148111003855

[187] L. Goddijn-Murphy, D. K. Woolf, and M. C. Easton, "Current Patterns in the Inner Sound (Pentland Firth) from Underway ADCP Data*," *Journal of Atmospheric and Oceanic Technology*, vol. 30, no. 1, pp. 96–111, jan 2013. [Online]. Available: http://journals.ametsoc.org/doi/abs/10.1175/JTECH-D-11-00223.1

[188] M. Easton, D. Woolf, and S. Pans, "An operational hydrodynamic model of a key tidal energy site: Inner Sound of Stroma, Pentland Firth (Scotland, UK)," in *3rd International Conference on Ocean Energy (ICOE)*, Bilbao, 2010. [Online]. Available: http://www.academia.edu/download/29857297/ICOE2010{_}MEaston.pdf

[189] Nova Innovation Ltd, "Notice to Mariners Initial Maritime Safety Information," Tech. Rep., 2014. [Online]. Available: https://www.shetland.gov.uk/ports/documents/NoticeToMariners-NovaInnovations-CullivoeTidalTurbine-FinalDeploymentLocation.pdf

[190] MeyGen Limited, "Meygen Inner Sound Project Maps," 2013. [Online]. Available: http://www.meygen.com/maps/

[191] MeyGen Limited, "Meygen Inner Turbine Technology," 2013. [Online]. Available: www.meygen.com/technology/

[192] A. Roberts, B. Thomas, P. Sewell, Z. Khan, S. Balmain, and J. Gillman, "Current tidal power technologies and their suitability for applications in coastal and marine areas," *Journal of Ocean Engineering and Marine Energy*, vol. 2, no. 2, pp. 227–245, 2016. [Online]. Available: http://link.springer.com/10.1007/s40722-016-0044-8

[193] M. C. Easton, A. Harendza, D. K. Woolf, and a. C. Jackson, "Characterisation of a Tidal Energy Site : Hydrodynamics and Seabed Structure," in *9th European Wave and Tidal Energy Conference (EWTEC 2011)*, 2011, pp. 1–10.

[194] G. D. Egbert and L. Erofeeva, "OSU Tidal Data Inversion," 2010. [Online]. Available: http://volkov.oce.orst.edu/tides/tpxo8{_}atlas.html

[195] A. S. Bahaj, A. F. Molland, J. R. Chaplin, and W. M. J. Batten, "Power and thrust measurements of marine current turbines under various hydrodynamic flow conditions in a cavitation tunnel and a towing tank," *Renewable Energy*, vol. 32, no. 3, pp. 407–426, 2007.

[196] D. R. Plew and C. L. Stevens, "Numerical modelling of the effect of turbines on currents in a tidal channel – Tory Channel, New Zealand," *Renewable Energy*, vol. 57, pp. 269–282, sep 2013. [Online]. Available: http://linkinghub.elsevier.com/retrieve/pii/S096014811300092X

[197] R. Karsten, A. Swan, and J. Culina, "Assessment of arrays of in-stream tidal turbines in the bay of fundy," *Philosophical Transactions of the Royal Society of London A: Mathematical, Physical and Engineering Sciences*, vol. 371, no. 1985, 2013. [Online]. Available: http://rsta.royalsocietypublishing.org/content/371/1985/20120189

[198] R. Bedard, O. Siddiqui, G. Hagerman, and M. Robinson, "Survey and Characterization of TISEC Devices. Report EPRI - TP-004-NA," Tech. Rep., 2005.

[199] G. I. Gretton, "The Hydrodynamic Analysis Of A Vertical Axis Tidal Current Turbine," Ph.D. dissertation, The University of Edinburgh, 2009.

[200] MIT, "Basics of Turbulent Flow," pp. 1–10, 2012. [Online]. Available: http://www.mit.edu/course/1/1.061/www/dream/SEVEN/SEVENTHEORY.PDF

[201] S. Walker and L. Cappietti, "Experimental Studies of Turbulence Intensity around a Tidal Turbine Support Structure," *Energies*, vol. 10(4), no. 497, pp. 1–22, 2017.

[202] J. Giles, L. Myers, A. Bahaj, and B. Shelmerdine, "The downstream wake response of marine current energy converters operating in shallow tidal flows," in *Proceedings World Renewable Energy Congress*, 2011. [Online]. Available: http://eprints.soton.ac.uk/334180/

[203] I. A. Milne, R. N. Sharma, R. G. J. Flay, and S. Bickerton, "Characteristics of the onset flow turbulence at a tidal-stream power site," *Philosophical Transactions of the Royal Society A*, 2013.

[204] J. Thomson, B. Polagye, V. Durgesh, and M. C. Richmond, "Measurements of turbulence at two tidal energy sites in puget sound, WA," *IEEE Journal of Oceanic Engineering*, vol. 37, no. 3, pp. 363–374, 2012.

[205] R. J. J. Barthelmie, L. Folkerts, G. C. C. Larsen, K. Rados, S. C. C. Pryor, S. T. T. Frandsen, B. Lange, and G. Schepers, "Comparison of wake model simulations with offshore wind turbine wake profiles measured by sodar," *Journal of Atmospheric and Oceanic Technology*, vol. 23, no. 7, pp. 888–901, 2006.

[206] I. G. Bryden, S. J. Couch, A. Owen, and G. Melville, "Tidal current resource assessment," *Proceedings of the Institution of Mechanical Engineers, Part A: Journal of Power and Energy*, vol. 221, no. 2, pp. 125–135, jan 2007. [Online]. Available: http://pia.sagepub.com/lookup/doi/10.1243/09576509JPE238

[207] D. L. McCann and P. S. Bell, "Marine radar derived current vector mapping at a planned commercial tidal stream turbine array in the Pentland Firth, U.K." in *2014 Oceans - St. John's*, 2014, pp. 1–4.

[208] F. Maganga, G. Germain, J. K. G. Pinon, and E. Rivoalen, "Experimental characterisation of flow effects on marine current turbine behaviour and on its wake properties," *IET RENEWABLE POWER GENERATION*, vol. 4, no. 6, pp. 498–509, 2010.